Nonlinear interactions using neutral atomic gases

by

Benjamin David Smith

A thesis submitted in partial fulfillment of the requirements for the degree of

Doctor of Philosophy

Department of Physics
University of Alberta

Abstract

Nonlinearities in quantum systems provide some of the most intriguing physics to be exploited for quantum technologies and for quantum simulations. In this thesis, we explore quantum nonlinearities in two different contexts: The first is an experimental demonstration of coherent microwave-to-optical conversion using a warm ^{87}Rb atomic vapor located inside a cylindrical microwave cavity. Frequency conversion is essential for transferring quantum information generated in the microwave domain to optical frequencies, where it can be transmitted and networked with minimal propagation loss. A hybrid, second-order nonlinear susceptibility in the vapor enables coherent frequency conversion of single- and multi-channel microwave signals. This conversion is tunable over a large 550(30) MHz range of output optical frequencies due to the thermal Doppler broadening of the excited atomic state. This system also permits phase-correlated amplitude control of select frequency channels, providing an analog to a frequency domain beam splitter across five orders of magnitude in frequency.

The second context is a computational approach for accelerating computational solutions of the nonlinear Schrödinger equation. We employ open-source code and readily available graphics processing unit hardware. This allows us to simulate a quasi-2D version of the Gross-Pitaevskii equation, a specific type of the nonlinear Schrödinger model, where the nonlinearity arises from density-dependent scattering interactions. The equation describes a trapped, interacting, two-component Bose-Einstein condensate (BEC) subject to a spatially dependent interspin coupling. This computational approach lets us probe high-resolution spatial features—revealing an interaction-dependent phase transition—all in a reasonable amount of time.

Preface

The experimental and computational work presented in this thesis is the product of more than seven years as a member of Prof. Lindsay J. LeBlanc's Ultracold Quantum Gases Laboratory at the University of Alberta. Like the physics and experiments presented therein, my Ph.D. journey has been a case study of taking things apart and putting them back together in nonlinear, unexpected ways. For the first five years of this journey, I worked on all aspects of the ultracold Bose-Einstein condensate experiment, with the goal of spin-orbit coupling quantum simulations. Despite the effort invested, two unrelated—but equally devastating—laboratory floods and the grip of a global pandemic prompted a research change. Fortunately, a new door opened: experiments with warm atoms inside a 3D microwave cavity; with the support of Prof. LeBlanc, and the extraordinary help of fellow student Bahar Babaei and visiting Prof. Andal Narayanan, I walked through. Taking that unforeseeable redirection with their help has made all the difference for me personally. I cannot say enough of these three incredible women!

Although my journey has traversed and wound through many topics and endeavors, this thesis will primarily focus on research in the warm-atoms arena; still, I have reserved one chapter to describe a computational effort supporting ultracold experiments.

Clearly, this thesis is not the result of one person, but has relied upon the participation of many people. I wish to recognize and highlight their contributions to the following core chapters:

Chapter 6: Theory of sum-frequency generation in neutral atoms

Prof. Andal Narayanan and I developed the coherent amplitude control theory, and Prof. Andal Narayanan provided the broad-tunable nonlinear optics model.

Chapter 7: Experimental setup and methods

Scott Wilson and Tian Ooi produced the customized, Python-based cycle control program discussed in Section 7.2. Scott began in 2017 to port an equivalent LabVIEW-based program to Python, which Tian completed in 2020 and installed it on our warm atoms control computer. This version of the program is a marvelous improvement over the old one.

Michelle Sullivan and Taras Hrushevskyi assembled components of a hybrid cold-atoms-quantum system in a new laboratory space [1]. They installed the control computer and devices described in Section 7.2; assembled the laser and optics system described in Section 7.3.2; and installed the current supplies and cables used for magnetic field control [see Section 7.2.1]. Although their envisaged experiment has not yet materialized, this thesis benefitted from their preparations. Additionally, technician James Chaulk designed and manufactured the dark acrylic plastic enclosure for the preparation optics table.

Andrei Tretiakov, Brittany (Ying-Ying) Lu, and Timothy Lee performed the first experiments in the LeBlanc group using this microwave cavity and a warm atom cell consisting of a vacuum system with rubidium dispensers [2–4]. Brittany and Andrei designed and ordered the sealed vapor cell we use today, which provides improved reliability and consistency over the vacuum system.

Dr. Clinton Potts machined the microwave cavity used in this work. Various

research groups at the University of Alberta generously loaned us equipment for the duration of this work: The Prof. John Davis group loaned us their Anapico APSIN12G microwave source, Keysight E5063A vector network analyzer, and sundry microwave/RF components; the Prof. Vadim Kravchinsky group loaned us their 1-meter square, three-axis Helmholtz coil set; and the Prof. Robert Wolkow group loaned us their Tektronix RSA5100B spectrum analyzer. The Prof. Mark Freeman group also periodically loaned us their Keysight N9020B MXA spectrum analyzer and gaussmeter.

Helpful conversations with Dr. Clinton Potts, Marvin Hirschel, and Dr. Yunhu Huang shed light on microwave engineering techniques. Also, Dr. Yunhu Huang shared the Python fitting routine used to extract the cavity quality factors from S_{11} resonance data.

Bahar Babael and I worked closely together to set up and test the power feedback servo loop; we also assembled and calibrated the magnetic Helmholtz coils. Bahar also performed the COMSOL simulations shown in Section 7.6.3, provided the key insight into the ^{87}Rb metalization, and repeatedly executed skillful alignments of the microwave cavity and its coupler pin. Jichu Shi assisted Bahar and I in setting up the experiment table optics and characterizing the polarization optics. Bahar and Jichu also assembled the home-built AOM driver electronics box used in this experiment. Finally, I designed and machined the water cooling block for the vapor cell stem, and wrote the code for automating spectrum analyzer measurements.

Chapter 8: Broad-tunable and multimode microwave-to-optical conversion in a warm atomic vapor

Prof. Andal Narayanan and Bahar Babaei worked together with me on experimental characterizations and data collection. I performed the data analysis with input from

Andal Narayanan. Prof. Ray DeCorby read an early manuscript and provided helpful feedback on this work.

Chapter 9: Accelerating simulations of the pseudospinor Gross-Pitaevskii equation

Prof. Lindsay LeBlanc provided the original simulation code, which was modified by Dr. Logan Cooke and myself. Dr. Logan Cooke then produced a GPU-compatible code version and implemented a spinor model. Next, I verified the computations and modified the code to produce a fully packaged, open-source code version. I also benchmarked the code's performance on various devices and performed the example spin Hall simulations. In this work, we were supported by NVIDIA Corporation with their grant of the Titan V GPU. The NVIDIA grant proposal was written by Dr. Logan Cooke, myself, and Prof. Lindsay LeBlanc. Zaheen Farraz Ahmad graciously provided insight on GPU computing, benchmarking, and the various Python libraries available.

$$* * *$$

The publication "Smith, B.D., Babaei, B., Narayanan, A., & LeBlanc, L.J. *Microwave-to-optical conversion in a room-temperature ^{87}Rb vapor for frequency-division multiplexing control*, Commun. Phys. **6** 338 (2023)" [5] forms the basis for certain sections in Chapters 6 and Chapter 8. The text and notation have been modified for consistency and to support the format and scope of this thesis. Sections 8.1, 6.2.2, 6.2.4, 8.2.4, 8.3, 8.6, and 8.7 uses material directly from [5]. Sections 8.2.3, 8.2.5, 8.2.6, 8.4, 8.5, 8.2.8 include text and figures modified from [5]. All other sections in these chapters are unique to this thesis. The data and analysis files that support their findings are available at [6].

Chapter 9 is taken directly from the publication "Smith, B. D., Cooke, L. W., & LeBlanc, L. J. *GPU-accelerated solutions of the nonlinear Schrödinger equation for simulating 2D spinor BECs*, Comput. Phys. Commun. **275** (2022): 108314" [7].

"...That the trial of your faith,

being much more precious than of gold that perisheth,

though it be tried with fire,

might be found unto praise and honour and glory

at the appearing of Jesus Christ."

1 Peter 1:7, The Holy Bible: King James Version

To my Father in Heaven.

Acknowledgments

I wish to express my immense appreciation and respect to my supervisor, **Prof. Lindsay J. LeBlanc**. I feel privileged to have worked in your lab, and I have learned so much from your example and knowledge. Thank you for patiently guiding me with compassion and high expectations of my work and writing. I am deeply grateful for the support you provided during the various rocky patches. It has truly been an honor to be one of your students.

My gratitude also goes out to the other members of my committee: **Prof. John Davis**, for asking good questions and for caring enough to challenge and stretch me. **Prof. Frank Marsiglio**, for allowing me to learn the value of *asking* questions. Not being afraid to ask has transformed my studies and personal life.

I am also grateful to the following: The newly-minted **Dr. Logan Cook**, for passing challenging alignments with meandering conversations; for being an empathetic listener, and for sharing my curiosities and struggles. It has been a long haul. We finally made it! **Prof. Andal Narayanan**, for your compassion, imagination, and creativity. Your presence here has made an enormous difference for me. I feel very privileged to have worked with you. **Bahar Babaei**, for the incomparable help you gave me at a crucial, vulnerable time of my degree. Thank you for being you. I hope you continue to believe in you as much as I do. **Dr. Erhan Saglamyurek**, for welcoming me into the lab that first day, letting me look over your shoulder, and teaching me essential lab skills—starting with fiber coupling. **Taras Hrushevskyi**, for teaching me to operate, debug, and optimize the BEC machine; for showing me how to approach issues with confidence and optimism. "My Friend" **Anindya Rastogi**, for your wit, ready smile, and helpful demeanor. **Dr. Arina Taschillina**, for your curiosity and for helping me find a good place in the lab. Because of you, things have turned out far better than expected. **Brielle Airey**, for your indefatigable attitude and enthusiasm.

I owe a tremendous debt to my ancestors and this thesis represents their efforts as much as mine. Only naming a few, I wish to thank: My great-grandparents **Albert and Milda Backstrom**, for leaving a remote village in northern Sweden to find a better life for your family in Canada. My widowed great-grandmother **Beth**

Table of Contents

List of Tables

List of Figures

List of Symbols

Constants

$\Delta E_{\mathrm{HF}}/h$	Rubidium 87 ground state hyperfine splitting	$6.834\,682\,610\,904\,29(9)\,\mathrm{GHz}$
ϵ_0	Vacuum electric permittivity	$8.854\,187\,812\,8(13) \times 10^{-12}\,\mathrm{F\,m^{-1}}$
γ_g	$F = 1$ & 2 ground state linear gyromagnetic ratio	$7.0\,\mathrm{kHz\,\mu T^{-1}}$
$\hbar$	Reduced Planck constant	$1.054\,571\,817 \times 10^{-34}\,\mathrm{J\,s}$
μ_0	Vacuum magnetic permeability	$1.256\,637\,062\,12(19) \times 10^{-6}\,\mathrm{N\,A^{-2}}$
u	Unified atomic mass unit	$1.660\,539\,066\,60(50) \times 10^{-27}\,\mathrm{kg}$
a_0	Bohr radius	$5.291\,772\,109\,03(80) \times 10^{-11}\,\mathrm{m}$
c	Speed of light in vacuum	$299\,792\,458\,\mathrm{m\,s^{-1}}$
e	Elementary charge	$1.602\,176\,634 \times 10^{-19}\,\mathrm{C}$
k_{B}	Boltzmann constant	$1.380\,649 \times 10^{-23}\,\mathrm{J\,K^{-1}}$
m_e	Electron mass	$9.109\,383\,701\,5(28) \times 10^{-31}\,\mathrm{kg}$
m_{87}	Rubidium 87 atom mass	$1.443\,160\,60(11) \times 10^{-25}\,\mathrm{kg}$

Abbreviations & Acronyms

ADC analog-to-digital converter.

AM amplitude modulation.

AOM acousto-optic modulator.

AWG American Wire Gauge.

BEC Bose-Einstein condensate.

BS beam splitter.

CEL cateye diode laser.

CPU central processing unit.

CUDA Compute Unified Device Architecture.

DFG difference-frequency generation.

DUT device-under-test.

ECDL external cavity diode laser.

EOM electro-optic modulator.

FDM frequency-division multiplexing.

FFT fast Fourier transform.

FM frequency modulation.

FWHM full width at half maximum.

GPE Gross-Pitaevskii equation.

GPU graphics processing unit.

HWP half-waveplate.

IF intermediate frequency.

LO local oscillator.

MB Maxwell-Boltzmann.

NLSE nonlinear Schrödinger equation.

PBS polarizing beam splitter.

PD photodiode.

PM phase modulation.

QWP quarter-waveplate.

RAM random-access memory.

RBW resolution bandwidth.

RF radio frequency.

SA spectrum analyzer.

SCPI Standrd Commands for Programming Intruments.

SFG sum-frequency generation.

SG signal generator.

TE transverse electric.

TEM transverse electro-magnetic.

TM transverse magnetic.

TSSP time-splitting spectral.

VBW video bandwidth.

VNA vector network analyzer.

VRAM video random-access memory.

ZVC zero velocity class.

Chapter 1

Introduction

1.1   Reductionism and emergence

The physical universe is a complex place. It features many types of matter with their respective environments and interactions. In developing an understanding of the universe, science often takes a two-pronged strategy. The first accepts a hypothesis of the universe's structure called *reductionism*[1], which may be summarized as "small is beautiful" [11, 12]. Reductionism assumes that we can understand the universe in terms of smaller, simpler, and more "fundamental" particles and interactions. Reductionist physical theories have been so successful because they possess great explanatory power. Developing such theories has been a continuous program of physics

---

[1]This has been called "one of the most used and abused terms" in philosophy [11]. In the context of this thesis, we specifically consider *methodological* reductionism.

for at least the last 130 years since the discovery of the electron [13], however, its underpinnings may be traced back even further [14–16].

However, we don't live in a universe of "just" fundamental particles and interactions[2]. Smaller objects tend to aggregate into larger, more complex structures and generally display qualitatively new properties, behaviors, states, or dynamics not found in their smaller-scale constituents. For example, superfluidity, turbulence, and surface tension do not make sense for isolated atoms; they are emergent properties.

Therefore, *emergence*, the second approach of science, states in a nutshell: "more is different" [17]. While it accepts the hypothesis that novel behavior is (at least in principle) determined by the properties and laws of the underlying components, that connection may not be straightforward[3]. Emergence typically arises among a large number of interacting, microscopic constituents in a way that breaks fundamental symmetries or produces topological order; irreversible processes that increase the entropy of a system are also emergent [17, 19]. Thus, science begins with reductionism [17] to understand the fundamental, and then proceeds to reconstruct the emergent complexity in our universe.

1.2   Linearity and emergent nonlinearity

To understand physical phenomena, physicists often seek models and regimes that are linear. Linear systems obey the superposition principles [22], which states that

---

[2]For example, a knowledge of the Standard Model is not useful for predicting the spread of an infectious disease through a population.

[3]It is challenging to find a single, widely-accepted definition of emergence [18, 19]. In this thesis, we are using the more commonly accepted notion of *weak emergence*. In contrast, Nobel laureate Philip Anderson had the viewpoint that there are properties of a complex system that may not be derived from the constituents, even in principle [17]. His views aligns closely with the notion of *strong emergence* [20, 21].

the sum, or linear combination, of individual linear states/solutions

$$h(x) = f(x) + g(x). \tag{1.1}$$

is also a linear state/solution of the system. We typically treat classical waves linearly, and their superposition leads to, for example, constructive and destructive interference [23]. Similarly, quantum mechanics is based on the evolution of de Broglie waves [24, 25], the linearity of which is taken as one of the postulates of quantum mechanics [26]. Because of the superposition principle, linear systems are relatively easy to develop theoretically and their dynamics can be readily solved analytically or computationally.

Systems that are initially linear and quite simple in isolation display complexity, richness, and unexpected behaviors in aggregate. In the presence of interactions between many constituent objects, we should no longer expect the superposition principle to hold. For example, even though quantum mechanics is a linear theory, a Bose-Einstein condensate is governed by a nonlinear Schrödinger equation. This *emergent* nonlinearity [27] arises from collisional interactions among the constituent atoms [see Chapter 9]. Similarly, a stream of photons interacting with numerous atoms in a symmetry-broken material produces emergent photons with different energies; the superposition of electromagnetic waves breaks down and gives way to nonlinear optical properties.

Emergent nonlinearities are being increasingly integrated into practical and useful technology. Nonlinear interactions are even now routinely engineered among single photons [28, 29] and atoms [30–33] for applications in quantum computing and secure quantum communication.

1.3 Outline of this thesis

This thesis focuses on two different systems with emergent nonlinearities, having distinct constituents, environments, and interactions. The first (and the largest) component of this thesis describes a nonlinear optical experiment: optical and microwave radiation fields interact with a room-temperature gaseous vapor of elemental metal rubidium atoms to produce a new source of light at the sum-frequency of the input fields. It demonstrates the coherent conversion of information from microwave to optical frequencies, a desired tool for networking quantum devices [34]. The properties of room-temperature atoms also provide an advantage of increased conversion flexibility. Warm atoms systems are technologically relevant due to their significantly reduced technical demands compared to laser-cooled atomic systems.

In organizing this part of the thesis, we have taken a "reductionism-emergence"-like approach. We begin by outlining the basic theoretical principles: **Chapter 2** explains the emergence of the quantized electronic structure of the rubidium atoms; **Chapter 3** describes how light induces transitions among the atomic structure; **Chapter 4** considers unique properties of room-temperature atoms; and **Chapter 5** provides a high-level overview of nonlinear optical processes.

From this basic groundwork, we construct an understanding of the theory, operation, and results of the experiment: **Chapter 6** explains theoretically the emergence and properties of the microwave-to-optical process; **Chapter 7** outlines how the experimental apparatus was constructed, characterized, and calibrated; finally, **Chapter 8** presents the experimental procedure and results.

We close this thesis by considering computationally a different physical model with emergent nonlinearity: the nonlinear Schrödinger equation (NLSE). Obtaining numeric solutions is generally much more intensive for nonlinear equations than linear

ones. **Chapter 9** describes a process to significantly accelerate computations to the NLSE using simple programming tools and graphics hardware. This flexible approach may be applied for solving similar nonlinear equations.

Together, these two parts provide experimental and computational perspectives for emergent nonlinear systems involving neutral atoms. These contribute to the larger work of understanding complex physical systems.

Chapter 2

The structure of alkali atoms

2.1 Introduction

Atomic physics is concerned with the study of isolated atoms. Atoms are composed of a charged nucleus and oppositely charged surrounding electrons that are organized in a specific structure [35]. This electronic structure is produced by interactions among the electrons and the nucleus, and their motion. The principles of quantum mechanics can determine, with high accuracy, the rich nature of this structure and how it changes in response to external perturbations.

We restrict our attention to the electrically-neutral rubidium atom with an approximate mass of 87 atomic units, notated as ^{87}Rb. This isotope is an alkali atom, which means it has a single valence electron outside the filled lower shells. The electronic structure of alkali atoms is relatively simple compared to other multivalent

atoms. While the theoretical techniques and methods presented in this and subsequent chapters apply to all alkali atoms, ^{87}Rb is discussed because it is employed in the experiments of this thesis.

2.2 The atomic Hamiltonian

In this chapter, we will first briefly describe the emergence of the fixed, discrete energy level structure of the valence electron. This description is based–but will tread as lightly as possible–on the well-worn path of the hydrogen atom solutions [36, 37].

Energy levels are abstractions of the electron's quantized states $|\psi_\xi\rangle$ and their structure (indexed by ξ) is responsible for the discrete optical transmission/absorption spectra produced by atomic gases [35, 38]. The states are solutions of the time-independent Schrödinger equation [37]

$$\hat{H}_{\mathrm{at}}|\psi_\xi\rangle = E_\xi|\psi_\xi\rangle, \tag{2.1}$$

where E_ξ is one of the corresponding energy eigenvalues of the isolated atom Hamiltonian $\hat{H}_{\mathrm{at}}$. This operator can be decomposed into several different terms[1] as

$$\hat{H}_{\mathrm{at}} = \left[\hat{H}_0 + \hat{V}(r)\right] + \hat{H}_{\mathrm{SO}} + \hat{H}_{\mathrm{HF}} + \hat{H}_{\mathrm{Z}}. \tag{2.2}$$

The terms in the brackets are analogous to the classical kinetic and potential energies of the electron, where $\hat{V}(r)$ represents the effect of the central nucleus' electrostatic Coulomb potential on the electron, where $r = |\mathbf{r}|$. The final three terms represent the spin-orbit $\hat{H}_{\mathrm{SO}}$, hyperfine $\hat{H}_{\mathrm{HF}}$, and Zeeman $\hat{H}_{\mathrm{Z}}$ perturbing interactions. The

---

[1]This Hamiltonian does not include the relativistic kinetic energy correction and Darwin terms; they generally affect the energies of the states, but a description of their origin goes beyond the scope of this thesis, and they are not included for brevity. This expression also does not consider the quantized electromagnetic field, fluctuations of which are responsible for spontaneous de-excitation and emission from higher energy atomic states.

following sections describe how each interaction affects the structure of electron states in the atom.

In general, the electron states $|\psi_\xi\rangle$ depend on spatial coordinates and various combinations of angular momenta. To simplify the description, these variables can be abstracted further to a set of quantum numbers, e.g. $\xi = \{n\ell m_\ell \dots\}$, that emerges due to physical constraints and conditions. Thus the state can be alternatively notated as $|\psi_\xi\rangle \equiv |\xi\rangle \equiv |n\ell m_\ell \dots\rangle$.

The left-to-right order of the three perturbations in 2.2 reflects a weakening hierarchy of their interaction strengths. Each perturbation splits electron energy levels into new levels that are separated by the interaction energy. This splitting hierarchy can be seen in Figure 2.1. The splitting is experimentally discernible via various forms of atomic spectroscopy [39]. The split levels are described by additional quantum numbers in ξ. The use of a particular set of quantum numbers also reflects a choice of basis (i.e. Hilbert space) in which to express the Hamiltonian. A "good" choice of ξ [40] will make the eigenstates of $\hat{H}_{\mathrm{at}}$ stationary, meaning they do not evolve in time [35]; both the unperturbed and perturbing Hamiltonians will satisfy Equation 2.1 for the same choice of $|\xi\rangle$.

2.3   Gross structure

The gross (or coarse) structure of the electron states emerges from the kinetic and potential energy terms in 2.2 and thus depends on spatial coordinates. These terms significantly influence the electron's energy. If we temporarily ignore the three other perturbing terms, then the resulting eigenstates of this Hamiltonian have the form $|n\ell m_\ell\rangle \equiv R_{n\ell}(r)Y_\ell^{m_\ell}(\theta, \phi)$, composed of radial $R_{n\ell}$ and angular $Y_\ell^{m_\ell}$ components, with radial r, polar θ, and azimuthal ϕ spherical coordinates [37]. The n, ℓ, and
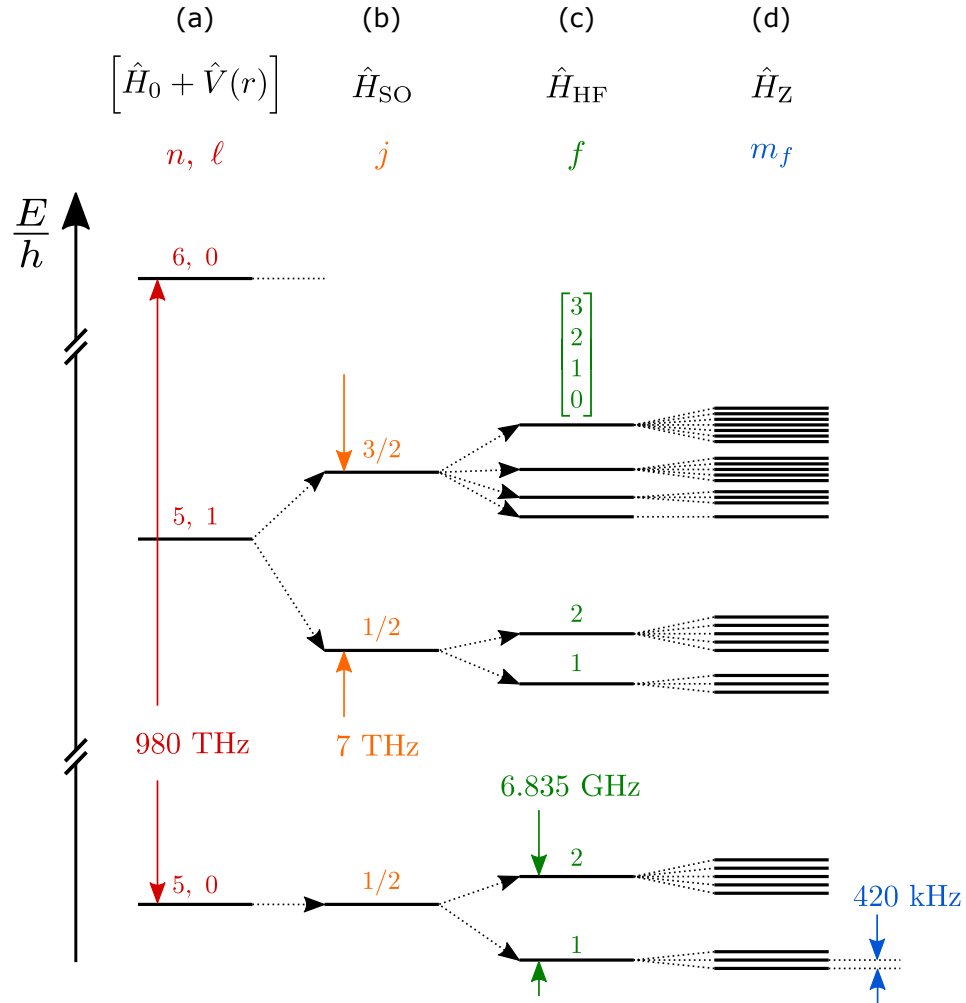
Figure 2.1: Energy level diagram of the rubidium 87 valence electron. The (a) gross, (b) fine, (c) hyperfine, and (d) Zeeman structures emerge from corresponding interactions in $\hat{H}_{\mathrm{at}}$. The horizontal lines represent the electron energy levels, and the number above each level is the respective quantum number. Characteristic level splitting magnitudes are provided for each interaction. This level diagram is not to scale.

m quantum numbers come from physical boundary conditions at $r = 0$ ($|R_{n\ell}(r)|^2$ is finite) and $r \to \infty$ ($|R_{n\ell}(r)|^2 \to 0$), and also because the states are single-valued at every point in space.

The principle quantum number $n \in \mathbb{N}$ determines the splitting of the gross electron structure. For alkali atoms, the energies of levels in this structure are approximately given by [40]

$$E_{n\ell} = -hc\frac{R_\infty}{n^{*2}}, \tag{2.3}$$

where an effective principle quantum number n^* accounts for interactions between the valence and core electrons[2]. Using Equation 2.3, we estimate the lowest gross structure splitting for ^{87}Rb, using $n^* = 1.81$ for the S ($\ell = 0$) states [40, 41], to be $h \times 600$ THz. This is a decent order-of-magnitude estimate for the $h \times 980$ THz measured $5S - 6S$ level separation in ^{87}Rb [38].

The $Y_\ell^{m_\ell}$ angular components are spherical harmonic functions. They are inherently linked to the quantized orbital angular momentum operator

$$\hat{\mathbf{L}} = \hat{L}_x\hat{e}_x + \hat{L}_y\hat{e}_y + \hat{L}_z\hat{e}_z \equiv (\hat{L}_x, \hat{L}_y, \hat{L}_z), \tag{2.4}$$

where $\hat{e}_i$ are Cartesian unit vectors. The $Y_\ell^{m_\ell}$ functions are characterized by two quantum numbers $\ell \in \mathbb{Z}^{0+} : \ell \le n - 1$ and $m_\ell \in \mathbb{Z} : |m_\ell| \le \ell$. In fact, $Y_\ell^{m_\ell}$ are eigenfunctions in the position basis of the squared angular momentum operator $\hat{\mathbf{L}}^2$ and the z-component $\hat{L}_z$,

$$\hat{\mathbf{L}}^2 \, Y_\ell^{m_\ell}(\theta, \phi) = \hbar^2\ell(\ell + 1) \, Y_\ell^{m_\ell}(\theta, \phi) \tag{2.5a}$$

$$\hat{L}_z \, Y_\ell^{m_\ell}(\theta, \phi) = \hbar m_\ell \, Y_\ell^{m_\ell}(\theta, \phi). \tag{2.5b}$$

These spherical harmonic functions are quantized in $\mathbb{R}^3$ space [42] along a particular *quantization* axis; in this thesis, they are quantized along the z-axis. The eigenvalue

---

[2]In this definition, $n^* = n - \delta_\ell$, where the angular momentum-dependent quantum defect δ_ℓ is an empirical correction to n.

$\hbar m_\ell$ is the atomic angular momentum projected along that axis [26, 37]. The use of a particular quantization axis represents an arbitrary choice of basis. However, there are often specific directions where the states and operators take on a simple form. For example, it is usually convenient to choose a quantization axis along the direction of an externally applied magnetic field. In the absence of an external field, the propagation direction of a polarized, interacting light beam is also an appropriate choice.

2.4 Interlude: Treatment of angular momentum operators

Beyond the gross structure, most of the interesting electronic structure emerges due to interactions between various sources of quantized angular momentum inside the atom. These include the electron's orbital angular momentum, the electron's intrinsic spin angular momentum, and the nucleus' intrinsic spin angular momentum. Angular momentum, in the quantum sense, is described by operators [e.g. see Equation 2.4]. The nature of these operators and what "interactions" between them mean are the subjects of this brief interlude.

2.4.1 Spherical Vector Operators

Consider the difference between classical scalar and vector quantities. What differentiates the two is the answer to the question: "If I tilt my head, does the quantity change?" For scalar quantities such as energy, temperature, and mass, the answer is no. The components of vector quantities such as acceleration, electric field, or angular momentum clearly do change when either the vector or coordinate system is rotated[3].

---

[3]Technically, angular momentum is a *pseudovector*; it transforms under rotations just like proper vectors, but the components do not invert under parity operations. However, since this discussion

In quantum mechanics, continuous quantities are replaced by operators, thus it is possible to define both scalar and vector operators. Scalar operators, such as the kinetic and potential energy[4] operators are invariant under rotations. Vector operators, such as $\hat{\mathbf{L}}$ [Equation. 2.4], are generalizations of scalar operators with unique rotational properties. Even further generalizations are called tensor operators, with elements $T_{fgh\ldots}$. A tensor is characterized by its rank k, which is equal to the number of subindices. Scalar operators have $k = 0$, while vector operators have $k = 1$. In the context of this thesis, we will limit the discussion to scalar and vector operators.

When a vector operator is rotated in 3D space, its components transform into each other, as encapsulated in the commutation relation

$$\left[\hat{L}_i, \hat{L}_j\right] = i\hbar\epsilon_{ijk}\hat{L}_k, \tag{2.6}$$

where ϵ_{ijk} is the antisymmetric Levi-Civita symbol. In fact, we may consider Equation 2.6 as the *definition* of a vector operator [41]. For the discussion of rotations, it is sometimes more convenient to convert the vector operators from the Cartesian basis to the so-called spherical basis. The spherical and Cartesian unit vectors are related as [43]

$$\hat{e}_\pm \equiv \frac{1}{\sqrt{2}}(\mp\hat{e}_x - i\hat{e}_y) \tag{2.7a}$$

$$\hat{e}_0 \equiv \hat{e}_z. \tag{2.7b}$$

This may be used to re-express the vector operator as

$$\hat{\mathbf{L}} = \hat{L}_1\hat{e}_+ + \hat{L}_0\hat{e}_0 + \hat{L}_{-1}\hat{e}_-, \tag{2.8}$$

focuses on rotations instead of inversions, for fixed reference frames, the term *vector* is used to describe both quantities.

[4]This is only true when the potential is central, meaning $V(\mathbf{r}) = V(|\mathbf{r}|)$.

where

$$\hat{L}_{\pm 1} \equiv \frac{1}{\sqrt{2}} \left[\mp \hat{L}_x - i\hat{L}_y \right] \tag{2.9a}$$

$$\hat{L}_0 \equiv \hat{L}_z. \tag{2.9b}$$

In this form, $\hat{\mathbf{L}}$ is a *spherical* vector operator. There is a deep connection between spherical vector operators and spherical harmonics. For example, the position vector operator $\mathbf{r}$ in the spherical basis has components $r_q = r\sqrt{\frac{4\pi}{3}}Y_1^q(\theta, \phi)$, where $q \in \{+1, 0, -1\}$. This says that the vector operator components have the same form and transform under rotations exactly like spherical harmonic elements Y_1^q. This is true generally for all spherical vector operators [43]. Figure 2.2 shows the cubic (Cartesian) harmonics P_i^1 functions with the corresponding spherical harmonics Y_q^1. The two sets of functions are related via the basis transformation Equation 2.7 [44].
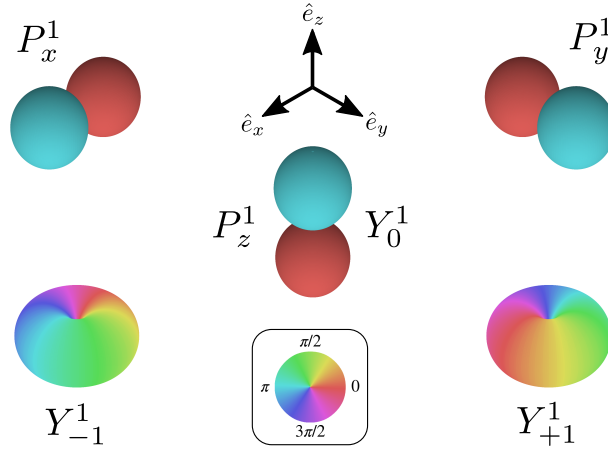
Figure 2.2: Comparison of the cubic and spherical harmonic components. For $\ell = 1$, the cubic P_i^1 and spherical Y_q^1 harmonic functions are related to each other by the transformation Equation 2.7. The colors reflect the functions' complex phase.

2.4.2   Addition of spherical vector operators

We now consider the addition of two vector operators. For simplicity, assume we have two generic angular momentum vector operators $\hat{\mathbf{J}}_1$ and $\hat{\mathbf{J}}_2$. Each of these acts on

distinct basis states $|j_i m_i\rangle$ as[5]

$$\hat{\mathbf{J}}_1^2 |j_1 m_1\rangle = \hbar^2 j_1 (j_1 + 1) |j_1 m_1\rangle \tag{2.10a}$$

$$\hat{J}_{1z} |j_1 m_1\rangle = \hbar m_1 |j_1 m_1\rangle \tag{2.10b}$$

and

$$\hat{\mathbf{J}}_2^2 |j_2 m_2\rangle = \hbar^2 j_2 (j_2 + 1) |j_2 m_2\rangle \tag{2.11a}$$

$$\hat{J}_{2z} |j_2 m_2\rangle = \hbar m_2 |j_2 m_2\rangle. \tag{2.11b}$$

When these operators combine to form the total angular momentum operator $\hat{\mathbf{J}} = \hat{\mathbf{J}}_1 + \hat{\mathbf{J}}_2$, the new relations become

$$\hat{\mathbf{J}}^2 |jm\rangle = \hbar^2 j (j + 1) |jm\rangle \tag{2.12a}$$

$$\hat{J}_z |jm\rangle = \hbar m |jm\rangle \tag{2.12b}$$

where the possible values of j are "triangle" combinations of j_1 and j_2

$$j \in \{|j_1 - j_2|, |j_1 - j_2 + 1|, \ldots, j_1 + j_2 - 1, j_1 + j_2\}. \tag{2.13}$$

This triangle condition will be notated compactly as $\triangle(j; j_1 j_2)$.

These new basis states $|jm\rangle$ are composed of certain combinations of the original states $|j_1 m_1; j_2, m_2\rangle$. This can be seen by projecting with the unity operator onto the new states.

$$|jm\rangle = \sum_{m_1, m_2} |j_1 m_1; j_2, m_2\rangle \langle j_1 m_1; j_2, m_2 | jm \rangle. \tag{2.14}$$

The inner product in the above expression is a real[6] constant called a Clebsch-Gordan (CG) coefficient. It states how strongly two angular momentum states couple to give

---

[5]Note the distinction between an operator $\hat{J}$ (capital, with a ˆ hat), its eigenstate $|j\rangle$ (lowercase, bra-ket), and its numerical eigenvalue factor j (lowercase).

[6]According to the common Condon-Shortly convention [45].

a third. Because of this, $|jm\rangle$ is known as the coupled basis, and $|j_1m_1; j_2, m_2\rangle$ as the uncoupled basis. We can alternatively express the CG coefficient as [41]

$$\langle j_1m_1; j_2m_2|jm\rangle = (-1)^{-j_1+j_2-m}\sqrt{2j+1}\begin{pmatrix} j_1 & j_2 & j \\ m_1 & m_2 & -m \end{pmatrix}, \qquad (2.15)$$

where the 2x3 matrix of values within the parentheses is called the Wigner 3j-symbol. Like the CG coefficient, the 3j-symbol is a real constant that expresses the coupling between two angular momenta. The explicit forms of the CG coefficient and 3j-symbol are quite complicated, but they can be read from tables [36], or readily calculated using computer algebra systems such as *Mathematica* [46], or from Python packages such as SymPy [47] and Alkali Rydberg Calculator [48]. The value of the 3j-symbol is zero unless the elements in the bottom row sum to zero, i.e. $m_1 + m_2 = m$; it is also zero unless the triangle condition $\triangle(j; j_1j_2)$ is satisfied. Furthermore, the 3j-symbol is invariant under even permutations of the columns and picks up a factor of $(-1)^{j_1+j_2+j}$ under odd permutations.

If we desire to add three arbitrary angular momenta $\left(\hat{\mathbf{J}}_1, \hat{\mathbf{J}}_2, \hat{\mathbf{J}}_3\right)$ together, the situation becomes more complicated. There is no longer a unique way to combine three angular momenta to get a fourth: one could choose to first define an intermediate $\hat{\mathbf{J}}_a = \hat{\mathbf{J}}_1 + \hat{\mathbf{J}}_2$, and then define $\hat{\mathbf{J}} = \hat{\mathbf{J}}_a + \hat{\mathbf{J}}_3$; alternatively, one could choose to first define an intermediate $\hat{\mathbf{J}}_b = \hat{\mathbf{J}}_2 + \hat{\mathbf{J}}_3$, and then define $\hat{\mathbf{J}} = \hat{\mathbf{J}}_1 + \hat{\mathbf{J}}_b$. In other words, angular momenta vector operators do not have the same additive associativity property as real numbers. The proper way to combine all these components using the so-called Wigner 6j-symbol

$$\begin{Bmatrix} j_3 & j & j_a \\ j_1 & j_2 & j_b \end{Bmatrix}, \qquad (2.16)$$

a 2x3 matrix within curly brackets. Like the 3j-symbol, it is a real number. Its explicit form is a nontrivial combination (i.e. sums and products) of CG coefficients

of the constituent angular momenta states; however, it can be readily calculated with computer software. It has the properties that it is invariant under (1) any permutation of the columns, and (2) the exchange of upper and lower elements in any two columns [49]. It is equal to zero unless the triangle condition 2.13 is satisfied for all the following combinations of elements:

$$\triangle (j; j_1, j_b), \tag{2.17a}$$

$$\triangle (j; j_3, j_a), \tag{2.17b}$$

$$\triangle (j_a; j_1, j_2), \tag{2.17c}$$

$$\triangle (j_b; j_2, j_3). \tag{2.17d}$$

These triangle conditions are preserved for the permutation operations stated above. While we have defined the CG coefficient, 3j-, and 6j-symbols in terms of angular momentum vector operators, they can be generally applied to represent the addition of any two or three spherical vector operators.

There is an important and useful theorem for computing the matrix elements of spherical vector operator components. The Wigner-Eckart theorem can be stated as

$$\langle j'm'|T_q^1|jm\rangle = \langle jm; q1|j'm'\rangle\langle j'||\mathbf{T}||j\rangle, \tag{2.18}$$

where T_q^1 is the qth component of a spherical vector operator $\mathbf{T}$ (i.e. a spherical tensor operator of rank $k = 1$)[7]. Specifically, this theorem relates the matrix element of a vector operator *component* to the product of a CG coefficient and $\langle j'||\mathbf{T}||j\rangle$, a reduced matrix element of the *vector operator*. The matrix element is "reduced" in the sense that the details and character of the specific qth component have been factored out into the CG coefficient. The resulting reduced matrix element is simply

---

[7]In the spherical harmonics Y_ℓ^m, ℓ is the rank and m is the element index. Notice that the order of the super/subscripts has been reversed for the element of the general spherical tensor operator T_q^k compared to the spherical harmonics.

a number, one which can be calculated either as a complicated integral or determined from independent physical quantities [50].

Sometimes in atomic physics, the T_q^1 of interest is a component of the electromagnetic dipole operator (d_q for electric dipole or μ_q for magnetic dipole) that induces transitions from states $|jm\rangle \to |j'm'\rangle$. In this context, the qth component refers to the polarization component (in the spherical basis) of the electromagnetic field "seen" by the atomic dipole. The power of the Wigner-Eckart theorem is that once $\langle j'||\mathbf{T}||j\rangle$ is calculated, it is easy to compute the matrix elements of any T_q^1 with the appropriate CG coefficient. As will be discussed in Section 3.2.3, the familiar selection rules of atomic transitions are simply manifestations of the properties of the electromagnetic dipole CG coefficients.

2.5 Fine structure

The fine structure of the electron is a correction that splits the gross structure levels. It emerges from a coupling between the electron's orbital angular momentum $\hat{\mathbf{L}}$ and its intrinsic spin angular momentum $\hat{\mathbf{S}}$. Hence, it is called the spin-orbit interaction, and its scalar Hamiltonian has the form

$$\hat{H}_{\mathrm{SO}} = \beta_{n\ell}\hat{\mathbf{L}} \cdot \hat{\mathbf{S}}, \tag{2.19}$$

where $\beta_{n\ell}$ is a constant that depends on the orbital angular momentum and the principle quantum number. The new states split by this interaction are therefore combinations of the gross and electron spin states, $|n\ell m_\ell; sm_s\rangle$. The expectation value of $\hat{H}_{\mathrm{SO}}$

$$\Delta E_{\mathrm{SO}} = \langle n\ell m_\ell; sm_s|\beta_{n\ell}\hat{\mathbf{L}} \cdot \hat{\mathbf{S}}|n\ell m_\ell; sm_s\rangle \tag{2.20}$$

gives the energy shift of the split sub-levels.

It turns out that separate orbital and spin angular momentum bases is a bad choice of basis in which to compute ΔE_{SO}. It is better to work in the coupled basis $|njm_j\rangle$[8] formed by the total electron angular momentum vector operator

$$\hat{\mathbf{J}} = \hat{\mathbf{L}} + \hat{\mathbf{S}}. \tag{2.21}$$

The square of $\hat{\mathbf{J}}$ is a scalar operator with the form

$$\hat{\mathbf{J}}^2 = \hat{\mathbf{L}}^2 + \hat{\mathbf{S}}^2 + 2\hat{\mathbf{L}} \cdot \hat{\mathbf{S}}, \tag{2.22}$$

which we rearrange to obtain

$$\hat{\mathbf{L}} \cdot \hat{\mathbf{S}} = \frac{1}{2} \left(\hat{\mathbf{J}}^2 - \hat{\mathbf{L}}^2 - \hat{\mathbf{S}}^2 \right). \tag{2.23}$$

Thus the spin-orbit Hamiltonian is proportional to the difference of three scalar operators that each commute with the unperturbed Hamiltonian. Thus, the basis change to $|jm_j\rangle$ keeps the Hamiltonian diagonal with stationary eigenstates.

To project onto the $|jm_j\rangle$ basis, we substitute Equations 2.23 and 2.19 into Equation 2.20 and insert "resolutions of unity" on either side of $\hat{H}_{\mathrm{SO}}$ to obtain

$$\Delta E_{\mathrm{SO}} = \sum_{\substack{jj' \\ m_j m_j'}} \langle \ell m_\ell; s m_s | j' m_j' \rangle \langle j' m_j' | \frac{\beta_{n\ell}}{2} \left(\hat{\mathbf{J}}^2 - \hat{\mathbf{L}}^2 - \hat{\mathbf{S}}^2 \right) |jm_j\rangle \langle jm_j | \ell m_\ell; s m_s \rangle. \tag{2.24}$$

We identify the inner products on the left and right of the R.H.S. as Clebsch-Gordan coefficients and replace the operators with their eigenvalues

$$\Delta E_{\mathrm{SO}} = \sum_{\substack{jj' \\ m_j m_j'}} \delta_{jj'} \delta_{m_j m_j'} \langle \ell m_\ell; s m_s | j' m_j' \rangle \langle jm_j | \ell m_\ell; s m_s \rangle$$

$$\times \frac{\beta_{n\ell} \hbar^2}{2} \left[j(j+1) - \ell(\ell+1) - s(s+1) \right] \tag{2.25}$$

$$= \frac{\beta_{n\ell} \hbar^2}{2} |\langle \ell m_\ell; s m_s | jm_j \rangle|^2 \left[j(j+1) - \ell(\ell+1) - s(s+1) \right].$$

[8]The principle quantum number n modifies the strength of the spin-orbit interaction in multi-electron atoms. However, because the fundamental physics of the coupling is unchanged, n will be suppressed in subsequent basis state labels.

The quantum numbers $\xi = \{n\ell s j m_j\}$ are abstractions of the electronic states. Another common way to label the states split by $\hat{H}_{\mathrm{SO}}$ is called spectroscopic notation. In this form, the states are depicted by a symbol of the form[9]

$$n^{\ 2s+1}X_j^{(\ell)}, \tag{2.26}$$

where $X^{(\ell)}$ is a letter corresponding the value of ℓ: S for $\ell = 0$; P for $\ell = 1$; D for $\ell = 2$; F for $\ell = 3$, etc. For example, $s = \frac{1}{2}$ in alkali atoms, therefore j takes on only two values $j = \ell \pm \frac{1}{2}$ for $\ell > 0$ [see Equation 2.13]. The ground state of the rubidium valence electron ($n = 5$) has $\ell = 0$ and $j = \frac{1}{2}$, and thus can be notated as 5 ^{2}S$_{1/2}$; the first excited state with $\ell = 1$ is split into two levels, 5 ^{2}P$_{1/2}$ and 5 ^{2}P$_{3/2}$. This fine structure doublet has an energy separation of $h \times 7.1$ THz, more than a hundred times smaller than the lowest gross structure separation. The transition lines from the ground state are sometimes denoted respectively as D$_1$ and D$_2$. The optical-domain wavelengths of these two transitions are 794.978 nm and 780.241 nm [38, 50], and are probed by optical spectroscopy.

2.6   Hyperfine structure

The hyperfine structure of the electron is an additional correction that splits the fine structure levels. It emerges from a coupling between the total electron angular momentum $\hat{\mathbf{J}}$ and the intrinsic spin angular momentum of the nucleus $\hat{\mathbf{I}}$. The Hamiltonian for the hyperfine interaction has the form

$$\hat{H}_{HF} = A_{n\ell s}\hat{\mathbf{I}} \cdot \hat{\mathbf{J}}, \tag{2.27}$$

---

[9]Sometimes the n and $2s + 1$ values are self-evident and omitted from the spectroscopic symbol.

where $A_{n\ell s}$ is a constant. The states split by this interaction are therefore a combination of the electron and nuclear angular momentum states, $|jm_j; Im_I\rangle$, where[10]

$$\hat{\mathbf{I}}^2|Im_I\rangle = \hbar^2 I(I+1)|Im_I\rangle \tag{2.28a}$$

$$\hat{I}_z|Im_I\rangle = \hbar m_I|Im_I\rangle. \tag{2.28b}$$

The value of I depends on the specific atomic isotope; for example, $I = 3/2$ in ^{87}Rb, while $I = 5/2$ in ^{85}Rb.

We next apply the exact same procedure as for computing the fine structure by changing to the coupled basis $|fm_f\rangle$ determined by the total atomic angular momentum operator

$$\mathbf{F} = \hat{\mathbf{J}} + \hat{\mathbf{I}}. \tag{2.29}$$

Next, the energy shift of the coupled basis states is found to be

$$\Delta E_{\text{HF}} = \frac{A_{n\ell s}\hbar^2}{2}|\langle jm_j; Im_I|fm_f\rangle|^2 \left[f(f+1) - j(j+1) - I(I+1)\right]. \tag{2.30}$$

The electron levels of ^{87}Rb experience this hyperfine splitting in the ground and excited states. In the electronic ground S$_{1/2}$ state, f takes on two values $f \in |j\pm3/2| = \{1, 2\}$. The energy difference between these two ground state hyperfine levels is $h \times 6.835$ GHz, about 1000 times smaller than the fine structure doublet separation. This separation is typically probed with microwave spectroscopy.

2.7 Zeeman structure

The Zeeman effect is the final, and smallest correction to the structure of the electron states that we will consider. It emerges due to the interaction of the atom's magnetic

---

[10]To avoid confusing usage of the lowercase i, the eigenstate $|I\rangle$ and eigenvalue factor I both use the capital letter I.

dipole $\hat{\boldsymbol{\mu}}$ with an external magnetic field $\mathbf{B}$. The Hamiltonian describing this effect is given by

$$\hat{H}_{\mathrm{Z}} = -\hat{\boldsymbol{\mu}} \cdot \mathbf{B}, \tag{2.31}$$

where the magnetic dipole has contributions from all sources of angular momentum in the atom [50]

$$\hat{\boldsymbol{\mu}} = -\frac{\mu_{\mathrm{B}}}{\hbar} \left(g_\ell \hat{\mathbf{L}} + g_s \hat{\mathbf{S}} + g_I \hat{\mathbf{I}} \right). \tag{2.32}$$

and where μ_{B} is the Bohr magneton and the g-factors relate the angular momenta to their respective magnetic moments[11]

We will consider the situation when the magnetic field is relatively weak, i.e. the energy shift from $\hat{H}_{\mathrm{Z}}$ is small compared to the hyperfine splitting [43]. In this case, $|f, m_f\rangle$ is a good basis to evaluate the expectation values of $\hat{H}_{\mathrm{Z}}$. By projecting $\hat{\boldsymbol{\mu}}$ onto the total angular momentum vector $\mathbf{F}$, we can derive the expression for the Zeeman energy shift of hyperfine levels [26, 40, 43]

$$\Delta E_{\mathrm{Z}} = \mu_{\mathrm{B}} g_f m_f B, \tag{2.33}$$

where g_f is the Landé g-factor. This interaction splits a hyperfine level into $2f + 1$ separate levels, each indexed by a distinct $m_f \in \{-f, -f + 1, \ldots, f - 1, f\}$. For the ground state hyperfine levels of ^{87}Rb, $g_f = -1/2$ for $f = 1$ and $g_f = 1/2$ for $f = 2$. The gyromagnetic ratio $\gamma_g \equiv \mu_{\mathrm{B}} g_f = 7.0$ kHz/μT [50]. For a typical geomagnetic field of 60 μT, this splits the levels by about $\Delta E_{\mathrm{Z}} = 420$ kHz. This separation is typically probed by radio-frequency spectroscopy.

---

[11]The experimental values for ^{87}Rb are $g_s = 2.002\ 319\ 304\ 373\ 7(80)$ and $g_I = -0.000\ 995\ 141\ 4(10)$. A good approximation of g_ℓ is $g_\ell \simeq 1 - m_e/m_{87}$ [50].

Chapter 3

Transitions in alkali atoms

3.1 Transitions in two-level atoms

3.1.1 Introduction

After establishing the rich structure of electrons in alkali atoms, we now consider a simplified, idealized model for inducing transitions between electron states. This semiclassical model [40, 51] consists of two quantized electron states and a classical, monochromatic electromagnetic (EM) wave (e.g. optical, microwave, or radio frequency radiation) that stimulates transitions between the states. In this "two-level approximation" of real atoms, the basis states are denoted as $|1\rangle$ and $|2\rangle$, with energies $E_1 = 0$ and $E_2 = \hbar\omega_0$. The elements $|1\rangle$ and $|2\rangle$ are orthonormal, meaning their inner product $\langle i|j\rangle = \delta_{ij}$. The atom's electron may interact with the magnetic $\mathbf{B}(z,t)$

or electric $\mathbf{E}(z, t)$ component of an electromagnetic field, assumed to propagate in one direction along the z-axis and oscillating with angular frequency ω. A plane, uniform electric wave, for example, has the form $\mathbf{E}(z, t) = \mathcal{E}_0 \hat{e}_x \left[\frac{1}{2} e^{i(kz - \omega t)} + \text{H.C.} \right]$. We can simplify later calculations by expanding the spatial part of the exponential as

$$e^{ikz} \approx 1 + (ikz) + \frac{1}{2!}(ikz)^2 + \dots \tag{3.1}$$

and retaining only the lowest order of this expression. This "dipole" or "long-wavelength" approximation [43] effectively removes the spatial-dependence of the wave; the field amplitude $\mathcal{E}_0$ is considered constant over the region occupied by the atom. This approximation is valid when $\lambda \gg a_0$, where $\lambda = c/2\pi\omega$ is the wavelength of the incoming radiation and a_0 is the Bohr radius, the characteristic atomic size.

A magnetic dipole (M1) transition occurs when $\mathbf{B}(t) = \mathcal{B}_0 \hat{e}_z \cos(\omega t)$ reorients the electron's magnetic moment $\hat{\boldsymbol{\mu}}$. In contrast, $\mathbf{E}(t) = \mathcal{E}_0 \hat{e}_z \cos(\omega t)$ physically displaces an atom's bound electron to produce an electric dipole $\mathbf{d} = -e\mathbf{r}$, where $-e$ is the charge of the electron; this induced dipole then interacts again with $\mathbf{E}(t)$ in an electric dipole (E1) transition. In the dipole approximation, the magnetic and electric dipole interaction Hamiltonians[1] are $\hat{H}_{\text{int}}^{(\text{M1})}(t) = -\hat{\boldsymbol{\mu}} \cdot \mathbf{B}(t)$ and $\hat{H}_{\text{int}}^{(\text{E1})}(t) = e\mathbf{r} \cdot \mathbf{E}(t)$. Magnetic dipole transitions are much weaker than electric ones. Their relative strength is given by the ratio of matrix elements [26]

$$\frac{\langle \psi_2 | \hat{H}_{\text{int}}^{(\text{M1})} | \psi_1 \rangle}{\langle \psi_3 | \hat{H}_{\text{int}}^{(\text{E1})} | \psi_1 \rangle} \simeq \frac{a_0}{\lambda_0} \sim 5 \times 10^{-5}. \tag{3.2}$$

In the treatments that follow, we determine the time evolution of the electron's state subject to an E1 perturbation[2]. We first examine a *closed* two-level system, perfectly isolated from its environment where the state is represented as a normalized

---

[1] Two-photon electric and quadrupole (E2) transitions [26] are also possible and have the same strength as M1 transitions. Their treatment goes beyond the scope of this thesis.

[2] These methods also pertain to M1 transitions.

vector in the two-dimensional basis. In the second approach, we examine an *open* system, where an interacting environment induces spontaneous decay and relaxation of the electron. When dissipation cannot be neglected, the electron state is best represented as a Hermitian density matrix. Both techniques can be generalized to an arbitrary number of basis elements. Each assumes that the atomic density is low enough to ignore absorption, and that the radiation field is weak enough to neglect nonlinear optical effects [51].

3.1.2   Closed quantum system
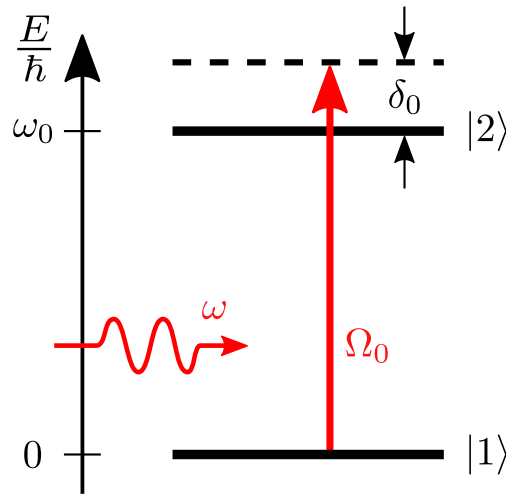
Figure 3.1: Energy level diagram of driven two-level system. A classical electromagnetic wave of frequency ω drives transitions between $|1\rangle$ and $|2\rangle$. The Rabi frequency Ω_0 and detuning δ_0 are defined in the text.

We first consider the time-evolution of the electron state $|\psi(t)\rangle$ in a closed two-level quantum system [26, 40, 43] driven by an oscillating electromagnetic field. In this idealized model depicted in Figure 3.1, the electron state is generally a superposition

of the basis element kets $|1\rangle$ and $|2\rangle$ as

$$|\psi(t)\rangle = c_1(t)|1\rangle + c_2(t)|2\rangle, \tag{3.3}$$

where c_i are complex, time-dependent amplitude coefficients, and $|c_i|^2$ are the basis populations. Because the system is free of dissipation from environmental perturbations, $|\psi(t)\rangle$ is normalized for all t such that $|c_1(t)|^2 + |c_2(t)|^2 = 1$. The state evolves according to the time-dependent Schrödinger equation

$$i\hbar\frac{\partial}{\partial t}|\psi(t)\rangle = \hat{\mathcal{H}}(t)|\psi(t)\rangle, \tag{3.4}$$

where the total Hamiltonian operator

$$\hat{\mathcal{H}}(t) = \hat{H}_{\text{at}} + \hat{H}_{\text{int}}^{(\text{E1})}(t) \tag{3.5}$$

is composed of the bare atomic $\hat{H}_{\text{at}} = \hbar\omega_0|2\rangle\langle 2|$ and E1 interaction terms. Analytical solutions to Equation 3.4 are initially complicated by the time-dependence of $\hat{H}_{\text{int}}^{(\text{E1})}(t)$. In the following, we show how a unitary transformation (i.e. change of basis) can approximately remove the time dependence from $\hat{\mathcal{H}}$, allowing for analytical solutions. While unitary transformations change the basis elements, they leave the eigenvalues unchanged. Thus, we are guaranteed the same spectrum and probabilities.

We begin by seeking concrete representations of $\hat{\mathcal{H}}$ and $|\psi(t)\rangle$ in the two-level basis. We do this by first plugging Equation 3.3 and 3.5 into Equation 3.4 to obtain

$$i\hbar\left(\frac{\partial c_1}{\partial t}|1\rangle + \frac{\partial c_2}{\partial t}|2\rangle\right) = \hbar\omega_0|2\rangle - d_0\mathcal{E}_0\cos(\omega t)\left(c_1|1\rangle + c_2|2\rangle\right), \tag{3.6}$$

where $d_0 \equiv -e\mathbf{r}\cdot\hat{e}_z = -er_0$ is an E1 dipole operator element in the spherical basis. (The explicit time dependence of $c_i(t)$ has been suppressed here and going forward.) Taking inner products of both sides of Equation 3.6 with each of the basis element bras $\langle i|$ produces two coupled, first-order differential equations of the amplitudes c_i.

Based on the orthogonality of the basis elements and the fact that the dipole operator's symmetry only admits nonzero off-diagonal matrix elements (i.e. the diagonal matrix elements $\langle i|d_0|i\rangle = 0$), we obtain

$$i\hbar\frac{\partial c_1}{\partial t} = -c_2\mathcal{E}_0\cos(\omega t)\langle 2|d_0|1\rangle, \tag{3.7a}$$

$$i\hbar\frac{\partial c_2}{\partial t} = \hbar\omega_0 c_2 - c_1\mathcal{E}_0\cos(\omega t)\langle 1|d_0|2\rangle. \tag{3.7b}$$

We define the Rabi frequency as $\Omega_0 \equiv \mathcal{E}_0\langle 2|d_0|1\rangle/\hbar$, which is real by convention [see footnote 6 on page 14]. Thus we can express the coupled differential equation in matrix form as

$$i\hbar\frac{\partial}{\partial t}\begin{pmatrix} c_1 \\ c_2 \end{pmatrix} = -\hbar\begin{pmatrix} 0 & \Omega_0\cos(\omega t) \\ \Omega_0\cos(\omega t) & -\omega_0 \end{pmatrix}\begin{pmatrix} c_1 \\ c_2 \end{pmatrix}, \tag{3.8}$$

where we notice

$$\psi(t) = \begin{pmatrix} c_1 \\ c_2 \end{pmatrix}, \tag{3.9}$$

a vector representation of $|\psi(t)\rangle$, and

$$\mathcal{H} = -\hbar\begin{pmatrix} 0 & \Omega_0\cos(\omega t) \\ \Omega_0\cos(\omega t) & -\omega_0 \end{pmatrix}, \tag{3.10}$$

a matrix representation[3] of $\hat{\mathcal{H}}$, both in the two-level basis.

---

[3]In quantum mechanics, an operator is an abstract algebraic object. The *representation* of an operator is a more concrete, matrix form of the operator, grounded in a particular choice of basis [37, 52]. Usually the operator and its matrix representation can be used interchangeably. This thesis distinguishes between the operator $\hat{\mathcal{O}}$ (with a ˆ hat) and its representation $\mathcal{O}$ (without). Representations are useful because they allow us to work with operators using the familiar machinery of linear algebra.

The state vector and the Hamiltonian matrix transform[4] according to [43, 49]

$$\tilde{\psi} = U\psi, \tag{3.11a}$$

$$\tilde{\mathcal{H}} = U\mathcal{H}U^{\dagger} + i\hbar\frac{\partial U}{\partial t}U^{\dagger}, \tag{3.11b}$$

where U is a unitary transformation matrix. By choosing the unitary matrix

$$U = \begin{pmatrix} 1 & 0 \\ 0 & e^{i\omega t} \end{pmatrix} \tag{3.12}$$

oscillating at the drive frequency ω, transforming Equation 3.10 according to Equation 3.11b gives

$$\tilde{\mathcal{H}} = -\frac{\hbar}{2}\begin{pmatrix} 0 & \Omega_0\left(1 + e^{-2i\omega t}\right) \\ \Omega_0\left(1 + e^{2i\omega t}\right) & 2\delta_0 \end{pmatrix}, \tag{3.13}$$

where the cosines have been expanded as complex exponentials and simplified. We have also defined the detuning $\delta_0 = \omega - \omega_0$.

In this "rotating frame", we have transferred some of the time-dependence of $\mathcal{H}$ onto $\tilde{\psi}$. Yet, there are frequency components of $\tilde{\mathcal{H}}$ oscillating at 2ω. In the following "rotating wave approximation," valid when $\Omega_0/\omega_0 \ll 1$ (weak coupling) and $\delta_0/\omega_0 \ll 1$ (near resonance) [53], we discard the twice-rotating terms. Because they are far from resonance, the fast oscillations time-average to zero without significantly perturbing the state. Finally, we obtain the approximately-time-independent Hamiltonian matrix

---

[4]To derive this transformation, operate on both sides of Equation 3.4 by a unitary transformation matrix U and insert a $U^{\dagger}U = \mathbb{1}$ on the R.H.S. to get

$$i\hbar U\frac{\partial \psi}{\partial t} = U\mathcal{H}U^{\dagger}U\psi.$$

Then substitute into this an expression from the chain rule

$$U\frac{\partial \psi}{\partial t} = \frac{\partial}{\partial t}\left(U\psi\right) - \frac{\partial U}{\partial t}\psi,$$

rearranging and simplifying to form an equivalent Schrödinger equation for the transformed vector $\tilde{\psi}$ [Equation 3.11a] and Hamiltonian $\tilde{\mathcal{H}}$ [Equation 3.11b].

in the rotating frame[5]

$$\tilde{\mathcal{H}} \approx -\frac{\hbar}{2} \begin{pmatrix} 0 & \Omega_0 \\ \Omega_0 & 2\delta_0 \end{pmatrix}. \tag{3.14}$$

Given Equation 3.14 and some initial conditions, we can determine the evolution of the level populations using the Schrödinger equation. For example, with $\tilde{\psi}(0) = \begin{pmatrix} \tilde{c}_1(0) & \tilde{c}_2(0) \end{pmatrix} = \begin{pmatrix} 1 & 0 \end{pmatrix}$, we obtain

$$|\tilde{c}_1(t)|^2 = \cos^2\left(\frac{\Omega t}{2}\right) + \frac{\delta_0^2}{\Omega^2} \sin^2\left(\frac{\Omega t}{2}\right) \tag{3.15a}$$

$$|\tilde{c}_2(t)|^2 = \frac{\Omega_0^2}{\Omega^2} \sin^2\left(\frac{\Omega t}{2}\right), \tag{3.15b}$$

where $\Omega \equiv \sqrt{\Omega_0^2 + \delta_0^2}$ is the generalized Rabi frequency of oscillation. These populations are displayed in Figure 3.2(a) as a function of t for various parameters. When $\delta_0 = 0$, the populations oscillate entirely back and forth at the Rabi frequency Ω_0; this scenario is known as Rabi flopping.

3.1.3 Open quantum system

The second part considers an *open* quantum system, where dissipation due to the environment may be present. In this situation, the electron state Equation 3.3 is not generally normalized, and it becomes necessary to study the time-evolution of the density operator $\hat{\rho}$, which is represented in the two-level basis by the matrix

$$\rho(t) = \begin{pmatrix} \rho_{11}(t) & \rho_{12}(t) \\ \rho_{21}(t) & \rho_{22}(t) \end{pmatrix}. \tag{3.16}$$

---

[5]By adding a constant energy shift to the Hamiltonian matrix, i.e. $\tilde{\mathcal{H}}' = \tilde{\mathcal{H}} + \frac{\delta_0}{2}\mathbb{1}$, it can be expressed more symmetrically as

$$\tilde{\mathcal{H}}' \approx \frac{\hbar}{2} \begin{pmatrix} \delta_0 & -\Omega_0 \\ -\Omega_0 & -\delta_0 \end{pmatrix} = -\Omega_0 \hat{S}_x + \delta_0 \hat{S}_z,$$

where $\hat{S}_i$ are the respective Cartesian spin vector operator components. This modified Hamiltonian gives the same dynamics as $\tilde{\mathcal{H}}$, up to a global phase.

The density matrix is a more general description of the state of the atom, one that incorporates degrees of incoherence and can even be used to describe ensembles of atoms. It has the important property that its trace is equal to one, i.e. $\text{Tr}[\rho(t)] = \rho_{11}(t) + \rho_{22}(t) = 1$, which is a statement of conservation of probability. Another property is that ρ is Hermitian, hence $\rho_{12} = \rho_{21}^*$. The diagonal elements are often called "populations" and the off-diagonal elements are called "coherences," implying the existence of phase relationships between basis element pairs.

The density operator has a characteristic called purity, defined as $\text{Tr}[\hat{\rho}^2]$. In the absence of dissipation, this value equals 1, and $\hat{\rho}$ is called a pure state. A pure state is constructed as the outer product of the state vector with itself

$$\hat{\rho}(t) = |\psi(t)\rangle\langle\psi(t)|, \tag{3.17}$$

and represented by the matrix

$$\rho(t) = \begin{pmatrix} |c_1(t)|^2 & c_1(t)c_2^*(t) \\ c_2(t)c_1^*(t) & |c_2(t)|^2 \end{pmatrix}. \tag{3.18}$$

In realistic, dissipative situations, the purity of $\hat{\rho}$ is less than 1, and $\hat{\rho}$ is called a mixed, or statistical, state; it is constructed as the statistical average of multiple pure states,

$$\hat{\rho}(t) = \sum_i p_i |\psi_i(t)\rangle\langle\psi_i(t)|, \tag{3.19}$$

where i indexes over the statistical components (e.g. atom in an ensemble, basis components[6]), and p_i is the statistical weight of each component, such that $\sum_i p_i = 1$.

We continue the treatment of the same two-level system, but now where it is exposed to dissipative perturbations from the environment[7]. Knowing the exact details

---

[6]Single atoms can be in mixed states, too.

[7]For example, we can consider the spontaneous de-excitation of the electron from the excited state caused by fluctuations of the electromagnetic vacuum field [51, 54, 55].

of this process is not necessary; we can assume that the electron decays from the excited to ground state with an exponential, phenomenological decay rate γ_0, analogous to the classical damping of a harmonic oscillator. In realistic atoms, the decay rate is inversely proportional to the natural, homogeneous linewidth, $\Delta\nu = 2\pi/\gamma_0$ [40].

As described above, the state of open quantum systems must be described by a density matrix ρ. Because we transformed our quantum system to a basis rotating at the drive frequency, we redefine the density operator as

$$\hat{\sigma}(t) = \hat{U}\hat{\rho}\hat{U}^{\dagger}, \tag{3.20}$$

represented by the matrix

$$\sigma(t) = U\rho U^{\dagger} = \begin{pmatrix} \sigma_{11} & \sigma_{12} \\ \sigma_{21} & \sigma_{22} \end{pmatrix}. \tag{3.21}$$

In the absence of any damping, the time evolution of the density matrix can be determined by the Liouville-von Neumann equation [49, 56]

$$\frac{d}{dt}\sigma(t) = \frac{1}{i\hbar}\left[\tilde{\mathcal{H}}, \sigma(t)\right], \tag{3.22}$$

where the square brackets are the commutator. This equation[8] represents four, coupled time-differential equations, one for each element of the 2×2 density matrix σ, and it is exactly equivalent to the time-dependent Schrödinger equation [Equation 3.4]. Actually, since σ is Hermitian, two of these equations are equivalent. The remaining three unique equations are solved together, either analytically or numerically.

In the presence of spontaneous decay or dissipation, additional terms need to be added to the R.H.S. of Equation 3.22, resulting in the Lindblad master equation [57,

---

[8]Except for a minus sign, Equation 3.22 has a very similar form to the Heisenberg equation; however, note that this equation is for the evolution of the *density matrix* instead of *observable* operators.

58]

$$\frac{d}{dt}\sigma(t) = \frac{1}{i\hbar}[\tilde{\mathcal{H}}, \sigma(t)] + \sum_i L_i \sigma(t) L_i^\dagger - \frac{1}{2}\left\{L_i^\dagger L_i, \sigma(t)\right\}, \tag{3.23}$$

The L_i are matrix representations of the corresponding collapse [57, 59] (or "jump" [58])
operators, indexed over various dissipation channels, and the curly brackets are the
anti-commutator. In the case of an exponential decay rate γ_0 in the two-level system,
the collapse operator is represented by the matrix

$$L_0 = \sqrt{\gamma_0}\begin{pmatrix} 0 & 1 \\ 0 & 0 \end{pmatrix}, \tag{3.24}$$

which produces an instantaneous jump from $|\tilde{2}\rangle \rightarrow |\tilde{1}\rangle$. We can now substitute L_0 and
$\tilde{\mathcal{H}}$ [Equation 3.14] into Equation 3.23 to obtain three coupled differential equations,
also known as the optical Bloch equations [40, 56, 60]

$$\dot{\sigma}_{11} = i\frac{\Omega_0}{2}(\sigma_{21} - \sigma_{12}) + \gamma_0\sigma_{22}, \tag{3.25a}$$

$$\dot{\sigma}_{22} = -i\frac{\Omega_0}{2}(\sigma_{21} - \sigma_{12}) - \gamma_0\sigma_{22}, \tag{3.25b}$$

$$\dot{\sigma}_{12} = \dot{\sigma}_{21}^* = i\frac{\Omega_0}{2}(\sigma_{22} - \sigma_{11}) + (\gamma_0/2 - i\delta_0)\sigma_{12}. \tag{3.25c}$$

Given initial conditions, the time-dependence of $\sigma(t)$ can be numerically integrated
with a Runge-Kutta method, or with dedicated software packages like QuTiP [57, 61].
Figure 3.2 illustrates the evolution of the populations $\sigma_{ii}(t)$ for various values of δ_0
and γ_0, given the initial conditions $\sigma_{11}(0) = 1; \sigma_{22}(0) = \sigma_{12}(0) = \sigma_{21}(0) = 0$. The
purity of the state is also plotted as a function of time. When $\gamma_0 = 0$, the populations
follow exactly the analytical expressions of Equation 3.15a and 3.15b, and the purity
is constant at 1.

With damping, the populations eventually relax to a stationary steady-state. We
can calculate these by setting all the time derivatives in Equation 3.25a-3.25c to zero.
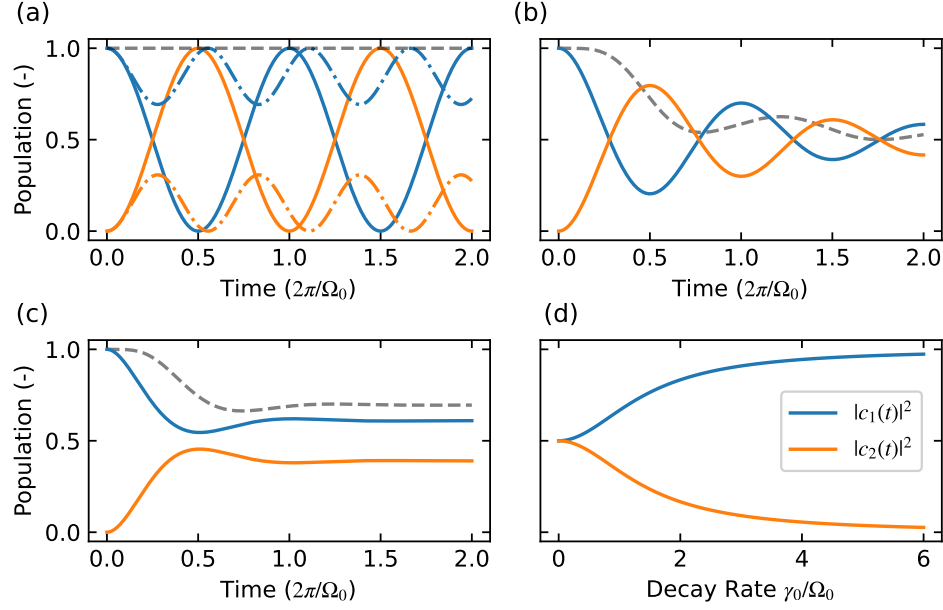
Figure 3.2: Two-level population evolution. (a) The evolution of a closed quantum system, where $\gamma_0 = 0$, for $\delta_0 = 0$ (solid) and $\delta_0 = 1.5$ (dashed-dotted). In the later case, the system oscillates at the generalized Rabi frequency $\Omega = \sqrt{13}/2$. (b-d) The evolution of an open quantum system. (b) The decay rate $\gamma_0 = 0.2$, for $\delta_0 = 0$. (c) $\gamma_0 = 0.75$, for $\delta_0 = 0$. In panels (a-c), the purity of the rotated density matrix $\mathrm{Tr}[\sigma^2]$ is displayed a gray dashed curve. (d) The steady-state populations as a function of γ_0. All quantities are given in terms of the Rabi frequency Ω_0.

By solving algebraically for the populations, we get

$$\sigma_{11}(\infty) = 1 - \sigma_{22}(\infty), \tag{3.26a}$$

$$\sigma_{22}(\infty) = \frac{\Omega_0^2}{\gamma_0^2 + 4\delta_0^2 + 2\Omega_0^2}, \tag{3.26b}$$

which are shown in Figure 3.2(d) as a function of γ_0.

The density matrix and its associated formalism are indispensable tools for determining the evolution of realistic quantum systems, especially in the presence of dissipation, such as spontaneous de-excitation.

3.2   Transitions in multi-level atoms

We have seen that the density matrix can accurately represent the state and evolution of an electron among two basis states in the presence of dissipation. More generally, the density matrix can represent atoms and ensembles with multiple electron states. In such cases, evolution among a complicated level structure is composed of transitions that individually approximate two-level systems [62, 63]. This "two-level approximation" is valid when the levels are well-separated and the radiation is approximately resonant [64]. We leave computing the density matrix evolution for a system with an arbitrary number of levels as a task that can be done in principle[9]. In this section, we restrict our attention to the problem of calculating the matrix elements, and hence the Rabi frequencies, that go into such calculations.

Transitions in a multilevel atom are produced between selected pairs of electron states. Each transition has a unique E1 or M1 matrix element (but not both! [26]) that depends on: (1) the angular momentum of the initial $|fm_f\rangle$ and final $|f'm_{f'}\rangle$ states involved in the transition, and (2) the amplitude and (3) the polarization (i.e spin angular momentum) of the electromagnetic field inducing the transition. In the treatment of the two-level atom, we did not strictly consider the polarization of the light. However, in Section 2.4.2, we stated that dipole operators are spherical vector operators; in general, their components will add -1, 0, or +1 quanta of angular momentum to the state of the electron, with distinct interaction strengths. These angular momentum-sensitive transitions are also called σ_-, π, and σ_+ transitions, respectively.

---

[9]In practice, the number of coupled equations in the optical Bloch equations increase quadratically with the basis size. Computations are also hindered by intensive averaging techniques that account for Doppler-broadening in thermal atomic vapors [60, 65]. Computations that depend on finite difference integration may benefit [66] from similar GPU acceleration techniques presented in Chapter 9, especially when the Hamiltonian and collapse operators are time-independent.

The purpose of this section is to derive the dipole matrix elements for ^{87}Rb. This derivation rightly assumes that the spin-orbit interaction is relatively weak, the hyperfine levels are well-resolved, and any applied magnetic field is weak, all such that f and m_f are good quantum numbers [26].

3.2.1 Magnetic dipole matrix elements

We will focus here on the M1 matrix elements within the $5\,^2S_{1/2}$ ground state hyperfine levels where $\ell = 0$, the most experimentally relevant M1 transitions in alkali atoms[10]; the ground-state microwave transitions employed in Chapters 6 and 8 are of this character.

In the ground state, the component of the magnetic moment [see Equation 2.32] associated with $\hat{\mathbf{L}}$ vanishes since $\ell = 0$. Furthermore, the nuclear magnetic moment is small compared to the spin where the electron's magnetic moment (i.e. $g_I/g_s \ll 1$). Therefore, the magnetic moment simplifies to

$$\hat{\boldsymbol{\mu}} \approx -\frac{g_s \mu_B}{\hbar} \hat{\mathbf{S}} \tag{3.27}$$

and the magnetic field vector may be expressed in the spherical basis and in the rotating frame as $\mathbf{B}(t) = \mathcal{B}_q^1 \hat{e}_q$, giving an M1 matrix element of

$$\langle f'm_{f'}|\hat{H}^{(\text{M1})}|fm_f\rangle = \frac{\mu_B g_S \mathcal{B}_q^1}{\hbar} \langle f'm_{f'}|\hat{\mathbf{S}} \cdot \hat{e}_q|fm_f\rangle \tag{3.28}$$

We now apply the Wigner-Eckart theorem [Equation 2.18] to reduce and evaluate the matrix element as [50]

$$\begin{aligned}
\langle f'm_{f'}|\hat{S}_q|fm_f\rangle &= \langle f'||\hat{\mathbf{S}}||f\rangle\langle f'm_{f'}|fm_f; 1q\rangle \\
&= \langle f'||\hat{\mathbf{S}}||f\rangle(-1)^{-f+1-m_{f'}}\sqrt{2f'+1}\begin{pmatrix} f & 1 & f' \\ m_f & q & -m_{f'} \end{pmatrix}.
\end{aligned} \tag{3.29}$$

---

[10]Recalling the relative weakness of M1 transitions [see Section 3.1.1], an electron in the excited state will usually decay to the ground state before an excited-state M1 transition might occur. Even in long-lived Rydberg levels, the stronger electric dipole transitions are more experimentally and technologically relevant, e.g. in electric field sensing [67, 68].

By expressing the $|f\rangle$ basis as $|jIf\rangle$, and noting that $\hat{\mathbf{S}}$ does not act on the $|I\rangle$ subspace, the reduced matrix element may be reduced further with additional applications of the Wigner-Eckart theorem [43, 50], yielding

$$
\begin{aligned}
\langle f'||\hat{\mathbf{S}}||f\rangle &= \langle j'I'f'||\mathbf{S}||jIf\rangle \\
&= \delta_{II'}\langle j'||\hat{\mathbf{S}}||j\rangle(-1)^{f+j'+1+I}\sqrt{(2f+1)(2j'+1)} \\
&\quad \times \begin{Bmatrix} j' & j & 1 \\ f & f' & I \end{Bmatrix},
\end{aligned}
\tag{3.30}
$$

where $\delta_{II'}$ is a Kronecker delta. We simplify $\langle j'||\hat{\mathbf{S}}||j\rangle = \langle s'||\hat{\mathbf{S}}||s\rangle$, since $\ell = 0$. This reduced matrix element can be evaluated [see Appendix C] to

$$
\langle s'||\hat{\mathbf{S}}||s\rangle = \langle s||\hat{\mathbf{S}}||s\rangle = \hbar\sqrt{s(s+1)}.
\tag{3.31}
$$

Putting everything together, the M1 matrix element is [48]

$$
\begin{aligned}
\langle f'm_{f'}|\hat{H}^{(\text{M1})}|fm_f\rangle &= \mu_{\mathrm{B}}g_S\mathcal{B}_q^1(-1)^{s'+I-m_{f'}}\sqrt{(2f'+1)(2f+1)(2s'+1)s(s+1)} \\
&\quad \times \begin{pmatrix} f & 1 & f' \\ m_f & q & -m_{f'} \end{pmatrix} \begin{Bmatrix} s' & s & 1 \\ f & f' & I \end{Bmatrix},
\end{aligned}
\tag{3.32}
$$

where values of j, j' have been replaced with s, s'. The form of this expression can be understood intuitively: it depends on a 3j-symbol because the polarization of the light only connects certain pairs of hyperfine Zeeman levels; it also depends on a 6j-symbol because there are three coupled angular momenta, the nuclear (I), the electron spin (s), and the electromagnetic radiation ($q = 1$), where f is the "intermediate" angular momentum.

Figure 3.3 depicts all possible M1 transitions in the ^{87}Rb ground state. Table 3.1 lists the matrix elements of microwave-frequency M1 transitions between the $|f = 1, m_f\rangle \rightarrow |f' = 2, m_{f'}\rangle$ levels, computed with the Alkali Rydberg Calculator, a
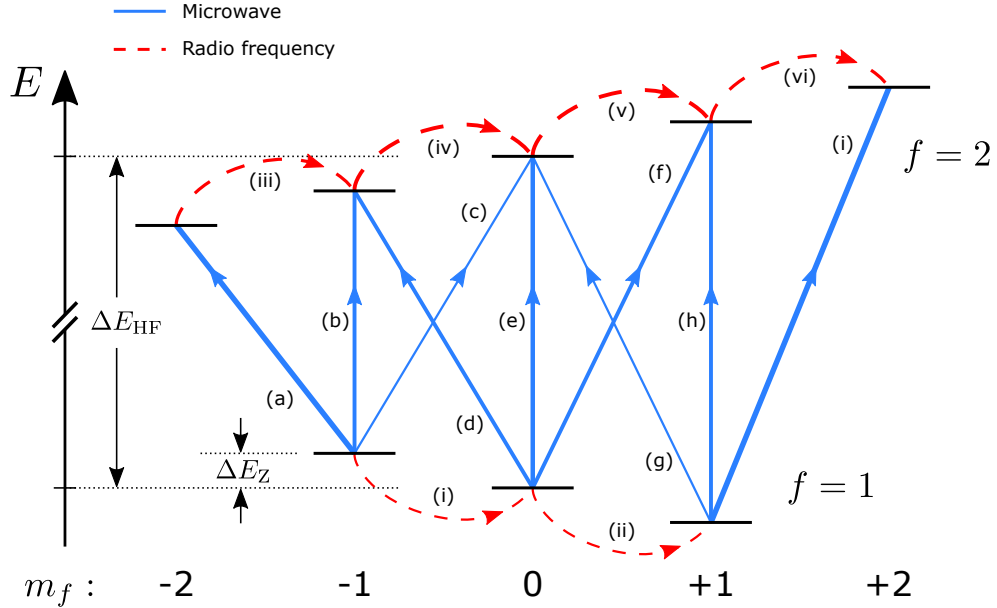
Figure 3.3: Energy level diagram depicting M1 transitions in the rubidium ground state. The blue and red curves represent microwave-frequency and RF transitions. The curve weight is proportional to the absolute value of the dipole matrix elements listed in Tables 3.1 and 3.2.

useful Python package for computing atomic properties and transition strengths [48]. We also compute and list in Table 3.2 the matrix elements of the radio-frequency M1 transitions within a single hyperfine level between the $|f, m_f\rangle \to |f, m_{f'}\rangle$ Zeeman levels. While this table only provides the matrix elements for the $q = +1$ transitions, the reversed circular transitions (i.e. Hermitian conjugated matrix elements) acquire a -1 phase factor [41].

3.2.2 Electric dipole matrix elements

The Wigner-Eckart theorem may be similarly employed to reduce the electric dipole matrix elements that connect ground and excited states. Since these values have been previously tabulated [50] and can be readily calculated [48], we will simply quote the explicit form of the electric dipole matrix elements [48, 50] given by

Label	$(m_f, m_{f'}, q)$	$\langle 2\ m_{f'} \lvert \hat{H}^{(M1)} \rvert 1\ m_f \rangle$
a	(-1, -2, -1)	$-\sqrt{3/2} \approx -1.22$
b	(-1, -1, 0)	$\sqrt{3}/2 \approx 0.87$
c	(-1, 0, 1)	$-1/2$
d	(0, -1, -1)	$-\sqrt{3}/2 \approx -0.87$
e	(0, 0, 0)	1
f	(0, 1, 1)	$-\sqrt{3}/2 \approx -0.87$
g	(1, 0, -1)	$-1/2$
h	(1, 1, 0)	$\sqrt{3}/2 \approx 0.87$
i	(1, 2, 1)	$-\sqrt{3/2} \approx -1.22$

Table 3.1: Magnetic dipole matrix elements for microwave-frequency transitions in the rubidium ground state. The label in each row corresponds to a specific transition displayed in Figure 3.3. Transitions occur between a lower-energy $\lvert f = 1\ m_f \rangle$ state and a higher energy $\lvert f' = 2\ m_{f'} \rangle$ state. q refers to the spherical component (i.e. polarization) of the incident microwave field. The matrix elements are given in units of $\mu_{\mathrm{B}} g_s \mathcal{B}_q^1$.

Label	$(f, m_f, m_{f'})$, $q = +1$	$\langle 2\ m_{f'} \lvert \hat{H}^{(M1)} \rvert 1\ m_f \rangle$
i	(1, -1, 0)	$-1/2$
ii	(1, 0, 1)	$-1/2$
iii	(2, -2, -1)	$1/\sqrt{2} \approx 0.71$
iv	(2, -1, 0)	$\sqrt{3}/2 \approx 0.87$
v	(2, 0, 1)	$\sqrt{3}/2 \approx 0.87$
vi	(2, 1, 2)	$1/\sqrt{2} \approx 0.71$

Table 3.2: Magnetic dipole matrix elements for radio-frequency transitions in the rubidium ground state. The label in each row corresponds to a specific transition displayed in Figure 3.3. Transition occur between states $\lvert m_f \rangle$ and $\lvert m_{f'} \rangle$ within a single hyperfine level. The RF field is taken to be right-circularly polarized ($q = +1$). The matrix elements are given in units of $\mu_{\mathrm{B}} g_s \mathcal{B}_{+1}^1$.

$$
\begin{aligned}
\langle f'm_{f'}|\hat{H}^{(\mathrm{E1})}|fm_f\rangle &= \mathcal{E}_q^1 \langle f'm_{f'}|e\mathbf{r}\cdot\hat{e}_q|fm_f\rangle \\
&= \mathcal{E}_q^1 (-1)^{j'+I-m_{f'}} \sqrt{(2f'+1)(2f+1)(2j'+1)} \\
&\quad \times \begin{pmatrix} f & 1 & f' \\ m_f & q & -m_{f'} \end{pmatrix} \begin{Bmatrix} f & 1 & f' \\ j' & I & j \end{Bmatrix} \langle j'||e\mathbf{r}||j\rangle.
\end{aligned}
\tag{3.33}
$$

The value of the reduced matrix element may be determined from independent experiments. For transitions on the D_1 ($j'=1/2$) and D_2 ($j'=3/2$) lines, the reduced matrix element $\langle j'||e\mathbf{r}||j=1/2\rangle$ has values of 2.992(3) and 4.227(5) ea_0 [50]. Additionally, this reduced matrix element can be reduced further to obtain

$$
\langle j'||e\mathbf{r}||j\rangle = \langle \ell'||e\mathbf{r}||\ell\rangle (-1)^{j+\ell'+1+s'} \sqrt{(2j+1)(2\ell'+1)} \begin{Bmatrix} j & 1 & j' \\ \ell' & s & \ell \end{Bmatrix},
\tag{3.34}
$$

where [see Appendix C]

$$
\langle \ell'||e\mathbf{r}||\ell\rangle \propto \begin{pmatrix} \ell' & 1 & \ell \\ 0 & 0 & 0 \end{pmatrix}.
\tag{3.35}
$$

3.2.3 Selection Rules

Using the explicit forms of the M1 and E1 matrix elements, we are prepared to identify selection rules that specify if a transition between two electron states is "allowed" according to a particular interaction. These rules emerge from the addition of angular momenta; they are a direct consequence of the symmetry properties of the Wigner 3j- and 6j-symbols. The selection rules for M1 and E1 transitions are summarized in Table 3.3 [26, 40].

We will first explain how the M1 selection rules emerge:

1. The $\Delta\ell = 0$ rule comes from the $\langle j'||\hat{\mathbf{S}}||j\rangle$ term in Equation 3.30; the $\hat{\mathbf{S}}$ vector operator does not act on the $|\ell\rangle$ subspace. Therefore, reducing this matrix element further for $\ell \neq 0$ produces a Kronecker delta $\delta_{\ell\ell'}$ coefficient.

M1	E1
$\Delta\ell = 0$	$\Delta\ell = \pm1$
$\Delta j = 0, \pm1^*$	
$\Delta f = 0, \pm1^\dagger$	
$\Delta m_f = 0, \pm1^\ddagger$	

Table 3.3: Summary of allowed selection rules for M1 and E1 transitions. Some of the selection rules are shared between the two dipole interactions, but the $\Delta\ell$ rules are distinct. These rules have three caveats that render the transitions forbidden ($\nleftrightarrow$): * $|j = 0\rangle \nleftrightarrow |j' = 0\rangle$;   † $|f = 0\rangle \nleftrightarrow |f' = 0\rangle$;   ‡ $|m_f = 0\rangle \nleftrightarrow |m_{f'} = 0\rangle$ when $\Delta f = 0$.

2. The $\Delta j = 0, \pm1$ rule comes from the triangle condition 2.17b for the 6j-symbol found in Equation 3.30.

   - The caveat to this rule is that transitions cannot be made between $|j = 0\rangle \leftrightarrow |j' = 0\rangle$; this rule emerges from the triangle condition 2.17b on the 6j-symbol in Equation 3.30.

3. The $\Delta f = 0, \pm1$ rule comes from the triangle condition 2.17c for the 6j-symbol found in Equation 3.30.

   - The caveat to this rule is that transitions cannot be made between $|f = 0\rangle \leftrightarrow |f' = 0\rangle$; this rule emerges from the triangle condition on the 3j-symbol found in Equation 3.29.

4. The $\Delta m_f = 0, \pm1$ comes from the property of the 3j-symbol in Equation 3.29 that all the bottom row elements must sum to zero, and the fact that $q = 0, \pm1$.

   - The caveat to this rule is that transitions cannot be made between $|m_f = 0\rangle \leftrightarrow |m_{f'} = 0\rangle$ when $\Delta f = 0$ [40, 69]; this rule emerges because the

3j-symbol in Equation 3.29,

$$
\begin{pmatrix} f & 1 & f \\ 0 & 0 & 0 \end{pmatrix},
\tag{3.36}
$$

always equals zero when the sum of the top elements is odd [41].

Similar statements can be made for the E1 transitions. In that case, however, the $\Delta\ell = \pm 1$ rule emerges because the 3j-symbol in Equation 3.35 can only be nonzero if the sum of its top row elements is even [41]. This is a statement of parity, or inversion symmetry [40]: since the $e\mathbf{r}$ operator is parity-odd, it can only connect ℓ states of opposite parity–those that differ by $|\Delta\ell| = 1$. The magnetic moment $\hat{\boldsymbol{\mu}}$, in contrast, is parity-even and not does change the parity of the electron state.

Chapter 4

Warm atomic vapor spectroscopy

We turn now to understanding the optical frequency spectrum of warm atomic vapors. A warm alkali vapor is a collection of untrapped alkali atoms inside a sealed (usually glass) cell at temperatures near room temperature. In many cases, the thermal motion of the atoms in the vapor resembles that of an ideal gas. This vapor is mostly transparent to the naked eye; it only absorbs or scatters light at discrete "lines" occurring at specific electromagnetic wave frequencies [35]. Each line is formed by electron transitions between pairs of low- and high-energy levels. The energy differences between a level pair $\hbar\omega_{ij}$ determines the central frequencies of the spectral lines; these are well-known for many transitions in atoms and ions [38, 70]. Some lines are very narrow in the frequency domain while others are relatively broad. In

this chapter, we will focus on the question: What determines the shape and breadth of each line?

4.0.1 Natural linewidth

We start by noting that a collection of identical, isolated atoms at rest (e.g. laser-cooled) will all have the same spectrum. As described previously [see Section 3.1.3], the probability of an electron in an excited state $|\psi_i\rangle$ generally decays exponentially in time as it relaxes to a ground state $|\psi_j\rangle$ at a rate γ_{ij}. This decay is caused by interactions of the electron and the quantized electromagnetic vacuum[1] [51, 54, 55]. In the Fourier frequency domain, this decay results in a *normalized* Lorentzian line profile given by

$$g_{\gamma,ij}(\omega) = \frac{1}{2\pi} \frac{\gamma_{ij}}{(\omega - \omega_{ij})^2 + (\gamma_{ij}/2)^2}, \tag{4.1}$$

broadened to a "natural" full-width at half-maximum (FWHM) of γ_{ij}, with an integrated profile area of 1. This profile is an example of homogeneous broadening, a mechanism that is the same for every atom in the collection [39, 40]. It is also helpful to define the *non-normalized* Lorentzian profile

$$g_{\gamma,ij}^*(\omega) = \frac{(\gamma_{ij}/2)^2}{(\omega - \omega_{ij})^2 + (\gamma_{ij}/2)^2}, \tag{4.2}$$

which has a value of 1 on-resonance and an integrated profile area of $\pi\gamma_{ij}/2$.

The shape and breadth of spectral lines are strongly affected by other mechanisms, particularly thermal motion, in which the atoms in the vapor move with a wide range of speeds and directions. The Doppler effect, caused by the relative motion of atoms and the interacting light, strongly broadens the spectral profile. Because the

---

[1]While the natural Lorentzian width and lineshape is the same for identical atoms, there are methods that modify the natural exponential decay of an electron inside an atom. For example, the Purcell effect occurs when an atom is placed inside a high-finesse resonant cavity; the cavity modifies the electromagnetic vacuum environment [54]. The decay rate can also be modified through collective effects between other nearby excited atoms in processes known as superradiance and subradiance [71].

Doppler effect is not the same for each atom, it produces what is called inhomogeneous broadening. In this chapter, we will explore the influence of the Doppler effect and additional homogeneous and inhomogeneous mechanisms on the profile of atomic spectral lines.

4.1 The Doppler effect and thermal broadening

We begin by considering an atom moving with velocity $\mathbf{v}$ through an infinite, plane electromagnetic wave. The wave propagates along the z-direction defined by the $\mathbf{k} = k\hat{e}_z = 2\pi\hat{e}_z/\lambda = \omega\hat{e}_z/c$ wavevector. If nothing interacts with an atom initially at position $\mathbf{r}_0$, its position at future times t will be $\mathbf{r}(t) = \mathbf{r}_0 + \boldsymbol{v}t$. In the reference frame of the atom[2], the electric field has the time-dependence

$$\begin{aligned}
\mathbf{E}(t) &\propto \sin\left[\omega t - \mathbf{k} \cdot \mathbf{r}(t)\right] \\
&= \sin\left[(\omega - \mathbf{k} \cdot \boldsymbol{v})t - \mathbf{k} \cdot \mathbf{r}_0\right],
\end{aligned} \tag{4.3}$$

where the temporal frequency "seen" by the atoms is

$$\omega' \equiv \omega - \mathbf{k} \cdot \boldsymbol{v} \equiv \omega + \Delta_v, \tag{4.4}$$

and Δ_v is the non-relativistic Doppler shift [49]. (Going forward, we will consider only v and k, the parallel z-components of $\boldsymbol{v}$ and $\mathbf{k}$.) This means that the electron will be resonantly excited by the electromagnetic wave when

$$\omega_{ij} - \omega\left(1 - \frac{v}{c}\right) = 0. \tag{4.5}$$

In a thermal vapor, the probability density function[3] of finding an atom with velocity v is given by the one-dimensional Maxwell-Boltzmann (MB) distribution [49,

---

[2]This discussion assumes that the electromagnetic wave is detected and its frequency determined in a stationary lab frame of reference, and that $|v|/c \ll 1$.

[3]The probability of finding an atom between v_0 and $v_0 + dv$ is $f_u(v_0)dv$.

72]

$$f_u(v) = \sqrt{\frac{m_{87}}{\pi 2 k_{\rm B} T}} \exp\left(-\frac{m_{87} v^2}{2 k_{\rm B} T}\right) \equiv \frac{1}{\sqrt{\pi u^2}} \exp\left(-\frac{v^2}{u^2}\right), \tag{4.6}$$

where $u = \sqrt{2 k_{\rm B} T / m_{87}}$ is the "most probable speed" of the atoms[4]; for ^{87}Rb atoms at a typical room temperature (20°C), $u = 237$ m/s. This normalized density distribution function is Gaussian and centered at $v = 0$.

Because of the Doppler effect, we can re-express the MB distribution in terms of the Doppler shift as

$$f_u(\Delta_v) = \frac{1}{\sqrt{\pi k^2 u^2}} \exp\left(-\frac{\Delta_v^2}{k^2 u^2}\right). \tag{4.7}$$

The Doppler-broadened FWHM of this distribution is

$$\Gamma_D = 2 k u \sqrt{\ln(2)}. \tag{4.8}$$

The subset of atoms moving with the same velocity (i.e. between v and $v + dv$) all experience the same Doppler shift (between Δ_v and $\Delta_v + d\Delta_v$) and interact with the light in the same way. This subset constitutes what is called a velocity class. The average occupation of this class is $f_u(\Delta_v) d\Delta_v$.

For a given average velocity, the magnitude of the Doppler shift is inversely proportional to the wavelength λ of the light. This means that atoms experience a larger Doppler shift for light at optical versus microwave frequencies. The Doppler broadening for optical ($\lambda_{\rm opt} = 780.241$ nm) frequencies is $\Gamma_D^{\rm opt} = 304$ MHz, while the corresponding microwave ($\lambda_{\rm MW} = 4.38$ cm) broadening is comparatively small, only $\Gamma_D^{\rm MW} = 5.4$ kHz.

In general, atoms experience both homogeneous (natural) and inhomogeneous (Doppler) broadening. The total shape of the resonance line is therefore the con-

---

[4]Additionally, the "average speed" can be computed from the MB speed distribution to be $\langle v \rangle = 2u/\sqrt{\pi}$. The "root-mean-squared speed" can be similarly computed to be $\sqrt{\langle v^2 \rangle} = \sqrt{3/2} u$.

volution of the Lorentzian and Gaussian MB distributions [49]

$$h_{\gamma,u}(\omega) = \int\limits_{-\infty}^{+\infty} g_\gamma(\omega - kv) \times f_u(v)dv \qquad (4.9)$$

and is called a Voigt profile. The widths of the two input distributions define the shape of $h_{\gamma,u}(\omega)$. While this distribution is generally calculated numerically [73], the FWHM of the Voigt profile width can be approximated as [74]

$$\Gamma_V \approx \gamma/2 + \sqrt{\gamma^2/4 + \Gamma_D^2}. \qquad (4.10)$$

In the limit where $ku \gg \gamma$, the most relevant regime for warm alkali vapors, $\Gamma_V \approx \Gamma_D$.

4.2 The transmission spectrum of warm atomic gases

One of the most natural ways for measuring the spectrum of an atomic vapor is to illuminate it with monochromatic light[5] of a known intensity $I(\omega, 0)$ and a frequency ω that varies near an atomic resonance ω_{ij}. When the probe light frequency is on-resonance (i.e. $\omega \simeq \omega_{ij}$), the atom absorbs a fraction of the light, and the light intensity is reduced after passing through the atomic vapor. The equation describing this absorption of light as a function of position z through the vapor is

$$\frac{dI(\omega, z)}{dz} = -\kappa(\omega)I(\omega, z), \qquad (4.11)$$

where κ is the absorption coefficient. This equation is the well-known Beer-Lambert law, which is valid for relatively weak optical intensities, with uniformly distributed

---

[5]In practice, it is very difficult to produce perfectly monochromatic light; the light source itself generally always has some finite spectral width. We assume in this section, however, that this width is much narrower than any atomic spectral features.

and independently absorbing atoms[6]. The light intensity will therefore decrease exponentially as it passes through the vapor

$$I(\omega, z) = I(\omega, 0) \exp\left[-\alpha(\omega)z\right]. \tag{4.12}$$

When most of the atoms are in the ground state, the absorption coefficient can be expressed as $\alpha(\omega) = \mathcal{N}\sigma(\omega)$, the product of the atomic density $\mathcal{N}$, a function of the vapor temperature [50], and the absorption cross-section $\sigma(\omega)$ [40]. This cross-section is a measure of how strongly an atom will interact with and absorb the light; it is frequency-dependent and largest near the atomic resonance. Near resonance, this absorption cross-section is proportional to (1) the Voigt line profile—which is also a function of temperature; (2) the degeneracy of the ground state; and (3) the strength of the transition dipole matrix element [39, 75]. When these quantities are known, the transmission profile

$$T(\omega) \equiv I(\omega, d)/I(\omega, 0) = \exp\left[-\mathcal{N}\sigma(\omega)d\right] \tag{4.13}$$

through a cell of width d can be calculated and then compared to measured transmission curves [see, for example, Figure 8.2.8(b)]. Following the approach of [75], Figure 4.1 shows the calculated transmission spectrum for multiple transitions of ^{87}Rb in vapor cell of width $d = 1$ cm held at 25°C. Again, this calculation is valid for weak probe intensities, and also does not include effects such as optical pumping, spontaneous emission, or laser noise–all of which will modify the spectrum.

---

[6]Deviations from this law occur at higher intensities during nonlinear optical processes; for example, when the atoms' electrons are already in the excited state and cannot continue to absorb light, thereby saturating the absorption [See Section 4.3.1].
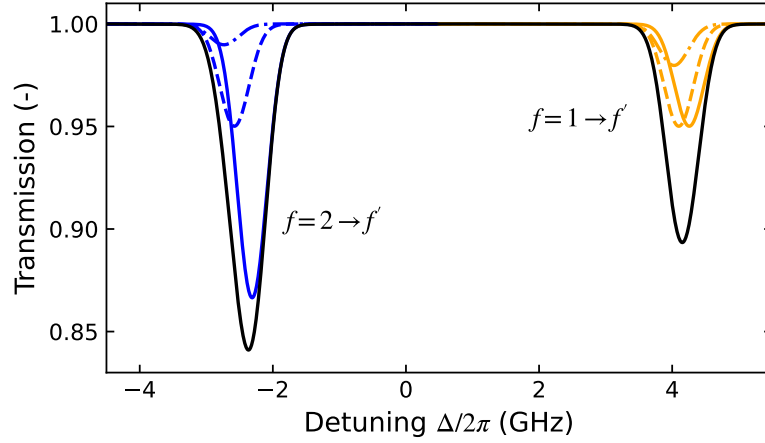
Figure 4.1: Calculated Doppler-broadened spectrum of D2 transitions in ^{87}Rb. The colored curves represent Doppler transmission profiles for individual transitions to excited hyperfine levels where f' is equal to $f - 1$ (dashed-dotted), f (dashed), and $f + 1$ (solid). The depth of each curve is indicative of its transition strength. The black solid curve is the combined (i.e. product) transmission profile for all transitions.

4.3 Additional broadening mechanisms

In the following section, we will briefly consider additional mechanisms that broaden spectral lines in warm or hot atomic vapors. Since the Doppler effect is much stronger than those discussed here, it will be temporarily set aside. The residual effects are organized into two categories: those that alter radiative decay rates from excited levels (generally more relevant for E1 transitions), and those that produce relaxation and dephasing of ground-state spin states (usually relevant for M1 transitions). Each will affect the measured width of spectral lines, probed either by an E1 or M1 transition.

4.3.1 Radiative broadening

Power broadening

This effect occurs at higher probe intensities when the Rabi frequency Ω_{ij} connecting two levels becomes comparable or greater than the corresponding decay rate γ_{ij}. Thus

at any given time, there exists a non-negligible fraction of the atoms' electrons in the excited state, and the ability of the atoms to absorb light degrades. In this situation, the absorption coefficient from Equation 4.11 becomes intensity-dependent according to [39, 40]

$$\alpha(\omega, I) = \frac{\mathcal{N}\sigma(\omega)}{1 + I/I_{\mathrm{s}}(\omega)}, \tag{4.14}$$

where $I_{\mathrm{s}}(\omega) = \hbar\omega\gamma_{ij}/2\sigma(\omega)$ is an atom-specific intensity parameter. Near resonance, $I_{\mathrm{s}}(\omega)$ has its minimum value called the saturation intensity $I_{\mathrm{sat},ij} \equiv I_{\mathrm{s}}(\omega_{ij})$. In this regime, we assume that the absorption cross-section can be expressed as $\sigma(\omega) = \sigma_0 g^*_{\gamma,ij}(\omega)$, proportional to the non-normalized Lorentzian function and scaled by the resonant scattering cross-section σ_0. By substituting all the frequency-dependent terms into Equation 4.14, we obtain

$$\alpha(\omega, I) = \mathcal{N}\sigma_0 \frac{\gamma_{ij}^2/4}{(\omega - \omega_0)^2 + (\Gamma_{\mathrm{sat},ij}/2)^2}, \tag{4.15}$$

where the width

$$\Gamma_{\mathrm{sat},ij} = \gamma_{ij}\left(1 + \frac{I}{I_{\mathrm{sat},ij}}\right)^{1/2}. \tag{4.16}$$

This shows that the width of the resonance equals the natural value for vanishing probe intensity and increases monotonically for increasing intensities. This is another example of homogeneous broadening. The D2 transition in ^{87}Rb has a typical value[7] of $I_{\mathrm{sat}} \simeq 3$ mW/cm^2 [50], which corresponds to a laser beam[8] with 47 μW of power and a waist of $w_0 = 1$ mm.

Transit-time broadening

This effect occurs due to the atoms transiting a probe beam of finite diameter. When this transit time is shorter than the excited state lifetime, the natural transition

---

[7]In general, I_{sat} depends on the specific transition matrix element, and also the relative orientation of the probe polarization and the atomic dipole [50].

[8]The power in a Gaussian beam is $P = \pi w_0^2 I_0/2$, where I_0 is the peak intensity and w_0 is the beam waist.

linewidth is broadened [39, 69]. Let's consider the perspective of an atom moving transversely through a Gaussian beam. It experiences a "pulse" of light with a Gaussian temporal electric field envelope of width $\Delta t_{1/e} = w/u$. Taking the Fourier transform of this envelope and squaring it produces a Gaussian spectral intensity profile with a $1/e$ angular frequency width of $\Delta\omega_{1/e} = \sqrt{2}u/w$, or a FWHM (in Hz) of

$$\Gamma_T/2\pi = \frac{\sqrt{\ln(2)}}{\pi}\frac{u}{w}. \tag{4.17}$$

For room-temperature atoms and the beam radius w_0 given above, this gives a $\Delta\Gamma_T = 63.3$ kHz. Because this effect depends on the atoms' velocity, it broadens the transition line inhomogeneously.

The estimate above is valid when the atoms move ballistically. In the presence of a buffer gas–an additional, higher-pressure noble atom or inert molecule, the alkali atoms will move diffusively and dwell longer in the beam. Reducing transit-time broadening is a primary motivation for employing a buffer gas.

Pressure broadening

In alkali atoms, pressure, or collisional, broadening is due to an induced dipole-dipole (i.e. van der Waals) interaction between the atomic nucleus and a nearby buffer gas atom/molecule. As the buffer and alkali atom approach each other, this interaction causes differential shifts in its ground and excited energy levels [39, 51]. For alkali atoms, this may be modeled as an effective hyperfine interaction [76], which homogeneously affects the atoms' linewidths.

The collision rate from ideal kinetic gas theory is [39, 76]

$$\Gamma = \mathcal{N}u\sigma, \tag{4.18}$$

where σ is the collisional cross-section and $\mathcal{N} = p_{\mathrm{B}}/kT$ is the buffer gas density. We

can then define the collisional broadening rate as

$$\Gamma_{\text{col}} = \left(\frac{\sigma_{\text{col}} u}{k_{\text{B}} T} \right) p_{\text{B}} \equiv a p_{\text{B}}, \tag{4.19}$$

where p_{B} is the buffer gas pressure and T is its temperature. The cross-section σ_{col}, or the broadening factor a, are empirically determined for different atomic and buffer gas combinations and are tabulated in sources such as [39]. In addition to this broadening, the extra kinetic energy involved in the collision creates a positive or negative shift in the transition line frequency. The degree of pressure broadening and the magnitude and sign of the frequency shift are specific to the alkali and buffer gas species, as well as the buffer gas pressure.

4.3.2 Spin-related broadening

Wall depolarization

Inelastic collisions with the cell walls strongly affect the coherence time of an atomic spin. In a collision, atoms temporarily adsorb onto the wall surface, where they experience an induced dipole-dipole (effective hyperfine) interaction with the wall's constituent molecules. By the time the atom desorbs again, the spin state is lost.

Precisely determining the effect of wall collisions and dwell times is an involved calculation [76, 77], but an upper-bound estimate is possible. We define a characteristic cell length

$$\varrho = \mathcal{V}/\mathcal{S}, \tag{4.20}$$

as the ratio of the cell's volume $\mathcal{V}$ to its surface area $\mathcal{S}$ [77]; it represents the average distance between wall collisions. If we assume that every collision with the wall relaxes the spin, then the upper limit of the wall relaxation rate is approximately

$$\Gamma_{\text{wall}}/2\pi \lesssim u/\varrho. \tag{4.21}$$

For a room-temperature cell with $\varrho = 1$ cm, this gives $\Gamma_{\text{wall}}/2\pi \sim 20$ kHz. Again, this upper bound does not consider dwell times or adsorption binding energies [76].

The wall dwell time can be reduced or practically eliminated by using an anti-relaxation coating on the cell wall. This coating is often composed of paraffin wax or another hydrocarbon molecule, such as alkene [78]. A good coating can provide about 10^4 [79, 80] to 10^6 [81] bounces before the spin relaxes. Coated cells are employed in warm atom experiments for quantum memories [81, 82], atomic clocks [83], magnetometry, and fundamental physics searches [84]. It is important to carefully monitor the temperature of a coated cell; elevated temperatures can melt and damage the coatings[9].

Spin-exchange collisions

Additional relaxation can occur from collisions between spin-polarized and -unpolarized atoms. The potential energy of the collision is highly dependent on the spin states of the atoms and can lead to an exchange of spin angular momentum, although the total spin is conserved [76]. The spin-exchange collision rate Γ_{SE} can be defined the same as in Equation 4.18, but where now we employ a spin-exchange cross-section σ_{SE}. Cross-sections are experimentally determined; for alkali atoms, they are typically on the order of $\sigma_{\text{SE}} \simeq 10^{-14}$ cm^2 [76]. Colliding pairs of ^{87}Rb atoms at room temperature have $\Gamma_{\text{SE}}/2\pi \simeq 1.4$ Hz.

Spin exchange does not always increase spin decoherence. When Γ_{SE} is larger than the Larmour frequency $\omega_{\text{L}} = \gamma_g B$, where B is the static magnetic field and γ_g is the gyromagnetic ratio, spin-exchange collisions with a buffer gas counter-intuitively preserve the spin state of the target atoms [85, 86]. This spin-exchange relaxation-free (SERF) regime usually occurs at high buffer gas pressure (i.e. $10^2 - 10^3$ torr) and

---

[9]For example, paraffin coatings degrade at temperatures above 60-80°C [80].

very low background magnetic fields ($\lesssim 10^{-3}$ G [87]). For this reason, SERF-based experiments often have 3 or 4 layers of magnetic shielding.

Magnetic fields

Magnetic fields can also be the source of relaxation or dephasing among the spin levels [76]. This can arise due to fluctuations or spatial gradients in the external magnetic field. In the atom's frame of reference, both sources of decoherence produce an effective precession of the spin state [69, 76].

Chapter 5

Nonlinear optical processes in neutral atoms

5.1 Linear optics

In Chapter 3, we examined the effect of coherent, monochromatic light on the electronic state of atoms. We now consider the opposite perspective and examine the effect of the atomic vapor, treated as a polarizable dielectric material, on the transiting, monochromatic light. When the light is relatively weak, the atoms' dielectric polarization[1] P is linearly proportional to the incident light's oscillating electric field E [89, 90] as

$$P(\omega, t) = \epsilon_0 \chi^{(1)}(\omega) E(\omega, t). \tag{5.1}$$

---

[1]P has units of electric dipole per unit volume, or Coulombs per meter squared [88].

The first-order electric susceptibility $\chi^{(1)}$ is a unitless, complex number that accounts for the different phase between P and E, both taken here as scalar quantities. The arguments[2] of P and E convey that each quantity depends on time t and oscillates at an angular frequency ω. The susceptibility is related to the complex index of refraction [89]

$$n(\omega) = \sqrt{1 + \chi^{(1)}(\omega)} = n'(\omega) + i\kappa(\omega), \tag{5.2}$$

where its real $n'(\omega)$ part governs the phase accumulation inside the medium, and its imaginary part $\kappa(\omega)$ governs the absorption and decay of the electric field amplitude. Once polarized, the material can re-radiate at the same frequency ω, although generally with a different phase; when $\kappa = 0$, the incident and emitted light are identical. In linear optics (i.e. materials that follow Equation 5.1), electric fields inside the material of different frequencies follow the superposition principle. For example, fields with two distinct frequencies, ω_1 and ω_2, create the combined polarization

$$\begin{aligned}
P^{(1)}(\omega_1, \omega_2, t) &= P_1^{(1)}(\omega_1, t) + P_2^{(1)}(\omega_2, t) \\
&= \epsilon_0 \left[\chi^{(1)}(\omega_1) E_1(\omega_1, t) + \chi^{(1)}(\omega_2) E_2(\omega_2, t) \right]
\end{aligned} \tag{5.3}$$

that re-radiates separately at the original two frequencies.

5.2   Nonlinear optics

We next turn our attention to contexts where the material affects the light in a nonlinear fashion. Nonlinear optics (NLO) is the study of processes where the dielectric polarization of the material does not obey the superposition principle, rather it is generally proportional to products of the incident fields. Nonlinear optical effects occur at high optical intensities or involve strong atomic resonances [88]. The polarization

---

[2]In this context, we have assumed the dipole approximation to remove the spatial-dependence of P and E [see Section 3.1.1].

can be expressed as a power series of incident fields [51]

$$
\begin{aligned}
P(\omega, t) &= \epsilon_0 \left[\chi^{(1)}(\omega) E(\omega, t) + \chi^{(2)}(\omega) E^2(\omega, t) + \chi^{(3)}(\omega) E^3(\omega, t) + \dots \right] \\
&= P^{(1)}(\omega, t) + P^{(2)}(\omega, t) + P^{(3)}(\omega, t) + \dots,
\end{aligned}
\tag{5.4}
$$

where each term is characterized by a nonlinear susceptibility[3] $\chi^{(i)}$ of order $i \in \mathbb{N}$. Higher-order NLO processes are weaker and therefore only observable with large input field intensities [55, 88]. Additionally, the physical symmetry of the material imposes constraints on whether certain NLO orders are permissible [see Section 5.4] [39, 51, 88]. A distinguishing feature of NLO processes is that the polarization [Equation 5.4] acts as a source for electric fields with frequencies not originally present in the incident waves; specifically, it can re-radiate at sums and differences of the input frequencies.

The power series of Equation 5.4 gives the accurate sense that NLO is a broad discipline; it touches many aspects of photonics and atomic physics. Since a full summary of this field is impossible, this section is limited to discussing NLO processes with a second-order susceptibility $\chi^{(2)}$.

We begin by considering the second-order polarization for an input wave with two frequency components,

$$
P^{(2)}(\omega_1, \omega_2, t) = \epsilon_0 \chi^{(2)}(\omega_1, \omega_2) \left[\mathcal{E}_1 \cos(\omega_1 t) + \mathcal{E}_2 \cos(\omega_2 t) \right]^2.
\tag{5.5}
$$

Using trigonometric identities, we expand this as

$$
\begin{aligned}
\frac{P^{(2)}(\omega_1, \omega_2, t)}{2\epsilon_0 \chi^{(2)}(\omega_1, \omega_2)} &= \left(\mathcal{E}_1^2 + \mathcal{E}_2^2 \right) + \mathcal{E}_1^2 \cos(2\omega_1 t) + \mathcal{E}_2^2 \cos(2\omega_2 t) \\
&\quad + 2\mathcal{E}_1 \mathcal{E}_2 \cos\left[(\omega_1 + \omega_2)t\right] + 2\mathcal{E}_1 \mathcal{E}_2 \cos\left[(\omega_1 - \omega_2)t\right],
\end{aligned}
\tag{5.6}
$$

where the terms on the R.H.S. represent emissions at distinct frequencies. The first term is called optical rectification, and it creates a non-radiating DC polarization

---

[3]Electric susceptibilities of order $i > 1$ have units of $(\mathrm{V/m})^{-(i-1)}$ and are also frequency-dependent.
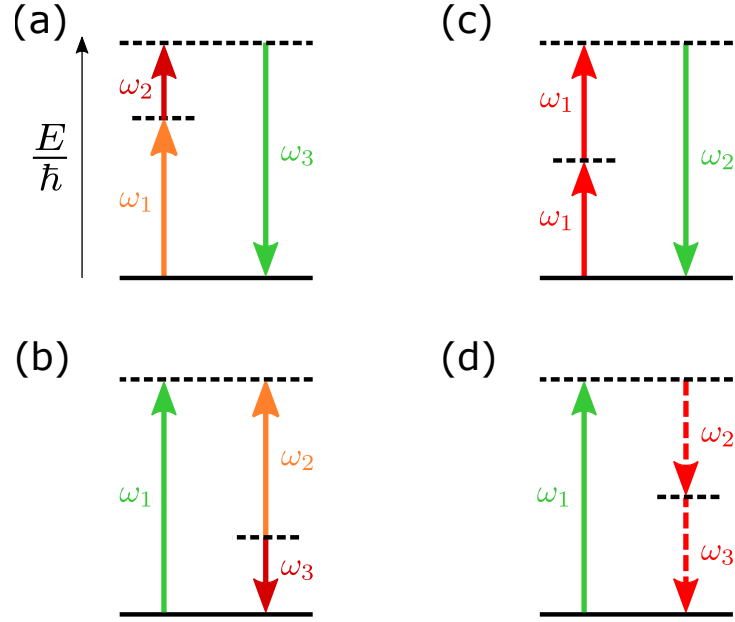
Figure 5.1: Energy level diagrams showing parametric $\chi^{(2)}$ processes. The solid horizontal lines represent real quantum eigenstates of the material, e.g. the ground electron level, while the dashed horizontal lines represent either a real or virtual level. Each arrow represents a photon with energy $\hbar\omega_i$. Upward arrows are the input photons, and downward arrows are the generated photons. Arrows with dashed tails indicate that the photon emission rates are small. (a) Sum-frequency generation. (b) Difference-frequency generation. (c) Second harmonic generation. (d) Spontaneous parametric down-conversion is a nonlinear quantum optics effect in which the emitted photons are much weaker than the pump [88, 91].

in the material; the second and third terms are called second-harmonic generation (SHG) or frequency doubling, where the material produces light at twice the input frequencies; the fourth and fifth terms represent sum-frequency (SFG) and difference-frequency generation (DFG). SHG is a special case of SFG, where the two input waves have degenerate frequencies. Spontaneous parametric downconversion [Figure 5.1(d)] is a time-reversed case of SHG (for degenerate photon frequencies) or SFG (for non-degenerate photon frequencies). Although it is a nonlinear optical process, it cannot

be described by the same classical description above, relying instead on a quantum optics description involving fluctuations of the electromagnetic vacuum field. Down-conversion is useful for creating pairs of entangled photons [92, 93].

Usually, no more than one of the $\chi^{(2)}$ processes in Equation 5.6 is observed simultaneously: this is because the phase-matching conditions [see Section 5.3] are not always satisfied for multiple frequencies at the same time [88]. The example above also demonstrates that multiple input fields are unnecessary for nonlinear effects such as SHG. Because three waves are present in every $\chi^{(2)}$ process, they are also known as three-wave mixing (TWM).

We employ "photon energy level" diagrams to visualize these different processes [88]. For example, in the SFG process shown in Figure 5.1(a), two photons of energy $\hbar\omega_1$ and $\hbar\omega_2$ are destroyed and one photon of energy $\hbar\omega_3$ is created. This figure also shows other examples of so-called parametric $\chi^{(2)}$ processes where the energy of all radiation fields is conserved [94]. Parametric NLO processes have completely real susceptibilities, and the material has identical initial and final quantum states[4].

5.3   Phase matching

In addition to energy conservation in a parametric $\chi^{(2)}$ processes, another important requirement for efficient nonlinear generation is the conservation of radiation momentum, otherwise known in this context as phase matching. Good phase matching is achieved when all the atoms distributed throughout the material emit coherently in-phase with each other [39]. When this occurs, the vector sum of the input wavevectors equals the output wavevector. Figure 5.2(a) shows the phase matching diagram

---

[4]In contrast, non-parametric processes generally have complex susceptibilities (implying absorption) and distinct initial and final states. Saturated absorption is an example of a non-parametric process [51, 88].
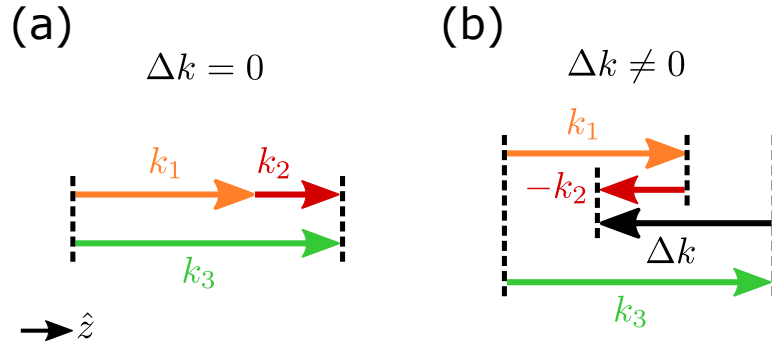
Figure 5.2: Phase matching diagram for one-dimensional sum-frequency generation. (a) When the fields propagate colinearly through the matrial, $\Delta k = 0$ and the amplitude of the SFG field $\mathcal{E}_3$ is maximized. (b) Reversing the direction of one input fields creates a large phase mismatch and suppresses the SFG amplitude.

for the SFG process depicted in Figure 5.1(a) where all beams propagate colinearly[5] through the material. Figure 5.2(b) shows the situation where one of the beams enters from the opposite direction, giving a phase mismatch

$$\Delta k = k_1 + k_2 - k_3 \tag{5.7}$$

that is no longer zero. Hence, the intensity of the generated light is strongly suppressed by the phase-matching function [39, 88, 95, 96]

$$\Phi(\omega_1, \omega_2) \propto \text{sinc}^2\left(\frac{\Delta k L}{2}\right), \tag{5.8}$$

where L is the length of the material. The generated intensity has its maximum value when $\Delta k = 0$ and is generally lower as $\Delta k L$ increases.

---

[5]The phase matching can become more complicated when the participating fields propagate through the material along multiple axes. Additionally, the conservation of angular momentum, i.e. the polarization of the light (not to be confused with the material polarization, Equation 5.4), is also an important factor in a nonlinear optical process.

5.4   Symmetry and allowed processes

In Section 3.2.3, we observed that the odd parity symmetry of electric fields dictates the selection rules of electric dipole transitions in multilevel atoms. There is a similar "selection rule" of NLO materials to determine whether certain processes are observable. We first define a heuristic parity function Π that acts on electromagnetic waves and material susceptibilities and polarizations; the function returns a +1 or -1 if the field/material has inversion symmetry (even parity) or not (odd parity).

Inversion symmetry[6] in the bulk of a material is defined by the property that the transformation of the position $\mathbf{r} \to -\mathbf{r}$ leaves the material unchanged. Materials such as liquids, gases/vapors, and amorphous solids, such as glass, possess this property. Some crystalline solids, such as diamond and silicon, also possess inversion symmetry, while other crystals, like quartz, do not.

The first observation of a NLO process was performed by Franken, et al. in 1961, shortly after the invention of the laser. They observed SHG after focusing their laser beam onto a sample of quartz; no SHG was observed using glass [97]. The absence of inversion symmetry is generally seen as a requirement for second-order NLO, which can be seen by examining the parities of the SHG terms from Equation 5.6

$$\Pi\{P^{(2)}\} = \Pi\{\chi^{(2)}\} \times \Pi\{\mathcal{E}\}^2 = (\pm 1)(-1)^2 = \pm 1, \qquad (5.9)$$

where the $\pm$ sign reflects the material's inversion symmetry property. Since parity is conserved in a nonlinear optical process, the electric polarization can only radiate a SHG electric field if the material is parity-odd, or $\Pi\{\chi^{(2)}\} = -1$. This is also true for the case of conventional SFG, where both input waves interact with a material via their electric fields.

---

[6]Equivalent terms are centrosymmetry and isotropy.

In this thesis, we consider another case of SFG, a process where one of the waves interacts with the material via an electric dipole interaction and the other wave via a magnetic dipole interaction. This situation is possible in an atomic gas where both types of transitions are present. This hybrid combination of fields alters the inversion symmetry requirement, allowing for SFG emission of light in an isotropic (parity-even) atomic gas. The parity of this SFG polarization

$$\Pi\{P^{(2)}\} = \Pi\{\chi^{(2)}\} \times \Pi\{\mathcal{E}_1\} \times \Pi\{\mathcal{B}_2\} = (+1)(-1)(+1) = (-1) \tag{5.10}$$

shows that this hybrid process can radiate an electric field at angular frequency $\omega_3 = \omega_1 + \omega_2$.

And Jacob was left alone;
and there wrestled a man with him
until the breaking of the day.

...And he said,
Let me go, for the day breaketh.
And [Jacob] said,
I will not let thee go, except thou bless me.

Genesis 32:24 & 29, The Holy Bible:
King James Version

Chapter 6

Theory of sum-frequency generation in neutral atoms

6.1   Introduction

After a general background in atomic transitions [Chapter 3], warm atom spectroscopy [Chapter 4], and nonlinear optics [Chapter 5], we are now prepared to theoretically examine the emergence of the unique SFG process alluded to in Section 5.4. In this chapter, we explore how this process allows for microwave-to-optical frequency conversion[1] with a large frequency-tunability and multi-frequency compatibility. The theory presented here is directly relevant to the experimental results of Chapter 8.

This chapter is organized into two parts. First, we follow the approach described

---

[1]See Chapter 8 for a discussion of the technological importance of microwave-to-optical frequency conversion and a review of other conversion techniques.

in Section 3.1.2 to derive the total Hamiltonian of a three-level atom influenced by electromagnetic idler, pump, and signal fields. Following previous work [98], we introduce the thermal, one-dimensional Doppler shift to the transitions, to derive an expression of SFG arising in a room-temperature atomic vapor sample. We show that the SFG spectrum follows the thermal Maxwell-Boltzmann distribution and examine the assumptions and phase-matching condition that pertain to this derivation.

Second, we describe the properties of analog-modulated waves and show how the separate modulations of the two input fields in the SFG process combine to generate spectral components with phase-dependent amplitudes.

6.2 Model of sum-frequency generation

6.2.1 Derivation of the three-level Hamiltonian

We begin by expressing the total Hamiltonian, composed of the bare atomic energy levels and the magnetic and electric dipole interactions

$$\hat{\mathcal{H}}(t) = \hat{H}_{\text{at}} + \hat{H}_{\text{int}}(t), \tag{6.1}$$

in the basis[2] $\{|b\rangle, |c\rangle, |a\rangle\}$. The zero of energy has been set to the $|b\rangle$ level, and the $|c\rangle$ and $|a\rangle$ levels have energies of $\hbar\omega_c$ and $\hbar\omega_a$, resulting in a bare atomic Hamiltonian of

$$\hat{H}_{\text{at}} = \hbar\omega_c|c\rangle\langle c| + \hbar\omega_a|a\rangle\langle a|. \tag{6.2}$$

The interaction Hamiltonian is composed of two terms $\hat{H}_{\text{int}} = \hat{H}_{\text{int}}^{(\text{M1})} + \hat{H}_{\text{int}}^{(\text{E1})}$ produced by three electromagnetic fields. In the two-level approximations, the idler field $\mathbf{B}_{\text{I}}$ connects $|b\rangle \leftrightarrow |c\rangle$, the pump field $\mathbf{E}_{\text{P}}$ connects $|c\rangle \leftrightarrow |a\rangle$, and the signal field $\mathbf{E}_{\text{S}}$ connects $|b\rangle \leftrightarrow |a\rangle$, as depicted in Figure 6.1. The magnetic dipole interaction

---

[2]Labeled as such for "bottom", "center", and "above".
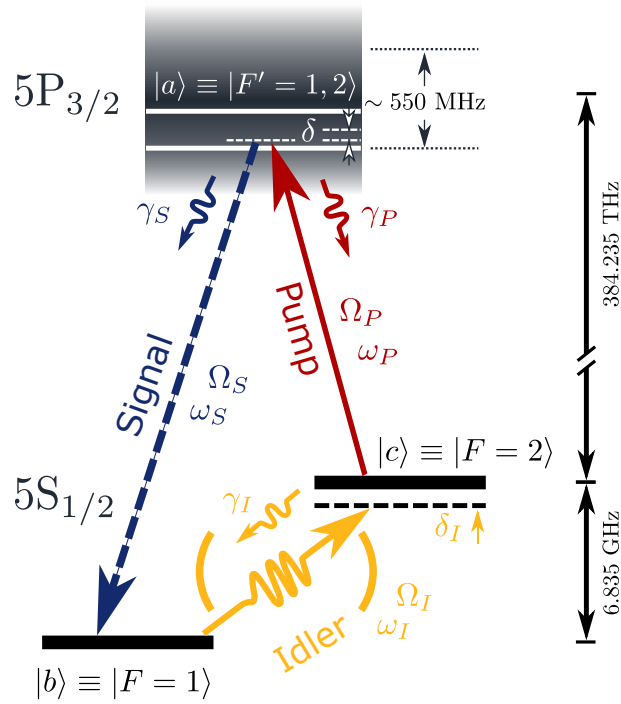
Figure 6.1: Three-level energy diagram showing the cyclical transition scheme. The idler (ω_I) and pump (ω_P) fields combine coherently in the vapor to produce the signal field (ω_S). The frequencies shown are for ^{87}Rb; in a room-temperature vapor, the excited state addressed by the pump field is Doppler-broadened by approximately 550 MHz.

induced by the idler field is

$$
\begin{aligned}
\hat{H}_\mathrm{int}^{(\mathrm{M1})} &= -\boldsymbol{\mu} \cdot \mathbf{B}_\mathrm{I}(t) |b\rangle\langle c| + \mathrm{H.C.} \\
&= -\mu_\mathrm{I} \mathcal{B}_\mathrm{I} \cos(\omega_\mathrm{I} t + \varphi_\mathrm{I}) |b\rangle\langle c| + \mathrm{H.C.},
\end{aligned}
\tag{6.3}
$$

where $\mathcal{B}_\mathrm{I}$ is the idler field amplitude and μ_I is the component of the magnetic dipole moment along the idler polarization. The electric dipole interaction induced by the pump and signal fields is

$$
\begin{aligned}
\hat{H}_\mathrm{int}^{(\mathrm{E1})} &= -\mathbf{d} \cdot [\mathbf{E}_\mathrm{P}(t)|c\rangle\langle a| + \mathbf{E}_\mathrm{S}(t)|b\rangle\langle a| + \mathrm{H.C.}] \\
&= -d_\mathrm{P} \mathcal{E}_\mathrm{P} \cos(\omega_\mathrm{P} t + \varphi_\mathrm{P}) |c\rangle\langle a| \\
&\quad - d_\mathrm{S} \mathcal{E}_\mathrm{S} \cos(\omega_\mathrm{S} t + \varphi_\mathrm{S}) |b\rangle\langle a| + \mathrm{H.C.},
\end{aligned}
\tag{6.4}
$$

where $\mathcal{E}_P$ and $\mathcal{E}_S$ are the pump and signal amplitudes, and d_P and d_S are the components of the electric dipole moment along their respective polarizations. In these expressions, we have already invoked the dipole approximation [see Section 3.1.1].

Using the same steps as in Section 3.1.2 we can obtain a representation of the total Hamiltonian

$$\mathcal{H} = -\hbar \begin{pmatrix} 0 & \Omega_I \cos(\omega_I t + \varphi_I) & \Omega_S \cos(\omega_S t + \varphi_S) \\ \Omega_I \cos(\omega_I t + \varphi_I) & -\omega_c & \Omega_P \cos(\omega_P t + \varphi_P) \\ \Omega_S \cos(\omega_S t + \varphi_S) & \Omega_P \cos(\omega_P t + \varphi_P) & -\omega_a \end{pmatrix}, \quad (6.5)$$

where the Rabi frequencies are defined as

$$\Omega_I \equiv \frac{\mathcal{B}_I \langle c | \mu_I | b \rangle}{\hbar}, \quad (6.6a)$$

$$\Omega_P \equiv \frac{\mathcal{E}_P \langle a | d_P | c \rangle}{\hbar}, \quad (6.6b)$$

$$\Omega_S \equiv \frac{\mathcal{E}_S \langle a | d_S | b \rangle}{\hbar}. \quad (6.6c)$$

We then choose the unitary matrix

$$U(t) = \begin{pmatrix} 1 & 0 & 0 \\ 0 & e^{i[(\omega_S - \omega_P)t + \varphi_S - \varphi_P]} & 0 \\ 0 & 0 & e^{i(\omega_S t + \varphi_S)} \end{pmatrix} \quad (6.7)$$

to transform the Hamiltonian and the basis states into a rotating frame according to Equation 3.11. Expanding the cosines as complex exponentials and simplifying results in

$$\tilde{\mathcal{H}}(t) = -\frac{\hbar}{2} \begin{pmatrix} 0 & \Omega_I \left(1 + e^{-2i[\omega_I t + \varphi_I]}\right) \times e^{i[(\omega_I + \omega_P - \omega_S)t + \varphi_I + \varphi_P - \varphi_S]} & \Omega_S \left(1 + e^{-2i[\omega_S t + \varphi_S]}\right) \\ \Omega_I \left(1 + e^{2i[\omega_I t + \varphi_I]}\right) \times e^{-i[(\omega_I + \omega_P - \omega_S)t + \varphi_I + \varphi_P - \varphi_S]} & -2(\omega_c + \omega_P - \omega_S) & \Omega_P \left(1 + e^{-2i[\omega_P t + \varphi_P]}\right) \\ \Omega_S \left(1 + e^{2i[\omega_S t + \varphi_S]}\right) & \Omega_P \left(1 + e^{2i[\omega_P t + \varphi_P]}\right) & -2(\omega_a - \omega_S) \end{pmatrix}. \quad (6.8)$$

The twice-rotating exponential terms time-average to zero and are discarded in the rotating wave approximation. Additionally, since nonlinear processes require energy conservation, i.e. $\hbar(\omega_I + \omega_P) = \hbar\omega_S$, we can simplify this expression further to get the final, time-independent Hamiltonian

$$\tilde{\mathcal{H}} \approx -\frac{\hbar}{2} \begin{pmatrix} 0 & \Omega_I e^{i\Delta\varphi} & \Omega_S \\ \Omega_I e^{-i\Delta\varphi} & 2(\delta_S - \delta_P) & \Omega_P \\ \Omega_S & \Omega_P & 2\delta_S \end{pmatrix}, \tag{6.9}$$

where we have defined the relative phase difference between all three fields as $\Delta\varphi \equiv \varphi_I + \varphi_P - \varphi_S$. We have also defined $\delta_S \equiv \omega_S - \omega_a$ and $\delta_P = \omega_P - (\omega_a - \omega_c)$ as the single-photon detunings in the lab frame [Figure 6.1 & Figure 6.2(a)], and $\delta_P - \delta_S \equiv \omega_c + \omega_P - \omega_S$ as the two-photon detuning. When $\Omega_I = 0$, Equation 6.9 is the conventional Λ-EIT Hamiltonian [65, 99].

6.2.2 Steady-state solutions of generation

In this one-dimensional model, the Rabi frequencies of the idler $\Omega_I(z)$, pump $\Omega_P(z)$, and signal $\Omega_S(z)$ fields are functions of position z through the vapor sample. Unlike in [98], however, we do not input signal light resonant with the signal transition, hence $\Omega_S(0) = 0$. In this context, the Hamiltonian operator in the rotating frame, under the rotating wave approximation [from Equation 6.9] can be expressed as

$$\begin{aligned} \widehat{\tilde{\mathcal{H}}}(\boldsymbol{v}, z)/\hbar = & -\Delta_S(\boldsymbol{v})|a\rangle\langle a| - [\Delta_S(\boldsymbol{v}) - \Delta_P(\boldsymbol{v})]\,|c\rangle\langle c| \\ & -\frac{\Omega_P(z)}{2}|a\rangle\langle c| - \frac{\Omega_I(z)e^{i\Delta\varphi}}{2}|c\rangle\langle b| + \text{H.C..} \end{aligned} \tag{6.10}$$

As seen in the atom frame, the Doppler-shifted detunings of the pump and the SFG signal fields [Figure 6.2 (c-e)] are $\Delta_P = \delta_P - \mathbf{k}_P \cdot \boldsymbol{v}$ and $\Delta_S = \delta_S - \mathbf{k}_S \cdot \boldsymbol{v}$. The microwave idler field has negligible Doppler shift for all velocities [see Section 6.2.3]. The natural decay rates from $|a\rangle$ to $|c\rangle$ and $|b\rangle$ are γ_P and γ_S, while the decay rate from $|c\rangle$ to $|b\rangle$ is γ_I [Figure 6.1(c)].
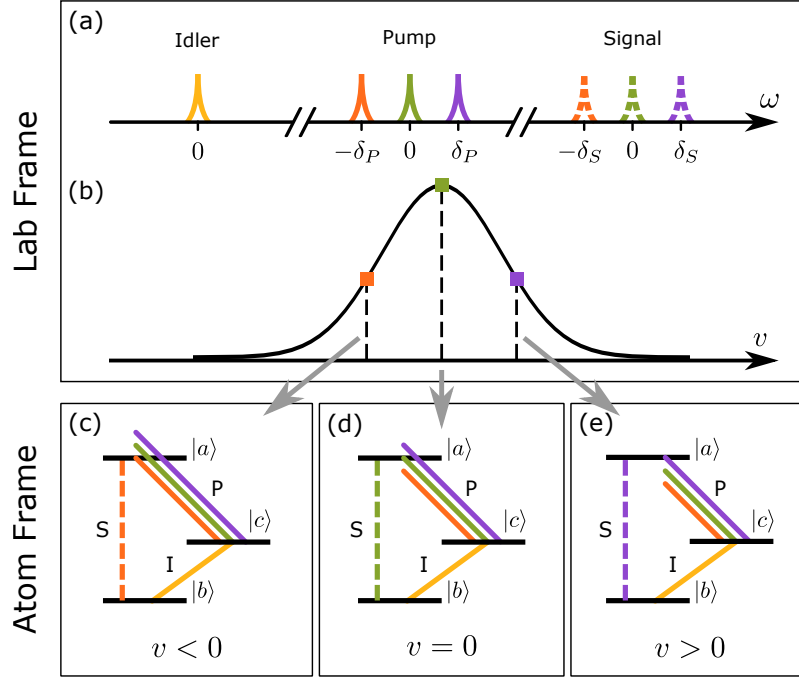
Figure 6.2: (a-b) Lab-frame depiction of multiple pump frequency channels (central-green, upper-purple, lower-organge) combining with a single idler to produce multiple signal channels. (b) These pump frequencies access independent atomic velocity classes from a thermal MB distribution. (c-e) In their reference frame, atoms in these velocity classes see their respective pump Doppler-shifted to resonance. Generation occurs in the velocity class for which the three-photon resonance condition (i.e. energy conservation) is satisfied.

We now seek steady-state solutions of the time evolution of the system. As discussed in Section 3.1.3, since dissipation channels are present in the system, we use the Lindblad equation [Equation 3.23] to solve for the dynamics of the density operator $\hat{\sigma}$ in the rotating frame [Equation 3.20]. The master equation takes the form

$$
\begin{aligned}
\frac{\partial \hat{\sigma}(\boldsymbol{v}, z, t)}{\partial t} = & -i\left[\widehat{\tilde{\mathcal{H}}}(\boldsymbol{v}, z), \ \hat{\sigma}(\boldsymbol{v}, z, t)\right] \\
& + \sum_{k=1}^{5} \hat{L}_i \hat{\sigma}(\boldsymbol{v}, z, t) \hat{L}_i^\dagger - \frac{1}{2}\left\{\hat{L}_i^\dagger \hat{L}_i, \ \hat{\sigma}(\boldsymbol{v}, z, t)\right\},
\end{aligned}
\tag{6.11}
$$

where the five collapse operators are defined as

$$\hat{L}_1 \equiv \sqrt{(\bar{n}+1)\gamma_{\mathrm{I}}}|b\rangle\langle c|, \tag{6.12a}$$

$$\hat{L}_2 \equiv \sqrt{\bar{n}\gamma_{\mathrm{I}}}|c\rangle\langle b|, \tag{6.12b}$$

$$\hat{L}_3 \equiv \sqrt{\gamma_{\mathrm{S}}}|b\rangle\langle a|, \tag{6.12c}$$

$$\hat{L}_4 \equiv \sqrt{\gamma_{\mathrm{P}}}|c\rangle\langle a|, \tag{6.12d}$$

$$\hat{L}_5 \equiv \sqrt{\gamma_{\mathrm{cav}}}\left(|b\rangle\langle b| - |c\rangle\langle c|\right). \tag{6.12e}$$

The decay rate γ_{cav} is related to the finite microwave cavity linewidth. The quantity $\bar{n}$ is the average number of thermal microwave photons. If we had sufficiently sensitivity, we would observe repopulation of the $|c\rangle$ state and power-broadening of the idler transition's natural linewidth due to these photons; in practice, thermal power broadening is relatively small compared to other mechanisms [see Section 6.2.3]. By assuming $\bar{n} \ll 1$ and $\gamma_{\mathrm{cav}} \ll \gamma_{\mathrm{P}}, \gamma_{\mathrm{S}}$, we reduce the total number of collapse operators to three.

We can solve for the density matrix coherence σ_{ab} corresponding to the signal transition at steady-state [98] to obtain

$$\sigma_{ab} = \frac{-\Gamma_3 \Omega_{\mathrm{P}}(z)\Omega_{\mathrm{I}}(z)e^{i\Delta\varphi}}{4\Gamma_1\Gamma_2\Gamma_3 + \Gamma_3|\Omega_{\mathrm{P}}(z)|^2 + \Gamma_2|\Omega_{\mathrm{I}}(z)|^2}, \tag{6.13}$$

where

$$\Gamma_1 = \frac{\gamma_{\mathrm{S}}}{2} + \frac{\gamma_{\mathrm{P}}}{2} - i\Delta_{\mathrm{S}}(\boldsymbol{v}) \tag{6.14a}$$

$$\Gamma_2 = \frac{\gamma_{\mathrm{I}}}{2} - i\left[\Delta_{\mathrm{S}}(\boldsymbol{v}) - \Delta_{\mathrm{P}}(\boldsymbol{v})\right] \tag{6.14b}$$

$$\Gamma_3 = \frac{\gamma_{\mathrm{S}}}{2} + \frac{\gamma_{\mathrm{P}}}{2} + \frac{\gamma_{\mathrm{I}}}{2} - i\Delta_{\mathrm{P}}(\boldsymbol{v}). \tag{6.14c}$$

The slowly-varying-envelope approximation [see Section 6.2.3] can be used to simplify and reduce the second-order Maxwell wave equation [88, 89]

$$\frac{\partial^2 \mathbf{E}(z,t)}{\partial z^2} - \frac{1}{c^2}\frac{\partial^2 \mathbf{E}(z,t)}{\partial t^2} = \mu_0 \frac{\partial^2 \mathbf{P}(z,t)}{\partial t^2} \tag{6.15}$$

to a first-order propagation equation [88, 98, 100]

$$\frac{\partial \Omega_\text{S}(z)}{\partial z} = i\eta_\text{S}\sigma_{ab},\tag{6.16}$$

which relates the coherence σ_{ab} to the corresponding SFG field amplitude envelope $\Omega_\text{S}(z) = \mathcal{E}_\text{S}(z)\mathbf{d}_{ab}/\hbar$. The signal-field coupling constant is $\eta_\text{S} = \mathbf{d}_{ab}^2\omega_\text{S}N(v)/2\epsilon_0 c\hbar$ [98, 101], where $N(v)$ is the Maxwell-Boltzmann density of atoms in the velocity class $v = |\boldsymbol{v}|$. The dielectric polarization of the $|a\rangle \leftrightarrow |b\rangle$ transition of interest is proportional to the density matrix coherence, i.e. $\mathbf{P}_{ab} = N(v)\mathbf{d}_{ab}\sigma_{ab}$.

We ignore the propagation of the microwave field because the relevant mode is a standing wave, and because $\boldsymbol{\mu}_{cb}$ and ω_I are so much smaller than their optical (electric) counterparts. We also assume that the absorption and depletion of the pump are negligible throughout the vapor cell; this is called the undepleted pump approximation and allows us to replace $\Omega_\text{P}(z) \to \Omega_\text{P}(0)$ [See Section 6.2.3]. This also presumes that the pump and idler fields have no spatial dependence and act as uniform plane waves. Although our pump field is a laser beam with a Gaussian cross-sectional profile, the plane-wave approximation is appropriate near the center of the beam.

After passing through length ℓ of the vapor, the SFG signal Rabi frequency is

$$\Omega_\text{S}(\ell) = \frac{i\Omega_\text{P}(0)\Omega_\text{I}(0)e^{i\Delta\varphi}}{2\Gamma_2}(e^{-\zeta\ell} - 1),\tag{6.17}$$

where the constant

$$\zeta = \frac{2\eta_\text{S}\Gamma_2\Gamma_3}{4\Gamma_1\Gamma_2\Gamma_3 + \Gamma_3|\Omega_\text{P}(0)|^2 + \Gamma_2|\Omega_\text{I}(0)|^2}.\tag{6.18}$$

To maximize the SFG signal field, sufficiently high input pump and idler field intensities and a small value for Γ_2 [Equation (6.17)] are required. From Equation (6.14b), this occurs at the two-photon resonance condition, or

$$\Delta_\text{S}(\boldsymbol{v}) - \Delta_\text{P}(\boldsymbol{v}) \approx \delta_\text{S} - \delta_\text{P} = 0.\tag{6.19}$$

6.2.3   Assumptions

Here we summarize the assumptions made in this derivation, and comment on their relevance and validity to this system.

Negligible thermal microwave photon broadening

The occupation of microwave photons at temperature T and at the idler frequency ω_I is given by the Bose distribution,

$$\bar{n}(T,\omega) = \frac{1}{\exp(\hbar\omega/k_B T) - 1}, \tag{6.20}$$

which has a value of $\bar{n} = 914$ at $T = 300$ K. The intensity of this thermal photon bath is its energy divided by the speed of light c

$$I_{\text{th}} = \frac{\bar{n}\hbar\omega_I}{c} \approx 1.4 \times 10^{-29} \text{ Wm}^{-2} \tag{6.21}$$

We compare this value to an estimate of the radiative saturation intensity of the ground state $F = 1 \to F = 2$ transition [40]

$$I_{\text{sat}} = \frac{\pi}{3}\frac{h\Delta\nu f_I^2}{c^2}, \tag{6.22}$$

where $\Delta\nu$ is the natural radiative linewidth of the $F = 2$ state. In practice, $\Delta\nu$ is challenging to measure because the hyperfine ground states have *extremely* weak radiative coupling. Many values in the literature give $\Delta\nu$ in the order of $10 - 10^2$ Hz [102–104], but these figures are dominated by pressure or optical broadening mechanisms [see Section 4.3], so we expect the intrinsic $\Delta\nu \ll 10^2$ Hz. With a conservative $\Delta\nu \sim 1$ Hz and the ground state separation of $f_I = 6.834$ GHz, we get a saturation intensity of $I_{\text{sat}} = 2.4 \times 10^{-21}$ Wm^{-2}, over eight orders of magnitude higher than I_{th}. Even with the uncertainty of the idler linewidth, with these estimates, we can confidently neglect thermal microwave photon power broadening.

Negligible idler Doppler shift

We consider the Doppler shift caused by the 1D motion of an atom with respect to an electromagnetic wave traveling along the **k** direction. In a room temperature vapor, the most probable velocity of the atoms is $u = \sqrt{2k_B T/m} \simeq 239$ ms^{-1}. In 1D, the Doppler shift is $\Delta_\mathrm{D} = |\mathbf{k}|u = (\omega_\mathrm{I}/c)u \simeq 2\pi \times 5.5$ kHz. This shift is much smaller than the corresponding optical Doppler shift, the ground state decoherence rate γ_I, and the cavity linewidth.

Undepleted pump approximation

The undepleted pump approximation treats the pump field as an unlimited reservoir from which to extract energy for creating signal photons. This means that atomic absorption and spatial variations of the pump field can be ignored, i.e. $\partial \Omega_\mathrm{P}(z)/\partial z \rightarrow 0$ [88]. In Section 7.7.3, we characterize the optical depth of the vapor cell to be about 0.05(1). This implies that only $1 - e^{-0.05} = 5\%$ of the input pump power is lost from the beam due to absorption, and we can reasonably treat the pump as undepleted [96].

Slowly-varying envelope approximation

$\mathcal{E}(z,t)$ is the amplitude envelope function of an input field $\mathbf{E}(z,t) = \mathcal{E}(z,t)\hat{e}_x \cos(kz - \omega t)$. The slowly-varying envelope approximation is valid when $\mathcal{E}$ doesn't change significantly over a wavelength [88, 101], or

$$|\partial_{zz}\mathcal{E}(z,t)| \ll k|\partial_z\mathcal{E}(z,t)|, \tag{6.23a}$$

$$|\partial_{tt}\mathcal{E}(z,t)| \ll \omega|\partial_t\mathcal{E}(z,t)|. \tag{6.23b}$$

This also applies to the amplitude envelope function $\mathcal{P}(z,t)$ of the dielectric polarization $\mathbf{P}(z,t)$

$$|\partial_{zz}\mathcal{P}| \ll k|\partial_z\mathcal{P}|, \tag{6.24a}$$

$$|\partial_{tt}\mathcal{P}| \ll \omega|\partial_t\mathcal{P}|, \tag{6.24b}$$

$$|\partial_t\mathcal{P}| \ll \omega|\mathcal{P}|, \tag{6.24c}$$

having the additional condition that we can neglect the first derivative of $\mathcal{P}$. Together, these provide a way to simplify, or reduce, the second-order Maxwell wave equation of the *vector fields* to a first-order differential equation of the slowly-varying *amplitudes*.

This approximation would not be valid for ultrafast pulses of idler or pump fields. However, in this thesis, we operate this experiment in the continuous-wave regime at steady-state.

6.2.4   Phase matching and velocity classes

In the Λ-type 3-level system, the optical wavelengths are similar, such that $|\mathbf{k_S}| \approx |\mathbf{k_P}| \gg |\mathbf{k_I}|$, in which case Equation (6.19) reduces to $(\delta_S - \delta_P) = 0$. Since the signal and pump fields travel in the same direction, the phase-matching condition $\mathbf{k_I} + \mathbf{k_P} = \mathbf{k_S}$ is automatically satisfied for all atomic velocity classes.

Because the maximum SFG signal is obtained when the signal-field detuning δ_S is the same as the pump-field detuning δ_P, we conclude that distinct velocity classes participate in the maximum signal-field generation at different pump/signal-field detunings. Therefore, changing the laboratory pump frequency within the Doppler-broadened width to $\omega_P' = \omega_P + \delta$ gives rise to a corresponding signal field at $\omega_S' = \omega_S + \delta$, thus enabling a large-tunable generation bandwidth. This is depicted numerically in Figure 6.2(b) for atoms at $T = 300°C$. The shape of the SFG signal profile is primarily determined by the MB velocity distribution.
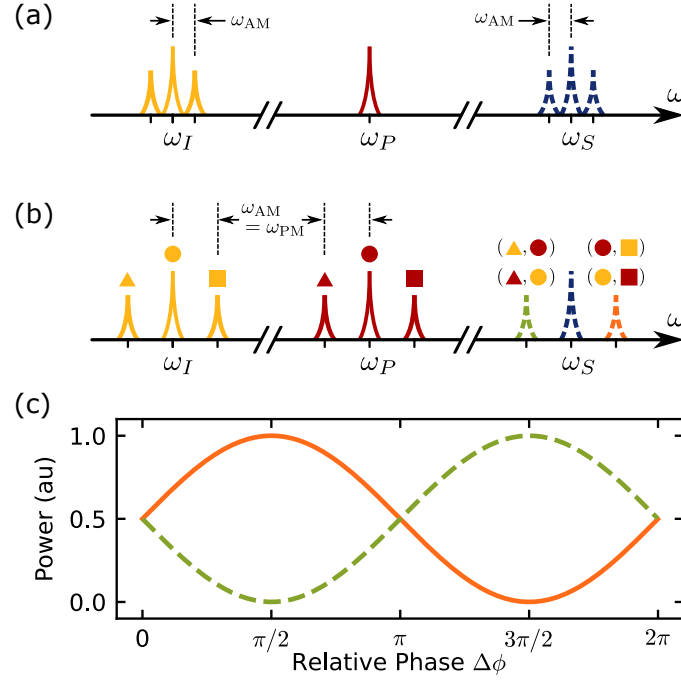
Figure 6.3: (a) An amplitude-modulated idler field spectrum showing sidebands (SBs). The idler carrier and SBs combine with the pump to produce a multichannel signal spectrum. (b) When the idler and pump are both modulated at the same frequency, multiple generation pathways interfere, producing upper and lower signal SBs. The input fields each have lower (▲), central (●), and upper (■) spectral peaks. (c) Calculated curves showing correlated signal SB amplitudes, which vary coherently with the relative phase of the amplitude and phase modulations. Here, both the AM depth and PM index are 0.2.

The broad Doppler width at room temperature, together with the guaranteed phase-matching for sum-frequency generation [Equation (6.19)], make possible the simultaneous conversion of multi-channel microwave or pump field inputs–obtained via amplitude or phase modulation–to multi-channel optical signal outputs, as depicted in Figure 6.3.

6.3   Wave modulation

In this section, we examine the effect of modulations on the input idler and pump fields, and how those coherently transduce to modulations of the output signal field. We begin introducing several modulation methods, how they are represented mathematically, and how combinations of them manifest in the three-wave mixing process.

Electromagnetic waves, such as optical light, are perhaps the best carrier of information. Not only do they travel at the speed of light, but they also have many different degrees of freedom in which to encode a message. For example, information can be encoded in the amplitude, phase, or frequency of a wave for transmitting analog or digital signals [105, 106]. Encodings are also possible using the polarization (spin-angular momentum) [107, 108], orbital angular momentum [106, 109, 110], and arrival times of single photons [111]. While the following section focuses on analog modulation of classical waves, photonic encodings are routinely used with quantum light sources.

6.3.1   Analog modulations

Modulations are low-frequency signals that are imprinted onto a high-frequency electromagnetic wave called a carrier. In the absence of any modulations, the carrier
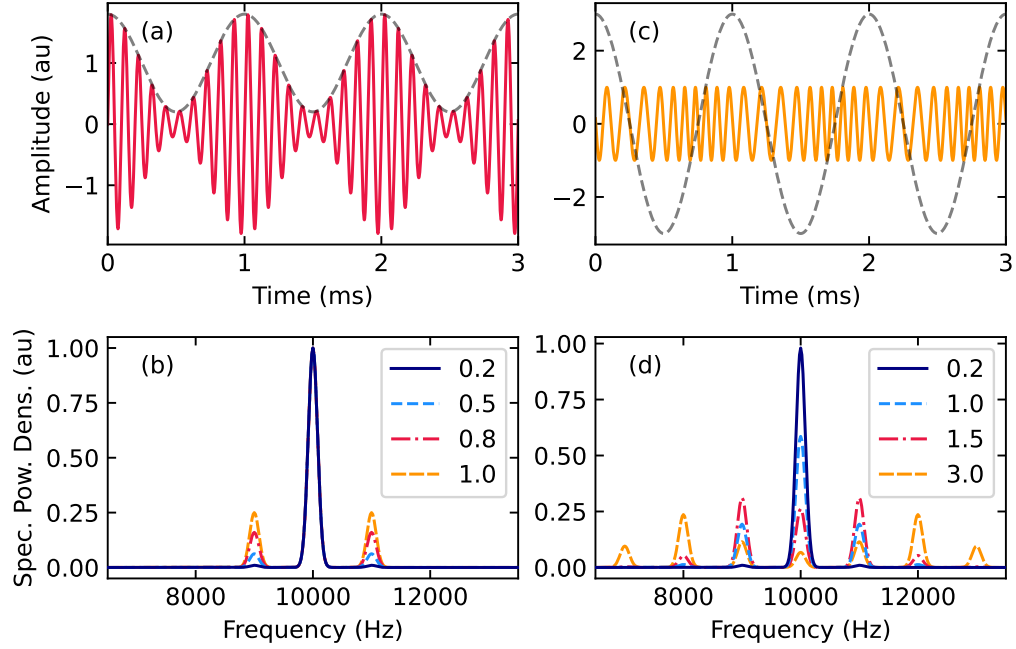
Figure 6.4: Calculated time-domain waveforms of a 10 kHz carrier wave (a) amplitude-modulated with a modulation depth $m = 0.8$, and (c) phase-modulated at 1 kHz with a modulation index $\beta = 3.0$ rad. In both time-domain plots, the dashed grey curve is the modulating wave. (b) The frequency spectrum of the (b) AM and (d) PM waves are shown for various modulation depths/indices. Unlike in the AM case, in PM the carrier amplitude depends on the modulation index. For visibility of the spectral peaks, the modulated carrier waves occur within a Gaussian envelope with $\Delta t_{\mathrm{FWHM}} \approx 5$ ms [not shown in (a) and (c)].

frequency spectrum is a delta function[3] at the carrier frequency ω_{car}. Modulating the wave's degrees of freedom creates additional spectral features around ω_{car}. The simplest modulation of a carrier wave is a sine wave at a low-frequency ω_m.

First, we consider the case of sine amplitude modulation (AM). Mathematically, the wave takes the form

$$B(t) = [1 + m \sin(\omega_m t)] \left[A \sin(\omega_{\mathrm{car}} t) \right], \tag{6.25}$$

where A is the original carrier amplitude. The modulation depth m represents the strength of the modulation. Figure 6.4(a) shows an AM wave with a $m = 0.8$ or 80%; the modulating sine wave is displayed as a grey dashed line. Using trigonometric identities, Equation 6.25 can be expanded to obtain

$$B(t) = A \left(\sin(\omega_{\mathrm{car}} t) + \frac{m}{2} \cos\left[(\omega_{\mathrm{car}} - \omega_m) t \right] - \frac{m}{2} \cos\left[(\omega_{\mathrm{car}} + \omega_m) t \right] \right). \tag{6.26}$$

This expression shows that this wave possesses frequency components at $\{\omega_{\mathrm{car}}, \omega_{\mathrm{car}} \pm \omega_m\}$ which are seen in the frequency spectrum of the wave [Figure 6.4(b)]. The positive and negative peaks are also called sidebands. Theoretically, sine AM has only a single upper and lower sideband; in practice, nonlinear elements in the electrical or optical system produce higher order sidebands $\omega_{\mathrm{car}} \pm n\omega_m$ at additional harmonics $n \in \mathbb{N} : n \geq 2$ of the modulation frequency [see, for example, Figure 7.23]. Amplitude modulation is the simplest of the modulation schemes. The microwave source used in this thesis' experiments supports amplitude modulation of the idler wave.

We also consider sine phase modulation (PM) of the form:

$$E(t) = A \sin[\omega_{\mathrm{car}} t + \beta \sin(\omega_m t)], \tag{6.27}$$

where the modulation index β, unlike m, has units of radians. Modulating the phase of the wave has the effect of accelerating or decelerating the phase winding of the

---

[3]Chopping this wave into a short pulse of temporal width Δt broadens this narrow spectral feature into a peak with width $1/\Delta t$.

wave. Figure 6.4(c) shows a PM wave with $\beta = 3$ and the modulating wave as a grey dashed line. When the modulating wave's slope is most positive, the PM wave experiences faster winding of the phase; conversely, when its slope is most negative, the PM wave experiences slower phase winding.

Section 7.3.5 will show how a PM wave like Equation 6.27 can be expanded into frequency components $\omega \pm n\omega_m$ with amplitudes $J_n(\beta)$, for $n \in \mathbb{N}$. These frequency components can be seen in Figure 6.4(d), where the amplitude of the nth sideband is proportional to the corresponding Bessel function of the modulation index, $J_n(\beta)$. Expanding out Equation 7.11 to second order in n gives[4]

$$E(t) = A\left[J_0(\beta)\sin(\omega_{\text{car}}t) + J_1(\beta)\sin([\omega_{\text{car}} + \omega_m]t) - J_1(\beta)\sin([\omega_{\text{car}} - \omega_m]t)\right.$$
$$\left. + J_2(\beta)\sin([\omega_{\text{car}} + 2\omega_m]t) + J_2(\beta)\sin([\omega_{\text{car}} - 2\omega_m]t)\right]. \tag{6.28}$$

Frequency modulation (FM) is another possible scheme that is not employed in the experiments of this thesis. Like PM, FM modifies the carrier wave function's argument. If we consider a simple wave $A\sin(\Phi(t)) = A\sin(\omega t)$, the frequency ω is the time-derivative of the overall time-dependent phase $\Phi(t)$. Thus, a sine FM appears in the carrier wave function's argument as the *integral* of the modulating wave, or

$$F(t) = A\sin\left(\omega_{\text{car}}t + f_\Delta \int_0^t \sin(\omega_m\tau)\mathrm{d}\tau\right)$$
$$= A\sin\left(\omega_{\text{car}}t - f_\Delta\frac{\cos(\omega_m t)}{\omega_m}\right), \tag{6.29}$$

where the modulation deviation f_Δ has units of frequency. In this situation, the phase accelerates the most when the *value* of the modulation wave is maximum, and the phase decelerates the most when the modulation wave is minimum. This is in

---

[4]The minus sign in Equation 6.28 arises due to the following properties of Bessel functions

$$J_{-n}(x) = (-1)^n J_n(x),$$
$$J_n(-x) = (-1)^n J_n(x).$$

contrast to PM where the phase advances depending on the *slope* of the modulation wave.

6.3.2 Sum-frequency of two modulated waves

In this section, we examine a specific case of the sum-frequency process where a PM pump combines with an AM idler. These fields are modulated with a sine wave at the same frequency $\omega_{\mathrm{PM}} = \omega_{\mathrm{AM}} \equiv \Delta_m$. The two sine modulations have a well-defined relative phase ϕ that can be varied between 0 and 2π. We examine this specific case theoretically, beginning with expressions for the two fields as derived previously. The idler field is similar to the AM wave from Equation 6.25, with the inclusion of ϕ:

$$\Omega_{\mathrm{I}}(t) = \Omega_{\mathrm{I}0} \left[1 + m \sin(\Delta_m t + \phi) \right] \sin(\omega_{\mathrm{I}} t). \tag{6.30}$$

As above, this expression can be expanded into frequency components, highlighting the carrier and two sidebands

$$\Omega_{\mathrm{I}}(t) = \Omega_{\mathrm{I}0} \left\{ \sin(\omega_{\mathrm{I}} t) + \frac{m}{2} \cos[(\omega_{\mathrm{I}} - \Delta_m)t - \phi] - \frac{m}{2} \cos[(\omega_{\mathrm{I}} + \Delta_m)t + \phi] \right\}. \tag{6.31}$$

The expression for the pump field is similar to the PM wave derived in Equation 6.28, here expanded to second-order in the sideband index.

$$\Omega_{\mathrm{P}}(t) = \Omega_{\mathrm{P}0} \left\{ J_0(\beta) \sin(\omega_{\mathrm{P}} t) + J_1(\beta) \sin[(\omega_{\mathrm{P}} + \Delta_m)t] - J_1(\beta) \sin[(\omega_{\mathrm{P}} - \Delta_m)t] \right.$$

$$\left. + J_2(\beta) \sin[(\omega_{\mathrm{P}} + 2\Delta_m)t] + J_2(\beta) \sin[(\omega_{\mathrm{P}} - 2\Delta_m)t] \right\}. \tag{6.32}$$

Going forward, we will suppress the arguments of the Bessel functions. Now, according to Equation 6.17, the amplitude of the signal field $\Omega_{\mathrm{S}}(t)$ is proportional to the product of $\Omega_{\mathrm{P}}(t) \times \Omega_{\mathrm{I}}(t)$. Thus, with 3 frequency components of the idler wave and 5 of the pump wave, the signal field possesses 15 cross-terms:

$$\Omega_{\mathrm{S}}(t) \propto \frac{\Omega_{\mathrm{P0}}\Omega_{\mathrm{I0}}}{2}\Bigg\{\; 2J_0 \sin(\omega_{\mathrm{P}}t)\sin(\omega_{\mathrm{I}}t)$$

$$+2J_1 \sin[(\omega_{\mathrm{P}}+\Delta_m)t]\sin(\omega_{\mathrm{I}}t)$$
$$-2J_1 \sin[(\omega_{\mathrm{P}}-\Delta_m)t]\sin(\omega_{\mathrm{I}}t)$$
$$+2J_2 \sin[(\omega_{\mathrm{P}}+2\Delta_m)t]\sin(\omega_{\mathrm{I}}t)$$
$$+2J_2 \sin[(\omega_{\mathrm{P}}-2\Delta_m)t]\sin(\omega_{\mathrm{I}}t)$$
$$+mJ_0 \sin(\omega_{\mathrm{P}}t)\cos[(\omega_{\mathrm{I}}-\Delta_m)t-\phi]$$
$$+mJ_1 \sin[(\omega_{\mathrm{P}}+\Delta_m)t]\cos[(\omega_{\mathrm{I}}-\Delta_m)t-\phi]$$
$$-mJ_1 \sin[(\omega_{\mathrm{P}}-\Delta_m)t]\cos[(\omega_{\mathrm{I}}-\Delta_m)t-\phi] \qquad (6.33)$$
$$+mJ_2 \sin[(\omega_{\mathrm{P}}+2\Delta_m)t]\cos[(\omega_{\mathrm{I}}-\Delta_m)t-\phi]$$
$$+mJ_2 \sin[(\omega_{\mathrm{P}}-2\Delta_m)t]\cos[(\omega_{\mathrm{I}}-\Delta_m)t-\phi]$$
$$+mJ_0 \sin(\omega_{\mathrm{P}}t)\cos[(\omega_{\mathrm{I}}+\Delta_m)t+\phi]$$
$$+mJ_1 \sin[(\omega_{\mathrm{P}}+\Delta_m)t]\cos[(\omega_{\mathrm{I}}+\Delta_m)t+\phi]$$
$$-mJ_1 \sin[(\omega_{\mathrm{P}}-\Delta_m)t]\cos[(\omega_{\mathrm{I}}+\Delta_m)t+\phi]$$
$$+mJ_2 \sin[(\omega_{\mathrm{P}}+2\Delta_m)t]\cos[(\omega_{\mathrm{I}}+\Delta_m)t+\phi]$$

$$+mJ_2 \sin[(\omega_{\mathrm{P}}-2\Delta_m)t]\cos[(\omega_{\mathrm{I}}+\Delta_m)t+\phi]\Bigg\}.$$

We simplify these terms using product-to-sum trigonometric identities. Oscillating terms emerge at frequencies near $\omega_{\mathrm{S}} \equiv \omega_{\mathrm{P}}+\omega_{\mathrm{I}}$ (sum-frequency), but also at frequencies near $\omega_{\mathrm{D}} \equiv \omega_{\mathrm{P}} - \omega_{\mathrm{I}}$ (difference-frequency). These difference terms are discarded given that we do not have an atomic density of states near ω_{D} for the transitions selected in this experiment.

We group these terms according to the sideband index $n \in \{0, \pm 1, \pm 2, \pm 3\}$ and, for simplicity, consider only $|n| \leq 2$. Additional sum-difference trigonometric identities isolate the phase ϕ. We are left with expressions of the SFG wave oscillating at $\omega_{\mathrm{S}} + n\Delta_m$ having the form

$$\Omega_{\mathrm{S},n}(t) = I_n(m,\beta,\phi)\cos[(\omega_{\mathrm{S}}+n\Delta_m)t] + Q_n(m,\beta,\phi)\sin[(\omega_{\mathrm{S}}+n\Delta_m)t], \qquad (6.34)$$

where I_n and Q_n are the in-phase and quadrature parts of the nth component. These

parts are given for each n as

$$
(I_n, Q_n) \propto \frac{\Omega_{\mathrm{P0}}\Omega_{\mathrm{I0}}}{4} \times
\begin{cases}
(-2J_0, \ 2mJ_1\cos\phi), & n = \ \ 0 \\[2mm]
(\mp 2J_1 - m[J_2 + J_0]\sin\phi, \ \pm m[J_2 - J_0]\cos\phi), & n = \pm 1 \\[2mm]
(-2J_2 \mp mJ_1\sin\phi, \ -mJ_1\cos\phi). & n = \pm 2
\end{cases}
$$

$$(6.35)$$

The amplitude of each frequency component is

$$
A_n(m, \beta, \phi) \propto \sqrt{I_n^2 + Q_n^2} = \frac{\Omega_{\mathrm{P0}}\Omega_{\mathrm{I0}}}{4} a_n(m, \beta, \phi),
\tag{6.36}
$$

where

$$
a_n =
\begin{cases}
2\sqrt{J_0^2 + m^2 J_1^2 \cos^2\phi}, & n = \ \ 0 \\[2mm]
\sqrt{4J_1^2 \pm 4mJ_1(J_2 + J_0)\sin\phi + m^2(J_2^2 + J_0^2) \pm 2m^2 J_0 J_2 \cos 2\phi}, & n = \pm 1 \\[2mm]
\sqrt{4J_2^2 \pm 4mJ_1 J_2 \sin\phi + m^2 J_1^2}, & n = \pm 2
\end{cases}
$$

$$(6.37)$$

and the quadrature phase $\Theta_n(m, \beta, \phi)$ is defined according to $\tan(\Theta_n) = Q_n/I_n$, where

$$
\tan(\Theta_n) =
\begin{cases}
-\dfrac{mJ_1}{J_0}\cos\phi, & n = \ \ 0 \\[3mm]
-\dfrac{m(J_2 - J_0)\cos\phi}{2J_1 \pm m(J_2 \pm J_0)}, & n = \pm 1 \\[3mm]
\dfrac{mJ_1 \cos\phi}{2J_2 \pm mJ_1 \sin\phi}. & n = \pm 2
\end{cases}
\tag{6.38}
$$

The power, or amplitude-squared, of the five frequency components are plotted in Figure 6.5(a), and the quadrature phases are shown in (b), with $m = \beta = 0.2$. The positive and negative sidebands are exactly out of phase with each other. The ± 1 sidebands have a relative visibility of 100%, taken with respect to their maximum value, while the ± 2 sidebands have 80% visibility, as seen in the inset of Figure 6.5(a).
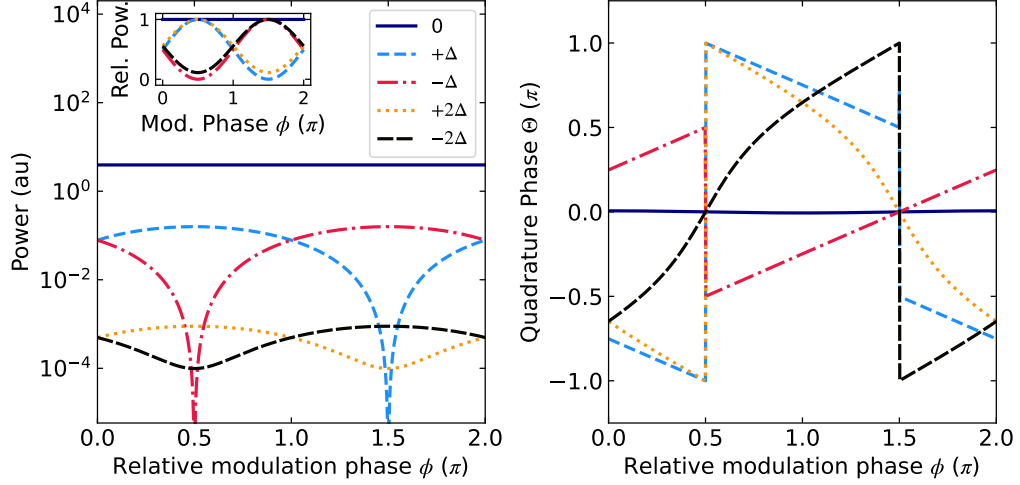
Figure 6.5: Sideband power and phase vs. modulation phase for sum-frequency generation via AM/PM mixing. (a) The power in the $|n| \leq 2$ mixed frequency components, $P_n \propto |A_n(m, \beta, \phi)|^2$, where $m = \beta = 0.2$. The inset shows the relative power, where each frequency component is independently normalized. (b) The phase of each frequency component as a function of $\phi \in [-\pi, \pi)$. The legend in (a) also serves (b).

The visibility is highest when m and β are equal. In the limit of $\beta \ll 1$, the Bessel functions can be approximated as:

$$J_0(\beta) \approx 1 + \mathcal{O}(\beta^2)$$
$$J_1(\beta) \approx \frac{\beta}{2} + \mathcal{O}(\beta^3) \tag{6.39}$$
$$J_2(\beta) \approx 0 + \mathcal{O}(\beta^2).$$

When $m = \beta \ll 1$, the ± 1 frequency component amplitudes simplify to $A_{\pm 1} = m\sqrt{2(1 \pm \sin \phi)}$, and their quadrature phases become $\tan(\Theta_{\pm 1}) = \cos \phi/(1 \pm \sin \phi)$.

In conclusion, this AM/PM mixing scheme shows a method for controlling the amplitude and phase of SFG sidebands via a relative modulation phase ϕ. The powers of the $n = \pm 1$ components vary sinusoidally with ϕ, but out of phase, qualitatively similar to the experimental results of Section 8.5.3. The experimental optical heterodyne technique is not able to detect the quadrature phase $\Theta_{\pm 1}$. However, in principle

this can be measured by mixing the detected signal with an independent microwave signal possessing a well-defined phase.

*...by small and simple things
are great things brought to pass...*

Alma 37:6, The Book of Mormon:
Another Testament of Jesus Christ

Chapter 7

Experimental setup and methods

7.1 Introduction

This chapter will describe the experimental setup, equipment, and measurement techniques employed in the microwave-to-optical conversion experiments presented in Chapter 8. At the heart of this setup is a vapor cell of enriched ^{87}Rb suspended inside a heated, cylindrical copper microwave cavity. However, there are several other peripheral subsystems that all must work together: a laser and optics system, along with various electronics, carefully prepares and detects the resonant light; magnetic coils null the external field and apply a calibrated, directed magnetic field to the vapor; the cavity and cell are temperature-controlled to regulate interdependent properties of the warm vapor cell and the microwave cavity mode. This chapter attempts to

describe each of these subsystems, their components, workings, and connections with sufficient, reproducible detail.

Along the way, we have refined our understanding of cavity characterization using vector network analyzers, and small signal measurements using spectrum analyzers. Background understanding and procedures for the effective use of these instruments are included in this chapter for the hopeful benefit of future group members.

7.2 Cycling Program

This warm atom experimental setup has a peculiarity that it was developed in a laboratory space using equipment originally intended for experiments with laser-cooled neutral atoms. The equipment itself and the manner in which it has been repurposed reflect this fact.

This is especially evident in the control program running on computer workstations. This specialized program is an interface to three hardware devices that respectively produce analog, radio-frequency (RF), and digital logic signals. The analog signals are generated by a 32-channel National Instruments PCIe-6738 card with SCB-68A shielded connector block; the RF signals are generated by a 4-channel Novatech 409B digital synthesizer; the digital logic signals are generated by a 24-channel Pulseblaster PB24-100-4k-USB-RM. The control program is an ordered sequence of user-defined time intervals, wherein each output channel of the three devices can be configured independently. For example, a certain analog output channel might correspond physically to a current flowing through a magnetic coil; throughout different time intervals, the current might be set to zero, positive values, negative values, or a time-series function of values.

After all the time intervals are completed, the sequence repeats in a cycle. This

type of program is particularly useful for cold atom experiments consisting of multiple cooling, trapping, and imaging stages. This sequence structure also allows for scanning individual channel parameters for optimizing a measured quantity.

7.2.1 Connections

In the microwave-to-optical conversion experiment, we use only analog (National Instruments) and RF signals (Novatech), as shown in Figure 7.1. Three analog voltages control the current output of three bipolar Kepco BOP 20-20DL power supplies; these currents flow through the three orthogonal Helmholtz coils. An RF signal at a frequency of 76.6 MHz and user-defined power is passed to the home-built AOM driver where it is amplified and then passed to the AOM. The RF power sent to this AOM determines how much laser light is diffracted into the first order and coupled into an optical fiber en route to the experiment. After the fiber, a beamsplitter directs a small fraction of the light into a photodiode. Polarization fluctuations in the fiber produce unwanted power fluctuations measured in the photodiode voltage. We correct for these fluctuations using a Newport New Focus proportional-integral servo controller. The controller compares the photodiode voltage with a fourth analog signal, giving an error output signal that passes back to the AM input of the AOM driver. As will be discussed further in Section 7.3.2, a variable voltage attenuator inside the driver regulates the input RF signal to stabilize these fluctuations and significantly reduce noise.

In this manner, the cycle control program controls the magnetic field amplitudes in three directions and the stabilized power of the laser beam. In future sections, we will describe and characterize these subsystems in more detail. Given that we operate all experimental parameters and measurements continuously at steady-state, only a single time interval with constant parameters is required in the control sequence.
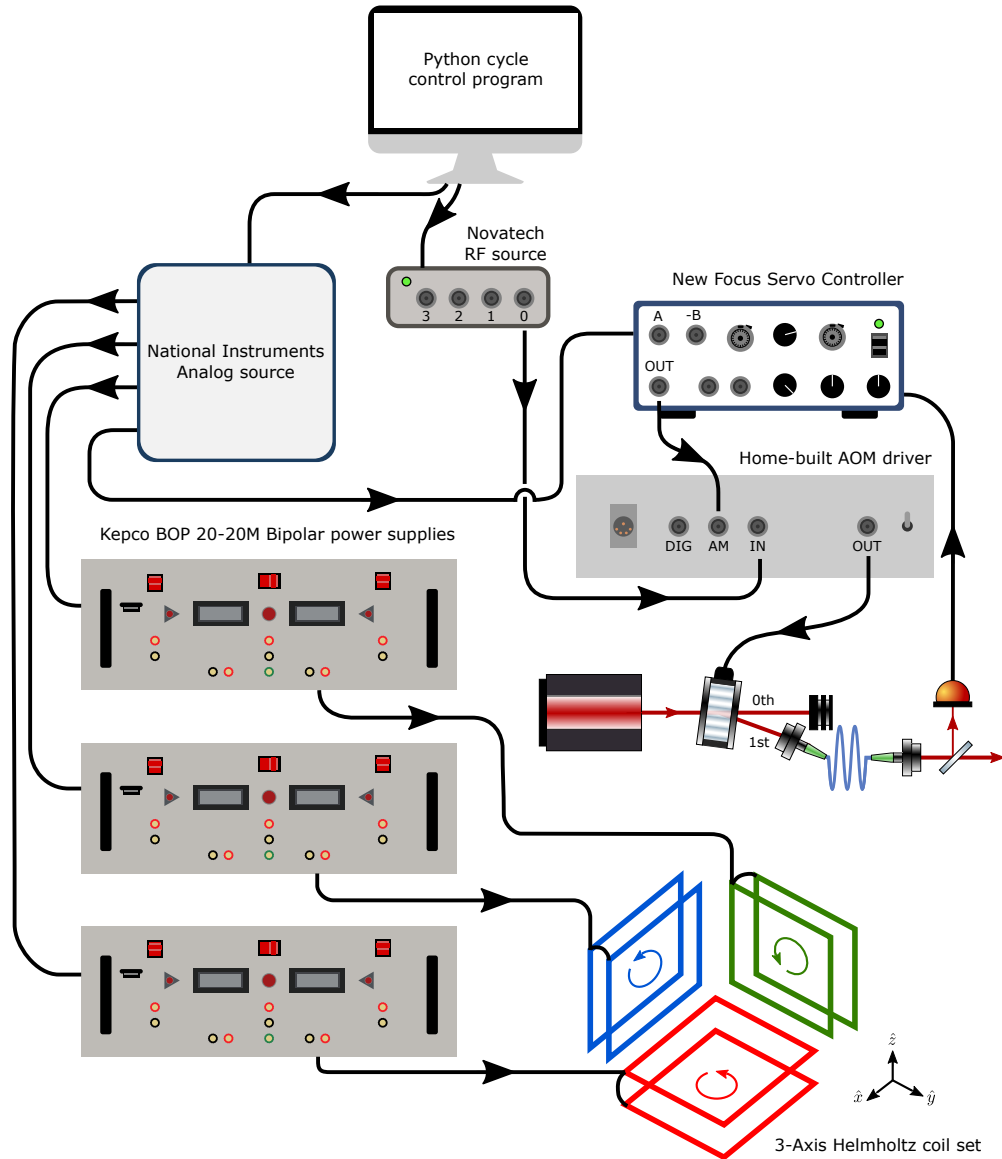
Figure 7.1: A Python cycling program running on a PC controls the main experimental parameters. It programs the National Instrument board to produce analog voltages for regulating the output current of three Helmholtz coil power supplies, one for each axis; it also provides the optical power setpoint for the New Focus servo controller. Additionally, the cycle program configures the Novatech device to produce a 76.6 MHz RF signal. This signal is modulated and amplified in the homebuilt AOM driver [see Section 7.3.2] and then sent to the main experimental AOM.

However, timed sequence control may be beneficial for anticipated experiments in the future.

7.3   Laser and Optics

In this section, we describe the steps and equipment used to prepare the polarization, frequency, and amplitude of the laser beam used to address the atomic transition of interest. We also describe the scheme used to detect and measure the converted light.

7.3.1   Diode laser

The laser light originates from a commercial MOGLabs tunable cateye diode laser (CEL). This is a novel type of tunable, external cavity diode laser (ECDL). Lasers in Littrow or Littman-Metcalf configurations use a diffraction grating to form the external laser cavity and to select a particular lasing wavelength. The CEL, by comparison, uses a fixed cavity formed by the diode surface and a reflective output coupler mirror. Interposed between the cavity mirrors is an interference filter whose angle is piezo-tunable. This filter provides both tunability and wavelength selectivity. We can scan the laser frequency over a range of 20 GHz with a variable repetition rate.

For a typical operating current of 240 mA and temperature of 23.75 °C, we get an output power (after the isolator) of 101 mW. Beams emerging from diode lasers are generally well-polarized, but not well-collimated. Usually, the beam profile has a "fast" axis of rapid divergence and an orthogonal "slow" axis of more moderate divergence. The divergence of this laser is uncorrected by the optics; this fact is noticeable throughout the optics system but is not a crucial issue.

This laser has a relatively small footprint, with a Faraday isolator mounted to

the optics table outside of the laser chassis. This laser was originally intended to be a "repump" beam for a laser-cooled rubidium magneto-optical trap and has a wavelength of about 780.246 nm.

7.3.2   Preparation Optics Table

In this section, we describe the laser beam paths that are relevant to the experiments discussed in this thesis. The preparation optics, as shown in Figure 7.2, are mounted to an optics table. The table is covered by a dark acrylic plastic enclosure to maintain the laser's temperature stability and reduce air currents near the optics.

The light from the laser is expanded 4:1 by a telescope and then is split into two paths via a half-waveplate and a polarizing beamsplitter. The transmitted path is compressed by another 4:1 telescope and is then diffracted by an AOM with a drive frequency of $f_{AOM} = 76.6$ MHz; the zeroth diffracted order is blocked, but the upshifted, 1st-order beam is attenuated by a neutral density filter and coupled into an optical fiber. This is the primary "pump" beam for the experiment and has about 1.5 mW of optical power, as measured on the fiber output. This power is controlled via the AOM drive power. Other beams are separated and directed to the "Local Oscillator" fiber coupler (for heterodyne detection), and to additional optics for saturated absorption spectroscopy laser locking.

Saturated absorption spectroscopy frequency locking

The basics of saturation absorption spectroscopy and locking are described else-where [40, 112]; however, since an understanding of its spectrum is essential for the experiments, we will briefly review this topic.

At the center of this locking scheme is a rubidium reference vapor cell (Thorlabs GC25075-RB) covered by a heater/temperature-control assembly (Thorlabs GCH25-
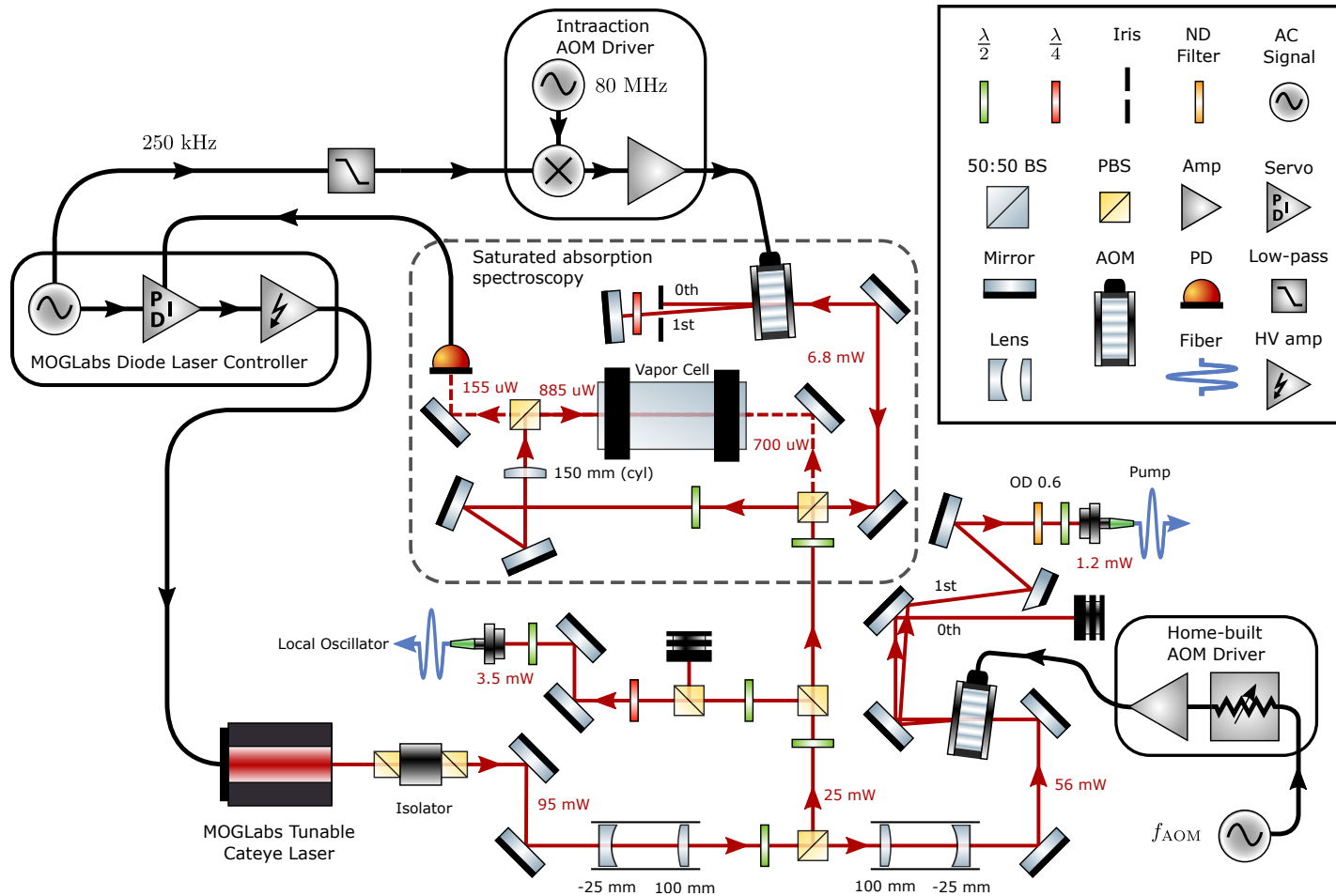
Figure 7.2: The beam emitted from the diode laser is split into three paths: The first beam is fiber-coupled and is the local oscillator reference used in the experiment; the second beam is split again and directed through a reference vapor cell for saturated absorption spectroscopy laser locking [see Section 7.3.2]; the third beam is frequency-shifted by an AOM before it is fiber-coupled and sent to the experiment table [see Section 7.3.3]. Typical optical powers at various points throughout the laser system are notated. AOM - acousto-optic modulator; ND - neutral density filter; PBS - polarization beam splitter; Amp - RF amplifier.

75) and an aluminum foil oven wrap (not shown in Figure 7.2). Despite the presence of the heater assembly, we have never heated the reference cell during the experiments, leaving the cell at room temperature. A weak "probe" beam passes through the reference cell and impinges on a photodiode. As the laser's frequency is scanned through the Doppler-broadened atomic resonance, the probe is absorbed in proportion to the Maxwell-Boltzman-distributed density of states [see Section 4.2].

A "pump" spectroscopy beam propagates against the probe, overlapping the other beam inside the cell. The frequency of this beam is also scanning. Since it comes from the opposite direction as the probe, it interrogates atoms of the *opposite* velocity class and negative Doppler shift. Because of this fact, only the zero velocity class (ZVC) having zero Doppler shift permits both the pump and probe to be simultaneously resonant. When this occurs, the pump burns a "spectral hole" and the probe experiences less absorption. In the transmission spectra, the increased transmission appears as a small, narrow bump superimposed on a broad Doppler transmission dip. This sub-Doppler feature precisely marks the atomic resonance of the ZVC; these features are visible in the spectrum in Figure 7.3(a). On top of each peak, the slope of the spectrum is approximately zero: the "derivative" of the spectrum therefore has a dispersive zero-crossing that can be used for negative feedback control of the laser frequency. Retrieving this error signal is the goal of saturation absorption spectroscopy.

What we have described is the case for a probe and pump beam with the exact same frequency. In actuality, the pump beam encounters a double-pass AOM before traversing the cell. This AOM has two functions:

1. It shifts the pump beam up in frequency by 160 MHz (80 MHz per pass[1]).

---

[1]This frequency is an arbitrary choice, however, the AOM devices used in our lab work optimally at 80 MHz.
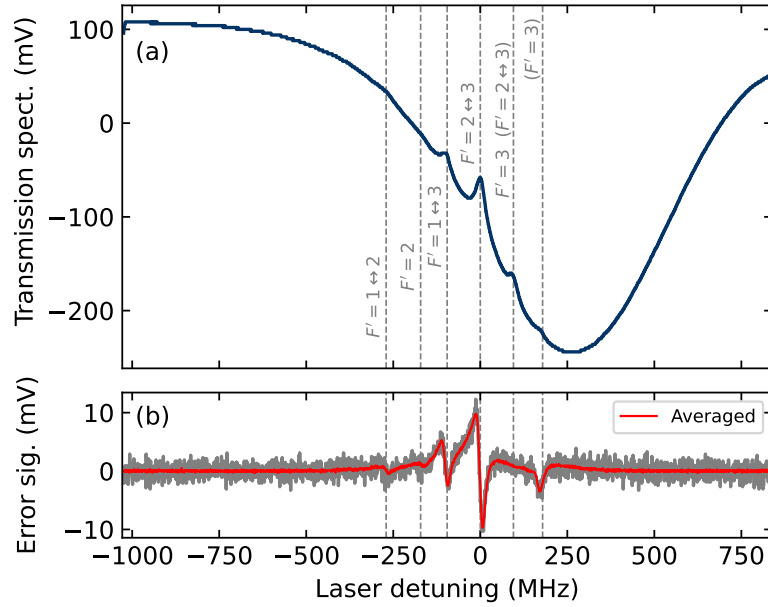
Figure 7.3: Saturated absorption spectroscopy and error signal for laser frequency stabilization. (a) The saturated absorption spectrum for the ^{87}Rb D2, $f = 2 \rightarrow f'$ transitions. The saturated absorption peaks are superimposed on the broad Doppler transmission dip. Each peak is labeled with the excited state f' value. The labels in parentheses are the transitioned level due to the self-pumping of the probe beam reflected from the far edge of the vapor cell. (b) The error signal produced by the laser controller. The grey trace is a single shot, and the red curve is averaged 64x. The laser can be locked at points where the dispersive error signal crosses zero. In this thesis, we typically lock the laser on the $f = 2 \rightarrow f' = 2 \leftrightarrow 3$ crossover transition.

The double pump-probe resonance now occurs on atoms with a velocity of $2\pi \times -80$ MHz$/(2\pi/780.24$ nm$) = -62.4$ m/s relative to the probe propagation, or, alternatively with a Doppler shift of 80 MHz *below* the ZVC atomic resonance [112]. In a laser-cooling scheme, it is convenient to lock the laser below the ZVC resonance; additional AOMs used to *switch on* the derived cooling/repump beams also shift their beam's frequencies *back* up to the ZVC resonance.

2. The double-pass AOM is also a key tool for generating the derivative error signal

needed for laser locking. The laser controller uses a lock-in detection technique: A 250 kHz "dither" from the laser controller frequency-modulates the 80 MHz AOM drive signal, making the pump frequency jitter back and forth as it sweeps through the saturated absorption peaks. This jittering is imprinted onto the spectrum signal, and is demodulated by the controller at the dither frequency. The result: the frequency jitter modifies the spectrum at every frequency point in proportion to its slope. This is the error signal. An example of this signal is shown in Figure 7.3(b).

Using the error signal, the PI-feedback loop in the laser controller adjusts the diode current and interference filter's piezo voltage to maintain the error signal at zero[2]. When this occurs, the laser is successfully locked. The lock can be adjusted by potentiometer knobs that adjust the gain parameters of the feedback loop, thereby scaling the amplitude of the error signal. This gain must be tuned so that the error signal is large enough to provide a clean zero crossing, but not too large so that the feedback loop oscillates. In practice, the gain is increased until the onset of oscillations, and then reduced slightly until they disappear.

In many atoms, there are multiple nearby hyperfine levels in the excited state. For example, in ^{87}Rb on the D2 line, there are four such levels, $|f' = 0, 1, 2, 3\rangle$. Optical electric dipole transitions from one of the ground states (say, from $|f = 2\rangle$) may excite up to three of these (to $|f' = 1, 2, 3\rangle$). In general, there is one saturated absorption peak for each of the excited levels. There are also so-called "crossover resonances" that appear exactly between each pair of individual resonances. In the example above, there are $|f' = 1 \leftrightarrow 2\rangle$, $|f' = 1 \leftrightarrow 3\rangle$, and $|f' = 2 \leftrightarrow 3\rangle$ crossover resonances. For certain velocity classes, the pump burns a "spectral hole" with one excited level, while

---

[2]This can only occur when the laser sweep range is reduced to zero.

the probe is absorbed by a separate level [40]. Between the individual and crossover resonances, we should expect a total of six saturated absorption resonances. Some of these resonances are seen in Figure 7.3(a). The largest peak is the $|f' = 2 \leftrightarrow 3\rangle$ crossover, and this resonance produces the strongest dispersive zero crossing in the error signal. In the experiments, we typically lock onto this peak; recall that because of the double-pass AOM, this lock is 80 MHz below the ZVC resonance [112]. In Figure 7.3, the transitions marked in parentheses correspond to saturated absorption peaks of the ZVC. These are caused by the probe back-reflecting off the far inner surface of the vapor cell and "self-pumping" the atoms. This set of saturated absorption peaks is shifted upwards relative to those produced by the shifted pump beam. When this cell was originally mounted to the table, it was oriented with surfaces perpendicular to the pump and probe beams. This type of self-pumping artifact is easily removed by giving a slight horizontal tilt to the vapor cell.

Home-built AOM driver

We primarily used Intraaction AOM deflectors (ATM-801A2). We have learned by experience that their accompanying drivers (IntraAction DE-801-6) have quite unacceptable frequency noise, both from the voltage-controlled oscillator and from the internal amplifier. This noise is imprinted onto the pump laser beam and appears in detection. In addition, we have noticed that the amplifiers on these commercial drivers often fail prematurely. To resolve this issue, we constructed home-built AOM drivers that amplify a low-noise RF signals sourced from a programmable Novatech synthesizer device. Two of these drivers were used in another ultracold atom experiment. Images and a schematic of one of the ultracold units are shown in Figure 7.4. We assembled a third driver for this warm atoms experiment; except for lacking a fast RF switch, it is identical to the former two.
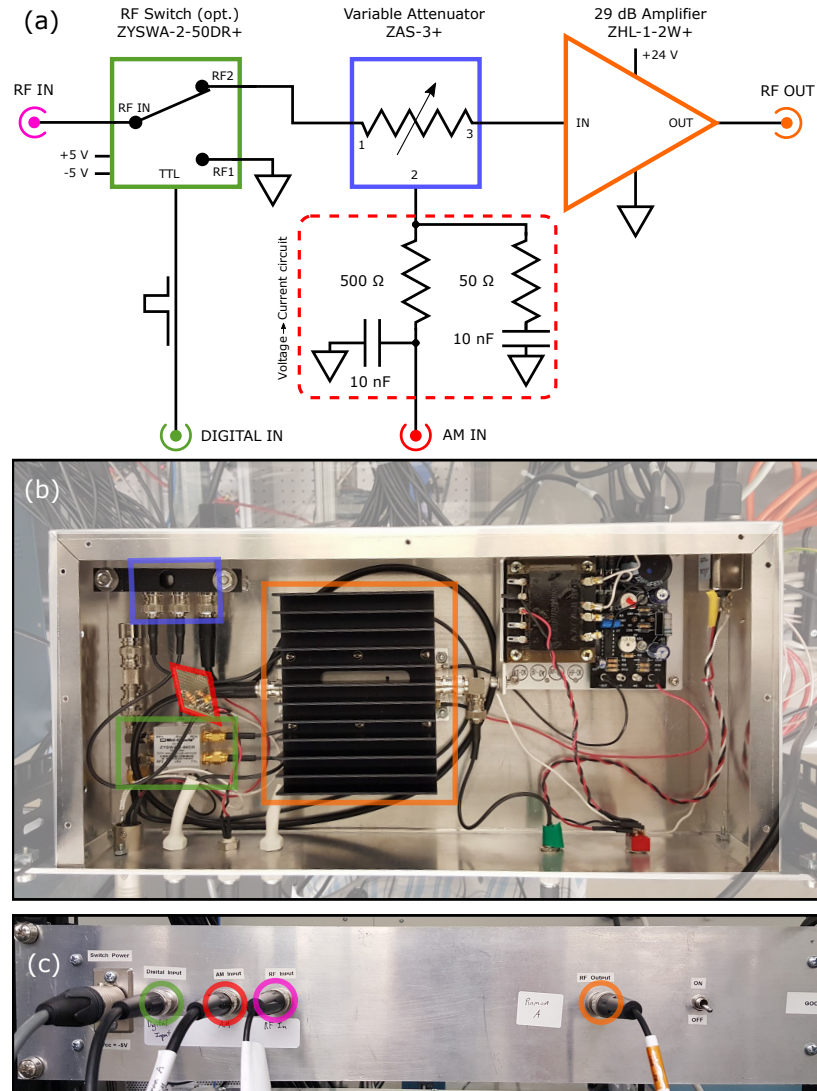
Figure 7.4: Schematic and images of the homebuilt AOM driver. (a) There are three main components of this device: a fast RF switch (green), a variable attenuator (blue), and a high-power RF amplifier (orange). This box has three input ports [an RF signal input (purple); a digital signal input (green); and an amplitude modulation input (red)] and one output RF port (orange). Because the attenuator is current-controlled, the circuit in the dotted red box converts the AM signal from a voltage to a proportional current. The amplifier output is delivered to the AOM. (b) A top image of the inside of the AOM box. The lumped elements shown in the schematic are outlined in color. The box also contains a 24 V power supply, shown in its upper right corner. (c) The front panel of the AOM box with the BNC input ports circled in color. The colors in (b) and (c) refer to the same elements as those in (a).

93

These devices are composed of a fast RF switch (Mini-Circuits ZYSWA-2-50DR+), a variable attenuator (Mini-Circuits ZAS-3+), and a high power amplifier (Mini-Circuits ZHL-1-2W+). The switch has a delayed response of about 800 ns and a rise time of 40 ns. The attenuator is current-controlled, so an intermediate circuit of resistors and capacitors converts the AM voltage to a current. The response of the attenuator to various positive voltages is nonlinear, saturating after about 8V; if desired, the response can be calibrated and linearized[3]. As described in Section 7.2, the attenuator is essential for stabilizing the power of the pump beam. The amplifier gives about 29 dB of gain. It has a dedicated 24 V power supply that draws up to 1 A of current. The amplitude of the input RF signal is set from the cycle control program and has typical values around -11 dBm.

7.3.3   Experiment Table

The fiber-coupled pump light passes in an overhead rack from the preparation optics table to an experiment table. This table is a 24" x 20" aluminum optics breadboard mounted on 43 cm-long posts at the center of three, square magnetic Helmholtz coils (see Section 7.4). The optics and equipment mounted to this table are depicted in Figure 7.5(a). The microwave cavity and vapor cell are located at the center of all three magnetic coils where the field is most uniform.

As the pump light exits the fiber, its polarization is immediately filtered by a PBS. As described in Section 7.2, the polarization of the pump light in the fiber fluctuates randomly due to fiber motion, thermal gradients, or air currents. The PBS eliminates polarization fluctuations but introduces unwanted power fluctuations. To solve this problem, a clear microscope slide reflects a small fraction of the beam power to a

---

[3]Because of the additional power feedback on the AOM, confusion was avoided by leaving the attenuator response uncalibrated.
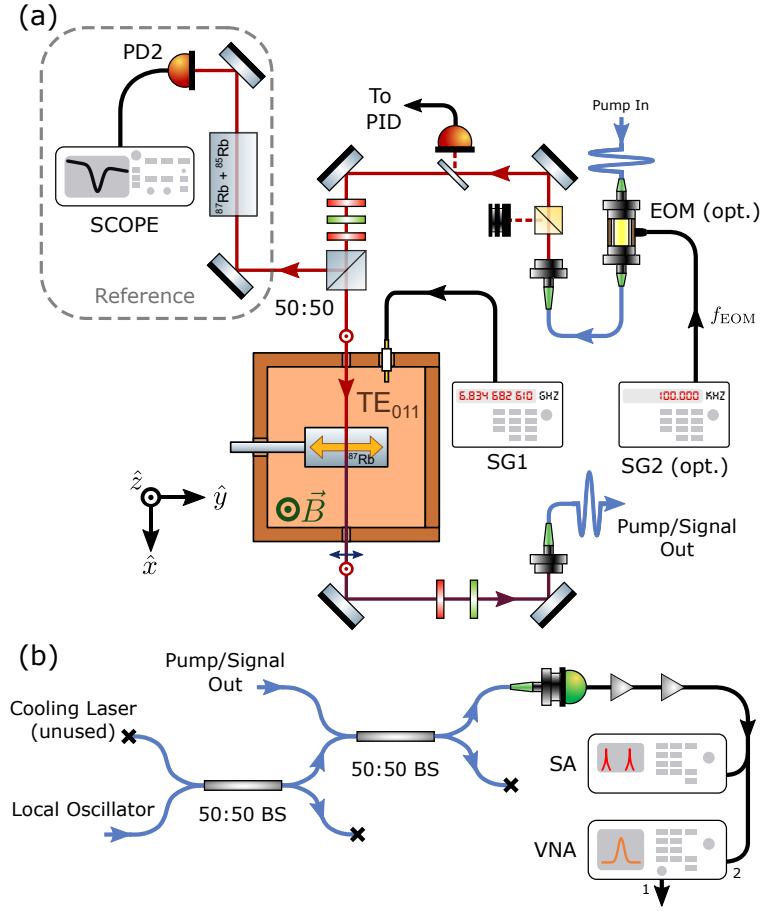
Figure 7.5: Diagram of the beam paths on the experiment table and the detection system. (a) Central to the experiment is the microwave cavity supporting a TE_{011} mode, supplied by a signal generator (SG1), and polarized along the y-axis. The pump light first passes through an optional electro-optic modulator (EOM), where the phase-modulating signal is provided by a second signal generator (SG2). The light is decoupled from the fiber, its polarization is purified by a PBS, and then a small fraction of power is sampled by a piece of glass and a photodiode. The polarization state is prepared along the z-axis by three waveplates before passing through the cavity along the x-axis. The vapor cell inside the cavity contains enriched ^{87}Rb. A 50:50 BS placed directly before the cavity sends half of the light through a separate vapor cell with natural rubidium abundance. (b) Unshifted light from the diode laser (ECDL) is used as a local oscillator for heterodyne detection; it is combined with the other beam in a fiber 50:50 beam splitter (BS), producing two beat signals which are detected by the fast photodiode at $f_{\text{het,P}}$ and $f_{\text{het,S}}$ and measured by the spectrum analyzer (SA). In certain measurements [see Section 8.2.5], port 1 of the vector network analyzer (VNA) drives the microwave cavity and port 2 detects. See Figure 7.2 for a legend of the optical components.

gain-switchable photodiode (Thorlabs PDA36A). The measured photosignal is used for power stabilization feedback of the pump (see Section 7.2). When the feedback loop is locked, the pump light has a constant, actively-stabilized polarization and power. The pump optical power, measured immediately before the cavity, has a typical value of 75 μW.

The mirrors before the cavity impart a slight phase shift to the pump light, making the light slightly elliptically polarized. Two zero-order quarter waveplates (OptiSource QWPO-780-10-4-AR/AR), and a multi-order half-waveplate (Thorlabs WPMH055M-780) correct the ellipticity and prepare the light vertically polarized as it enters the cavity. After exiting the cavity, the generated light is copropagating with the pump but has orthogonal polarization. Before these beams are coupled into an optical fiber, a half- and quarter-waveplate maximizes the coupling efficiency, as described in Section 8.2.2.

We have verified that the pump beam is collimated over a distance of 3 meters. We have also measured the pump beam profile with a scanning slit beam profiler (Thorlabs BP209-VIS) to be approximately Gaussian with $1/e^2$ radii of $(r_x, r_y) = (870, 872)$ μm, or an average $1/e^2$ radius of $r_0 = 0.87$ mm.

The interaction volume is defined as the region inside the vapor cell illuminated by the pump laser beam. We assume that the microwave cavity mode is uniform over this volume. Due to the cavity aperture radius $r_{\mathrm{h}} = 1.5$ mm, about 95% of the incident light passes through. The effective uniform beam has an area of:

$$
\begin{aligned}
A_{eff} = \int_0^{r_{\mathrm{h}}} r e^{-(r/r_0)^2} dr &= \pi r_0^2 \left(1 - e^{-(r_{\mathrm{h}}/r_0)^2} \right) \\
&\simeq 0.95 \times \pi r_0^2 \\
&= 2.21(4) \text{ mm}^2
\end{aligned}
\tag{7.1}
$$

A calculated 2D and 1D cross-sections of the hole-clipped beam, and the effective
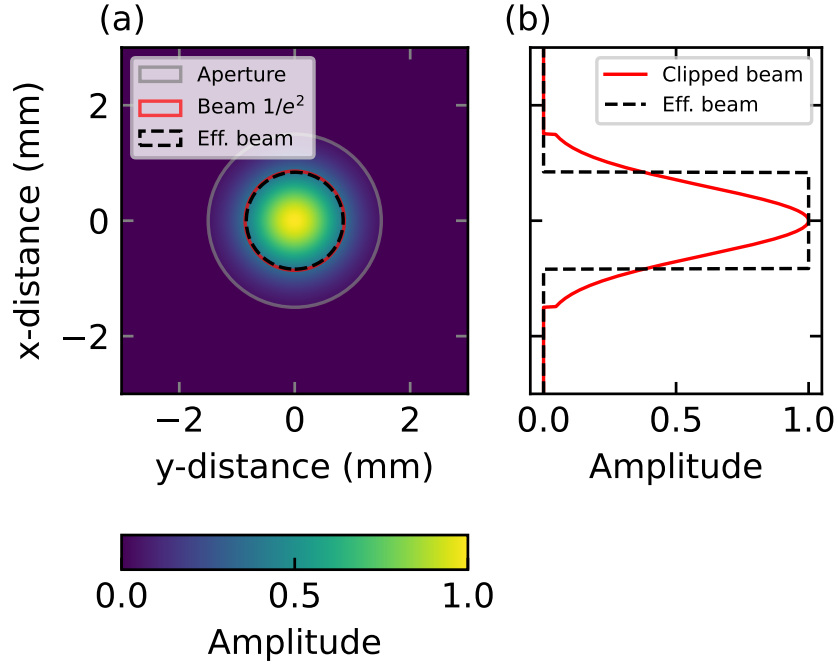
Figure 7.6: Pump beam profile and effective beam radius. (a) The calculated 2D cross-section intensity profile of the pump laser beam, which is based on measured beam parameters. The red circle shows the extent of the beam $1/e^2$ radius of 0.86 mm; the $r_\mathrm{h} = 1.5$ mm cavity aperture is shown as a grey circle. The dashed black circle shows the effective radius (0.84 mm) of a flat-top beam with the same integrated power as the aperture-clipped beam. (b) A linear 1D slice of the beam profile in (a).

flat-top beam area are shown in Figure 7.6. Given that the cell has an internal width of 10.4 mm, the volume overlapping with the atoms is $V_\mathrm{int} = 23.0(6)$ mm^3.

We mention briefly that a 50:50 beamsplitter before the cavity samples a portion of the beam and directs it through a separate rubidium reference vapor cell. As discussed in Section 8.2.8, this vapor cell is used to calibrate the frequency of the laser during a frequency sweep.

7.3.4 Polarization characterization

In this section, we describe how to prepare specific and accurate polarizations of the pump beam prior to its entrance into the vapor cell. Even though the polarization of the pump beam has been feedback-stabilized against fluctuations in the fiber (see Section 7.2), we still require a sequence of three waveplates—$\lambda/4$ followed by a $\lambda/2$, followed by another $\lambda/4$—to prepare an arbitrary desired polarization state [113, 114][4]. The Poincaré sphere provides an intuitive visualization of why three waveplates are necessary:

1. The first quarter waveplate takes an arbitrary state on the sphere and rotates it to the equatorial plane;

2. The half waveplate rotates the state around the equator;

3. The final quarter waveplate rotates the state to a desired point on the upper or lower hemisphere.

We would like to find the relationship between specific waveplate angles and optical polarization states. To do this, we first remove all the waveplates and then place a PBS immediately before the microwave cavity, measuring the transmitted power with a Thorlabs S121C power meter head. We mount the half-waveplate followed by one of the quarter waveplates in front of the Thorlabs PBS122, and iteratively rotate the waveplates' angles until the transmitted power is maximally extinguished. We typically obtain a 1000:1 extinction ratio in the transmitted mode[5]. With transmission minimized, we know that the light is linear and vertically polarized to a high degree. We then mount the final quarter waveplate and likewise rotate it to minimize the

---

[4]This same sequence is used in paddle fiber polarization controllers. It also applies to arbitrary rotations of spherical vectors in 3D space, as detailed in Appendix A.

[5]The PBS optics we use usually have better extinction in transmission versus reflection.

transmitted power. The angle of this last quarter waveplate is locked and will remain unchanged going forward; as described in step (1) above, this waveplate provides the initial preparation from elliptical to linear. Next, the other quarter waveplate is rotated in equal angle increments, and the transmitted power is recorded and normalized to the input power. As shown in Figure 7.7(a), the power varies sinusoidally as a function of angle. This scan is repeated for the half waveplate, and which data are displayed in (b).

(a) (b)
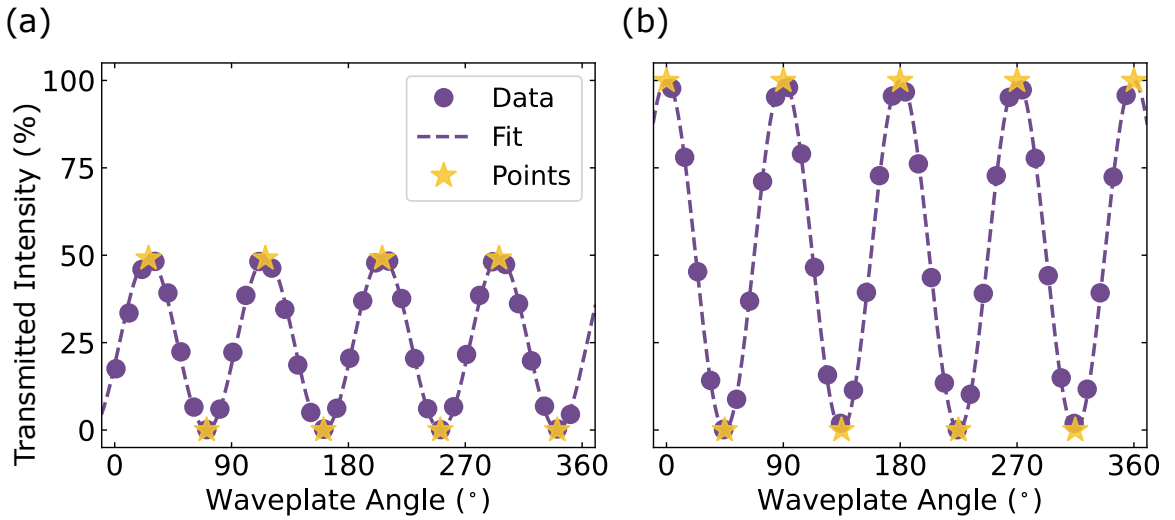
Figure 7.7: Waveplate calibrations for the pump beam. The transmitted intensity of the pump laser through a polarizing beam splitter upon rotations of the (a) quarter- and (b) half-waveplates. In (a), the half-waveplate angle was fixed at $45°$ in its rotation mount; in (b) the quarter-waveplate angle was fixed at $161°$ in its rotation mount. A Jones matrix model was fit to the data and certain special polarization states were identified. these special states are marked with yellow stars, and are summarized further in Table 7.1.

We fit a Jones matrix model to each of these data: An input vertical polarization vector

$$|V\rangle = \begin{pmatrix} 0 \\ 1 \end{pmatrix} \tag{7.2}$$

is transformed by a general linear phase retarder matrix $W(\theta, \theta_0, \eta)$ and analyzed by

a horizontal polarizer matrix P_H, where θ is the rotation angle, θ_0 is an offset angle, and η is a the retardation phase. [See Appendix B for tables of these matrices.] The output polarization amplitude is then

$$|S\rangle = \check{P}_H \, \check{W}(\theta, \theta_0, \eta) \, |V\rangle \tag{7.3}$$

When comparing the model to the data, it's important that the angles θ advance relative to the same axis direction. In the Jones calculus convention described in Appendix A.1.2, the waveplate rotation angles are taken from the perspective of the receiver, meaning positive angles advance CW around the optical axis when viewed against the propagation axis to the source. Inconveniently, we oriented the waveplate rotation mounts so that the angles advanced CCW when seen from the same perspective. Therefore the measured angles had to be flipped as $\theta \to \theta' = -\theta + 2\pi$.

State	$\lambda/4$ (°)		State	$\lambda/2$ (°)
$|L\rangle$	26		$|H\rangle$	0
$|V\rangle$	71 (26 + 45)		$|V\rangle$	45
$|R\rangle$	116 (26 + 90)		$|H\rangle$	90
$|V\rangle$	161 (26 + 135)		$|V\rangle$	135

Table 7.1: Special polarization states of the pump beam. The left table shows the states identified from rotations of the quarter-waveplate [Figure 7.7(a)], where the half-waveplate angle is fixed at 45° in its rotation mount. The right table does the same for rotations of the half-waveplate [Figure 7.7(b)], where the quarter-waveplate is fixed at 161° in its rotation mount. The tables only display the first four special polarization states. The subsequent four states for each waveplate repeat in the same pattern, at 45° increments. $|V\rangle$ - vertical; $|H\rangle$ - horizontal; $|R\rangle$ - right circular; $|L\rangle$ - left circular.

We then fit the transmitted intensity $I(\theta, \theta_0, \eta) = \langle S|S\rangle$ to the data, and the results are visible in Figure 7.7. The quarter waveplate fit a retardation phase of $\eta = 1.553(7)$ rad, slightly lower than $\pi/2 = 1.571$ rad. The half waveplate fit a

retardation phase of $\eta = 3.20(9)$ rad. This fit shows that the waveplates have the expected retardation phase, despite slight manufacturing errors in the optics. The fits allow us to identify which specific angles produce special linearly ($|V\rangle$ and $|H\rangle$) or circularly ($|R\rangle$ and $|L\rangle$) polarized states. These angles are marked with yellow stars and are summarized in Table 7.1.

7.3.5   Fiber Electro-optic phase modulator

As seen in Figure 7.5(a), we have the option to insert a fiber electro-optic modulator (EOM) into the light's path before going to the experiment table. The device is a lithium niobate (LiNbO$_3$) phase modulator (EOSpace PM-0S5-20-PFA-PFA-780). This particular material is host to a type of electro-optic process called the Pockels effect, whereby the material's index of refraction changes linearly[6] in response to an applied electric field amplitude [88]. This effect is described by a second-order susceptibility in non-centrosymmetric materials.

The optical phase change experienced by a change in the refractive index is

$$\Delta\phi = \Delta n \frac{\omega L}{c}, \tag{7.4}$$

where, L is the length of the crystal, ω is the angular frequency of the optical wave, and c is the speed of light. In the Pockels regime,

$$\Delta n = \kappa E, \tag{7.5}$$

where E is the applied electric field, and κ is a material-dependent parameter. When E is applied longitudinally to the beam propagation, $E = V/L$ and equation 7.4 becomes

$$\Delta\phi = \kappa \frac{\omega V}{c}. \tag{7.6}$$

---

[6]In contrast, the Kerr effect refers to nonlinear changes of the index of refraction with the electric field amplitude, which are described by higher-order susceptibilities in centrosymmetric materials [88].

We can then define the half-wave voltage, or the voltage required to change the optical phase by π radians:

$$V_\pi = \frac{\pi c}{\kappa \omega} = \frac{\lambda}{2\kappa}. \tag{7.7}$$

Crucially, this half-wave voltage depends on the optical wavelength. The phase change then becomes

$$\Delta\phi = \frac{\pi V}{V_\pi} \tag{7.8}$$

We might modulate the applied voltage as $V(t) = V_0 \sin(\omega_m t)$, where ω_m is the angular modulation frequency and V_0 is the amplitude. Due to the Pockels effect, this modulates the phase of the optical electric field as

$$E(t) = E_0 \sin[\omega t + \beta \sin(\omega_m t)], \tag{7.9}$$

where ω is the optical angular frequency, and $\beta \equiv \pi V_0/V_\pi$ is called the "modulation index" [115]. We note that in practice, V_π also depends on ω_m [116]. EOSpace specified $V_\pi = 2.7$ V at $\omega_m/2\pi = 1$ GHz for this device.

Equation 7.9 can be expanded in complex exponentials and expanded further using the Jacobi-Anger identity,

$$e^{i\beta \sin(\omega_m t)} = \sum_{n=-\infty}^{\infty} J_n(\beta)e^{in\omega_m t}, \tag{7.10}$$

to get

$$E(t) = \frac{E_0}{2i} \sum_{n=-\infty}^{\infty} J_n(\beta) \left[e^{i(\omega_{car}+n\omega_m)t} - (-1)^n e^{-i(\omega_{car}-n\omega_m)t} \right], \tag{7.11}$$

where $J_n(\beta)$ are Bessel functions of the first kind[7]. Each of the terms in the sum represents different frequency components separated by integer multiples of ω_m. In

[7]Had we expressed Equation 7.9 (6.27) with a cosine in the argument, we would simply replace $\omega_m t \to \omega_m t + \pi/2$ to obtain

$$E(t) = \frac{E_0}{2i} \sum_{n=-\infty}^{\infty} i^n J_n(\beta) \left[e^{i(\omega_{car}+n\omega_m)t} - (-1)^n e^{-i(\omega_{car}-n\omega_m)t} \right].$$

See also footnote 4 on page 76.

the spectral domain, these components appear as sidebands on the carrier separated by a spacing of ω_m, as illustrated in Section 6.3.1. The fractional power in the nth sideband is proportional to $|J_n(\beta)|^2$, as shown in Figure 7.8 for the central and first three sideband orders.
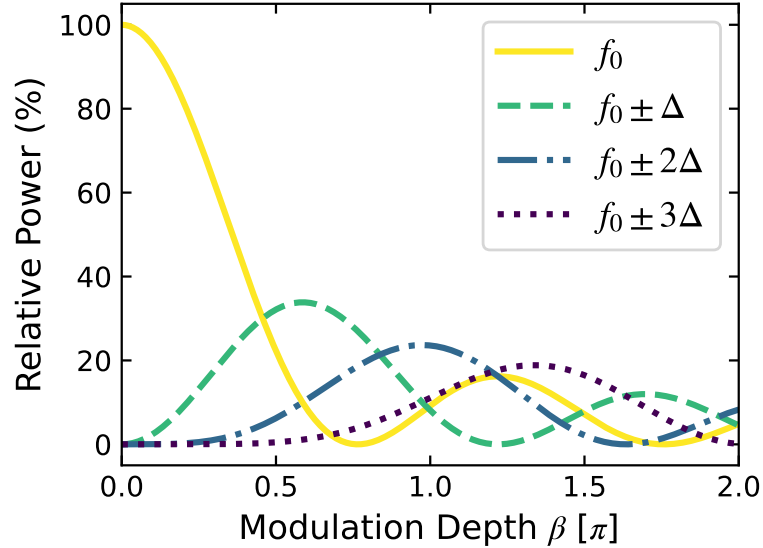
Figure 7.8: Amplitudes of the phase-modulated (PM) frequency components [i.e. carrier (solid) and the first (dashed), second (dashed-dotted), and third (dotted) harmonics] as a function of modulation depth β. The nth component powers are proportional to $|J_n(\beta)|^2$, where J_n is the Bessel function of the first kind. These Bessel functions emerge from the constraint that the combined power of the carrier and sidebands equal 100% for every β.

EOM sideband frequency response

We characterize the amplitudes of the first upper and lower sideband relative to the carrier as a function of $\omega_m/2\pi$, as shown in Figure 7.9, for a drive power of 0 dBm. Using the half-wave voltage quoted above, the modulation index is $\beta = 0.12$. The data is not consistent with an expected power difference of $10 \times \log[\,|J_1(\beta)|^2 \,/\, |J_0(\beta)|^2\,] \simeq$

−24.6 dB; this might mean that the half-wave voltage is perhaps up to four times smaller than specified.
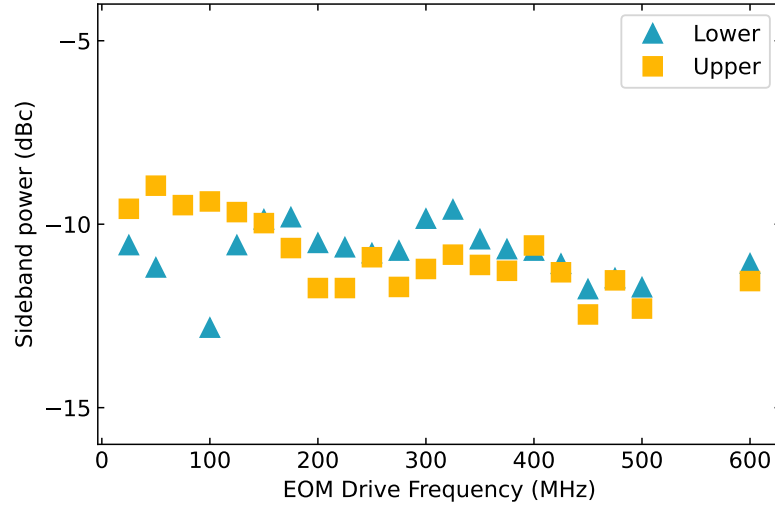
Figure 7.9: EOM first-order sideband power as a function of modulation frequency for a fixed modulation depth. The powers are displayed in dBc, relative to the carrier. We observe that the device's response is fairly flat over 300 MHz. The variations might be due to drifting optical polarization in the detection fibers.

Safety

Lithium niobate modulators can easily experience photorefractive damage at higher optical powers. This is a phenomenon whereby the light generates mobile charge carriers in the material that locally change the refractive index [117]. Damage may be partially remedied by heating the crystal, however, the wavefront distortions of the beam usually remain a significant issue [118]. Given that power specifications are absent for this EOM, to be on the safe side, we keep the input optical power below 500 μW. This has considerably limited the modulated pump powers we can access.

7.3.6   Detection

Next, we describe the optics, equipment, and methods used for measuring optical signals. This relies on beamsplitters, a photodetector, and RF amplifiers intended for beat-note frequency stabilization of a separate laser [112]. For these experiments, we combine the light to be measured (i.e. from the cavity) with another beam (called "local oscillator") derived from the same laser. As depicted in Figure 7.5(b), this combination occurs within the second of two 50:50 fiber beamsplitters (Thorlabs TN785R5A2). The first beamsplitter was installed for the beat-note locking, and does not affect the experiment, except to reduce the local oscillator power by 1/2. The combined light then impinges on a fiber-coupled, high-bandwidth photodetector (EOT ET-4000AF), and the interference of the two beams produces an AC wave oscillating at f_{het}, the difference of the two input frequencies. Detecting the frequency and amplitude of this oscillating beat tone is the essence of optical heterodyne detection [119].

After the signal is amplified by up to two Mini-Circuits (ZJL-7G+) RF amplifiers, it is transmitted by a 50-inch Mini-Circuits (141-50SM+) coaxial cable to a spectrum analyzer or a vector network analyzer. To get good interference and a strong signal, the polarizations of the two input beams must be closely matched. This is another reason for the half- and quarter-waveplate sets before the "Pump/Signal Out" and "Local Oscillator" fiber couplers. In practice, the signal strength is optimized by manually adjusting the angles of these waveplates.

The beat signal frequencies of interest lie within DC-7.5 GHz, comfortably within the 10 GHz bandwidth of the photodiode. However, we should consider if the photodiode, amplifiers, and coaxial cables, have a response/loss that varies as a function of frequency. This becomes important when we try to compare the heterodyne ampli-

tudes at two different frequencies for calculating the microwave-to-optical conversion efficiency [see Section 8.4].

We therefore characterize the frequency response of the detection system in two ways. First, we take the segment of the RF circuit located between the photodiode and the spectrum analyzer and place it between ports 1 and 2 of the VNA. By driving and measuring with the VNA in S_{21} mode, we obtain the negative of the insertion loss of this circuit subset in the frequency ranges of interest. Figure 7.10(a) and (b) show the insertion loss near f_{AOM} and f_{het}, with the two frequencies clearly marked. The difference between the two is -4.2(3) dB.
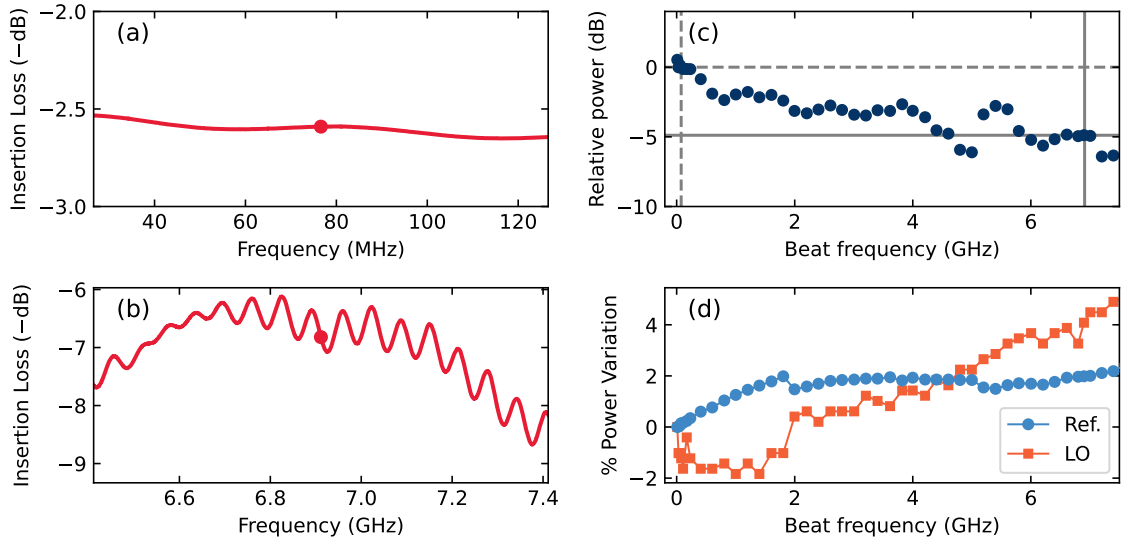
Figure 7.10: Photodetector circuit frequency response. The insertion loss (S_{21}) of the amplifiers and coaxial cables around (a) $f_{\text{AOM}} = 76.6$ MHz and (b) $f_{\text{het}} = 6.911$ GHz, as measured on the VNA. (c) The relative frequency response of the fast photodiode as a function of beat frequency. This measurement comes from the interference of the frequency-locked local oscillator (LO) and a separate frequency-tuned reference (Ref.) laser. There is -4.9 dB difference between f_{AOM} and f_{het}. (d) The percent power variation of the two interfering lasers during the frequency scan of (c).

The second method uses a separate laser, designated "cooling" and used for the cold-atom system. When this is mixed with the local oscillator beam from the primary

laser, we observe a clear heterodyne signal on the spectrum analyzer. If the primary laser is locked, the cooling laser's frequency is tuned such that f_{het} varies between DC and 7 GHz, The power of the heterodyne signal is recorded at these frequencies, and is shown in Figure 7.10(c). Because laser power is slightly coupled to frequency, we also record the power variation of the two beams, as shown in (d). These variations represent about 5% of the total power. While tuning the cooling laser, we found that its frequency would suddenly mode hop. These mode hops are visible near 2 and 5 GHz. When this occurred, the diode current had to be adjusted to bring the beat signal back. Because of power variations and mode hops, this characterization method may not be ideal. However, we can still get a rough idea of the frequency response of the detection circuit that includes the detector. The response difference between the two frequencies of interest is about -5(1) dB.

7.4   Magnetic Coils

One of the original motivations for this experimental setup (one we still hope to pursue) is optical magnetometry. For these experiments, we require three-dimensional control of the magnetic field direction and amplitude experienced by the atoms. We also require high uniformity of the magnetic field across the cell. To this end, we borrowed a set of large square Helmholtz coils from Prof. Vadim Kravchinsky and installed them around the microwave cavity. These coils work marvelously. While not directly related to magnetometry, the microwave-to-optical conversion experiment described in Chapter 8 benefits greatly from magnetic field control.

7.4.1 Construction

The coils were made out of aluminum u-channel that is 1" wide and 0.5" thick. The u-channel was formed and welded into six square frames, two for each axis. The three pairs nest inside each other. 20 AWG copper wire is wound around the coils and soldered at banana terminals. The three coils have effective side lengths of of $L_{\{x,y,z\}} = \{1.027,\ 0.990,\ 0.954\}$ m, measured center-to-center on each side; therefore they require an optimal separation of $0.545 L_{\{x,y,z\}} \simeq \{56, 54, 52\}$ cm [120]. The x- and y-axis coils are clamped vertically onto the optics table, while the z-axis coils are secured to the y-axis pair using zip ties. This is seen in Figure 7.11. The experiment table is positioned inside the coils such that the cavity and vapor cell are centered in all three coil pairs and aligned to the coils' axes. With a gaussmeter borrowed from the Prof. Mark Freeman lab and a handheld ammeter, the proper Helmholtz wiring configurations for the coils were found and rough current-to-field calibrations were determined.

We did not initially know the number of turns in each coil. From the coil perimeter $4L_{\{x,y,z\}}$, resistance $R_{\{x,y,z\}} = \{5.6, 5.4, 5.2\}$ Ω, and the expected resistance per unit length $\sigma = 34$ mΩ/m for 20 AWG wire at room temperature [121], we calculate $N = R/4L\sigma = 40$ turns in each coil.

7.4.2 Safety

At all costs, we want to avoid passing too much current through these coils, which could melt and short catastrophically. The National Electric Code gives a 20 AWG ampacity of $I_0 = 7.5$ A for a temperature rating of 105°C [122], or about $\Delta T_0 = 85$ degrees above room temperature. Assuming that the coil behaves ohmic, $\Delta T_0 \propto I_0^2$. Therefore, by derating the maximum current to 1.5 A, we expect the temperature
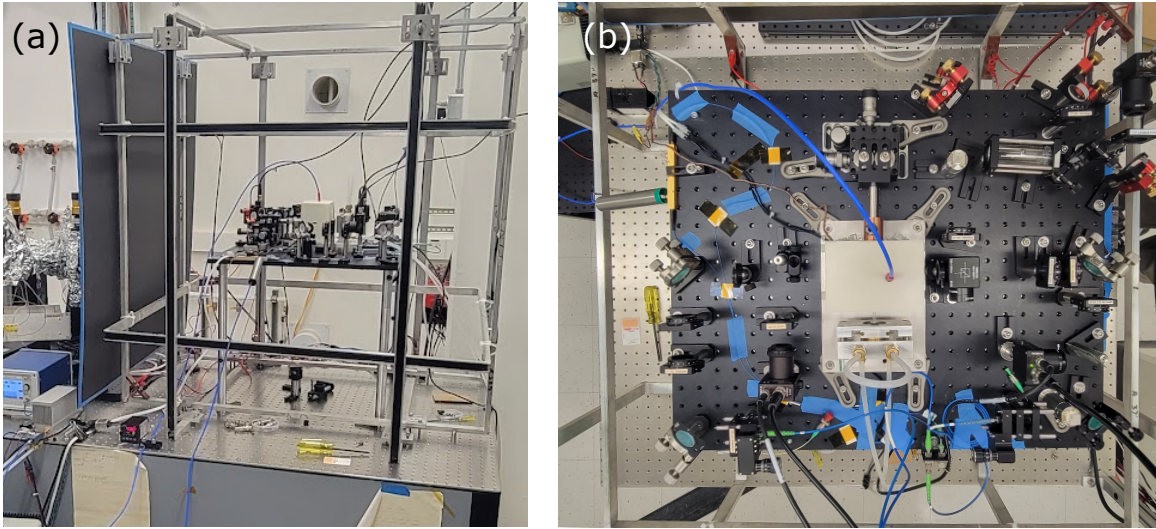
Figure 7.11: The magnetic coils and experiment table. (a) Image of the 3-axis square Helmholtz coils used in this experiment. The largest coil has about a 1-meter side length. (b) Top image of the experiment table. In the center is the oven with the endcap translation stage (above) and stem cooling block (below). The reference vapor cell is in the top right. The laser light enters from the bottom right fiber coupler, is directed through the cavity, and exits from the bottom left fiber coupler.

of the wires to only rise about 3.4 degrees. In practice, the air and coil frames will dissipate much of the heat generated in the coils, and the temperature increase may not be noticeable to the touch. We program limits to the cycle control program, restricting the current through each coil pair to between ±1.5 A. Note that the current these coils need to null the 0.65 G geomagnetic field is about 1.02 A [120], so these limits still give us much to work with.

7.4.3 Calibration

For a more accurate and precise current-magnetic field calibration, we use the rubidium atoms as magnetic field sensors in a double-resonance spectroscopy technique [2, 39, 123]. This method involves a frequency-scanning microwave field and an optical pump beam resonant with the D2 $f = 2 \rightarrow f'$ transition. This beam initially optically

pumps the electron to the $f = 1$ ground state. In a magnetic field, the $f = 2$ and $f = 1$ ground state hyperfine levels each experience Zeeman splitting, with a linear gyromagnetic ratio of $\gamma_g = \pm 0.7$ MHz/G [50]. This splitting creates seven unique microwave transitions that are separated in energy by the Larmour frequency $f_L = \gamma_g B$. By scanning the microwave frequency, there are certain frequencies in the sweep that are resonant with one of these transitions, thereby transitioning the electron from the $f = 1$ to the $f = 2$ state. The atom then immediately absorbs light from the resonant pump laser beam, and its transmission, as monitored by a photodiode, experiences a dip.

With an arbitrary field direction, all seven dips may be visible during a given scan. Operationally, however, the number of dips depends on the direction of the magnetic field. If it is oriented along the axis of the cavity or parallel to the microwave polarization, only three dips emerge [Figure 7.12(a)]; when the field is oriented transverse, four dips emerge [Figure 7.12(b-c)]. In these two special cases, the peaks are separated by twice the Larmor frequency, and the spacing depends linearly on the magnetic field strength.

The first step of calibration is to null the magnetic field. Zero magnetic field is determined by the combination of x, y, and z currents, i.e. (-0.125, 0.15, -0.385) [A], that collapse all seven dips to a single dip with minimum width. The width of this single peak is about 150 kHz, and we take this as an estimate for the ground state decoherence rate $\gamma_I/2\pi$.

Next, we apply fields along each of the three axes in turn, scanning from negative to positive field directions and monitoring the spacing between the dips [Figure 7.12(d-f)]. Converting from Δf to B, a linear fit of $B(I) = aI + b$ [mG] determines the coil calibration parameters given in Table 7.2.
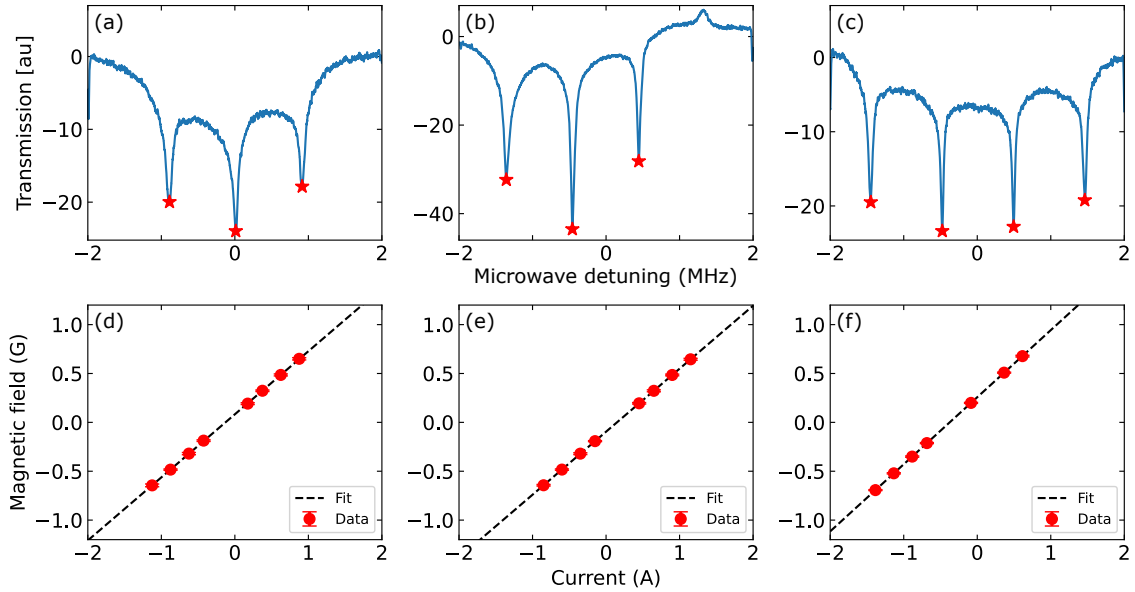
Figure 7.12: Magnetic field-current calibrations using double-resonance microwave-optical spectroscopy. (a-c) Sample spectra from a magnetic field applied along the (a) x-, (b) y-, and (c) z-axes, for a fixed microwave power. As explained in the text, the average spacing between the dips (marked with red stars) is proportional to the magnetic field. (d-f) In the weak-field Zeeman regime, the average peak separation is proportional to the magnetic field strength and the current in the Helmholtz coils. The results of linear fits to these data, their slopes a and intercepts b, are summarized in Table 7.2. The vertical error bars, representing the standard deviation, are smaller than the markers.

	a (mG/A)	b (mG)
X	645(2)	83(1)
Y	644.7(3)	-95.6(2)
Z	686.2(4)	257.3(4)

Table 7.2: Calibration parameters for the Helmholtz coils. Slope a and intercept b parameters for the linear calibration from current to magnetic field, i.e. $B(I) = aI + b$ [mG], corresponding to the fits shown in Figure 7.12(d-f).

The field uniformity was never measured for these coils. Based on the coil size, we assume that the uniformity is quite good. We previously saw the effect of field

inhomogeneity caused by a steel translation stage used for tuning the cavity endcap. When magnetized, it produced a noticeable broadening of the zero-field double resonance dip; we replaced this stage with a less magnetic one. To avoid magnetized hardware, we used, with a few exceptions, non-magnetic (316 stainless steel) bolts and washers on the experiment table near the cavity and vapor cell.

7.5 Vector network analyzer

The work described in this thesis relies on measurements using a vector network analyzer (VNA). We and other members of the LeBlanc research group had not had much prior experience using VNAs as quantitative instruments. We therefore made many inappropriate interpretations of its measurements. Members of the Davis research group, especially Dr. Clinton Potts, Marvin Hirschel, and Dr. Yunhu Huang, helped us tremendously to get on the right track. The purpose of this section is to summarize the lessons we have learned for using and interpreting VNAs properly, in hopes it will benefit future members of the LeBlanc group.

7.5.1 Scattering parameters

Consider a device-under-test (DUT) with two electrical ports. This device accepts an input voltage signal at one of the ports (V_i^+, for $i \in \{1, 2\}$), transforms the signal's amplitude and/or phase, and emits the signal at the original port (V_i^-, reflection) or the opposite port (V_j^-, transmission). A convenient way to express the transformation is by using a matrix of complex S-parameters [124], or

$$\begin{pmatrix} V_1^- \\ V_2^- \end{pmatrix} = \begin{pmatrix} S_{11} & S_{12} \\ S_{21} & S_{22} \end{pmatrix} \begin{pmatrix} V_1^+ \\ V_2^+ \end{pmatrix}. \tag{7.12}$$

When $V_2^+ = 0$, we can define the forward reflection coefficient

$$S_{11} = \frac{V_1^-}{V_1^+} \equiv \Gamma \tag{7.13}$$

and the transmission coefficient

$$S_{21} = \frac{V_2^-}{V_1^+}. \tag{7.14}$$

In general, the coefficients $\Gamma(f)$ and $S_{21}(f)$ are functions of frequency f. The return loss quantifies the relative reflection of a signal produced by an impedance discontinuity and is defined (in dB) as

$$\mathrm{RL} = -20\log|\Gamma| = -10\log\left|\frac{P_1^-}{P_1^+}\right|, \tag{7.15}$$

while the insertion loss quantifies the relative transmission of a signal and is defined as

$$\mathrm{IL} = -20\log|S_{21}| = -10\log\left|\frac{P_2^-}{P_1^+}\right|, \tag{7.16}$$

where the P_i^{x} are the power in each signal, assuming the port impedances are identical. The parameters S_{22} and S_{12} are the reflection and transmission coefficients for the reverse direction.

7.5.2   VNA operation

Using a VNA, the S-parameters of a device are measured as a function of frequency. Since any arbitrary voltage signal may be decomposed as a sum of sines and cosines, it is sufficient to use a single main oscillator that sweeps over a range of frequencies; the parameters are determined for every point during the sweep. As shown in the block diagram of Figure 7.13, the VNA has two ports that connect to the two DUT ports. At a given time, a switch sends the sweeping main oscillator to either Port 1 to measure the forward parameters or to Port 2 to measure the reverse parameters. The
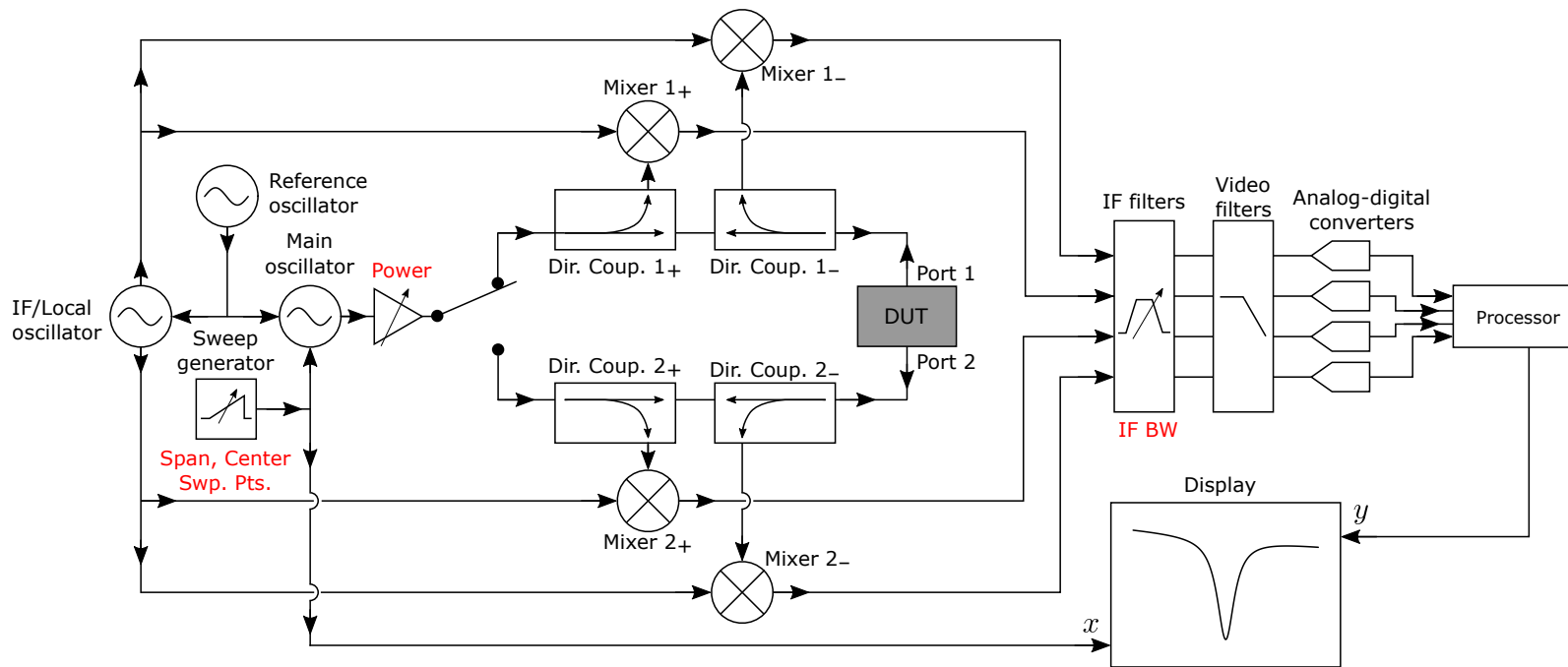
Figure 7.13: Schematic of a two-port vector network analyzer (VNA). A VNA measures the frequency-dependent RF/microwave reflection or transmission coefficients of a given device under test (DUT). The instrument consists of a main swept-frequency oscillator that is amplified and switched between one of two ports of the DUT. The transmitted and reflected signals on each port are sampled by an RF directional coupler and down-mixed with a fixed intermediate frequency (IF) reference signal. After filtering the mixer outputs, the signals' amplitudes and phases are digitized, processed, and displayed on the front panel screen. The common user-defined settings are labeled in red, and described in Section 7.5.3.

S-parameters are obtained by comparing the amplitudes and phases of the voltages that exit and enter the two ports. Figure 7.13 shows a pair of directional couplers on each port line: one directional coupler samples the outgoing wave, and the other samples the ingoing one. The sampled signals are individually down-mixed with a swept IF/local oscillator signal. The frequency of the local oscillator is such that the output frequency coincides with the center frequency of an IF bandpass filter. The filtered signal is digitized, processed, and the desired scattering parameters are displayed on the screen.

7.5.3   Key Parameters

The signal generation and processing of a VNA are largely self-contained. It reports S-parameters of the DUT referenced against internal signals. This means there are relatively few user-defined parameters. The following describes four configurable parameters that users should be aware of:

- **Span and center frequency**: These parameters adjust the extent and center of the main oscillator frequency sweep. These parameters typically take values in MHz to GHz.

- **IF Bandwidth**: This is the width in frequency of the bandpass IF filter, with typical values in Hz to kHz. The narrower the bandwidth, the less spectral noise is averaged with the desired signal. However, there is a trade-off between lower noise and longer sweep times.

- **Power**: The S-parameters of linear devices will not usually depend on the power of the main oscillator signal. However, nonlinear devices may be sensitive to this power. The power may be adjusted manually and takes values between -20 and 0 dBm.

- **Sweep Points**: This has typical values between 201 and 10001. More points increase the total sweep time.

7.5.4 Display modes & coupling
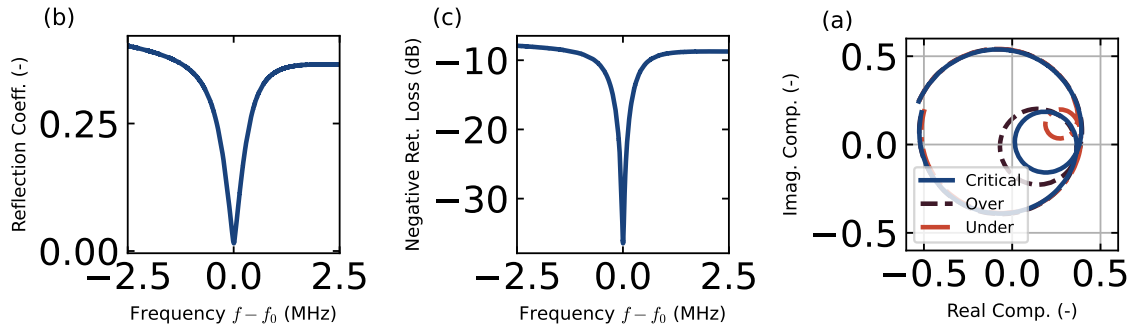
Figure 7.14: A critically-coupled S_{11} VNA trace in three different display modes. (a) Linear magnitude (reflection coefficient). (b) Logarithmic magnitude (return loss, measured in dB). (c) Polar (the real and imaginary parts of the reflection coefficient). It also includes separate over-coupled (black, dashed) and under-coupled (red, dashed-dot) traces for comparison.

While the VNA can display S-parameters in a number of different ways, we want to highlight only three: linear magnitude, logarithmic magnitude, and polar (real & imaginary). In Figure 7.14, the same critically-coupled cavity resonance signal is displayed in each of these modes. For simplicity, we consider the S_{11} parameter.

- **Linear Mag.**: This mode displays the absolute value of the reflection coefficient $|\Gamma(f)|$ versus the swept frequency f. These values are unitless. This mode is useful for getting a rough measure of the cavity resonance width.

- **Log. Mag.**: This mode displays the return loss (RL; see Equation 7.15) versus the swept frequency f. These values are in dB. Because of the large dynamic range, the Log. Mag. mode is useful for precisely tuning the cavity resonance frequency f_0 to a desired frequency.

116

- **Polar**: This mode displays the imaginary part $\Im[\Gamma(f)]$ versus the real part $\Re[\Gamma(f)]$. Far from any cavity resonance, the polar trace forms circular loops, roughly centered around the origin. These loops are caused by phase delay in the coaxial cable. (The VNA has a calibration routine to remove variations in this phase delay.) As the scanning frequency approaches the cavity resonant frequency, the trace dips within the outside circle, forming an additional circular loop approaching the origin. This resonant circle clearly shows the extra phase change experienced by a wave near a DUT resonance [125]. The polar display mode is useful for determining the coupling into the cavity: if the small loop passes through the origin, then the cavity is what's called critically coupled; if the loop encloses the origin, it is over-coupled; if it does not enclose or pass through the origin, the cavity is under-coupled.

The energy decay rate due to internal dielectric or resistive dissipation inside the cavity is κ_{int}; the decay rate due to dissipation from external connections and circuitry is κ_{ext}. The total decay rate $\kappa_{\mathrm{tot}} = \kappa_{\mathrm{int}} + \kappa_{\mathrm{ext}}$. The relative strengths of the loss channels in the cavity system are related to the coupling, as listed in Table 7.3.

The decay rate κ_i is related to a device-specific quantity called the quality factor or $Q_i = 2\pi f_0 / \kappa_i$. This figure of merit can be thought of as the number of oscillations undergone by a resonator before it damps out. Equivalently, it can be defined as [124]

$$Q = 2\pi f_0 \frac{\text{(average energy stored)}}{\text{(energy loss/second)}} \tag{7.17}$$

near the resonant frequency. The higher the Q for a given f_0, the narrower the resonance and the smaller the loss. In accordance with the total decay rate definition, the total quality factor is defined as

$$\frac{1}{Q_{\mathrm{tot}}} = \frac{1}{Q_{\mathrm{int}}} + \frac{1}{Q_{\mathrm{ext}}}. \tag{7.18}$$

Because of the loading to external connections and circuitry, Q_{tot} is also known as the "loaded Q"; Q_{int} is sometimes known as the "unloaded Q" [124, 126].

Table 7.3: Table showing cavity coupling relationships.

Critical	$\kappa_{\text{int}} = \kappa_{\text{ext}}$	$Q_{\text{int}} = Q_{\text{ext}}$
Over	$\kappa_{\text{int}} < \kappa_{\text{ext}}$	$Q_{\text{int}} > Q_{\text{ext}}$
Under	$\kappa_{\text{int}} > \kappa_{\text{ext}}$	$Q_{\text{int}} < Q_{\text{ext}}$

7.5.5 Quality factor measurements

The internal and external quality factors are determined using the full complex S_{11} data from the polar display mode. (The internal quality factor cannot be determined from a transmission measurement, because a reference baseline is absent [126].) We can fit to the reflection data a general model for a notch resonator [126, 127]

$$S_{11}(f) = \underbrace{ae^{i\alpha}e^{-2\pi i f \tau}}_{\text{environment}} \underbrace{\left[1 - \frac{(Q_{\text{tot}}/|Q_{\text{ext}}|e^{i\phi}}{1 + 2iQ_{\text{tot}}(f/f_0 - 1)}\right]}_{\text{ideal resonator}}, \tag{7.19}$$

where the first part of the equation represents the response of factors external to the cavity; a, α, and τ are the amplitude, phase shift, and electronic delay of the cable. The second term is a model for an ideal resonator, where the phase shift ϕ is caused by the cable-cavity impedance mismatch. After fitting, Q_{int} is determined from the fit parameters and Equation 7.18. A successful fit to a cavity resonance trace is shown in Figure 7.15.

One early, repeated mistake was attempting to estimate the cavity quality factor using the linear or log magnitude display modes. In the linear mode, we would find the full width at half-maximum (FWHM) of the $|\Gamma|$ resonance dip. The issue with this approach is that the information contained within the complex phase is absent.
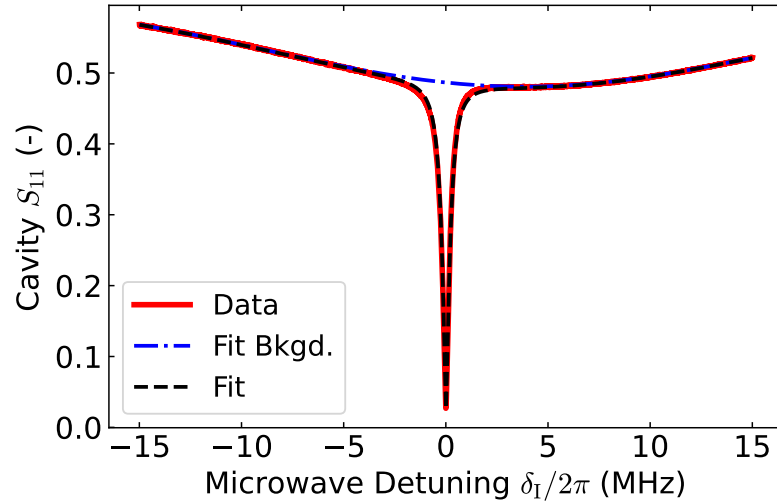
Figure 7.15: Cavity resonance S_{11} reflection coefficient trace and fit as a function of the idler detuning δ_I. The resonance spectral dip sits on a sloping background due to the coaxial cable "environment." By fitting Equation 7.19 to the trace, the resonance and background parameters are independently determined. The trace shown here has a fitted $Q_{tot} = 10\,185(6)$ and $Q_{ext} = 19\,315(9)$, from which we compute $Q_{int} = 21\,550(30)$.

Additionally, the resonance dip sits on a sloping background, making the full depth of the dip an ill-defined quantity. Usually, estimates of Q_{tot} using the linear mode are up to 20% off the true value. Using the log magnitude mode has similar difficulties, not to mention the different units and logarithmic scaling.

7.6   Microwave Cavity

7.6.1   Waveguides and cavities

Freely propagating electromagnetic waves have wave solutions where both the electric and magnetic field components are orthogonal to each other and to the $\hat{z}$ propagation direction; these are called transverse electro-magnetic (TEM) waves. In confined waveguides with conducting walls, the components of a traveling electromagnetic field are not generally transverse. One of the components sometimes has a non-

119

zero longitudinal component: waves with $E_z = 0$ are called "transverse electric" (TE) and those with $B_z = 0$ are called "transverse magnetic" (TM) waves [90]. By terminating the two open ends of a waveguide, a resonant cavity may be formed. In this enclosed, confined space, electromagnetic energy exists as oscillating, standing waves. The conducting boundary conditions produce a set of TE and TM modes with various resonant frequencies and unique field distributions. Maxwell's equations can be solved to determine the modes and their properties.

7.6.2   Design & Construction

Our microwave cavity was designed and machined by Dr. Clinton Potts. The dimensions of the microwave cavity are shown in Figure 7.16, having a fixed, internal radius $a = 29$ mm, and length $d = 53(2)$ mm that is adjustable over a finite range with an endcap attached to a micrometer translation stage [2, 59]. The cavity is not a perfect cylinder. A thin ring of 2 mm height and 2 mm width is machined onto the endcap. This ring breaks the degeneracy between the TE_{011} mode and the lossier TM_{111} mode [128–130]. By breaking this degeneracy, almost all of the microwave energy is coupled into the desired, high-Q mode. Additionally, the TE_{011} mode has no current flowing through metal seams of the cavity, giving a higher quality factor. This fact allows for optical access holes in the cavity walls.

The quartz vapor cell resides in the center of the cavity, aligned along the x-axis, with the rectangular sides square to the y- and z-axes. The dielectric properties of the quartz tend to draw in and concentrate the magnetic mode component inside the cell volume, making the microwave power more spatially uniform than without the cell. With the cell in place, we precisely move the endcap to tune the resonance frequency of the cavity TE_{011} mode to the ^{87}Rb ground state transition, $\Delta E_{HF}/h = 6.834\,682$ GHz.
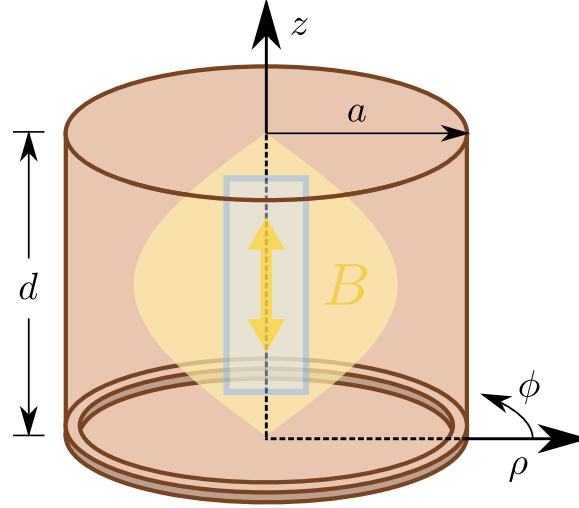
Figure 7.16: The geometry of the cylindrical microwave cavity in cylindrical coordinates. The cavity's radius a and length d determine the frequency and shape of the TE_{011} mode. The thin ring at $z = 0$ breaks the degeneracy between the TE_{011} and TM_{111} modes. The magnetic component B dwells primarily in the center of the cavity, overlapping with the ^{87}Rb vapor cell, and oscillating along the z-axis.

As the ground state magnetic-dipole transition is weak, the cavity mode enhances this transition probability.

Microwave power to the cavity is supplied by a low-noise signal generator (SG1, AnaPico APSIN12G) via 2 m-long coaxial cable (Mini-Circuits 141-2MSM+). This cable attaches to a coupler pin that penetrates into the cavity and radiates the electric field of the microwave signal parallel to the TE_{011} mode's circulating electric field [128]. To do this, the pin enters the cavity along an axis that is 8 mm offset from the radial plane.

The TE_{011} mode and performance of this vapor cell/cavity design were first simulated using COMSOL software using the geometry and dielectric properties of the quartz vapor cell and stem. The results are shown in Figure 7.17(b-e); panels (b-c) represent the powers of the magnetic component and (d-e) the electric component. The simulation gives a resonant frequency of around 6.8 GHz and an internal quality

factor of $Q \sim 27\,000$ [59]. With the simulation results, we calculated a mode volume of 9.19 cm^3 according to the equation [34]

$$V_{\mathrm{m}} = \frac{\int_{V_{\mathrm{cav}}} |\mathbf{B}(\mathbf{r})|^2 / \mu(\mathbf{r})}{\max\left(|\mathbf{B}(\mathbf{r})|^2 / \mu(\mathbf{r})\right)}, \tag{7.20}$$

where V_{cav} is the internal volume of the microwave cavity. Based on this design, the cavity was machined out of low-oxygen copper, and the internal surface was given a high-quality, polished finish.

7.6.3 Cavity mode solutions

The electromagnetic modes functions of a cylindrical cavity are well-known [124]. We won't repeat these derivations; however, we will provide some intuition for the symmetry of the modes, quote the form of the functions, and then plot the TE$_{011}$ mode of interest.

All modes have the same cylindrical symmetry as the cavity and are characterized by three "quantum" numbers imposed by the boundary conditions and corresponding to the three separable cylindrical variables: n (azimuthal ϕ); m (radial ρ); and ℓ (axial z). Since the atoms respond to the magnetic component of the mode, we restrict our attention to TE$_{nm\ell}$ modes that have magnetic fields overlapping the cell. The quality factor of these modes is $Q_{nm} \sim 1 - (n/p'_{nm})^2$, where p'_{nm} is one of the roots of the J'_n Bessel function; this means that greater field enhancement is possible when $n = 0$, or for the TE$_{011}$ mode.

Because the fields are single-valued, they must be periodic in ϕ, i.e. $F_i(\rho, \phi, z) = F_i(\rho, \phi + 2\pi, z)$, where F_i represents the ith component of the electric E or magnetic B fields. The azimuthal part will therefore be a sine or cosine of $n\phi$, and the field will have $2n$ azimuthal nodes. Along the axial direction, the terminating boundaries produce an analogous infinite square well scenario. The axial parts will therefore be a

sine or cosine of $\pi \ell z/d$, where $\ell \geq 1$. Solutions to the radial part are Bessel functions, owing to the cylindrical symmetry of the cavity, analogous to the modes of a vibrating circular drumhead. The field is finite at $\rho = 0$, so only J_n Bessel functions of the first kind (or its derivative) are permitted. The conducting walls require that the electric field goes to zero at $\rho = a$, enforcing the $(p'_{nm}\rho/a)$ argument of the Bessel functions. The magnetic and electric components of the $\text{TE}_{nm\ell}$ modes of a cylindrical cavity are [124]

$$B_z = B_0 J_n \left(\frac{p'_{nm}\rho}{a} \right) \cos(n\phi) \sin \left(\frac{\ell \pi z}{d} \right), \tag{7.21a}$$

$$B_\rho = \frac{\beta a B_0}{p'_{nm}} J'_n \left(\frac{p'_{nm}\rho}{a} \right) \cos(n\phi) \cos \left(\frac{\ell \pi z}{d} \right), \tag{7.21b}$$

$$B_\phi = \frac{-\beta a^2 n B_0}{(p'_{nm})^2 \rho} J_n \left(\frac{p'_{nm}\rho}{a} \right) \sin(n\phi) \cos \left(\frac{\ell \pi z}{d} \right), \tag{7.21c}$$

$$E_\rho = \frac{ik\eta a^2 n B_0}{(p'_{nm})^2 \rho} J_n \left(\frac{p'_{nm}\rho}{a} \right) \sin(n\phi) \sin \left(\frac{\ell \pi z}{d} \right), \tag{7.21d}$$

$$E_\phi = \frac{ik\eta a B_0}{p'_{nm}} J'_n \left(\frac{p'_{nm}\rho}{a} \right) \cos(n\phi) \sin \left(\frac{\ell \pi z}{d} \right), \tag{7.21e}$$

$$E_z = 0, \tag{7.21f}$$

where the propagation constant

$$\beta_{nm} = \sqrt{k^2 - \left(\frac{p'_{nm}}{a} \right)^2} \tag{7.22}$$

is like a generalized wavenumber, B_0 is the amplitude, and where $\eta = \sqrt{\mu_0/\epsilon_0}$ and $k = \omega/c$. The resonant frequency of the cavity is determined from β_{nm} to be

$$f_{nm\ell} = \frac{c}{2\pi} \sqrt{\left(\frac{p'_{nm}}{a} \right)^2 + \left(\frac{\ell \pi}{d} \right)^2}, \tag{7.23}$$

where c is the speed of light in vacuum. In the TE_{011} mode, $H_\phi = E_\rho = E_z = 0$. Figure 7.17(a) shows the magnitude squared of the magnetic field $B_{\text{tot}}^2 = B_\rho^2 + B_z^2$ for a 2D slice along the axis of the cavity; the pump laser beam and vapor cell regions are

also highlighted. By substituting the physical cavity dimensions into Equation 7.23, we calculate a resonant frequency of 6.910 05 GHz, reasonably close to the target frequency. Of course, this model does not capture the dielectric properties of the vapor cell, which are accurately considered in the COMSOL simulations.
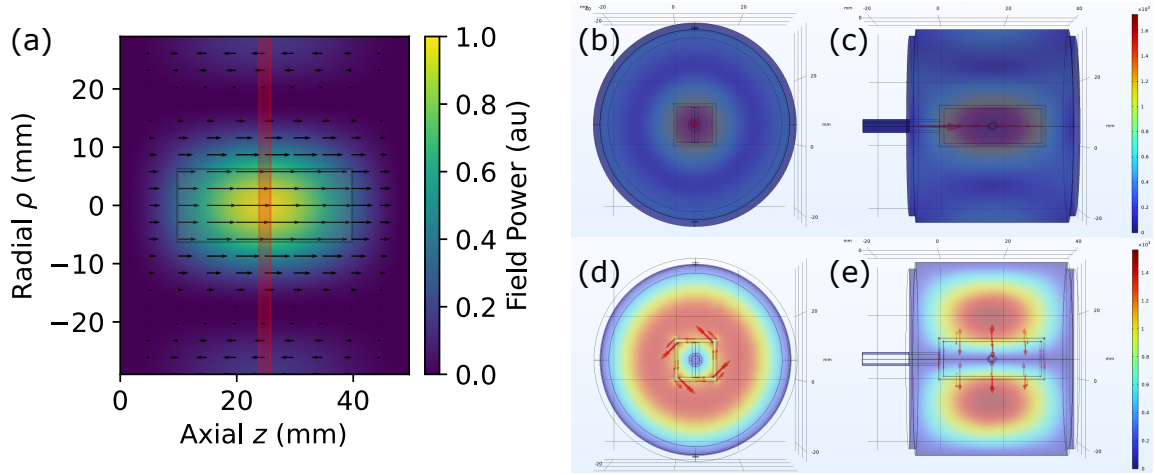
Figure 7.17: Cavity TE_{011} mode structure. (a) A 2D axial cross-section of the cavity's magnetic power distribution, proportional to B_{tot}^2 and calculated from Equations 7.21a and 7.21b. The vector field shows the direction and amplitude of the instantaneous magnetic field. The rectangular cross-sections of the vapor cell and pump laser beam are outlined. (b-e) Calculations of the cavity TE_{011} mode power performed in COM-SOL, considering the geometry and dielectric constants of the quartz cell. The images show the transverse and axial cross-sections of the magnetic (b & c) and electric (d & e) field powers. Images courtesy of Bahar Babaei.

7.6.4 Characterization

As described in Section 7.5.5, the cavity's internal, external, and total quality factors are determined by fitting to the complex S_{11} reflection data. One such fit is shown in Figure 7.15. As will be discussed in Section 7.7.2, the internal quality factor depends on atomic deposition on the cell inner wall, which is controlled by the cell's temperature. The external quality factor depends on the position and dimensions of the coupler pin that penetrates the cavity [131]. Power transmission into the cavity

is maximized when it is critically coupled, or $Q_{\text{int}} \approx Q_{\text{ext}}$ [124]. Therefore, we use a bench grinder to make small adjustments to the length of the coupler pin until this condition is satisfied. We measure internal and external quality factors of ~ 20k.

The coaxial transmission line connecting the signal generator to the cavity also introduces some power loss. We directly measure the S_{21} insertion loss of this cable to be about 3 dB. This is consistent with the -6.3 dB background return loss - there and back again - obtained from the cavity S_{11} resonance fits.

7.7   Atomic vapor cell

7.7.1   Cell description

Inside the cavity is a sealed, rectangular quartz cell manufactured by Precision Glass-blowing. It has external dimensions of 30 x 12.5 x 12.5 mm (1 mm thick walls) and contains enriched ^{87}Rb. It has a long cylindrical stem with a diameter of 4.1 mm that protrudes out of the center of one of the small faces; the stem is gently clamped in place by a support structure that is water-cooled to about 16°C. In addition, the cavity is wrapped with silicone thermal heating pads and a thermal enclosure; the cavity region is temperature-stabilized at 37°C.

Temperature is a key parameter of any warm alkali atom system. Specifically, rubidium has a melting temperature of 39.31°C; the vapor pressure, and hence the atomic density and optical depth, increase exponentially with temperature [50].

7.7.2   Influence on the cavity

Because the vapor cell is sealed, colder atoms condense out of the gas phase onto the inner cell wall. A thin metallic film of rubidium forms on the wall, interacting with and scattering the microwave cavity mode. This reduces the cavity's internal
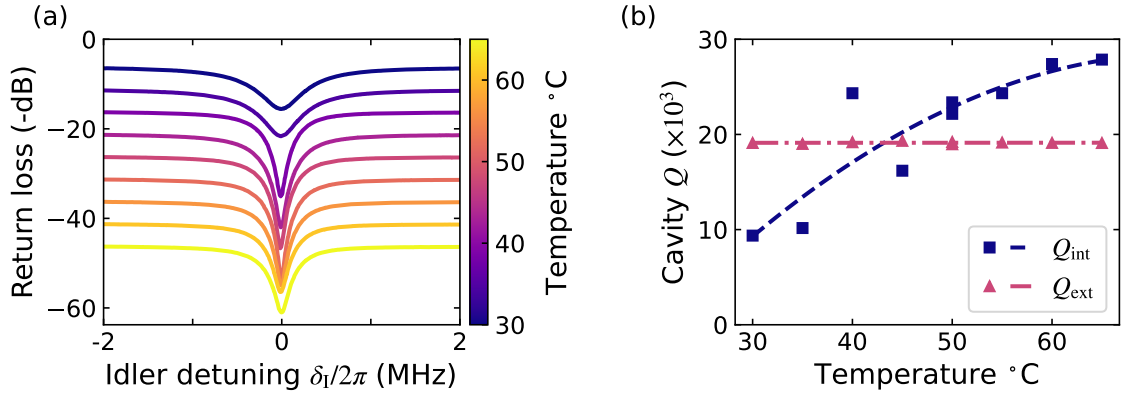
Figure 7.18: The influence of the vapor cell temperature on the microwave resonance. (a) Return loss traces for the cavity held at temperatures between 30° and 65°C. The traces are vertically offset in -5 dB increments. (b) The extracted Q_{int} and Q_{ext} parameters for the traces in (a) as a function of temperature. The vertical error bars are smaller than the marker points. At low temperatures, the cavity is under-coupled but becomes over-coupled at higher temperatures. The external coupling is unaffected by temperature. The blue (dashed, Q_{int}) parabolic and magenta (dashed-dotted, Q_{ext}) linear fits are "guides to the eye", and intersect at about 43°C, where the cavity is critically-coupled.

quality factor. At higher temperatures, however, the atoms are less likely to dwell on the cell wall and form a film[8]. By heating the cavity and water-cooling the stem, we encourage atoms to condense in the stem outside of the cavity, thus preserving the cavity resonance.

The effect of temperature on the cavity resonance is seen in Figure 7.18(a). The width of the cavity resonance narrows and then broadens again, as the temperature is varied between 30° and 65°C. By fitting these resonances as described in Section 7.5.5, we extract the internal and external quality factors as a function of temperature [Figure 7.18(b)]. The external quality factor is almost independent of temperature. Due to the dissipation of the metallic film, the internal quality factor

---

[8]High intensity microwave power (e.g. 30 dBm) also encourage desorption of the atomic film.

increases monotonically with temperature over this range. The internal and external Qs coincide at roughly 43°C, at which point the cavity is critically coupled.

7.7.3 Optical Depth

As mentioned above, the optical depth and atomic density also vary with temperature. The optical depth of a material is defined as [132]

$$OD = -\ln\left(\frac{P_{\text{out}}}{P_{\text{in}}}\right), \tag{7.24}$$

determined from the input (P_{in}) and output (P_{out}) optical powers. In the case of the atomic vapor cell, the transmitted optical power of the pump beam is reduced due to resonant atomic absorption (P_{abs}), but also from scattering off the cell glass walls and the hole aperture (P_{scat}). The atomic density may be determined by the optical depth due *only* to absorption, or OD_{abs}. To determine this from experimental parameters, we begin with a statement of energy conservation, or

$$P_{\text{out, on}} = P_{\text{in}} - P_{\text{abs}} - P_{\text{scat}}. \tag{7.25}$$

When the laser is off-resonance,

$$P_{\text{out, off}} = P_{\text{in}} - P_{\text{scat}}. \tag{7.26}$$

Using Equation 7.24, this gives us two optical depth equations, both on- and off-resonance:

$$\exp(-OD_{\text{on}}) = \frac{P_{\text{out, on}}}{P_{\text{in}}} = 1 - \frac{P_{\text{abs}}}{P_{\text{in}}} - \frac{P_{\text{scat}}}{P_{\text{in}}}, \tag{7.27}$$

$$\exp(-OD_{\text{off}}) = \frac{P_{\text{out, off}}}{P_{\text{in}}} = 1 - \frac{P_{\text{scat}}}{P_{\text{in}}}. \tag{7.28}$$

By subtracting these two equations and adding one, the P_{scat} terms cancel, and we obtain

$$1 + e^{-OD_{\text{on}}} - e^{-OD_{\text{off}}} = 1 - \frac{P_{\text{abs}}}{P_{\text{in}}} = \frac{P_{\text{out, abs}}}{P_{\text{in}}} \equiv e^{-OD_{\text{abs}}}, \tag{7.29}$$

where $P_{\text{out, abs}}$ is the output power only considering absorption. This can be alternatively expressed as

$$OD_{\text{abs}} = -\ln\left(e^{-OD_{\text{on}}} - e^{-OD_{\text{off}}} + 1\right), \qquad (7.30)$$

or, in terms of measured optical powers,

$$OD_{\text{abs}} = -\ln\left[\frac{P_{\text{in}} - (P_{\text{out, off}} - P_{\text{out, on}})}{P_{\text{in}}}\right]. \qquad (7.31)$$
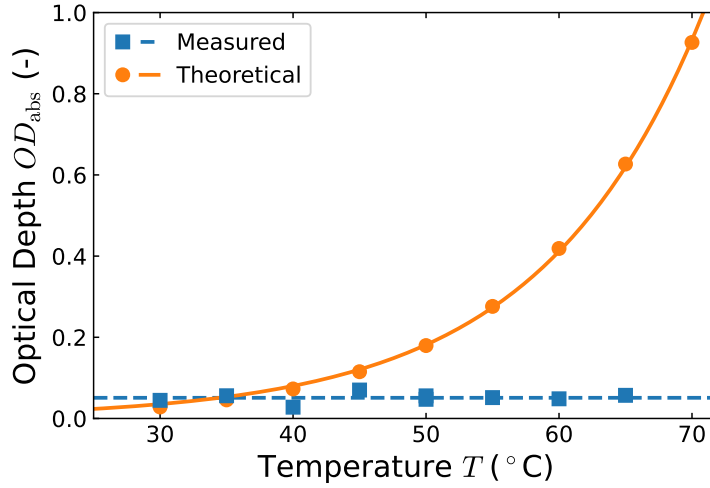
Figure 7.19: Measured and theoretical optical depth versus temperature. The measured optical depth is independent of the cavity temperature, with an average value of 0.05 shown by the dashed horizontal line. In equilibrium with the heat source, the optical depth of a theoretical ^{87}Rb vapor rises exponentially with temperature. From these data, we conclude that the cold cell stem temperature primarily determines the atomic density and optical depth.

We measure a constant absorption optical depth as a function of temperature, as shown in Figure 7.19, with an average value of 0.05(1), meaning only about 5% of the input resonant light is absorbed. This behavior is quite different from the exponentially rising optical depth of a uniformly heated vapor cell [50, 75]. The critical difference here is due to the water-cooled stem: the rubidium vapor pressure is ultimately set by the temperature of the coldest part of the cell through a "reservoir"

effect [133]. Because the laser's frequency is stabilized during these measurements, the 0.05(1) value represents the optical depth of only the resonant velocity class.

The optical depth is related to the atomic density $\mathcal{N}$ as

$$OD_{\text{abs}} = \mathcal{N}\sigma L, \tag{7.32}$$

where σ is the Doppler-broadened atom-photon cross-sectional area [see Section 4.2], and L is the width of the cell. We calculate a number density for the resonant velocity class of $\mathcal{N} = 3(1) \times 10^{17}$ m^{-3}, about 100 times higher than the expected density for a rubidium vapor at 16°C, $\mathcal{N}_{\text{exp}} = 3.65 \times 10^{15}$ m^{-3} [50, 75]. Although the cold stem regulates the density, this discrepancy may imply that the main cell body and stem are not in thermal equilibrium.

7.7.4 Temperature Control
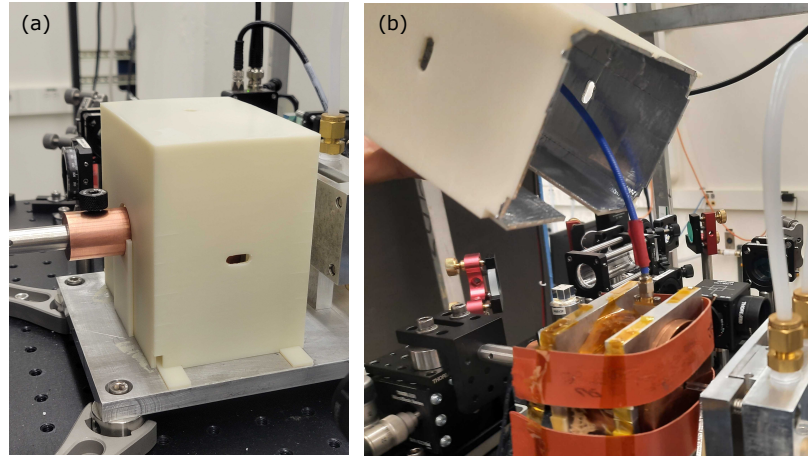
Figure 7.20: Images of the 3D-printed ABS oven. Images of the 3D-printed ABS oven, showing (a) the assembled oven from the outside, and (b) the inside, which is coated with foil tape for thermal insulation. The oven has holes for the pump laser and grooved panels for easy removal of the oven without disturbing the cavity end cap and cell stem. The red silicone heating pads are also visible in (b). Photos courtesy of Prof. Andal Narayanan.

This section describes how we regulate the temperature of the cavity-vapor cell system using a combination of heating and cooling elements with temperature shielding and feedback control.

To control the cavity-cell temperature, we form a closed feedback control loop composed of a heating element, a thermocouple, a temperature controller, and an electrical relay. Silicone electrical heating strips are wrapped around the cavity and secured to the aluminum clamps using Kapton tape[9]. A K-type thermocouple is taped to the top of the microwave cavity. An Omega CN740 temperature controller reads the thermocouple temperature value and compares it to a set temperature value. If the actual temperature is lower, the controller sends a high logic pulse to the electrical relay, which opens the heating elements to a 120 VAC drive[10]. The Omega device has a pre-programmed routine to automatically test and tune the P, I, and D parameters of the controller.

The first thermal enclosure for the cavity was formed from a layer of aluminum foil, leaving holes for the laser beam, the coaxial cable, heater wires, the cold stem, and the endcap post. It was difficult to create an effective foil enclosure with so many access points. With (at least) daily adjustment of the cavity endcap, the foil was regularly disturbed, producing large gaps in the enclosure where heat could escape convectively. We then designed and 3D-printed an oven with precisely placed and sized holes. This oven, seen in Figure 7.20, features tongue-and-groove slots that mate from above and below the endcap and cold stem; this allows the oven to be

---

[9]We have since discovered that loops of copper wire with the ends twisted tightly together holds the heating elements in place much better than tape.

[10]The downside of electrical vapor cell heating is the introduction of additional 60 Hz magnetic field noise [134]. We have observed broadening and reduction of our generated signals when the relay is open. These deleterious effects can be averaged out or sidestepped if the relay cycle period is long and the duty cycle is as low as possible. A superior solution, however, is to use hot air heating of the cell and cavity [134].

easily lifted off the cavity and replaced as a single piece without disturbing the cavity and heating elements underneath[11].

Because of the elevated operating temperatures, it was necessary to make the oven out of a more durable ABS plastic. The durability advantage also makes ABS a more difficult material to print compared to more malleable plastics such as PLA. Multiple printing trials failed due to delamination between the layers of the thin oven walls. These issues were remedied by (1) operating the 3D printer inside an enclosure; this keeps the entire print at a higher temperature, helping the layers bond better; and (2) increasing the wall thickness from 1.5 to 3 mm. As a safety note, printing ABS is known to release noxious, irritating fumes. To reduce this risk, we placed a soldering fume extraction snorkel arm near the door of the printing enclosure. After printing, the oven's interior was coated with metallic adhesive tape.

7.8 Spectrum Analyzer

7.8.1 Principle of operation

Important information about a signal can be gleaned from the spectral frequency components that compose it. The purpose of a spectrum analyzer is to measure the frequency and strength of these components in an electrical signal. Mathematically, the way to do this is with a Fourier transform [135, 136]. In practice, a device samples and digitizes the input analog waveform with a sampling rate f_s, and then a digital processor computes the discrete Fourier transform. This is how "real-time" spectrum analyzers operate. For this to work, f_s must be greater than the Nyquist frequency of the signal, or twice the highest frequency component in the signal. Real-time

---

[11]Despite somewhat reducing convective thermal dissipation, this oven still conducts heat away to the environment via the copper endcap mount, the aluminum base plate, and even the oven walls. Future oven designs should also consider and eliminate these sources of conductive thermal dissipation.
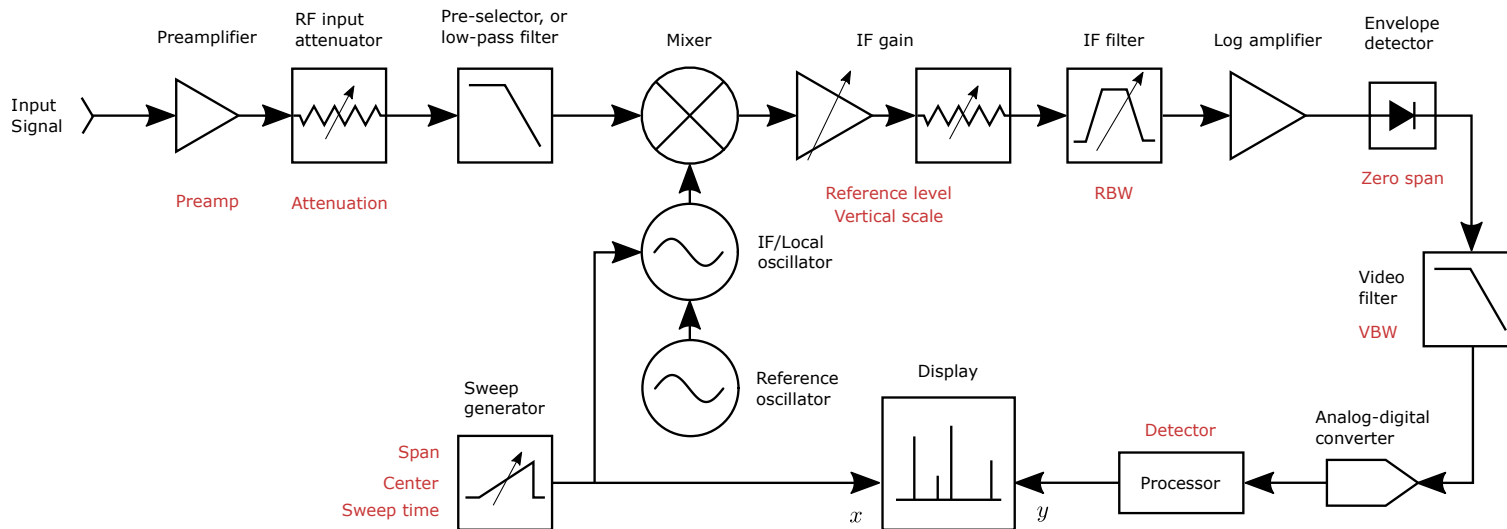
Figure 7.21: Schematic of a swept-tuned spectrum analyzer. The input signal is preconditioned with a preamplifier and a variable attenuator. Frequency scanning is achieved by combining the conditioned signal with a frequency-sweeping, IF/local oscillator signal on a mixer. The IF gain stage brings the scanning mixed signal into a usable dynamic range. After passing through the IF filter, the signal is further conditioned before being digitized and displayed. The common user-defined settings are labeled in red, and described in Section 7.8.3.

spectrum analyzers have the advantage that they capture a spectrum in a single shot, making them ideal for capturing transient signals. In addition to the amplitude, they also contain the phase information at each frequency. The disadvantage of real-time analyzers, however, is that analog-to-digital converters (ADCs) have historically had sampling rates limited to a few GSa/s; this is not enough to measure signals around 6.8 GHz in our lab. Faster ADCs are becoming available, but they are expensive, particularly when combined with an adequate digital processor.

A more economical approach is called a "swept-tuned" spectrum analyzer. To understand its operation, first imagine a hypothetical narrow bandpass filter with a tunable central frequency. Only the signal frequency components that lie within the filter bandwidth are transmitted to and averaged by a power detector. By sweeping the filter's central frequency across the frequency region of interest, the transmitted power as a function of the filter frequency can be mapped out, with a spectral resolution set by the filter bandwidth. A filter with a narrower bandwidth will more closely approximate the true spectrum but at the expense of longer sweep times. Because the filter is swept, this method is better suited for measuring continuous or periodic signals. A disadvantage of this method is that the phase information of the spectral components is lost.

In reality, a bandpass filter's central frequencies cannot be readily scanned. It's much easier to have a fixed filter and to sweep the frequency of the signal. The input signal frequency is down-mixed such that the frequency of interest always coincides with a fixed frequency—but tunable bandwidth—bandpass filter. This scheme is depicted in the block diagram of Figure 7.21, an adaptation of figures found in [136, 137].

7.8.2 Safety

Spectrum analyzers are very sensitive to DC voltages which can easily damage the mixers and attenuator. Some instruments have an AC-coupling mode: a blocking capacitor eliminates any DC offset, but also attenuates low-frequency signals. Our Rohde & Schwarz instrument is AC coupled by default but can be switched to DC coupling if sensitive low-frequency measurements are required. In this case, it is important to be vigilant against DC signals entering the instrument.

7.8.3 Key Parameters

A modern spectrum analyzer is generally quite flexible and sophisticated in the signals it can measure. There are many user-defined device measurement parameters that enable this flexibility. We will briefly summarize and explain the most important parameters that the user should be aware of:

- **Span & Center**: The span (Δf) and center (f_0) control the local oscillator frequency sweep range and thus the range of frequencies in the sweep.

- **Preamplifier**: An additional amplifying gain is sometimes applied to the input signal for improving the instrument's sensitivity. It is mostly beneficial for weak signal measurements. In general, this gain is frequency-dependent, which should be considered for precise level measurements [136]. Our Rohde & Schwarz spectrm analyzer has nominal preamp gain values of 0, 15, and 30 dB.

- **Reference level & vertical scale**: These parameters control the IF gain stage. The reference level is the maximum power level (in dBm) read by the ADC and displayed on the instrument. Overload occurs when the signal power exceeds the reference level. While a spectrum analyzer can measure the power

of signals across a large dynamic range, it cannot measure the entire range at once [136]. The vertical scale (set in dB) selects a range of powers below the reference level to be recorded and displayed.

- **Attenuation**: The input variable attenuator is used to prevent overloading of the ADC, gain compression, and harmonic distortion [137]. When measuring weak signals, the attenuation should be 0 dB for maximum sensitivity. For strong signals, at least 10-30 dB of attenuation may be necessary.

- **RBW**: This is the bandwidth of the IF filter and therefore the smallest spectral resolution that can be measured with the instrument. If two narrow spectral peaks are separated by a frequency less than the RBW, they will not be resolved. On a good instrument, the RBW can be tuned between 0.1 Hz to around 10 MHz. Measurements with a smaller RBW more closely approximate the true signal's spectrum; it also reduces the noise in the signal.

- **VBW**: The video low-pass filter helps smooth the noise in the measured trace. In general, the level of noise smoothing depends on the VBW and the RBW.

- **Sweep time**: Usually the sweep time takes values according to

$$t_{\text{sweep}} \geq k \frac{\Delta f}{\text{RBW} \times \text{VWB}}, \tag{7.33}$$

where k is a device-specific parameter [136]. The inequality shows that the sweep time may be manually adjusted longer than the minimum value, which is often set automatically.

- **Sweep Points**: The number of frequency points displayed in the trace. The trace resolution, or the pixel width on the display, is unrelated to the RBW.

7.8.4   Detectors

Digital spectrum analyzers show the measured signal power within discrete frequency bins. This discreteness is artificial, and there may be significant power variation within a single bin [136, 137], especially due to noise. The chosen "detector" option determines which value should be shown on the display for a given frequency bin.

- **Max./Min. peak**: Displays the largest/smallest power value within the frequency bin. The Max. peak detector is useful for measuring upper limits.

- **Auto**: Displays both the max and min peak values simultaneously.

- **Sample**: Displays the power value at the bin edge.

- **RMS**: Displays the root-mean-squared value of all the powers measured within the frequency bin. This detector is especially useful for revealing weak signals buried in the noise.

7.8.5   Measurement Optimization

When measuring very weak, narrowband signals, a number of parameters generally need to be adjusted and optimized. Figure 7.22 shows a sequence of optimizations made on the same signal. Panel (a) shows the input signal peak using the default instrument parameters. To illustrate small signal measurement optimization, 75 dB input attenuation was applied in subsequent panels to hide the signal below the noise floor. This figure then shows how the signal-to-noise ratio is improved with reduced RBW, increased preamp gain, RMS detector, narrower span, reference level and scale adjustment, and finally trace averaging. More details are found in the figure caption. In practice, there are trade-offs when optimizing signal measurements. For example, a smaller RBW provides better resolution, but increases the measurement sweep time.
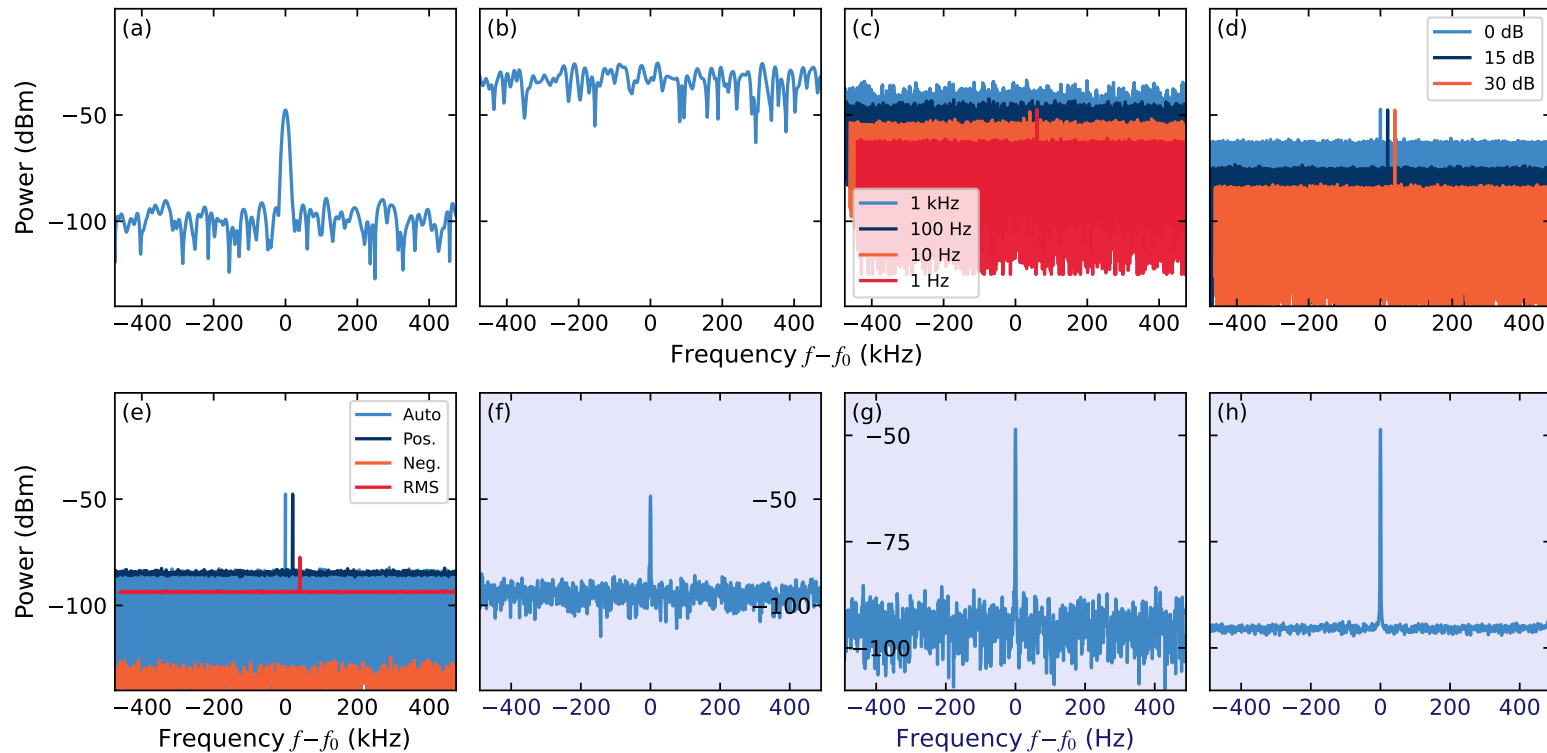
Figure 7.22: Optimization sequence of a small signal measurement on a spectrum analyzer. (a) The input signal spectrum, using the default instrument settings: 0 dB attenuation and preamplifier; 10 kHz RBW; "Auto" detector; 1 MHz span; 0 dBm reference level, and 140 dB vertical scale. (b) An input attenuation of 75 dB raises the noise floor to artificially hide the signal. Subsequent adjustments to other settings will reduce the noise again and reveal the signal peak. (c) The spectra of various RBW settings, offset horizontally by 20 kHz; a 1 Hz RBW is selected. (d) The spectra of various preamplifier gains, offset horizontally by 20 kHz; a 30 dB preamp gain is selected. (e) The spectra of various detectors, offset horizontally by 20 kHz; detector "RMS" is selected. (f) Decreasing the span to 1 kHz. (g) Reducing the reference level to -40 dBm and the vertical scale to 70 dB. (h) Reducing the noise further by trace averaging 64 times. Each sweep takes about 4.2 seconds, meaning the entire average requires almost 4.5 minutes.

7.8.6   Zero-span mode

Up to this point, we have primarily described the spectrum analyzer operating in spectral mode. "Zero-span" is another display mode that is especially useful for time-dependent signals. This mode shows temporal variations of the detected power *at and around* a given frequency. As the name suggests, in this mode, the span is reduced to zero and the IF/local oscillator no longer scans around the center frequency. Instead, the detector averages all frequency components that lie within the RBW. If the RBW is too large, then it will sample and average over too much noise, thereby reducing the signal-to-noise ratio and changing the offset. If the RBW is too small, then it may not capture the temporal dynamics of the signal. To "freeze" the time-varying signal on the display, the spectrum analyzer may be triggered off an external TTL pulse or the time trace itself. In Figure 7.23, we show the same 10 kHz amplitude-modulated signal in spectral and zero span. The zero-span panel reveals the result of various RBW values.

7.8.7   Programming

In typical operation, instrument parameters are manually set from the front panel of the spectrum analyzer; trace data is similarly saved to file. In measurements that involve scanning certain experimental parameters, this process of setting instrument parameters and saving traces becomes very tedious and time-consuming. Fortunately, the parameters and operations of modern spectrum analyzers can be programmed remotely using the Standard Commands for Programmable Instruments (SCPI) protocol. SCPI commands are ASCII strings that are sent to the instrument via a serial port or LAN connection. Every front-panel operation has a corresponding SCPI command, therefore the instrument can be programmed in spectral or zero-span modes.

(a)

(b)
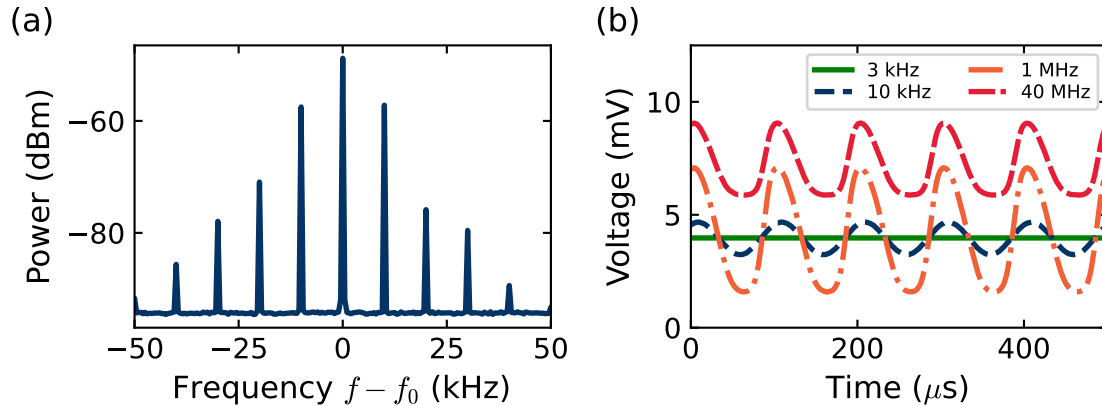
Figure 7.23: Comparing the spectral and zero-span modes of a signal amplitude-modulated at 10 kHz. (a) In spectral mode with an RBW of 20 Hz, adjacent spectral peaks are highly resolved. (b) In zero-span mode, the instrument filters out all frequency components around the carrier that lie outside of the RBW range. For a 3 kHz RBW, only the carrier is measured, and the trace is constant. A 100 μs period oscillation is revealed when the RBW is equal to or greater than the spectral peak separation. For large RBW values, the cumulative noise of a large frequency range raises the zero-span noise floor.

This can automate measurements and greatly accelerate data collection. Further explanations of the programming setup and process are described in Appendix D. Examples of Python scripts are also provided.

Chapter 8

Broad-tunable and multimode microwave-to-optical conversion in a warm atomic vapor

8.1 Introduction

Quantum information processing using solid-state qubits, such as superconducting qubits or spins associated with defects in solid state systems, has shown rapid progress in the field of quantum information technology [138, 139]. The typical operation frequency of these devices is ∼1-10 GHz, in the microwave region of the electromagnetic spectrum. Due to the inherent room-temperature thermal-photon occupation of cables and components at GHz frequencies manifesting as signal noise, practical implementation of scalable and distributed quantum networks at these frequencies poses

140

a formidable challenge [140]. In recent years, progress has been made in addressing coherent conversion of signals from the microwave to optical regimes [34, 141]. At optical frequencies, not only are the thermal noise photons negligible at room temperature, but there exist efficient single-photon detectors and technologies for quantum state storage and reconstruction.

Several physical platforms have been used to coherently convert signals at microwave frequencies to the optical regime. These include electro- and magneto-optical devices [142, 143], opto-mechanical structures, [144] and atoms with suitable internal energy level spacings [145–148]. Impressive progress on improving the efficiency of the conversion process led to efficiency near 80% [147], and the largest conversion bandwidths reported for magnetically-coupled systems are 15 to 16 MHz [148–150], and 100s of MHz for a superconducting resonator/quantum dot system [151]. Along with conversion bandwidth, a transducer that can accommodate several channels of input and output frequencies is advantageous, and tunability over input microwave frequencies across 3 GHz width was recently reported [152]. Yet transducers that operate over multiple optical output frequencies have not been demonstrated to date.

In this chapter, we show that a limited bandwidth input microwave signal can be converted to a large tunable range of output optical frequencies, across 550(30) MHz. This capacity enables information encoded in a narrow-bandwidth microwave field to be mapped to several frequencies in the optical domain, achieving coherent frequency-division multiplexing (FDM). The ability to tune the optical signal output over such a large frequency range arises because of the presence of a large inhomogeneous optical Doppler width for Rb atoms at room temperature. The Doppler width also enables an input multiple-channel microwave idler to be simultaneously and coherently converted to a multiple-channel optical-signal output. In addition, we demonstrate correlated

141
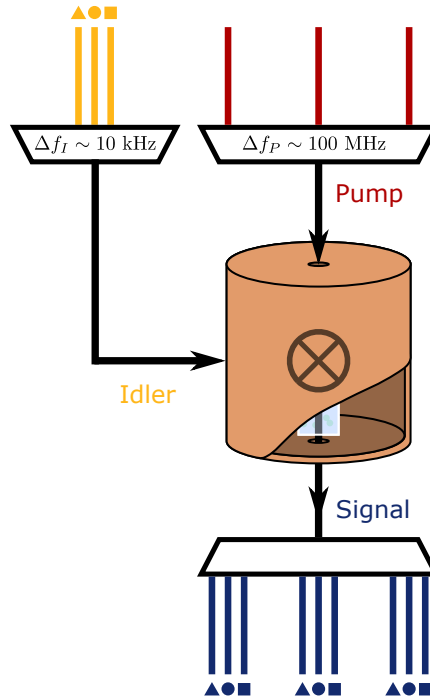
Figure 8.1: Schematic of the atomic frequency-division multiplexing scheme. The microwave cavity-vapor cell system acts analogously to an RF mixer, and information encoded in idler (yellow) channels (▲, ●, ■) is combined coherently with multiple pump (red) channels to produce many output signal (blue) channels over a range of optical frequencies.

amplitude control of the converted multi-channel optical field with the ability to selectively extinguish a desired output frequency channel. This action is very similar to the frequency domain beam-splitting operation for frequency bins, demonstrated using electro-optic modulators (EOMs) and pulse shapers [153].

Coherent frequency-division multiplexing enables qubits encoded in a microwave frequency to be placed in any desired output optical channel within the ~ 500 MHz tunable range. Multiple qubits in different input microwave channels can also be coherently mapped to the optical domain. With a channel linewidth of about 30 Hz, this results in a large channel capacity of about 10^7 channels over the output tunable

range. Thus, neutral atom systems are promising candidates as quantum frequency processor platforms for quantum information encoded in frequency-bin qubits [154].

Microwave-to-optical conversion in a room-temperature ^{87}Rb atomic vapor is possible through the SFG process shown in Figure 6.1, and is analogous to an RF mixer, as illustrated in Figure 8.1. The nonlinear process uses a hybrid, magneto-optical second-order $[\chi^{(2)}]$ susceptibility induced in the vapor by the interaction of three energy levels with an optical pump (electric-dipole transition) and a microwave idler (magnetic-dipole transition) fields. (Isotropic atomic systems with only electric-dipole transitions have a $\chi^{(2)}$ of zero [see Section 5.4].) The idler field with frequency ω_I is supported by the TE$_{011}$ mode of a cylindrical copper microwave cavity [2, 155] [Figure 8.2] and connects the $|b\rangle \equiv |5S_{1/2}, f = 1\rangle$ and $|c\rangle \equiv |5S_{1/2}, f = 2\rangle$ ground state levels. The pump frequency ω_P is chosen anywhere within the Doppler width [Figure 8.9] and connects the $|c\rangle$ and $|a\rangle \equiv |5P_{3/2}, f' = 1, 2\rangle$ levels. We define δ as the detuning of the pump field from the the mid-energy point between the $|f' = 1\rangle$ and $|f' = 2\rangle$ excited levels. In SFG, the pump combines coherently with the idler to generate a new optical signal field at frequency $\omega_S = \omega_P + \omega_I$ [see Section 6.2.2].

8.2   Experimental characterizations & optimizations

In this section, we describe various characterizations and optimizations of the broad-tunable SFG experiment. It builds upon the description of the experimental setup and characterizations found in Chapter 7.

A cut-away rendering of the sum-frequency experiment is shown in Figure 8.2. The copper cylinder supports the microwave idler mode, depicted as yellow surfaces inside the cavity; the magnetic field of the idler mode is polarized and oscillates axially to the cavity [2, 155], along the y-axis. The pump beam, shown in red, enters from
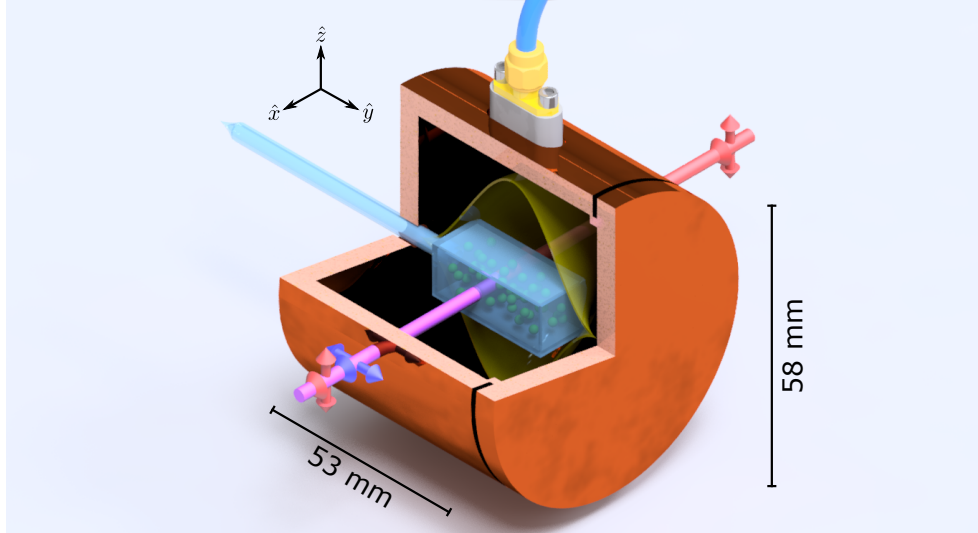
Figure 8.2: Microwave cavity and the generation process. The optical pump beam passes transversely through the cavity and cell and is polarized along the z-axis, parallel to a weak magnetic field (not shown). The cavity's TE_{011} mode (yellow) overlaps with the pump interaction region inside the quartz vapor cell (light blue). The double-headed arrows transverse to the beam direction show the polarization of the pump (red) and signal (blue) beams.

the back through a small hole and propagates through the cavity and internal vapor cell. As shown by the double-headed arrows, the pump beam is polarized along the vertical z-axis. The interaction between the idler field, the pump field, and the atoms generates a signal field that is polarized along the y-axis, shown by the blue double-headed arrow. Since the signal and pump fields are automatically phase-matched, they co-propagate out of the cavity, represented here as a purple beam.

8.2.1   Measurement process

Because the pump and signal beams co-propagate, we must discriminate the power found in each beam. Given that the beams exit orthogonally polarized [156], a natural option might be to use a polarizing beam splitter (PBS) to separate the components, measuring the power in each path. In practice, the signal beam power is 60 dB weaker

than the pump; an excellent PBS obtained from Thorlabs can only provide 34 dB of extinction, assuming, of course, that the beam polarizations are very pure. Nevertheless, the signal beam would still be swamped by residual pump light. Additionally, the maximum power of the signal beam is several hundred picowatts; it is difficult for conventional commercial photodetectors to resolve such small powers.

Instead, to accurately determine the power in both the pump and the signal beams we use an optical heterodyne method. We combine the two beams with a third, strong beam with a nearby, but distinct, frequency. The frequency of this local oscillator (LO) beam is offset from the pump by an AOM shift, $f_{\mathrm{AOM}} = 76.6$ MHz. When all three beams impinge on the photodetector, the detector produces interference beat notes between the pump and LO at $f_{\mathrm{het,P}} = f_{\mathrm{AOM}}$, and between the signal and LO at $f_{\mathrm{het,S}} = \omega_\mu/2\pi + f_{\mathrm{AOM}} = 6.911\ 282$ GHz. These electronic signals are amplified (Mini-Circuits ZJL-7G+) and measured by a spectrum analyzer (Rohde & Schwarz FSV3013).

8.2.2   Fiber coupling and waveplates

The pump-signal beams are fiber-coupled, mixed with the LO in a 50:50 fiber beamsplitter (Thorlabs TN785R5A2), and then measured by a fiber-coupled, high-bandwidth photodetector (EOT ET-4000AF). We use single-mode, polarization-maintaining fibers; these have a specific axis that preferentially transmits the parallel polarization component. Thus the fibers also act like polarizing-filtering elements. When the light's linear polarization angle is not precisely aligned with the fiber axis, the polarization inside the fiber fluctuates due to temperature gradients and mechanical movement/vibration of the fiber. Therefore, we place a multi-order half-waveplate (HWP) and a quarter-waveplate (QWP) between the cavity and the output fiber coupler and select waveplate angles that align the pump and signal beams to the fiber axis,

thus optimizing their respective beat signal amplitudes. Since the two beams are or-
thogonally polarized, the HWP angles that produce optimal beat interference are 45
degrees apart and must be manually alternated between measurements of each beam.
The need to always adjust the waveplates prevents us from faithfully measuring the
pump's and signal's beat note amplitudes in a single shot.

There is also a set of HWP and QWP before the LO beam injection fiber coupler.
The beat amplitudes also depend on the LO polarization, and all the polarizations
must match for good interference. If the LO polarization is not aligned to the fiber
axis, we observe additional, long-term fluctuations in the beat amplitudes, as large
as 10-12 dB.

8.2.3   Generated signal & linewidth
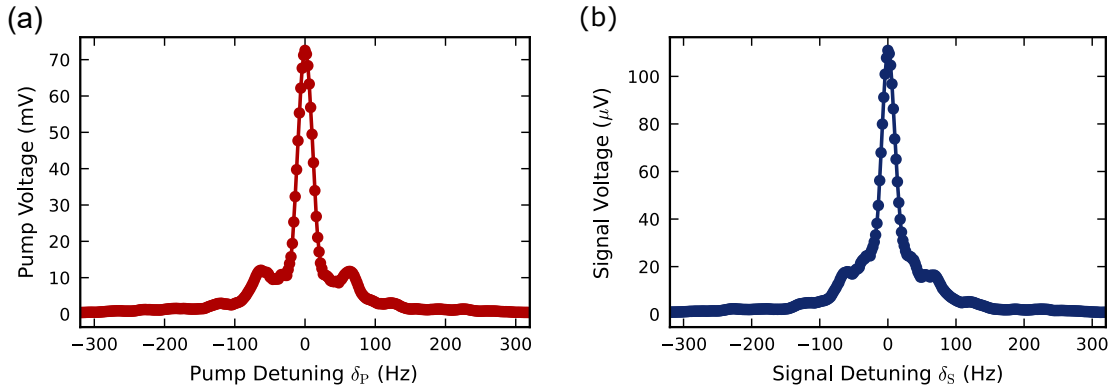
Figure 8.3: Close-up heterodyne spectra of the unmodulated (b) LO-Pump line at
$f_{\mathrm{het,P}}$ and the (b) LO-Signal generated line at $f_{\mathrm{het,S}}$, revealing a FWHM of 26(2) Hz
for both lines.

Next, we consider characteristics of the light generated on the $|a\rangle \rightarrow |b\rangle$ transition.
We see in measurements of the beat signal at $f_{\mathrm{het,S}}$ that the SFG peak has a FWHM
of 26(2) Hz, as shown in Figure 8.3(b). This peak was initially indiscernible on the
spectrum analyzer until we used a very fine RBW of ≤ 20 Hz. The narrowness of

the line suggests that this nonlinear generation process is phase coherent; fluctuations in a signal's phase disrupt its temporal coherence and lead to a broader spectral linewidth. Energy conservation also requires that the linewidth of the generated light is determined by the narrowest of the input field linewidths, which, in our case, is the microwave idler field, with a FWHM of < 2 Hz. The presence of additional perturbations broadens or modulates the generated signal. The width of the signal is influenced by 60 Hz modulations from the electrical heating elements, noise from the AOM drivers' oscillators and amplifiers, and the inherent linewidth of the laser. The beat note peak at $f_{\text{het,P}}$ has a FWHM identical to that of the signal peak [Figure 8.3(a)]. This linewidth cannot be taken as the intrinsic laser linewidth, which is likely closer to ~ 100 kHz. Rather, this result demonstrates that this experiment occurs within the coherence length of the laser beam. Residual phase noise in the generated process is similar, but somewhat less than the initial pump light itself.

The generated peak measured on the spectrum analyzer has a typical optimized power of -70 dBm, significantly weaker than the -10 dBm pump peak power. To ensure that the generated signal is indeed coming from the atoms, we look for a generated signal when the pump laser frequency is far-detuned from the atomic Doppler resonance: the LO signal is present, but the generated signal is absent.

8.2.4   Magnetic field direction & amplitude

As explained in Section 7.4, orthogonal Helmholtz coils null the external magnetic field along the x and y-axes, and provide a weak DC magnetic field $\vec{B}_z$ along the z-axis. The magnetic field strength makes a striking impact on the conversion efficiency. As shown in Figure 8.4, conversion is strongly suppressed (by > 30 dB) at zero magnetic field and reaches maxima at approximately ± 200 mG. This behavior is well-described by a symmetric, generalized Fano lineshape [157] that has the simplified form
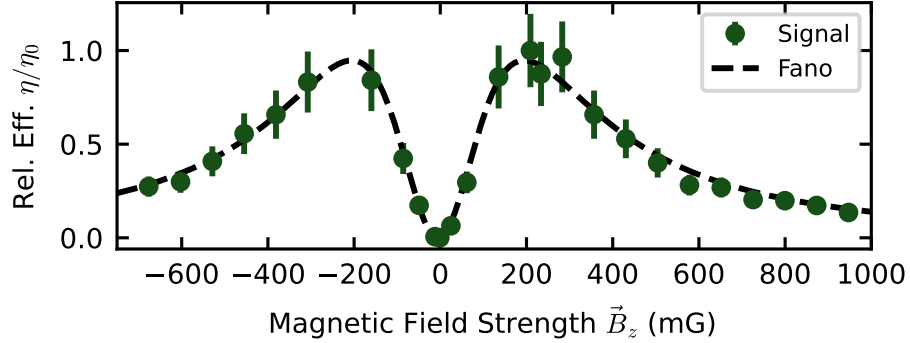
Figure 8.4: The generated signal's response to a variable magnetic field strength $\vec{B}_z$ along the z-axis. We operate at 209 mG for maximum generation. We fit a symmetric Fano profile [Equation (8.1)] to these data, with fit parameters $\eta_0' = 0.95(2)$, $\gamma_B = 200(4)$ mG and $B_0 = -5(3)$ mG. This behavior might indicate the interaction and interference of multiple Zeeman level resonances within the atomic decoherence width. Error bars represent the standard deviation.

$$\eta(B_z) = \eta_0' \left[\frac{2\gamma_B(B_z - B_0)}{\gamma_B^2 + (B_z - B_0)^2} \right]^2. \tag{8.1}$$

This expression generically represents the response of three coupled, resonant oscillators with slightly different decoherence rates [157]. We determine the fit parameter $\gamma_B = 200(4)$ mG, and observe that $\gamma_B \times \gamma_g = 140$ kHz $\sim \gamma_I \ 2\pi$, the ground state decoherence rate, recalling that γ_g is the ground state gyromagnetic ratio of ^{87}Rb [50].

The magnetic field dependence points to the participation and interaction of multiple Zeeman levels in the generation process. At Zeeman degeneracy (i.e. zero magnetic field), generation pathways may destructively interfere. The possibility of multiple interfering paths is particularly interesting. We believe these effects could be better understood by extending the theoretical model to include additional levels with appropriate transition strengths, which will be the subject of future work [see Section 10.2.5].

8.2.5 Conversion bandwidth

We characterize the conversion bandwidth of the microwave-to-optical conversion process, defined as the range of input idler frequencies that can be converted to signal photons. To determine this, we operature a vector network analyzer (VNA, Keysight E5063A) in S_{21} mode at the idler frequency: the VNA drives the microwave cavity from Port 1 and detects the amplified photodetector beat signal from the combined pump and signal light on Port 2. In this configuration, the LO beam does not play a role. To see a discernible signal on the VNA, the IF bandwidth was reduced to 20 Hz, similar to the RBW values used for the spectrum analyzer. We also added a second amplifier following the photodetector. The VNA scanned over a 10 MHz span around the idler frequency and averaged the trace over many samples.

No generation is apparent when the laser is off resonance. When the laser is locked on resonance and the background magnetic field is fixed at the optimal value of 209 mG along the z-direction, a peak in the S_{21} signal is visible with FWHM of 910(20) kHz, as shown in Figure 8.5(a). These data also reveal two barely-resolved side peaks. We fit to these data a model of three superimposed Gaussians, with a common separation and width. The fit results give a FWHM of each single-Gaussian subpeak as 478(1) kHz, which is comparable to the $\kappa_{\mathrm{tot}}/h = 417$ kHz width of the cavity resonance, suggesting that the microwave cavity's linewidth limits the conversion bandwidth of the generation process.

We also examine how the conversion bandwidth varies as a function of applied magnetic field, as shown in Figure 8.5(b). As the magnetic field increases, the sidelobes separate from the main peak, while the overall amplitude of the peaks decreases. In the higher-field case, generation is still discernible at idler frequencies far outside of the cavity linewidth. The splitting has similarities to a Zeeman interaction. However,
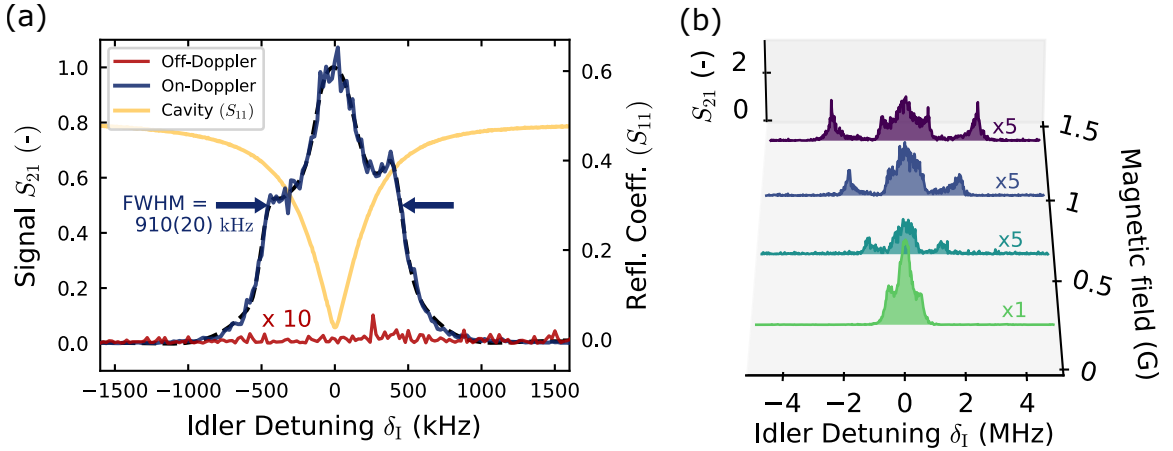
149

(a)

(b)

Figure 8.5: (a) The raw SFG signal during a scan of δ_I, as driven and measured with a vector network analyzer in S_{21} mode. We measure a conversion bandwidth (FWHM) of 910(20) kHz when the laser is locked on-resonance and with an optimal z-magnetic field of 209 mG. The dashed line is a smoothing spline used to determine the bandwidth. No generation is visible when the laser is off-resonance (red trace). The cavity resonance (yellow trace), as measured with the VNA in S_{11} mode, has a FWHM of 417 kHz. (b) The same SFG trace as in (a), but for various z-magnetic fields: $\{0.238, 0.652, 1.021, 1.390\}$ G. The generated line splits and decreases in amplitude as the magnetic field strength increases.

it does not match those expected by the ^{87}Rb Larmor frequencies: the measured peak separation varies with magnetic field as $2.7\gamma_g B$. This effect is interesting, warranting further theoretical and experimental investigation.

8.2.6   Idler and pump power

We characterize the effects of pump and idler intensities on the generation efficiency, as shown in Figures 8.6(a) and (b). These data can be compared to Figure 5(b) in [146], where the generated signal power increases linearly with the pump power before eventually saturating. We assume that the idler power coupled to the cavity is evenly distributed over the cell cross-section area. As a function of this idler intensity, the generated *power* increases linearly, then saturates, exactly as in Figure 5(a) of [146]. Figure 8.6(b) shows the *efficiency* exponentially decrease, since the idler power

150

appears in the denominator of the conversion efficiency expression [see Equation 8.3; also see Section 8.4 for more details on the conversion efficiency calculation].

Due to the limited dynamic range of the power stabilization control loop, we typically operate with a pump power near 76 μW, well below 500 μW to avoid photorefractive damage to the EOM. The 3 mm diameter pump beam gives an intensity of $\sim$ 3 mW/cm^2, near the ^{87}Rb saturation intensity [50]. We do not explore as large a range in the pump intensity as in [146] (referred to as "coupling intensity" in that reference); our data lies in the linear regime, far away from its saturation. Working without the EOM, or with a free-space device, together with an improved power servo loop, would permit exploration of a larger parameter space.
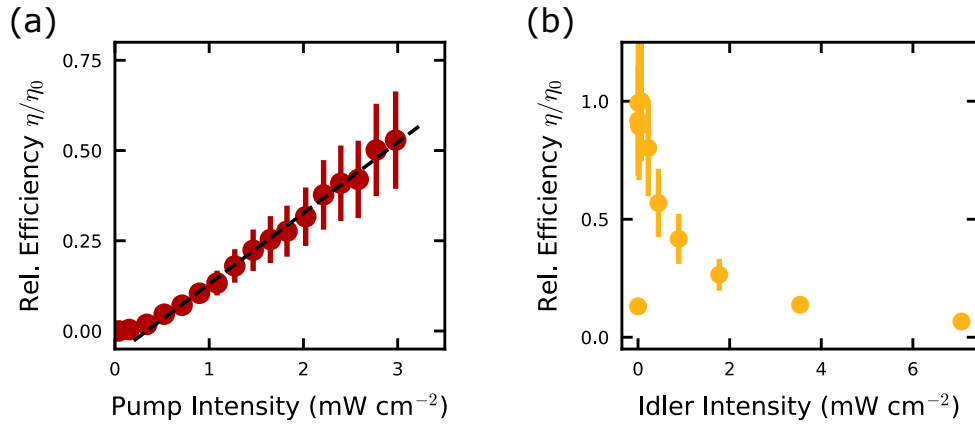
Figure 8.6: (a) The generated signal conversion efficiency responds roughly linearly to increased pump optical intensity in the regime below and near the saturation intensity [see Section 4.3.1]. (b) The generated signal conversion efficiency response for various idler intensities, as supplied from SG1. Error bars represent the standard deviation. The largest pump and idler powers measured correspond to intensities of about 3 & 7 mW/cm^2.

8.2.7   Cavity temperature

We also characterize the SFG process at various cavity temperatures. These measurements were taken over several days using a previous oven formed from a layer of aluminum foil. The temperature was measured by a thermocouple placed inside the oven, adhered to the top of the microwave cavity with Kapton tape. We find that the efficiency depends weakly on temperature, as shown in Figure 8.7. In Section 7.7.3, we observe that the atomic density (obtained from the optical depth measurements) is very low and independent of temperature. This result is due to the vapor cell's stem that is water-cooled to a constant 16°C.

The weakness of this measurement is our ignorance of the temperature of the glass cell walls *inside* the cavity. Despite waiting several hours between subsequent measurements for good thermalization, the aluminum-foil oven had large openings around the endcap; these gaps may have produced large temperature gradients across the cavity.
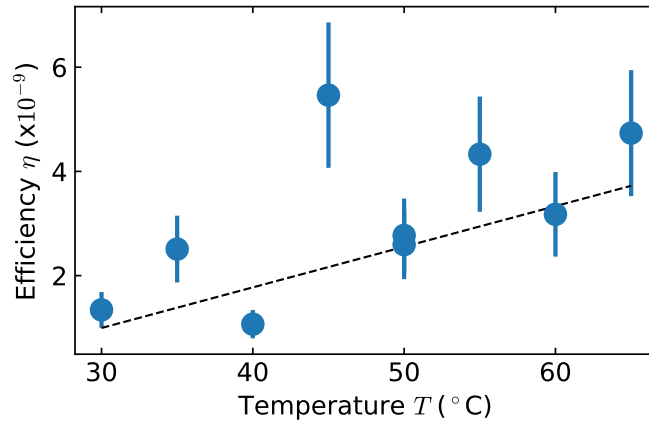

Figure 8.7: Generation efficiency responds only weakly as a function of cavity temperature. The dashed line is a linear fit to the data. We did not observe strong increase in the SFG efficiency, which we attribute to the cold, fixed-temperature vapor cell stem.

8.2.8 Pump frequency scan

In addition to scanning the idler frequency as in Section 8.2.5, a key part of this experiment involves scanning the pump frequency. A controlled variation of this frequency allows us to sample the generation process across many different velocity classes of the Doppler profile. Our primary approach was to unlock the pump laser and scan its frequency. Because this process scans both the pump and LO frequencies concurrently, the interference beat note frequencies are stationary. To observe temporal variations in the SFG signal, we measure the generated peak on the spectrum analyzer in zero-span mode, synchronizing the spectrum analyzer with the sweep trigger from the laser controller. To reduce distortion in the measured signal, we reduced the laser sweep rate to about 18 Hz, and increased the RBW of the laser controller to 2 kHz. Using these settings, we sample the entire Doppler profile in a single sweep, with high frequency resolution. As expected, the generation efficiency is proportional to the velocity class occupation density and follows a roughly Gaussian profile, as shown in Figure 8.8(b).

A 50:50 beamsplitter placed immediately before the cavity divides the pump beam into two. The reflected beam passes through a separate rubidium vapor cell at ambient $21.6(3)°C$, and we detect the transmission through this reference cell on a photodiode, as seen in Figure 8.8(a). Although there are laser power/polarization variations through the sweep, they are relatively small compared to the depth of the Doppler profiles. We compare this transmission signal to a rubidium transmission model [75, 158] to calibrate the sweep detuning rate: 17.24(1) MHz/ms. The uncertainty in absolute frequency is relatively large; however, many of the final results are frequency ranges, and systematic uncertainties generally cancel out.
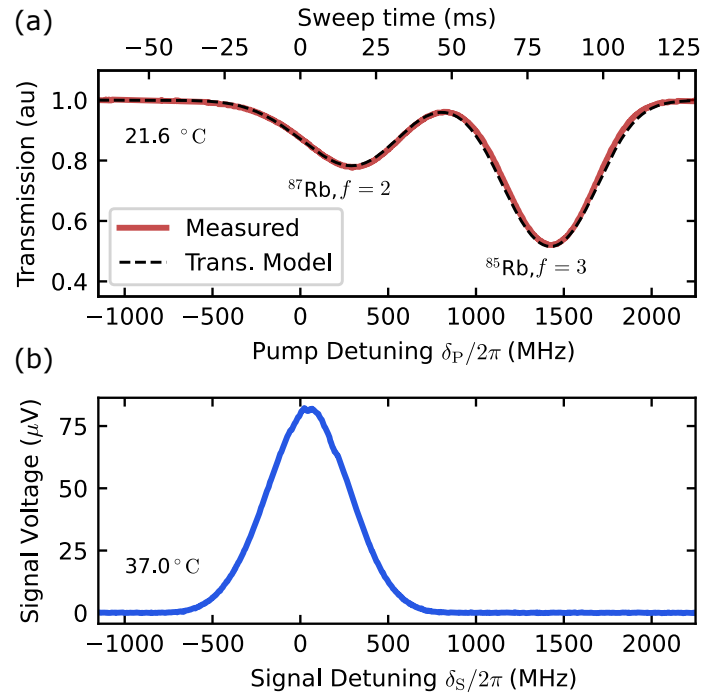
Figure 8.8: Scanning the pump laser frequency across the Doppler background. (a) The Doppler-broadened transmission spectrum of a room-temperature rubidium reference vapor cell (outside the microwave cavity), recorded on an oscilloscope while sweeping the pump laser frequency. The dotted line shows a transmission model curve with good agreement to the measured trace. The laser sweep is assumed to be linear, with the positions of the two Doppler peaks calibrating the horizontal frequency scale, where zero frequency is taken as the midpoint between the $f' = 1\&2$ levels. (b) The generated signal measured on the spectrum analyzer in zero-span mode. This trace was taken simultaneously with (a).

8.3 Spin decoherence estimates

In this work, we group all decoherence effects—including transit-time decoherence Γ_T, spin-exchange collision Γ_{SE}, and wall depolarization Γ_{wall}—into a single decoherence rate $\gamma_{\mathrm{I}} = \Gamma_T + \Gamma_{\mathrm{SE}} + \Gamma_{\mathrm{wall}}$, which we estimate from double-resonance measurements to be $\gamma_{\mathrm{I}}/2\pi \simeq 130(30)$ kHz. As seen in the denominator of Equation 6.17, the strength of the generated signal is suppressed by a factor of γ_{I}, implying that greater efficiency is possible by reducing decoherence.

The individual decoherence components are estimated for room temperature: the transit-time decoherence rate is $\Gamma_T/2\pi \sim u/4\pi r_{\mathrm{eff}}$ for a uniform beam profile [69] [see also Section 4.3.1 for a Gaussian profile estimate], where the most probable thermal velocity $u \simeq 240$ m/s and the effective beam radius $r_{\mathrm{eff}} = 0.85$ mm, giving $\Gamma_T/2\pi \simeq 20$ kHz. Next, the spin-exchange collision rate is $\Gamma_{\mathrm{SE}}/2\pi = \mathcal{N} u \sigma_{\mathrm{SE}}^{(\mathrm{Rb-Rb})}$ [see Section 4.3.2], where $\mathcal{N}$ is the atomic density and $\sigma_{\mathrm{SE}}^{(\mathrm{Rb-Rb})} = 1.9 \times 10^{-14}$ cm^2 is the spin-exchange cross-section between two rubidium atoms [77], giving $\Gamma_{\mathrm{SE}}/2\pi \simeq$ 100 Hz. This value is relatively small, implying that the atoms have a mean free path of $\lambda_{\mathrm{mfp}} = 1/\mathcal{N}\sigma_{\mathrm{SE}}^{(\mathrm{Rb-Rb})} \simeq 2$ m before experiencing a spin-flip collision with another atom. This distance is much larger than any cell dimension, implying that the atoms are mostly ballistic, with wall collisions dominating decoherence. With the average distance between wall collisions

$$\varrho = \mathcal{V}/\mathcal{S} \simeq 3 \text{ cm}^3/14 \text{ cm}^2 \simeq 0.2 \text{ cm}, \tag{8.2}$$

the average wall collision rate is $\Gamma_{\mathrm{wall}}/2\pi \simeq 120$ kHz [see Section 4.3.2].

In evaluating ways to reduce decoherence, consider, for example, adding 5 torr of neon buffer gas and a high-quality, alkene anti-relaxation wall coating to the vapor cell. The rubidium atoms in the buffer gas have a mean free path of $\sim 100~\mu$m, putting

them in a diffusive regime. Wall effects are effectively eliminated by the coating and the slower atomic diffusion. The spin-exchange and relaxation cross sections between the rubidium and the neon are much smaller, $\sigma_{\mathrm{SE}}^{\mathrm{(Rb-Ne)}} \sim 10^{-23}$ cm^2 [159], and do not contribute significantly. However, without entering the SERF regime, it is impossible to eliminate the rubidium-rubidium spin-exchange collisions [69]. For an equivalent atomic density, this effect will dominate $\gamma_{\mathrm{I}}/2\pi$, with an ultimate value of ~ 100 Hz.

8.4   Conversion efficiency

The microwave-to-optical conversion efficiency is defined as the ratio of the SFG photon production rate to the rate of available microwave photons in the cavity mode [145, 146]

$$\eta \equiv \frac{P_{\mathrm{S}}/\hbar\omega_{\mathrm{S}}}{P_{\mathrm{I}}/\hbar\omega_{\mathrm{I}}}. \tag{8.3}$$

P_{S} is the power of the generated signal light, and P_{I} is the power of the idler field involved in the transition. This expression is valid for the continuous (CW) fields employed. Here, we derive an expression for the efficiency in terms of experimental parameters.

The generated optical power P_{S} is weaker than the residual pump optical power P_{P} by a factor determined by the relative amplitudes of the two heterodyne peaks $P_{\mathrm{het,P}}$ and $P_{\mathrm{het,S}}$ measured (in dBm) on the spectrum analyzer:

$$P_{\mathrm{S}} = P_{\mathrm{P}} \, 10^{\left(P_{\mathrm{het,S}} - P_{\mathrm{het,P}} + \zeta\right)/10}. \tag{8.4}$$

The correction term ζ accounts for any differential response of the photodetector and amplifier between the two heterodyne frequencies. The detector should have a fairly flat frequency response, but, in practice, there is some dependence. Failure to

account for these factors would make the efficiency appear smaller than it really is. We characterize a 3.6(3) dB differential detector response by measuring the amplitude of the beating note signal of the LO light (locked laser) mixed with light from a separate tunable diode laser. The amplifier also responds stronger at $f_{\text{het,P}}$ compared to $f_{\text{het,S}}$ by 4.3(7) dB. We measure the insertion loss of the isolated amplifier and coaxial cable with the VNA in S_{21} mode, giving a total correction of $\zeta = 7.9(8)$ dB.

To estimate the available microwave photon rate, we first determine the fraction of the supplied source power P_{cav}/P_0 that is coupled into the cavity, residing there in steady-state. With a S_{21} measurement of the microwave coaxial cable, we measure its insertion loss $IL = 2.928(3)$ dB. The cavity absorbs $\Delta RL = 23$ dB beyond this (from an S_{11} measurement of the cavity), meaning that all but 0.5% of the power delivered to the end of the coaxial cable is transmitted to the cavity. In total, the expression for the coupled power fraction is

$$P_{\text{cav}}/P_0 = 10^{-IL/10} - 10^{-\Delta RL/10}. \tag{8.5}$$

Now P_{cav} is scaled by the ratio of the interaction to magnetic mode volumes. This scaling gives the fraction of the microwave power that transitions the atoms between the two ground states. Therefore, the microwave power involved in the conversion is

$$P_{\text{I}} = P_0 \frac{V_{\text{int}}}{V_{\text{m}}} \left(10^{-IL/10} - 10^{-\Delta RL/10}\right) \tag{8.6}$$

A critical difference between this efficiency calculation and the previous work [146] is that those authors divided by V_{cav} instead of the more accurate V_{m} [34]. Were we to calculate in their terms, the efficiency values would increase by a factor of about 14.

Finally, we calculate the efficiency by inserting Equations 8.4 and 8.6 into Equa-

tion 8.3 to get

$$\eta = \frac{P_{\mathrm{P}}}{P_0} \frac{V_{\mathrm{m}}}{V_{\mathrm{int}}} \frac{\omega_{\mathrm{I}}}{\omega_{\mathrm{S}}} \frac{10^{\left(P_{\mathrm{het,S}} - P_{\mathrm{het,P}} + \zeta\right)/10}}{\left(10^{-IL/10} - 10^{-\Delta RL/10}\right)}.$$

(8.7)

For typical experimental parameters, we determine a maximum conversion efficiency of $\eta_0 = 1.5(1) \times 10^{-9}$. Efficiency in our system is primarily limited by a very low optical depth of $0.05(1)$. In comparison, cold-atom conversion experiments have employed optical depths of up to 15 [145] and 120 [147]. The measured optical depth corresponds to a number density of about 4×10^{16} cm^{-3}, with $8.7(1) \times 10^8$ atoms in the interaction region. This atom number is $\sim 10^9$ times lower than the $3.2(1) \times 10^{18}$ available microwave photons in the same volume. At room temperature, the thermal noise is at the level of 900 photons, which is negligible compared to the signals used here. We note that it is this noise, determined by the temperature of the microwave electronics and transmission components (rather than of the conversion medium), that sets the limit of low-photon-number operation. Moving toward true quantum transduction requires reducing the noise in these components by operating them at cryogenic temperatures [160]. The maximum temperature required to enter the thermal microwave photon ground state is approximately $T \simeq \Delta E_{\mathrm{HF}}/k_{\mathrm{B}} = 0.33$ K.

Increasing the number of atoms would certainly increase the conversion efficiency. This fact can be seen by estimating the microwave cavity-atom cooperativity C, or the ratio of the atom-cavity coupling to their respective losses. It is defined as [161, 162]

$$C = \frac{N g_0^2}{\kappa_{\mathrm{tot}} \gamma_{\mathrm{I}}},$$

(8.8)

where g_0 is the single-atom-photon coupling strength/single-photon Rabi frequency, κ_{tot} is the cavity decay rate, and γ_{I} is the atomic decay/decoherence rate. We estimate that we have about $N \sim 10^9$ atoms inside the interaction region. To determine g_0, we start by calculating the magnetic field amplitude produced by a single idler photon

inside the cavity [161],

$$B_{\mathrm{I}}^0 = \sqrt{\frac{\mu_0 \hbar \omega_{\mathrm{I}}}{2V_{\mathrm{m}}}}, \tag{8.9}$$

where V_{m} is the cavity mode volume. The corresponding single-photon Rabi frequency is:

$$g_0 = \boldsymbol{\mu}_{cb} \mu_B B_{\mathrm{I}}^0, \tag{8.10}$$

where μ_B is the Bohr magneton, and $\boldsymbol{\mu}_{cb}$ is the transition matrix element [see Section 3.2.1]. For the $|1,1\rangle \to |2,2\rangle$ transition, this evaluates to $g_0 = 0.0190$ Hz. The estimated cooperativity is then:

$$C \sim \frac{10^9 \ (0.0190 \ \mathrm{Hz})^2}{(417 \ \mathrm{kHz})(130 \ \mathrm{kHz})} = 6.7 \times 10^{-6} \tag{8.11}$$

This cooperativity is almost four orders of magnitude larger than the 10^{-9} ratio of atoms to available microwave photons in the interaction region. This fact suggests that increasing the atom number 10^4 times would proportionally increase the efficiency; also that the cooperativity would increase if we used a buffer gas to reduce the atomic decoherence rate γ_{I}.

In principle, increasing the cavity temperature, and hence the optical depth, is experimentally straightforward. However, during this chapter's data collection, we were still using the former aluminum foil oven [see Section 7.7.4]. The large gaps in the foil enclosure prevented us from accurately reaching high cavity temperatures (i.e. $T \gtrsim 60°$C); with low temperatures came the requirement to water-cool the cell stem [see Section 7.7.2], thus restricting the atomic density. Follow-up measurements should be undertaken using the improved oven without the stem cooling.

8.5 Results

The following sections will describe and present the results of three different experiments undertaken using the nonlinear SFG process described theoretically in Chapter 6 and characterized in Section 8.2. They will establish the frequency tunability and amplitude control of generated light.
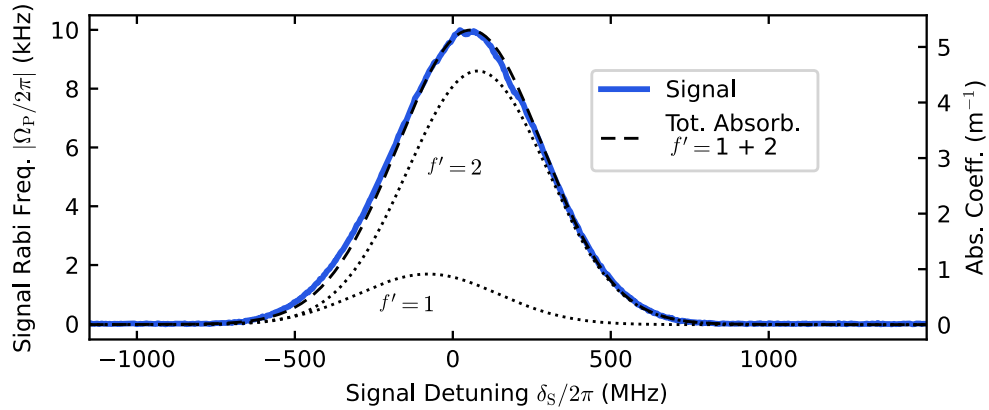
8.5.1 Broad-tunability

Figure 8.9: The generated signal measured with the spectrum analyzer in zero-span mode, showing a FWHM of 550(25) MHz The dashed curve shows the calculated Doppler-broadened absorption coefficient of the pump light; the individual components due to the $f' = 1$ and $f' = 2$ excited hyperfine levels are shown as dotted curves. The SFG signal data is proportional to the MB absorption distribution of the pump transitions without any fitting or free parameters.

In microwave-to-optical conversion, tunability of the input and output frequencies is a desirable feature. In the emerging subject of quantum networks, quantum devices operating at a variety of frequencies may be interconnected for quantum information transmission, storage, and processing. Flexibility in the input and output frequencies allows interconnection between different types of devices, as well as accommodates manufacturing differences. In Section 8.2.5, we characterized the conversion band-

width of the system: the input idler frequency tunability for coherent transduction to optical. In this section, we consider the *output* frequency tunability, i.e. for a fixed input idler frequency, what are the possible output optical frequencies, or optical channels, that it can be transduced into? In this SFG scenario, the output frequency tunability is controlled by the frequency of the pump laser.

To probe this behavior, we scan the pump laser frequency across the Doppler width as described above. At any instant during the scan, the pump field interacts with one velocity class of atoms, which "see" this frequency on-resonance with the pump transition. As described in Sections 6.2, the atoms in this velocity class will dominate the generation process at that moment. The generated signal follows a roughly Gaussian profile throughout the sweep, as shown in Figure 8.9. The generated signal reaches a maximum amplitude between the $f = 2 \rightarrow f' = 1$ and $f' = 2$ transitions, with a full width at half maximum (FWHM) of 550(25) MHz. This generated profile is almost exactly proportional to the combined Doppler-dependent absorption coefficients for the $f = 1 \rightarrow f' = 1$, 2 transitions, which together have a FWHM of 540 MHz. The $f' = 3$ state does not participate in this nonlinear process, since selection rules prohibit an electric-dipole transition to the $f = 1$ ground state. Similarly, the pump transition from $f = 2 \rightarrow f' = 0$ is electric-dipole forbidden. These absorption coefficient curves are independently calculated, and do not represent a fit to the data.

8.5.2   Multichannel

The ability to convert microwaves into various frequency channels, or into multiple channels simultaneously, may be useful for the purposes of frequency(/wavelength) division multiplexing—a scheme employed in optical telecommunications. In this section, we explore the multi-channel potential of the conversion process. We consider
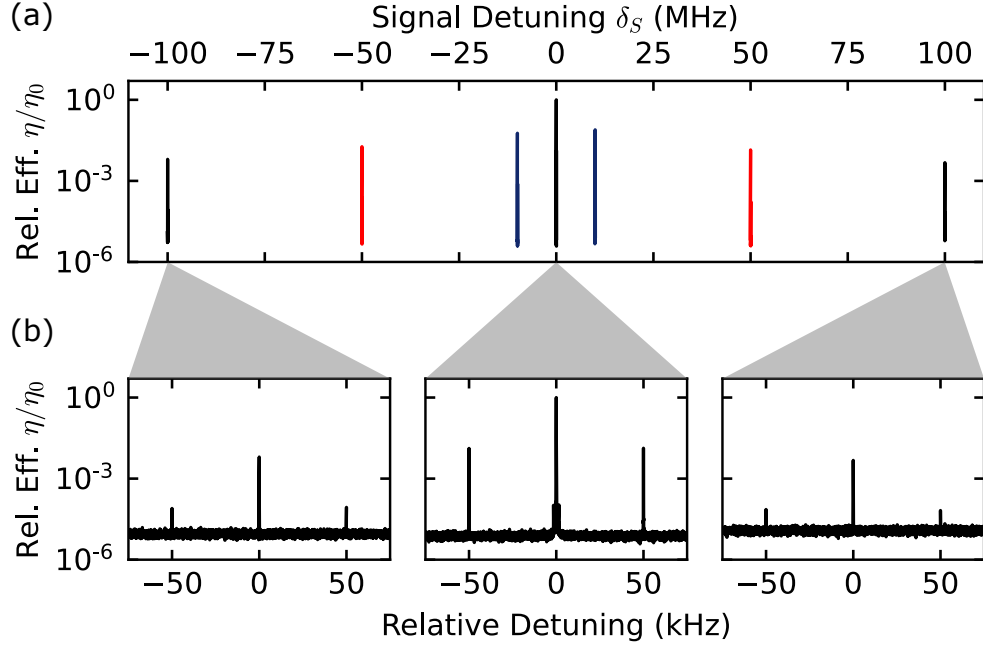
Figure 8.10: (a) Multichannel generation using a fixed microwave amplitude modulation frequency of $\omega_{\mathrm{AM}}/2\pi = 50$ kHz and a variable pump phase modulation frequency $\omega_{\mathrm{PM}}/2\pi$ of 10 (blue), 50 (red) and 100 (black) MHz. The relative sideband amplitude decreases for increased ω_{PM} because the pump light accesses velocity classes with decreased occupation. (b) Zoomed-in data revealing AM sidebands flanking each of the central and SB EOM peaks.

the effects of multiple input idler and multiple input pump frequencies interacting and combining in the nonlinear atomic medium.

For this measurement, the pump laser is tuned and locked halfway between the $f = 2 \rightarrow f' = 2$ & 3 transitions. We generate a multichannel optical signal field in two different ways: First, the signal generator supplying the idler field (SG1, AnaPico APSIN12G) is amplitude-modulated at a variable ω_{AM}; the idler carrier and sidebands combine with the pump to produce peaks in the signal spectrum at $\{\omega_{\mathrm{S}}, \omega_S \pm \omega_{\mathrm{AM}}\}$. Due to the finite microwave cavity resonance, $\omega_{\mathrm{AM}}/2\pi$ can be tuned up to 455(10)

kHz before the sidebands become significantly suppressed. The amplitudes of the signal sidebands depend on the idler modulation depth m.

Second, we modulate the pump light by using a fiber electro-optic phase-modulator (EOSPACE PM-0S5-20-PFA-PFA-780) inserted into the pump light optical path. We drive the EOM with a second signal generator (SG2, SRS SG384) at a variable ω_{PM}. This produces sidebands in the pump optical spectrum, and corresponding sidebands in the generated spectrum at $\{\omega_{\mathrm{S}}, \omega_S \pm \omega_{\mathrm{PM}}, , \omega_S \pm 2\omega_{\mathrm{PM}}, \dots\}$. For a fixed modulation index β, the MB width and density determine the bandwidth and amplitudes of the pump-modulated generated sidebands.

Both types of sideband generation, idler AM and pump PM, are simultaneously illustrated in Figure 8.10. In the three cases depicted, $\omega_{\mathrm{AM}}/2\pi = 50$ kHz is fixed with $m = 0.25$, and $\omega_{\mathrm{PM}}/2\pi$ is varied from 10 MHz to 100 MHz with $\beta = 1.65$ rad. The spectrum analyzer and SG2 are both phase-locked to the internal 10 MHz clock reference of SG1. These data show that we can coherently transduce multiple input idler frequencies to multiple output signal frequencies, even simultaneously. The tunability of the pump frequency permits wider frequency access.

8.5.3   Coherent sideband control

We have shown remarkable tunability and control of the generated optical frequencies. We will briefly describe here an additional method for coherently manipulating the amplitudes of generated sidebands.

When the pump and idler are modulated at the same frequency, $\omega_{\mathrm{PM}} = \omega_{\mathrm{AM}} \equiv \Delta_m$, then we have the scenario described and calculated in Section 6.3.2: Multiple idler-pump sideband combinations produce overlapping and interfering signal frequency peaks [see also Figure 6.3(b)]. By tuning the relative phase of the modulating waves, one sideband or the other is constructively enhanced or destructively eliminated. The

modulation depth ($m = 0.075$) and index ($\beta = 0.041$ rad) are empirically chosen to optimize this interference. These variations are recorded by the spectrum analyzer at each of the signal sideband frequencies in zero-span mode. As in the other experiments, it is especially important here that the spectrum analyzer and modulation sources are reference locked to a common 10 MHz clock source. We measure a relative visibility of 97% [Figure 8.11(b)] for the upper and lower sidebands, in good agreement with the calculated variation shown in Figure 6.3(c). The two SB amplitude have a phase offset of 2.76 radians. The difference of the phase offset from π is not a function of magnetic field, pump power, or polarization and requires further investigation.
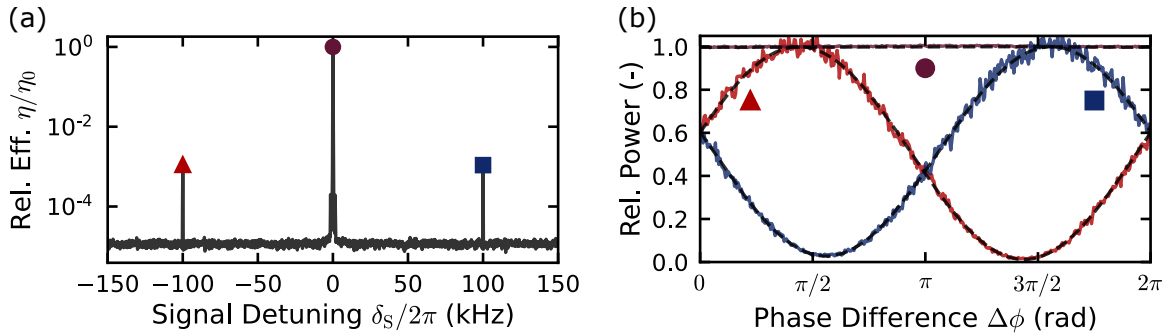

Figure 8.11: When the two modulation frequencies are equal, i.e. $\omega_{\mathrm{PM}} = \omega_{\mathrm{AM}}$, the EOM and AM sidebands overlap and interfere. The relative phase difference $\Delta\phi$ between the modulating waves controls the height of the two correlated generated sidebands. (a) The generated spectrum at zero relative phase. (b) The power amplitude response of the peaks have a relative visibility of 97%, while the central peak is independent of the relative phase. The two SB amplitude curves are offset from each other by ($\pi - 0.38$) radians of phase. The dashed lines show independent fits to a cosine.

This phase control of the sideband amplitudes makes the generation process akin to a tunable frequency beam splitter [123, 153, 163]. We'll point out that this tunability comes at the summed frequency. When the phase is chosen to eliminate one of the sidebands, this is equivalent to a single-sideband modulator [164].

8.6 Discussion

The frequency tunability of the generated signal field results from the existence of a large Doppler width at room temperature. While this work uses a warm vapor cell of enriched ^{87}Rb without an anti-relaxation coating or a buffer gas, a buffer gas would provide additional tunability due to collisional broadening [165–167]. This tunability may be limited to the order of the ground-state hyperfine splitting of the atoms used.

Although other conversion schemes display degrees of tunability of the output frequency [145, 147, 150, 152], these are often restricted by natural atomic or optical cavity resonance frequencies. In the warm-atom system, continuous tunability over the entire Doppler width is possible. While Doppler effects are often undesirable and eliminated through laser cooling techniques, ironically in this conversion system, they are a resource. This frequency multiplexing capability enables multiple microwave sources to be interfaced with a single atomic transducer, and the conversion can be used to place differing sources in distinct optical frequency domains. Switching between different optical frequencies for a single source is also possible. This scheme features a conversion bandwidth of 910(20) kHz [see Figure 8.5(a)], which is primarily limited by the cavity linewidth. As previously demonstrated in a different context [168], the reverse optical-to-microwave conversion process is achievable in an atomic three-wave mixing system.

The high-contrast amplitude control of signal sidebands, enabled by simultaneous pump and idler modulation [Figure 8.10], is equivalent to a tunable beam-splitter operating in the frequency domain [153]. The modulation indices and the relative phase act together as reflection and transmission coefficients. For particular values of these coefficients, we can selectively generate a chosen sideband channel in the

optical domain while completely suppressing the other, resulting in single-sideband conversion.

Thus, this neutral atom system is capable of performing as a "quantum frequency processor" [154, 169, 170] with particularly low input-field intensities. This allows us not only to encode and manipulate information in multiplexed frequency bins but also to convert it from microwave to optical frequency domains.

The measured conversion efficiency is comparable with magnon-based microwave-to-optical conversion schemes [150, 152]. The warm-atom efficiency is limited by the intrinsic weakness of the magnetic-dipole microwave transition, as well as the ground-state spin decoherence γ_{I} which includes wall-collisions, transit-time decoherence, and Rb-Rb spin-exchange collisions. A larger optical beam, combined with a buffer gas [65, 171] and anti-relaxation coating on the cell walls [78, 81, 172, 173], would help reduce spin decoherence from the dark state and boost conversion efficiency. For example, we expect that a high-quality anti-relaxation coating and a modest 5 torr of neon would significantly reduce transit-time and wall effects, and reduce $\gamma_{\mathrm{I}}/2\pi$ by a factor of 10^3 to 100 Hz, limited by Rb-Rb spin-exchange [See Section 8.3]. Everything else being equal, this would provide a 10^6-fold improvement to the generation efficiency. Furthermore, based on [146], we expect that increased pump powers will produce a moderate 4-fold efficiency gain before the efficiency saturates due to absorption and incoherent scattering of the pump.

8.7 Conclusion

In this proof-of-concept demonstration, we have shown that inhomogeneous Doppler broadening in a warm vapor cell provides significant tunability of the output optical frequency in a microwave-optical transduction, resulting in frequency division multi-

plexing. The inhomogeneous width also enables simultaneous frequency up-conversion of multi-channel microwave inputs. Amplitude control of up-converted optical channels demonstrates analogous frequency domain beam splitting action across five orders of frequency. The frequency division multiplexing capability, combined with amplitude control, can make neutral atoms as quantum processors for information encoded in frequency-bin qubits.

Chapter 9

Accelerating simulations of the pseudospinor Gross-Pitaevskii equation

9.1   Introduction

There are many problems in physics for which the only realistic approach to a solution is through numerical techniques. The nonlinear Schrödinger equation (NLSE) is one such mathematical model with widespread applications throughout physics. Notably, this equation explains superfluid and magnetic properties of dilute Bose-Einstein condensates (BECs) [174, 175], but it also successfully describes plasma Langmuir waves [176], soliton dynamics [177], the propagation of light in nonlinear media [178–180], surface gravity water waves [181] and rogue waves [182], supercon-

168

ductivity [183], and even certain financial situations [184]. The connecting thread between these disparate physical phenomena is the slowly-varying evolution of a weakly nonlinear, complex wave packet in a dispersive environment [183].

A NLSE can take many forms [185], but many physical phenomena can be adequately described with a cubic nonlinearity. For a complex scalar function ψ, the NLSE can be written in the general form:

$$i\frac{\partial \psi}{\partial t} = -a\nabla^2\psi + b\psi + c|\psi|^2\psi, \tag{9.1}$$

where the parameter $a > 0$, and where c (which can be positive or negative) represents the strength of the nonlinearity. It is worthy to note that as c goes to zero, the NLSE reduces to the familiar Schrödinger equation.

While very few analytical solutions of the NLSE exist, the literature is replete with techniques for finding numerical solutions [185–190]. Usually these methods involve direct time-integration of the equation. Throughout the last decade, these techniques have been maturing and growing more accessible, evidenced by self-contained solver packages, such as the `GPELab` toolbox for MATLAB® [191, 192], `BEC2HPC` [193], and `GPUE` [194]. Despite the wealth of numerical techniques, the NLSE's nonlinear term makes it quite computationally intensive to solve [195]. Representing small features, such as superfluid BEC vortices, often requires small mesh spacings [190], and hence large grid sizes.

A computer's central processing unit (CPU) operates on grid points one at a time as a "serial processor." Although serial devices are optimized for low-latency, in many cases they cannot reasonably meet the demands of integrating the NLSE across large grid sizes. This results in very long computational run-times [185], which, in extreme cases, can span days to weeks [196].

For certain operations and algorithms, graphics processing units (GPUs) offer a

significant increase in computational power via parallelism. There are two notable types of parallel computing: (1) In *task-parallelism*, akin to vehicles on an assembly line, distinct and independent sets of data are operated on concurrently. (2) In *data-parallelism*, all elements of a single data collection are operated on at the same time. The Hadamard product, or element-wise matrix multiplication (represented as $A \circ B$, where A and B are matrices of identical size), is an example of an operation that is exceedingly data-parallel [197]. With access to anywhere from hundreds to thousands of multiprocessors and shared memory, GPUs can leverage both types of parallelism to accelerate computations far beyond the capacity of a CPU. "Speedup" is a relative metric for hardware performance enhancement; it is defined as $\tau_{\text{CPU}}/\tau_{\text{GPU}}$, where τ_{CPU} is the time per iteration on a CPU, and τ_{GPU} is the time per iteration the GPU. GPU accelerations of NLSE problems have ranged from tens [198, 199] to hundreds [182, 200] of times. We also acknowledge that several third-party modules for GPU-accelerating the NLSE already exist [197, 201], however, these are not amenable to all highly-specialized research problems.

In this chapter, we introduce a general approach for GPU-accelerating numerical computations of the NLSE. Using NVIDIA graphics hardware and tools from the open-source Python community, we demonstrate how CPU-based computations with power-law scaling in grid size can scale linearly using GPU hardware. We also provide a packaged version of our accelerated code titled `spinor-gpe`. While this code does not claim to be generally applicable, it serves as an example of our approach for hardware-accelerating NLSE code, and as a resource to the physics community. In our particular hardware configurations, we observed $6\times$, $36\times$, and $85\times$ speedup of the pseudospinor NLSE code. This required no detailed knowledge of our GPUs' architectures, and it demonstrates that a substantial computational speedup is pos-

sible using high-level programming tools like those found in the Python ecosystem. This is particularly important for numerical calculations that make predictions for or comparisons to experimental results; rapid calculations allow for timely parameter iterations and optimizations.

This chapter is organized as follows. Section 9.2 gives a basic introduction to NVIDIA GPU operation. Section 9.3 introduces a physically-motivated form of the NSLE and the algorithm for solving it. Section 9.4 describes the GPU-accelerating implementation, and Section 9.5 shows a performance comparison of the implementation across different CPU and GPU devices. Section 9.6 discusses the physics and results from an example calculation: a simulation of a spin-dependent gauge potential that produces quantized vortices in the spin-Hall regime. Finally, Section 9.7 discusses the broader significance of our approach, before concluding with Section 9.8.

9.2 General-purpose graphics processing unit computation

In this section, we give a high-level introduction to GPUs, pointing out essential features and concepts, and leave details of their use in general-purpose computing to other excellent reviews [202, 203].

9.2.1 Basic operation

Graphics cards and GPUs were originally developed to render virtual 3D graphics in real-time, a task which is highly data- and task-parallel in nature [203]. While early GPUs were exceptionally good for rendering graphics, they worked with strict fixed-function pipelines. Recognizing the utility of general-purpose GPU comput-

171

ing, graphics card manufacturers soon developed programming interface frameworks to directly program almost all of their GPUs' resources. There are two predominant frameworks for this: OpenCL (open source, maintained by Khronos Group) and CUDA (proprietarily developed by NVIDIA Corporation). In this work, we will restrict the discussion to CUDA and NVIDIA hardware. Similar to other frameworks, CUDA is a low-level interface to the GPU and using it requires a detailed knowledge of the GPU layout and resources [203]. Alternatively, the Python community has developed accessible packages with high-level "pythonic" access to back-end CUDA computing libraries, such as cuBLAS (linear algebra) and cuFFT (fast-Fourier transforms). While often used for machine learning, these packages provide a user-friendly platform for GPU-accelerating conventional scientific computations.

In general-purpose GPU computing, one should also be aware of a device's *architecture*, or the particular hardware version. Architecture includes the layout design and techniques implementing the operations, instructions, data types, registers, memory hierarchies, control units, and processors [1] that are key factors for performance. Each NVIDIA device has a *compute capability* (CC) metric to describe the CUDA computing features available therein. To illustrate, CC > 6.x (Pascal) devices can natively perform 64-bit addition operations, whereas CC ≤ 5.x (Maxwell) ones cannot [205].

When comparing the performance of different GPU devices, it is important to note that, *within* a certain architecture, performance scales with processing core numbers, memory, and clock rates. *Between* architectures, however, the vastly different hardware and instruction sets make this relationship not so simple. A rigorous performance analysis requires a detailed understanding of how the algorithm maps onto a given architecture, and is beyond the scope of this chapter. Instead, benchmark-

---

[1]Although companies market this as "architecture", this definition technically refers to a device's *microarchitecture* [204].

ing the execution time of a particular task provides a simple relative performance comparison [185, 200].

9.2.2   Implementation

This section describes how we adapted our previously-existing simulation code for GPU acceleration. The original (non-GPU-compatible) implementation of the GPE exclusively employed the NumPy scientific computing library. The algorithm relied heavily on the FFT and Hadamard product, both of which have the potential to be highly data-parallel operations. In search of accelerated execution times, we considered both the software and hardware computational aspects.

Several established CUDA-compatible Python packages, such as Tensorflow, provide wrappers of the needed cuFFT library [206]. However, we settled on PyTorch, a relatively newer package, because it has a "native Python" interface and is intentionally designed to have similar, if not identical, syntax to NumPy. This implies a short learning curve and minimal changes to our original code [207]; most of the changes we made to our code while migrating were drop-in replacements. As with other machine learning packages, PyTorch code can execute on either a CPU or a CUDA-enabled GPU, with a simple software switch between the two; this made it convenient to develop and test our code on a CPU before scaling it up to run on a GPU workstation. Our GPU code also takes advantage of the complex data type recently released for PyTorch.

On the hardware side, we constructed two different computer workstations with NVIDIA graphics cards. Our first workstation contains a GeForce 980 Ti (Maxwell arch., C.C. 5.2), a common commercial gaming graphics card. Our second workstation contains a Titan V (Volta arch., C.C. 7.0). In addition to the two workstations, we also had a commercial Acer Aspire laptop with an integrated NVIDIA GeForce MX150

GPUs	GeForce MX150	GeForce 980 Ti	TITAN V
Architecture	Pascal	Maxwell	Volta
Compute Capability	6.1	5.2	7.0
# CUDA Cores	384	2816	5120
Clock (Boost) [GHz]	1.47 (1.53)	1.0 (1.07)	1.2 (1.45)
VRAM Mem. [GB]	2.0	6.0	12.0
Mem. Bandwidth [Gbps]	48.06	336.6	651.3
Mem. bus width [bits]	64	384	3072

CPUs	Intel i5-7200U	AMD FX-6300	Intel i9-9900K
Clock (Boost) [GHz]	2.5 (3.1)	3.5 (4.1)	3.7 (5.0)
Available RAM [GB]	8	16	32

Table 9.1: GPU and CPU hardware specifications. Our PyTorch implementation can execute on any of our CUDA-enabled NVIDIA graphics cards (top) and our CPUs (bottom). The corresponding GPU/CPU hardware pairs are installed on a commercial laptop and two custom-built workstations, respectively. Key specifications of these devices are given. While RAM is not a property of CPUs, it's included here as a computational resource for the devices.

graphics card (Pascal arch, C.C. 6.1). Specifications for these three devices, along with their corresponding CPUs, are summarized in Table 9.1.

9.3   GPE Model

To demonstrate GPU acceleration, we investigate the Gross-Pitaevskii equation (GPE), a form of the NLSE which benefits from the GPU's features. The GPE is is used to model weakly interacting superfluids in the mean-field regime, and it is especially

well-suited to describe a dilute neutral-atom BEC [175]. The GPE is well-studied in this context. Significant work has improved the path to solutions [186, 187, 189, 208, 209], and illuminated a variety of physical phenomena, including vortex creation and dynamics, [174, 210–217] and the many-body states of spinor systems [187, 216, 218–222]. Here, we take the opportunity provided by the GPU to move beyond the standard GPE: we study the physical consequences of spin- and momentum-dependent coupling, and exploit the power of the GPU to render high-resolution solutions that would otherwise be prohibitively time-expensive. GPU-based calculations can simulate realistic experimental conditions in a reasonable amount of time, allowing for numerically informed optimizations of experimental procedures.

9.3.1 GPE Derivation

9.3.2 The coupled pseudospinor Gross-Pitaevskii equation

A standard approach to studying trapped neutral-atom BECs uses the GPE, where a single-component order parameter $\psi(\mathbf{r}) = \sqrt{\rho(\mathbf{r})}e^{i\phi(\mathbf{r})}$ represents the state of the system, where $\rho(\mathbf{r})$ is the real-space density and $\phi(\mathbf{r})$ is the phase profile. For a trapped gas of atoms, the GPE describes this order parameter as

$$i\hbar\frac{\partial}{\partial t}\psi(\mathbf{r}) = \left[-\frac{\hbar^2}{2m}\nabla^2 + V(\mathbf{r}) + g|\psi(\mathbf{r})|^2\right]\psi(\mathbf{r}), \qquad (9.2)$$

where the first term in the right-hand bracket represents the kinetic energy with atomic mass m; the second is the trapping potential energy; and the third term is the interaction energy, where an interaction parameter $g = 4\pi\hbar a_{\mathrm{sc}}^2/m$ is characterized by the interatomic scattering length a_{sc}.

Moving beyond this single-component model, we next consider the *spinor* condensate: a two- (or more-) component system where a higher-dimensional order parameter describes the density of atoms in two (or more) spin states. In describing

experimental systems with alkali metal atoms, these spin states are pseudospins whose real identities are defined by m_F levels in the ground state manifold. In the case of a two-spinor, or pseudospinor, the order parameter takes the form $\psi \to \Psi = \{\Psi_\uparrow, \Psi_\downarrow\}$. The interaction terms of the spinor GPE model must also account for the possibility of distinct inter- and intra-spin scattering lengths. Indeed, pseudospinors have three unique interaction strengths: $g_{\uparrow\uparrow}$, $g_{\downarrow\downarrow}$, and $g_{\uparrow\downarrow} = g_{\downarrow\uparrow} \equiv g_{\updownarrow}$.

Next, we introduce external fields that are carefully chosen to give a spin-dependent coupling between the pseudospins. These yield "artificial gauge fields" [223, 224] that can mimic the effects of magnetic fields, electric fields, and/or spin-momentum coupling in these atomic systems. We consider here the case where two lasers with opposite propagation directions $(\pm\hat{x})$ effect a two-photon Raman transition, thereby producing a spatially-periodic spin-wave in the BEC along the $\hat{x}$ recoil direction[2]. This spatial-periodicity can be removed via a unitary transformation, resulting in the two bare spin dispersion relations shifting opposite directions in $\hat{k}_x$ momentum space. In this rotated picture, this system is described by the effective single-particle energy Hamiltonian [174, 227]:

$$\hat{\mathcal{H}} = \left[\frac{\hbar^2 \mathbf{k}^2}{2m} + V(\mathbf{r})\right] \breve{\mathbb{1}} - \frac{\hbar^2 k_\mathrm{L} \hat{k}_x}{m} \breve{\sigma}_z + \frac{\hbar\Omega(\mathbf{r})}{2}\breve{\sigma}_x + \frac{\hbar\delta(\mathbf{r})}{2}\breve{\sigma}_z, \qquad (9.3)$$

where k_L is the magnitude of the lasers' wavevector, $\delta(\mathbf{r})$ is the two-photon Raman detuning and $\{\breve{\mathbb{1}}, \breve{\sigma}_x, \breve{\sigma}_y, \breve{\sigma}_z\}$ are the identity and Pauli matrices in the spinor basis. The Raman coupling between the ground states is generated via two electric fields having an equally far detuning Δ_e from some excited level. In this regime, the excited state can be adiabatically eliminated, and the total coupling strength takes the form $\Omega(\mathbf{r}) = \Omega_1(\mathbf{r})\Omega_2(\mathbf{r})/2\Delta_e$, where the Ω_i are the Rabi frequencies, a measure of the

---

[2]In this work, we limit the discussion to a spin wave, and thus momentum transfer, along one dimension, but this type of interaction can be extended to additional dimensions [225, 226]

electric dipole couplings between the excited and individual ground states [50]. The characteristic energy scale of this Hamiltonian is $E_{\mathrm{L}} = \hbar^2 k_{\mathrm{L}}^2/2m$, the kinetic energy imparted to an atom by a single-photon recoil. Experimentally, spatial dependence in the detuning and Raman coupling can readily be achieved with a spatially-dependent magnetic field (via the Zeeman effect) or a spatially-varying optical intensity (via the ac Stark effect), respectively. Spatial-dependence in the optical field can be obtained using, for example, a spatial light modulator device.

Finally, we incorporate the last three terms of Equation 9.3 into the GPE pseudospinor Hamiltonian [Equation 9.2], taking into account the appropriate signs of the detuning and the momentum shift. We interpret the spinor components $\{\Psi_\uparrow(\mathbf{r}), \Psi_\downarrow(\mathbf{r})\}$ as bare spins that have undergone a spin-dependent momentum shift $\{|\uparrow, -k_L\rangle, |\downarrow, +k_L\rangle\}$ [223]. After converting all quantities to dimensionless ones (denoted by tildes), the NLSE equation describing $\widetilde{\Psi}$ is

$$-i\frac{\partial}{\partial \tilde{t}}\widetilde{\Psi} = \left[\mathcal{H}^{(1)} + \mathcal{H}^{(2)} + \mathcal{H}^{(3)}\right]\widetilde{\Psi} + \mathcal{H}^{(4)}\widetilde{\Psi}, \tag{9.4}$$

where

$$\mathcal{H}^{(1)} = -\tfrac{1}{2}\tilde{\mathbf{k}}^2\check{\mathbb{1}} + \tilde{k}_{\mathrm{L}}\tilde{k}_x\check{\sigma}_z \tag{9.5}$$

$$\mathcal{H}^{(2)} = \widetilde{V}(\tilde{\mathbf{r}})\check{\mathbb{1}} + \tfrac{1}{2}\tilde{\delta}(\tilde{\mathbf{r}})\check{\sigma}_z \tag{9.6}$$

$$\mathcal{H}^{(3)} = \begin{pmatrix} g_{\uparrow\uparrow}|\tilde{\Psi}_\uparrow(\tilde{\mathbf{r}})|^2 + g_{\updownarrow}|\tilde{\Psi}_\downarrow(\tilde{\mathbf{r}})|^2 & 0 \\ 0 & g_{\downarrow\downarrow}|\tilde{\Psi}_\downarrow(\tilde{\mathbf{r}})|^2 + g_{\updownarrow}|\tilde{\Psi}_\uparrow(\tilde{\mathbf{r}})|^2 \end{pmatrix} \tag{9.7}$$

$$\mathcal{H}^{(4)} = \tfrac{1}{2}\tilde{\Omega}(\tilde{\mathbf{r}})\check{\sigma}_x \tag{9.8}$$

represent the kinetic [Equation 9.5], potential [Equation 9.6], interaction [Equation 9.7], and the Raman coupling [Equation 9.8] energies. This pseudospinor GPE describes the emergence of both superfluid effects (e.g. quantized vortices [174]) as well as magnetic structures (e.g. stripes, spin domains [221]).
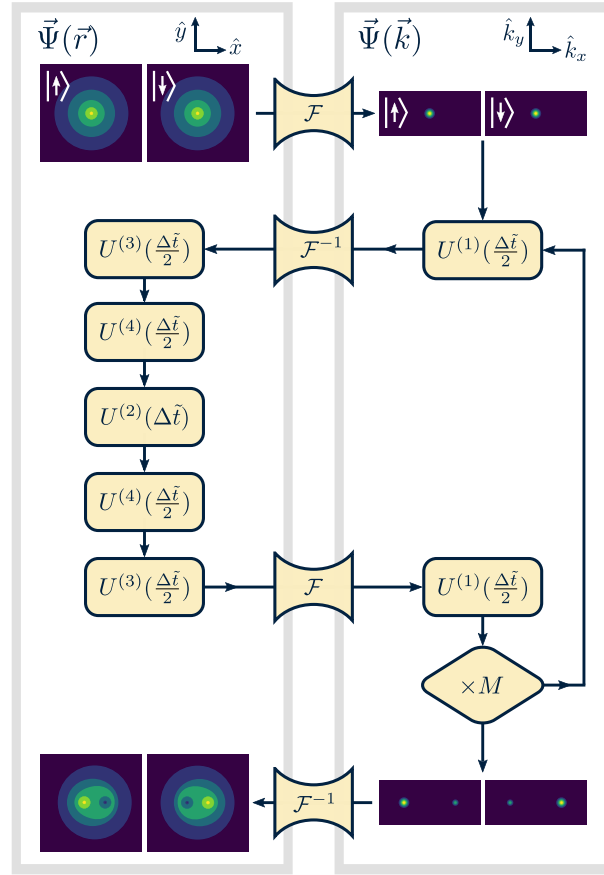
Figure 9.1: Flow diagram of the time-splitting spectral algorithm. Starting from some initial order parameter $\mathbf{\Psi}(\tilde{\mathbf{r}})$, we propagate in time by applying evolution operators U_i [see Equations 9.5-9.9] and fast Fourier transforms $\mathcal{F}$. The operations applied sequentially in the loop represent those for a single propagation time step $\Delta \tilde{t}$. In our Python code, the operations for a single time step are organized into a function that is called in a loop M times. After the loop terminates, the final order parameter is available.

9.4 Simulation algorithm

In this section, we describe the basic elements of the algorithm for integrating solutions to the GPE of Equation 9.4. We begin by assuming that the BEC is confined to the $x - y$ plane by a strong harmonic trapping potential in the transverse direction with frequency ω_z. Out-of-plane excitations are suppressed, and the dimensionless

order parameter along this dimension takes on a Gaussian profile with unit norm. If the energy level spacing $\hbar\omega_z$ is larger than the interaction energy, we can approximate the system as quasi-2D [174, 228] and represent the order parameters and operators on 2D grids.

The method for integrating solutions to the pseudospinor GPE relies on the well-established time splitting spectral (TSSP) method [229] [see Figure 9.1]. Solutions are evenly discretized in space on $N_x \times N_y$ grids. The real-space grid extends over $(\pm x^{\mathrm{max}}, \pm y^{\mathrm{max}})$, with spacings $(\Delta x, \Delta y)$; the momentum space grid extends over $(\pm \pi/\Delta x, \pm \pi/\Delta y)$ with spacings $(\Delta k_x, \Delta k_y) = (\pi/x^{\mathrm{max}}, \pi/y^{\mathrm{max}})$. The solutions are propagated through time by repeatedly applying time-evolution operators to the previous time step's order parameter. The time-evolution operators are given by

$$U^{(n)}(\Delta \tilde{t}) = \exp(i\mathcal{H}^{(n)} \Delta \tilde{t}), \tag{9.9}$$

where $\Delta \tilde{t}$ is a unitless discrete time step smaller than any relevant time scales of the system. Propagation in real-time yields the dynamics of the spinor system, while propagation in imaginary-time $(\Delta \tilde{t} \to i\Delta \tilde{\tau})$ asymptotically approaches ground state solutions. "Applying" an evolution operator amounts to Hadamard multiplication of the complex operator array and the order parameter array. In the TSSP method, a Fourier transform takes the order parameter to momentum space where $\mathcal{H}^{(1)}$ is diagonal, i.e. $\nabla^2 \to -\tilde{\mathbf{k}}^2$. In this way, we perform two 2D FFTs to avoid the more computationally-expensive finite-difference Laplacian in the $U^{(1)}$ operator.

Starting from an initial spinor order parameter, we propagate the GPE in a loop over M discrete time steps of length $\Delta \tilde{t}$. We pre-compute and store the evolution operators [Equation 9.9] corresponding to the potential $\tilde{V}(\tilde{\mathbf{r}})\check{\mathbb{1}}$, kinetic $\mathcal{H}^{(1)}$, Raman coupling $\mathcal{H}^{(4)}$, and Raman detuning $\tilde{\delta}(\tilde{\mathbf{r}})\check{\sigma}_z$ energy components, since they are constant throughout the propagation loop; the nonlinear mean-field terms $\tilde{g}_{ij}|\widetilde{\Psi}_i(\tilde{\mathbf{r}})|^2$

depend on the densities, and therefore are calculated at each time step. As shown in Figure 9.1, we apply the $U^{(1)}$, $U^{(3)}$, and $U^{(4)}$ operators with the familiar Strang splitting for stability and to reduce errors induced by the various non-commuting $U^{(i)}$ operators [188]; because the 2D operators additionally live in spin space, the real-space evolution operators $U^{(2,3,4)}$ do not necessarily commute and should be split to second-order [230, 231]. Previous demonstrations using higher-order splitting have further improved spatial accuracy, but the form of these splittings as applied to spinor systems was not straightforward [231]. Within a single time-step loop, four 2D FFTs and $\gtrsim 20$ Hadamard products are performed. Since probability density is not conserved in imaginary-time propagation, we normalize the order parameters to the total atom number at each time step.

While the individual operations are highly data-parallel, they must be applied sequentially. Hence in this case, it was advantageous to maintain data on a single device, avoiding the additional transfer times between various devices in so-called "heterogenous" or distributed computing configurations [185]. This way, the data does not leave the device until the entire simulation is complete.

9.5 Performance Benchmarking

In this section, we show and analyze the benchmark results of timing the propagation stepping function [see the caption of Figure 9.1]: we compare the performance and scaling of our three GPUs and three CPUs with increasing grid sizes. Note that these benchmarks only compare the performance of our PyTorch code on different devices, one device at a time.

To make a fair comparison between GPU and CPU performance, we transferred the order parameter and energy grids to the GPU's memory before running the bench-
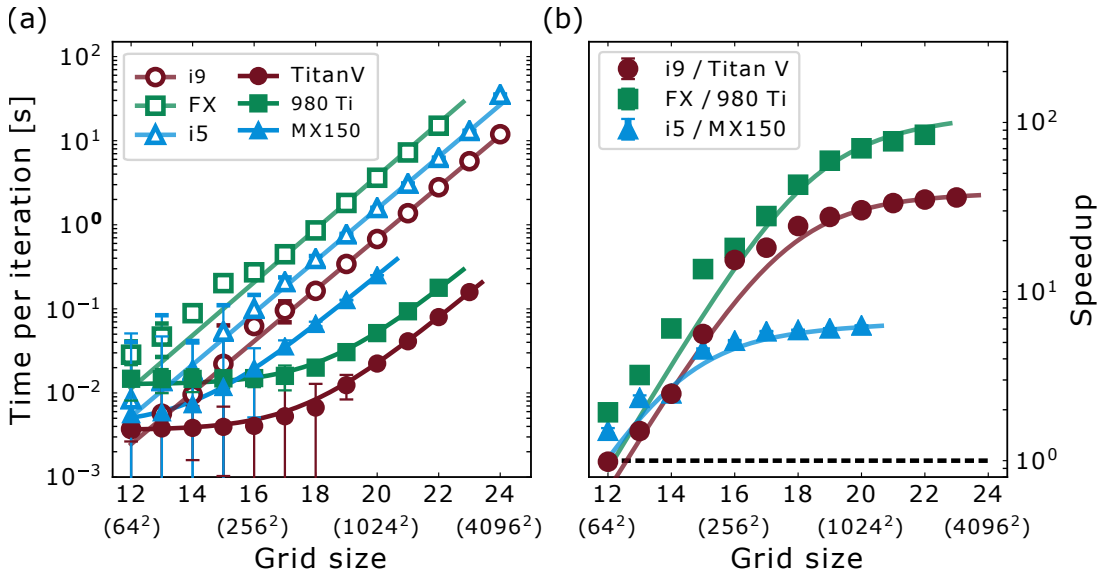
Figure 9.2: Performance and speedup comparison of the propagation step on various devices. (a) Performance comparison benchmark of the propagation step function for the six devices across various grid sizes, shown here on a log-10/log-2 plot. The points represent the median evaluation time of many trials, and the error bars represent the median absolute deviation. The CPU and GPU evaluation times were fit by power law [open symbols, $\kappa = 1.03(3)$] and linear [filled symbols, $\theta = 9.7(1) \times 10^{-8}$ s] models, respectively. (b) Speedup of the hardware pairs as a function of grid size. The black dashed line represents the break-even performance for the hardware pairs. For comparison and reference, the files used to generate these data are found in the repository subdirectory /spinor_gpe/benchmarks.

marks on those devices, thereby avoiding the relatively slow data transfer rate between computer RAM and GPU VRAM [182]. We exclusively employ complex double-precision floats (`torch.complex128`) in the simulations and benchmarks.

We measured the propagation function evaluation times using the Python `timeit` module. We separately timed many different evaluations of the propagation step-ping function, and repeated this process on each device for various 2D grid sizes $N = N_x \times N_y = 2^\eta$, where $\eta \in \mathbb{N}$ and N is the size of a single spinor component. Due to concurrent system processes that we could not eliminate, the distributions of evalu-

ation times were highly non-Gaussian. Although there exist sophisticated benchmark analysis techniques for understanding these types of distributions [232, 233], the median and median absolute deviation provided a simple and interpretable statistic and uncertainty for our purposes. With each GPU device, there was a maximum grid size above which the data could no longer fit into VRAM, and the benchmark halted. The results of evaluation time versus η are plotted in Figure 9.2(a) and the speedup between particular CPU/GPU pairs is given in Figure 9.2(b); both plots represented on log-10 vs. log-2 scales. At the smallest grid sizes ($\eta = 12$), the performance of the GPUs and CPUs were comparable. The largest speedups we measured for each device pair (from smallest to largest) were 6.3, 36, and 85.

The CPU evaluation time data are well-described by a power-law function of the form $f_C(N) = \lambda N^\kappa$. The three CPU evaluation times scale vary similarly, and, on average, $\kappa = 1.03(3)$. The GPUs, in contrast, scaled linearly as $f(N) = \theta N + \xi$, with $\theta = 9.7(1) \times 10^{-8}$ s and a device-dependent offset ξ. The scaling difference between the two device classes highlights the power of GPU data parallelism. This linear scaling means that doubling of smaller grid sizes makes negligible difference to the evaluation times. The GPUs basically provided increased resolution for free.

As mentioned previously, it is generally difficult to interpret benchmarks for GPUs from different device architectures. There are some insights, however, that we can gain from testing the performance of the atomistic 2D FFT and Hadamard functions that compose the algorithm. Figure 9.3(a) shows evaluation times for each of these functions on the i9 CPU and the Titan V GPU. The times measured on the i9 all display a power-law scaling with increasing grid size. The Titan V data show an entirely different behavior: at small grid sizes, the Hadamard and FFT times are all constant, but begin to rise near $\eta = 19$ to 20. We interpret this inflection point
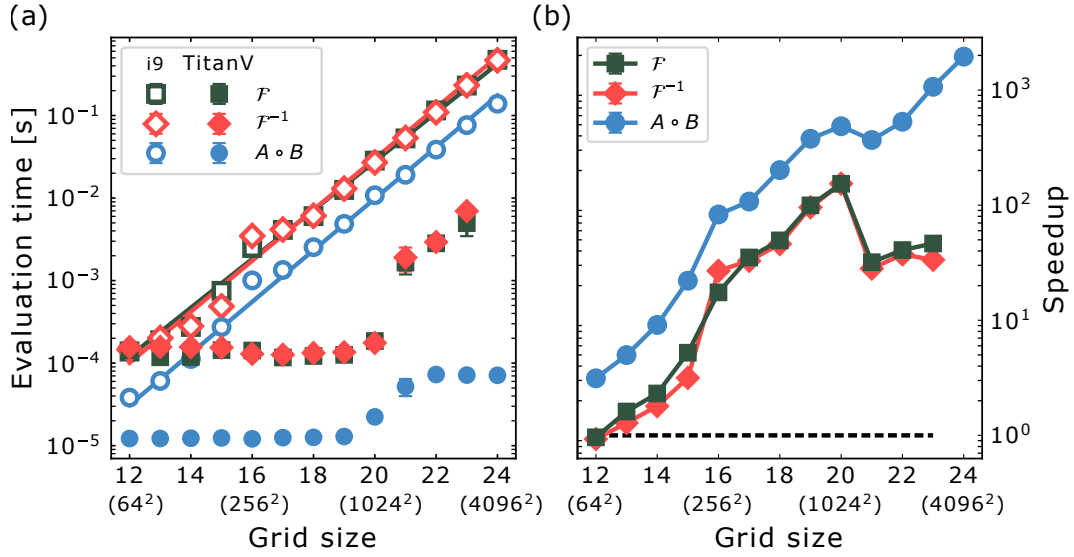
Figure 9.3: Performance and speedup comparison of the 2D FFT and Hadamard operations on various devices. (a) The evaluation times for individual forward and inverse 2D FFT and Hadamard product $(A \circ B)$ function calls over various grid sizes, computed on the i9 CPU (open symbols) and the Titan V graphics card (filled symbols). The points represent the median evaluation time over many trials, and the error bars represent the median absolute deviation. The CPU function times are well-described by a power-law, with an average exponent of $\kappa = 1.0154(2)$. (b) The speedup of the three function evaluation times as a function of grid size.

as the Titan V's limit for simultaneous data operations; at grid sizes larger than this, the device must batch the data and operate on those batches sequentially. The use of GPU computing for our algorithm is supported by the improved scaling of the functions' evaluation time by the Titan V device for grid sizes smaller than the inflection point.

9.6   Simulation example: spin Hall system

In this section, we demonstrate our GPU-accelerating method by simulating the ground states of a spin Hall system. In such a system, the spin-up and spin-down

constituents experience effective magnetic fields of equal magnitude but opposite direction. The spin Hall effect has been investigated theoretically [234, 235] and experimentally [236] using Raman-induced spin-orbit coupling in ultracold atoms; the presence of a spatial gradient in the Raman coupling and an effective "electric" force (a role played by gravity) generate transverse spin Hall currents. Other work showed that interspin interactions can greatly alter the properties of spin Hall states [237, 238]. In the simulations that follow, we investigate the mean-field ground states of a two-component BEC subject to a spatially varying spin-dependent gauge potential, considering various interspin interaction strengths. Similar to the proposal given in [236], these states are generated *in situ* in the absence of any effective electric force and reside in the classical spin Hall regime; this occurs when the filling factor $\nu = N/N_\phi \gg 1$, where N is the number of atoms and N_ϕ is the number of flux quanta penetrating the system [237].

We consider a harmonically confined, pseudospinor BEC of 10^4 atoms, where the trapping frequencies $\omega_z \gg \omega_x = \omega_y \equiv \omega_\perp$. The harmonic oscillator length $a_0 = \sqrt{\hbar/m\omega_\perp}$ and energy $E = \hbar\omega_\perp$ set the characteristic length and energy scales of the system. The intraspin interaction parameters are $g_{\uparrow\uparrow} = g_{\downarrow\downarrow} \equiv g$.

The single-particle physics of this problem can be analysed by diagonalizing the Hamiltonian [Equation 9.3]. For weak coupling ($0 < \hbar\Omega < 4E_\mathrm{L}$), the lower-energy band of the dispersion relation takes on a double-well shape [227]; as $\Omega \to 0$, the two minima reside at $\pm k_\mathrm{L}$. The eigenstates in this band vary across k, with $|\downarrow\rangle$ dominating the state near $+k_\mathrm{L}$, and $|\uparrow\rangle$ dominating the state near $-k_\mathrm{L}$ (even for nonzero Ω). If the atoms are confined to the lowest energy band, this amounts to a spin-dependent Abelian gauge potential, and the following effective Hamiltonian

applies:

$$\hat{\mathcal{H}}_{\text{eff,x}} = \frac{\hbar^2}{2m} \left(k_x + \mathcal{A}_x^* \breve{\sigma}_z \right)^2,$$
(9.10)

where the magnitude of the artificial gauge potential $\mathcal{A}_x^*$ multiplies the Pauli matrix in the dressed-spin basis, and scales as

$$\mathcal{A}_x^* = k_{\text{L}} \left[1 - \left(\frac{\hbar\Omega}{4E_{\text{L}}} \right)^2 \right]^{1/2}$$
(9.11)

for $\hbar\Omega \leq 4E_{\text{L}}$ and $\delta = 0$ [227]. A spatially-varying $\Omega(y)$, and hence $\mathcal{A}_x^*(y)$, produces a synthetic magnetic field for each spin

$$B_{\uparrow(\downarrow)}^* \hat{z} = \pm \left(\frac{\hbar}{q} \right) \nabla \times \mathcal{A}_x^*(y)$$
(9.12)

that is equal in magnitude, but opposite in direction. q is the synthetic electric charge of the atoms.

We imposed a spatially-varying Raman coupling profile of the form

$$\frac{\hbar\Omega(y)}{E_{\text{L}}} = \sqrt{8y - y^2}$$
(9.13)

to linearize $\mathcal{A}_x^*(y)$. As shown in Figure 9.4(b), this created two degenerate spin-dependent wells in k-space that moved inward from $k_x = \pm 1 \to 0$ as y increased. The induced uniform, synthetic spin-dependent magnetic field had a magnitude of $|B_{\uparrow(\downarrow)}^*| = 0.369 \ \hbar/qa_0^2$ across the region of the BEC. Before each simulation trial, we seeded each order-parameter component with 50 randomly-placed vortices having a spin-dependent winding. Due to the spin-dependent nature of the magnetic field, we expected the components to acquire opposite angular momentum. We then propagated the solution in imaginary time over two segments of 60,000 steps each. In the first segment, we periodically "annealed" the system with Gaussian noise to

185

(a)

(b)
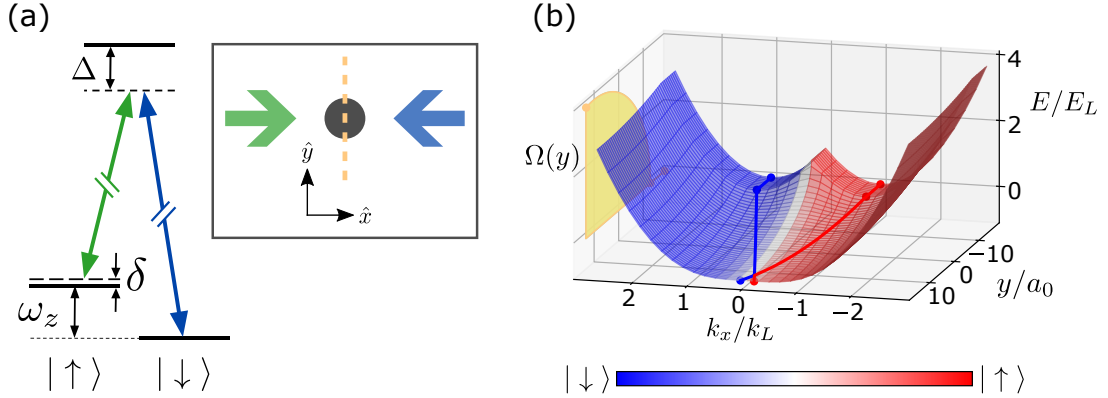
Figure 9.4: A BEC in a spin- and spatially-dependent artificial gauge potential. (a) A pair of counter-propagating Raman lasers couple two atomic levels of a harmonically-confined BEC. A spatial light modulator device (not shown) tailors the laser intensity to vary proportional to $\Omega(y)$ [Equation 9.13] along the yellow dashed line. (b) The Raman momentum-energy dispersion as a function of y-position due to the spatially-tailored Raman coupling profile shown in on the left 3D wall. This coupling is assumed to be uniform along the x-direction. The solid red and blue curves indicate the double-well minima, or the gauge potentials $\mathcal{A}_x^*(y)\hat{\sigma}_z$.

more quickly find the ground state; second, we propagated without annealing. Good convergence to the ground state could typically be obtained following this method.

We simulated and characterized ground state solutions of this system for different values of $g_{\updownarrow}$. From the real space densities $\rho_{\uparrow(\downarrow)}(\mathbf{r}) = |\Psi_{\uparrow(\downarrow)}(\mathbf{r})|^2$, we calculated the system-averaged phase separation parameter [227],

$$s = \sum_{\mathbf{r}} \left[1 - \frac{\langle \rho_{\uparrow}(\mathbf{r})\rho_{\downarrow}(\mathbf{r})\rangle}{\sqrt{\langle \rho_{\uparrow}^2(\mathbf{r})\rangle \langle \rho_{\downarrow}^2(\mathbf{r})\rangle}} \right], \tag{9.14}$$

where the sum runs over all points $\mathbf{r} = (x, y)$ in the 2D region. For small interspin interactions, stable vortex configurations arose with high vortex eccentricity along the y-direction [239]. From the phase profile $\phi_{\uparrow(\downarrow)}(\mathbf{r})$ of each order parameter component, we calculated the total average angular momentum, or circulation, of the pseudospinor
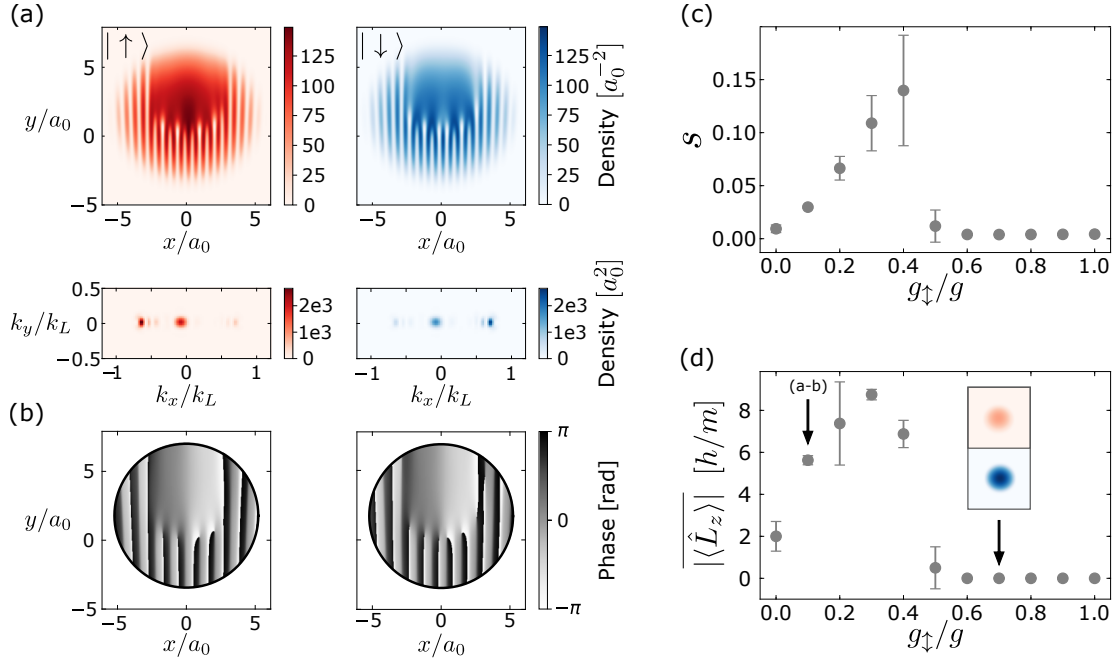
Figure 9.5: Spin-Hall simulation results. (a) Enlarged detail of the calculated real-space (top, 2.6× mag.) and k-space (bottom, 9.8× mag.) ground state densities on a 1024 x 1024 grid for $g_\updownarrow = 0.1$. The trapping frequencies are $(\omega_\perp, \omega_z)/2\pi = (50, 2000)$ Hz. The smooth central regions of each real-space density correspond to momentum components near $k_x = 0$. (b) The spatial phase profiles $\phi_{\uparrow(\downarrow)}(x, y)$ of the solutions from (a), showing opposite vortex windings in each component. (c) The phase separation of the two components as a function of the interspin interaction strength $g_\updownarrow/g$. Error bars indicate the standard deviation of several trials. (d) The absolute value of $\langle \hat{L}_z \rangle_{\uparrow(\downarrow)}$ averaged for both components, as a function of $g_\updownarrow/g$. We expected that the circulation, and hence the magnitude of the $B^*_{\uparrow(\downarrow)}$, experienced by each spin component would be the same, however, interactions and the initial random seeding generally tended to imbalance the respective angular momenta for a given simulation trial. For values of $g_\updownarrow/g$ larger than ~ 0.5, the spins were completely phase-mixed with no angular momentum present in either component.

components,

$$\langle \hat{L}_z \rangle_{\uparrow(\downarrow)} = \oint_{\mathcal{C}} \boldsymbol{\nabla} \phi_{\uparrow(\downarrow)}(\mathbf{r}) \cdot \mathrm{d}\boldsymbol{\ell} = \frac{2\pi\hbar}{m} n_{\uparrow(\downarrow)}, \tag{9.15}$$

where $\mathcal{C}$ is a closed, counter-clockwise contour enclosing 99% of the total atom population [the thick black line in Figure 9.5(d)]; the total number of 2π-phase windings $n_{\uparrow(\downarrow)}$ takes on integer values since the components are single-valued. In both the phase separation and the average angular momentum characterizations, we see a clear phase transition in the ground state at $g_\updownarrow/g \approx 0.5$ [Figure 9.5(e-f)].

Some obvious continuations of this work would investigate negative $g_\updownarrow$ values, as well as various synthetic magnetic field strengths. Field strengths are limited to a maximum value of $|B^*_{\uparrow,\downarrow}| \approx 0.700\ \hbar/qa_0^2$ by the possible gauge potentials (i.e. $|\mathcal{A}^*/k_L| \in [0,1]$) and by the physical size of the BEC. It would also be interesting to search for edge effects in a 2D uniform disk BEC [236, 240].

Throughout all this, the acceleration of our GPU method is extremely evident: a single trial typically executed in about 45 minutes on the Titan V GPU versus an estimated ~ 1 day on the i9 CPU. Moreover, all the results presented in Figure 9.5 would have taken almost 3 months of continuous computation on the i9, a highly performant device [see Table 9.1].

9.7   Discussion

We have described a GPU-based approach for solving the NLSE that provided a significant speed-up, and which let us investigate details of a system that would have been otherwise inaccessible. Our computational approach was motivated by the specifics of the GPE: while some of the terms are best calculated in real space, others are better suited to momentum space, motivating FFTs between real and momentum space representations; mean field interactions and direct coupling between

Year	Source	Problem	Language/Interface	GPU Speedup		
				float32	float64	complex128
2010	[195]	1D dark solitons	CUDA	$75\times$	$25\times$	-
2011	[200]	BEC in exiton semiconductor	CUDA	$19\times$	-	-
2013	[177]	1D dark solitons	MATLAB® CUDA MEX	$37\times$	$31\times$	-
2013	[241]	Non-linear optical Bloch equations	CUDA	$23\times$	$11\times$	-
2014	[182]	Rogue waves	CUDA	-	$>400\times$	-
2015	[199]	Dipolar solitons in driven BEC	-		$10\times^{\dagger}$	
2017	[198]	Dipolar BEC	CUDA	-	-	21 & $25\times$
2016	[178]	Optical pulse propagation in fibers	CUDA	-	$50\times$	-
2020	[180]	Multimode optical fiber transmission	-	$93\times$	$71\times$	-
2021	This work	Pseudospinor BEC	Python/PyTorch	-	-	36 & $85\times$

† Precision was not specified.

Table 9.2: Research works demonstrating GPU accelerated solutions to nonlinear Schrödinger equations. Almost all the works cited here were conducted in CUDA, while ours used Python. Although speedup is a relative metric, this table highlights the growing accessibility of GPU-accelerating NLSE solutions.

spinor components demanded sequential calculations. The GPU architecture and its excellent handling of FFTs is well-suited to this algorithm.

For realistic modeling of experimental systems, it often becomes necessary to simulate in three dimensions. Our code is not designed for 3D, and, due to hardware memory limitations, we note that extending our procedure to 3D using a single GPU device could remain quite challenging: even storing a complex scalar order parameter on a cubic 3D mesh of size 1024^3 would require over 17 GB of memory, exceeding the VRAM capacity of most graphics cards on the market today. Although better graphics cards are becoming available, solving the 3D NLSE with high resolution would certainly require more advanced hardware and sophisticated computational techniques than those presented here. Distributed GPU computing of the 3D NLSE has been demonstrated previously using CUDA, OpenMP, and MPI [242]; similar

multi-device computations may be possible with PyTorch and other machine learning libraries, albeit with additional code complexity.

The conversion of the existing TSSP implementation has yielded excellent performance gains; many other successful algorithms may stand to benefit from GPU acceleration in a very similar way. For instance, the previously demonstrated nonlinear conjugate-gradient technique [193, 243] also relies heavily on FFTs for both the main propagation and preconditioning steps. Additionally, derivative operations can also be implemented on GPUs, so other techniques such as forward/backward-Euler finite-difference or Crank-Nicholson finite-difference [244] may yield faster results as well. Regardless, it is also possible to pair the presented work with an existing ground-state solver [191–194]; ground-state solutions found with the preferred technique can later be propagated in real-time using the presented package for faster results.

With the availability and specifications of GPU hardware continuing to improve, we anticipate the approach taken here becoming even more widespread throughout the physics and scientific communities: without needing to know or manipulate details of the hardware architecture, one can access the advantages of GPUs while working with high-level programming tools and relatively inexpensive hardware. Though here we worked within the Python community, this approach is broadly applicable to other similarly high-level frameworks. Within the open-source Python ecosystem, we found that many tools available through packages like Numpy and PyTorch worked well for us. We anticipate that recent updates to other packages like Numba and CuPy will offer advantages for future work in this area.

9.8   Conclusion

In this chapter, we demonstrated a straightforward approach to accelerate Python code solving the 2D pseudospinor nonlinear Schrödinger/Gross-Pitaevskii equation. CPU-based calculations having a power-law scaling in grid size became linear by moving to a GPU-compatible system. We accomplished this with NVIDIA hardware upgrades, and with relatively minimal changes to our previous code, migrating from NumPy to PyTorch for the heavy calculations. Furthermore, we demonstrated their performance by simulating a spin Hall system with a spatially-varying Raman coupling. This work is a first step in the development process towards hardware-accelerated code. Even greater speedups are possible by rigorously optimizing the algorithm and computing resources. The grid sizes during the benchmarks were primarily limited by memory; larger grid sizes could be probed by carefully managing pre-loaded arrays and reusing temporary arrays [198]. Nonetheless, the approach and `spinor-gpe` package presented in this chapter illustrate the simplicity and accessibility of high-performance GPU computing for solving computationally expensive, nonlinear differential equations; these tools and methods are increasingly accessible for "everyday" scientific computing. This approach is especially relevant for experimental research groups who routinely work with custom-built simulation code that is not optimized on a low level.

Chapter 10

Conclusion

10.1   Summary

In this thesis, we have explored two different types of physical systems with emergent nonlinearities. These nonlinearities produce solutions and dynamics that were not present in their microscopic constituents. The first is an experimental demonstration of nonlinear microwave-to-optical conversion in an upgraded warm atom/microwave cavity system. To understand this process, we have explained the relevant electronic structure of the ^{87}Rb atoms [Chapter 2] and provided a semiclassical description for transitions among the quantized energy levels [Chapter 3]; we have shown how the thermal properties of the atoms influence their interactions with light [Chapter 4], and provided an overview of second-order nonlinear optical processes [Chapter 5]. With this foundation, we constructed a theoretical model for this unique nonlinear SFG oc-

curring in an isotropic atomic material [Chapter 6]. After detailing the construction and calibration of our apparatus [Chapter 7], we presented the experimental results [Chapter 8], reporting a conversion efficiency of 1.5×10^{-9}, comparable to other warm atom [148] and magnon [143, 150, 164] conversion platforms. The significant contributions of this work included the consideration of the thermal Doppler-broadened resonance to extend the tunability of the output frequency over a 550 MHz range. Independent velocity classes of atoms provided an opportunity for independent conversion of multiple frequencies simultaneously. We demonstrated the coherent nature of this conversion process and phase control of modulation sideband amplitudes.

Second, we considered a model of interacting, pseudospin-1/2 atoms in an ultracold Bose-Einstein condensate [Chapter 9], where the evolution of the collective wavefunction is described by a nonlinear Schrödinger equation. The primary contribution was the development of a procedure to significantly accelerate computed solutions of this equation using simple programming tools and readily available graphics hardware. To demonstrate the power of this approach, we observed an 80-100× computational speedup and numerically studied a spin-Hall system with spatially varying Raman coupling.

10.2 Future outlook

This section will focus on the future of the warm atom/cavity system, for which there are abundant potential research opportunities, both fundamental and applied.

10.2.1 Conversion efficiency improvements

The most straightforward research direction is the improvement of the microwave-to-optical conversion efficiency. This can first be done with higher pump power, as

was shown in [146]. As described in Section 8.4, we expect that a higher optical depth/atomic density will increase the generation efficiency. Halting the cell stem water-cooling and heating the cavity and cell to higher temperatures are experimentally simple ways to achieve this.

An obvious technical improvement is the use of an inert buffer gas inside the cell. Because of collisions with the buffer atoms, the rubidium atoms move diffusively through the cell, and the transit broadening is reduced [see Section 4.3.1]. This lowers the effective ground state atomic decoherence rate γ_I and extends the coherence time considerably. The buffer gas will pressure-broaden the atomic Doppler spectrum [see Section 4.3.1] leading to even greater tunability of output frequency conversion. Of course, broadening comes at the cost of reduced atomic density in a given velocity class, so there will be a trade-off with efficiency. In anticipation of these improvements, we have already begun tests with an identical vapor cell, containing 5 torr of Neon buffer gas and an internal alkene anti-relaxation coating.

Another interesting research direction would be to work in the SERF regime where spin decoherence is virtually eliminated [see Section 4.3.2]. This regime has been shown to be beneficial for spin-based quantum memories [245], and could produce a significant enhancement of conversion efficiency. Necessary upgrades would include a high buffer-gas pressure cell, proper magnetic shielding, heating, and field cancellation coils.

10.2.2 Difference frequency generation

By tuning the pump laser to the $f = 1 \rightarrow f'$ transition, light is produced in a difference-frequency generation (DFG) configuration. To our knowledge, DFG has not previously been observed for this hybrid nonlinear process in thermal neutral

atoms. Preliminary experimental evidence of this process is shown in Figure 10.1, but should be examined more systematically and compared to the SFG process.
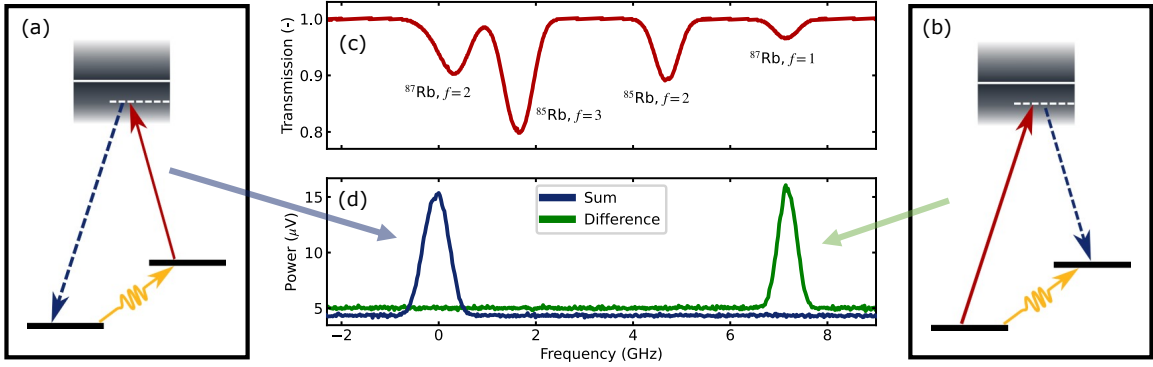
Figure 10.1: Preliminary data showing the generated signal for the pump laser frequency sweep across all rubidium Doppler peaks. Energy level diagrams for (a) sum- and (b) difference frequency generation. (c) The Doppler transmission spectrum of the reference vapor cell. The spectrum has been normalized, with a linear slope subtracted off. (d) Sum- and difference-frequency generation signals. When the pump frequency sweeps over the $f = 2$ Doppler peak, the atom responds in a non-linear sum-frequency process and generates light detected via optical heterodyne at $f_{\mathrm{het,S}} = f_{\mathrm{I}} + f_{\mathrm{AOM}}$; when swept over the $f = 1$ Doppler peak, the difference-frequency process occurs and the generated light is detected at $f_{\mathrm{het,D}} = f_{\mathrm{I}} - f_{\mathrm{AOM}}$.

10.2.3 Time-dependent SFG

This thesis only presents SFG experiments with continuous wave fields, however, we believe that many research opportunities exist for generation in a pulsed regime. For example, a recent theoretical proposal has shown that it should be possible to observe a generated pulse group delay time $t^{(2)}$ that varies with the intensity of the input idler pulse [246]. Pulse delays $t^{(1)}$ in linear atomic media, even under EIT conditions, depend on the real part of the first-order susceptibility $\Re\left\{\chi_{\mathrm{S}}^{(1)}\right\}$, which is proportional to the total atomic density [247]. In contrast, the $t^{(2)}$ delay time depends on the phase of the complex, second-order susceptibility $\phi^{(2)} = \arg\left[\chi_{\mathrm{S}}^{(2)}\right]$ and is therefore density-*independent*. Measuring this group delay would allow for the

generation and controllable group delay of pulses using a second-order nonlinearity, particularly in miniturized, dilute atomic media.

More generally, we would be able to study SFG pulse propagation, Rabi-like oscillations, and optical precursors [248–251] for a second-order nonlinear process. Furthermore, some initial tests, both experimental and numerical simulations of the Maxwell-Bloch equation [101], suggest the formation of a spin-wave excitation during the SFG process. A controllable temporal separation between the idler and pump pulses will allow us to probe the nature of this hypothetical spin wave. If confirmed, this spin wave would integrate naturally with other warm-atom quantum memories [82, 245, 252].

All of these research avenues require the capability to properly pulse the idler and pump fields at high-enough temporal resolution, ideally on a time scale much faster than the ground-state decoherence time $2\pi/\gamma_I \simeq 7\ \mu$s. The pump pulses can be shaped by AOMs[1] or intensity EO modulators [253, 254]. The common architecture for producing fast microwave pulses for superconducting quantum processors involves mixing a continuous microwave source with a fast digitally-generated RF waveform [255].

10.2.4 SFG involving single photons

With higher conversion efficiencies and pulsed control, SFG involving single photons becomes a possibility. Future work will be able to address open questions such as how the quantum statistics of the generated photons differ from the coherent input fields [55]. If the system displays quantum statistics, it could be operated as an on-demand single-photon source. With larger efficiencies and cooperativities, it

---

[1]The pulse rise time depends on the acoustic wave speed and the diameter of the laser beam. Faster pulse rise times are achieved by focusing the beam into/out of the AOM. The collimating lens' focal length should be long enough to spatially separate the diffracted orders.

may also be possible to detect conversion using a single-photon pump source. These opportunities are strengthened by the current construction and testing of a rubidium-compatible, heralded single-photon source and superconducting single-photon detectors in our lab space.

Because the SFG signal and pump emerge from the cavity co-linearly, they must first be spatially separated (or the pump light must be sufficiently filtered) before detection; it is essential to not overwhelm the single-photon-counting modules with pump light. An atomic spectral filter [256] based on ^{85}Rb may be helpful [257, 258], but the most practical filtering option may be any or a combination of polarization[2] and optical filters[3].

10.2.5   Multilevel modeling for magnetometry

The strong SFG suppression at zero magnetic field [see Section 8.2.4] can only be understood as a multi-level effect, and its understanding requires more detailed theoretical modeling. An accurate model would involve a Zeeman-dependent density matrix solution with a total of sixteen participating levels; together with Doppler averaging [100], this easily becomes computationally intensive. We suggest approaching this problem incrementally. The relevant multilevel physics of our experiment could be captured with the five-level model, shown in Figure 10.2, at steady-state and with equal transition strengths. One could then build toward a more realistic model that includes Doppler averaging, all levels (including both $f' = 1$ & 2 excited hyperfine manifolds), the correct transition strengths, and the vector magnetic field. We believe

---

[2]Glan polarizers can achieve extinctions of 100,000:1, or 50 dB. Using these polarizers requires upgrading to zero-order waveplates for precise polarization control.

[3]Examples include Fabry-Perot cavities [259] with extinctions of $\sim$ 45 dB [260], or fiber Bragg gratings with extinctions of $\sim$ 30 dB.
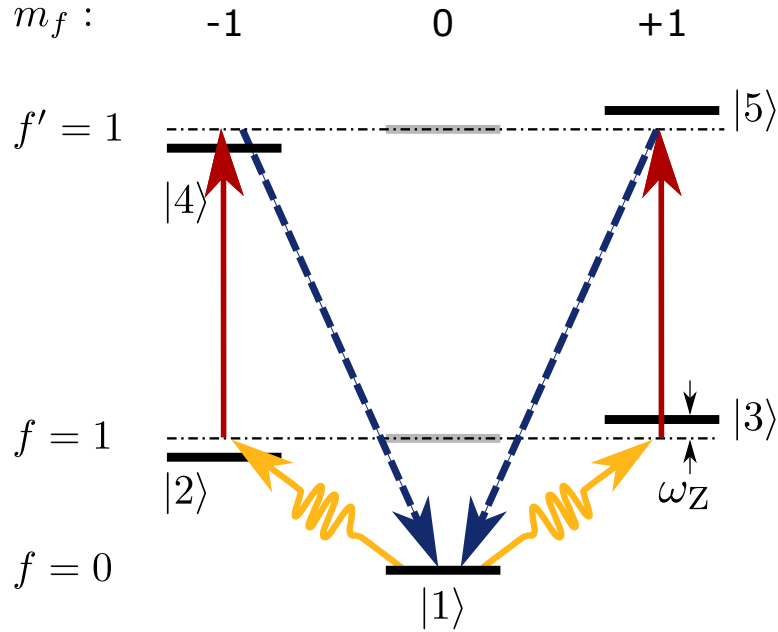
Figure 10.2: A simplified, multilevel microwave-to-optical conversion scheme for studies of zero-field SFG suppression. We assume two ground hyperfine states $f = 0$ & 1 and an excited hyperfine state $f' = 1$, with their respective Zeeman sublevels. In an external DC magnetic field, the Zeeman levels split by ω_{Z}. Not shown are the decoherence rates from excited levels ($|2\rangle$ through $|5\rangle$) to lower ones. The yellow, red, and blue lines show the idler, pump, and signal transitions. Given the same quantizing magnetic field and field polarizations from our main experiment, the SFG forms two closed loops involving five levels; the upper $m_f = 0$ levels do not couple and are greyed out. We hypothesize that these two looped paths destructively interfere when $\omega_{\mathrm{Z}} \to 0$.

this nonlinear process has potential for sensitive optical magnetometry, both in the continuous and time-domain modes [261].

10.2.6 Frequency-bin processing

A final, interesting direction to pursue, as was alluded to in Section 8.6, is frequency-bin information processing. In Section 6.3.2, we showed how the frequency components of a PM pump beam and an AM idler field interact: the relative modulation

phase imparts a change in the sideband amplitudes and quadrature phases of the SFG light. We might consider encoding information in the sidebands of the pump, analogous to that of a qubit; the AM idler acts like a "gate" to transform the amplitude and phase of the "state". We see from the calculations of Figure 6.5 that there is hope for spanning a significant portion of a hypothetical "Bloch sphere" representation of the sideband basis with AM idler operations.

While these experiments initially employ classical fields, the capability for single-photon experiments opens up possibilities for quantum information processing [123, 153, 154, 169, 262]. In that case, the challenge will be to spatially separate the photons from the various frequency bins. This separation process is typically achieved with commercial spectral demultiplexers, however, they typically operate with mode spacings around 10-25 GHz [105], much larger than the 100 kHz mode spacings used in the amplitude phase-control experiment. Pressure broadening in the SERF regime may permit larger frequency-bin separations.

10.3   Closing remarks

The physical universe is indeed a complex place, but the topics of this thesis show that complexity can be tamed through a combination of reductionist and emergent perspectives. Certainty, there is much more work to do in order to understand emergent nonlinear complexity, and it is possible that the universe continues to surprise us for a long time yet. I certainly hope so.

This thesis exemplifies the "nonlinear" path that my Ph.D. program has taken. Although many unexpected events and aspects have emerged along the way, they have combined to generate a cherished richness and depth of growth and learning. For that privilege, I stand in wonder and gratitude.

Bibliography

[1] M. A. Sullivan, "A cold atoms apparatus for a new hybrid quantum system,"
     Master's Thesis, University of Alberta, 2020.
     {p. iv}

[2] A. Tretiakov *et al.*, "Atomic microwave-to-optical signal transduction via magnetic-
     field coupling in a resonant microwave cavity," *Applied Physics Letters*, vol. 116,
     no. 16, 2020. DOI: 10.1063/1.5144616. arXiv: 2001.03150.
     {pp. iv, 109, 120, 143}

[3] A. Tretiakov, C. A. Potts, Y. Y. Lu, J. P. Davis, and L. J. LeBlanc, "Engi-
     neering atomic polarization with microwave-assisted optical pumping," 2021.
     arXiv: 2110.10673.
     {p. iv}

[4] Y.-Y. Lu, "Magnetometry with microwave-assisted optical oumping in warm
     Rb vapor and microfabricated Rb vapor cells," Master's Thesis, University of
     Alberta, 2021.
     {p. iv}

[5] B. D. Smith, B. Babaei, A. Narayanan, and L. J. LeBlanc, "Microwave-to-
     optical conversion in a room-temperature 87Rb vapor with frequency-division
     multiplexing control," *Communications Physics*, vol. 6, no. 1, p. 338, 2023.
     DOI: 10.1038/s42005-023-01455-y. arXiv: 2305.19221.
     {p. vi}

[6] B. Smith, B. Babaei, A. Narayanan, and L. LeBlanc, *Replication data for:
     Microwave-to-optical conversion in a room-temperature 87Rb vapor with frequency-
     division multiplexing control*, 2023. DOI: 10.5683/SP3/LGCNHZ.
     {p. vi}

[7] B. D. Smith, L. W. Cooke, and L. J. LeBlanc, "GPU-accelerated solutions of
     the nonlinear Schrödinger equation for simulating 2D spinor BECs," *Computer
     Physics Communications*, vol. 275, p. 108 314, 2022. DOI: 10.1016/j.cpc.2022.
     108314.
     {p. vii}

[8]   B. L. M. Johnson, "Food practices and nutrient intake of aging home-bound individuals by dietary history and biochemical data," Master's Thesis, University of Manitoba, 1964.
{p. xi}

[9]   C. S. Williams and G. H. Jensen, "An air thrust boat for waterfowl management," US Department of the Interior, Brigham City, UT, Tech. Rep., 1944.
{p. xi}

[10] G. H. Jensen, "Alligator airboats," in *Flyways: Pioneering Waterfowl Management in North America*, A. S. Hawkins, R. C. Hanson, H. K. Nelson, and H. M. Reeves, Eds., Washington, D.C.: The United States Department of the Interior, Fish and Wildlife Service, 1984.
{p. xi}

[11] M. Ruse, "Reductionism," in *The Oxford Companion to Philosophy*, T. Honderich, Ed., 2nd, Oxford: Oxford University Press, 2005.
{p. 1}

[12] S. Weinberg, *Third Thoughts: The Universe We Still Don't Know*. Cambridge, Massachusetts: The Belknap Press of the Harvard University Press, 2018.
{p. 1}

[13] J. Thomson, "Carriers of negative electricity," *Nobel Lectures*, 1906.
{p. 2}

[14] C. Cercignani, *Ludwig Boltzmann: The Man Who Trusted Atoms*. Oxford University Press, 2006. DOI: 10.1093/acprof:oso/9780198570646.001.0001.
{p. 2}

[15] I. Newton, "Optics," in *The World of Physics*, J. H. Weaver, Ed., New York: Simon and Schuster, 1987.
{p. 2}

[16] S. Berryman, "Democritus," in *The Stanford Encyclopedia of Philosophy*, E. N. Zalta and U. Nodelman, Eds., Spring 202, Metaphysics Research Lab, Stanford University, 2023.
{p. 2}

[17] P. W. Anderson, "More is different," *Science*, vol. 177, no. 4047, pp. 393–396, 1972. DOI: 10.1126/science.177.4047.393.
{p. 2}

[18] O. Artime and M. De Domenico, "From the origin of life to pandemics: Emergent phenomena in complex systems," *Philosophical Transactions of the Royal Society A: Mathematical, Physical and Engineering Sciences*, vol. 380, no. 2227, 2022. DOI: 10.1098/rsta.2020.0410. arXiv: 2205.11595.
{p. 2}

[19]   S. Kivelson and S. A. Kivelson, "Defining emergence in physics," *npj Quantum Materials*, vol. 1, no. 1, p. 16 024, 2016. DOI: 10.1038/npjquantmats.2016.24.
{p. 2}

[20]   J. Kim, "Emergent properties," in *The Oxford Companion to Philosophy*, T. Honderich, Ed., 2nd, Oxford: Oxford University Press, 2005. DOI: 10.4324/9781315516011-14.
{p. 2}

[21]   T. O'Connor, "Emergent properties," in *The Stanford Encyclopedia of Philosophy*, E. N. Zalta, Ed., Winter 202, Metaphysics Research Lab, Stanford University, 2021.
{p. 2}

[22]   D. K. Campbell, "Nonlinear science: From paradigms to practicalities," *Los Alamos Science*, no. 15, pp. 218–262, 1987.
{p. 2}

[23]   R. D. Knight, *Physics for Scientists and Engineers: A Strategic Approach*, 3rd. Pearson, 2013.
{p. 3}

[24]   L.-V. de Broglie, "On the theory of quanta," trans. by A. F. Kracklauer, *Ann. de Physique*, vol. 10, no. 3, 1925.
{p. 3}

[25]   L. de Broglie, "The wave nature of the electron," *Nobel Lectures*, vol. 24, no. 1, pp. 6–14, 1929.
{p. 3}

[26]   C. N. Cohen-Tannoudji, B. Diu, and F. Laloë, *Quantum Mechanics*, 1st ed. Paris, France: John Wiley & Sons, Inc., 1977.
{pp. 3, 11, 21, 23, 24, 33, 34, 38, 234, 235}

[27]   J. P. Mendonça, F. A. B. F. de Moura, M. L. Lyra, and G. M. A. Almeida, "Emergent nonlinear phenomena in discrete-time quantum walks," *Physical Review A*, vol. 101, no. 6, p. 062 335, 2020. DOI: 10.1103/PhysRevA.101.062335.
{p. 3}

[28]   L. S. Madsen *et al.*, "Quantum computational advantage with a programmable photonic processor," *Nature*, vol. 606, no. 7912, pp. 75–81, 2022. DOI: 10.1038/s41586-022-04725-x.
{p. 3}

[29] D. E. Chang, V. Vuletić, and M. D. Lukin, "Quantum nonlinear optics - photon by photon," *Nature Photonics*, vol. 8, no. 9, pp. 685–694, 2014. DOI: 10.1038/nphoton.2014.192.
{p. 3}

[30] M. Saffman, T. G. Walker, and K. Mølmer, "Quantum information with Rydberg atoms," *Reviews of Modern Physics*, vol. 82, no. 3, pp. 2313–2363, 2010. DOI: 10.1103/RevModPhys.82.2313. arXiv: 0909.4777.
{p. 3}

[31] S. Jeong, M. Kim, M. Hhan, J. Park, and J. Ahn, "Quantum programming of the satisfiability problem with Rydberg atom graphs," *Physical Review Research*, vol. 5, no. 4, p. 043 037, 2023. DOI: 10.1103/PhysRevResearch.5.043037. arXiv: 2302.14369.
{p. 3}

[32] C. S. Adams, J. D. Pritchard, and J. P. Shaffer, "Rydberg atom quantum technologies," *Journal of Physics B: Atomic, Molecular and Optical Physics*, vol. 53, no. 1, p. 012 002, 2020. DOI: 10.1088/1361-6455/ab52ef. arXiv: 1907.09231.
{p. 3}

[33] O. Firstenberg, C. S. Adams, and S. Hofferberth, "Nonlinear quantum optics mediated by Rydberg interactions," *Journal of Physics B: Atomic, Molecular and Optical Physics*, vol. 49, no. 15, p. 152 003, 2016. DOI: 10.1088/0953-4075/49/15/152003. arXiv: 1602.06117.
{p. 3}

[34] N. J. Lambert, A. Rueda, F. Sedlmeir, and H. G. L. Schwefel, "Coherent conversion between microwave and optical photons—An overview of physical implementations," *Advanced Quantum Technologies*, vol. 3, no. 1, p. 1 900 077, 2020. DOI: 10.1002/qute.201900077. arXiv: 1906.10255.
{pp. 4, 122, 141, 157}

[35] N. Bohr, "The structure of the atom," in *Nobel Lecture*, 1922.
{pp. 6–8, 41}

[36] D. J. Griffiths, *Introduction to Quantum Mechanics*, 2nd. Pearson, 2005.
{pp. 7, 15}

[37] D. H. McIntyre, *Quantum Mechanics*. Pearson, 2012.
{pp. 7, 8, 11, 26}

[38] A. Kramida, Y. Ralchenko, J. Reader, and N. A. T., *NIST Atomic Spectra Database (version 5.10)*, Online, 2022. DOI: https://doi.org/10.18434/T4W30F.
{pp. 7, 10, 19, 41}

[39] W. Demtröder, *Laser Spectroscopy: Basic Concepts and Instrumentation*, 3rd. Springer-Verllag, 2003.
{pp. 8, 42, 46, 48–50, 55, 57, 58, 109}

[40] C. J. Foot, *Atomic Physics*. New York: Oxford University Press, 2005.
{pp. 8, 10, 21, 22, 24, 30, 31, 38–40, 42, 46, 48, 69, 87, 92}

[41] I. I. Sobelman, *Atomic Spectra and Radiative Transitions*. Springer-Verlag, 1979.
{pp. 10, 12, 15, 36, 40, 234, 245}

[42] J.-f. V. Huele and J. Stenson, "Stern-Gerlach experiments: Past, present, and future," *Journal of the Utah Academy of Sciences, Arts and Letters*, vol. 81, pp. 206–212, 2004.
{p. 10}

[43] D. A. Steck, *Quantum and Atom Optics*. 2020.
{pp. 12, 13, 21, 23, 24, 27, 35}

[44] J. Muggli, "Cubic harmonics as linear combinations of spherical harmonics," *Zeitschrift für angewandte Mathematik und Physik ZAMP*, vol. 23, no. 2, pp. 311–317, 1972. DOI: 10.1007/BF01593094.
{p. 13}

[45] D. M. Brink and G. M. Satchler, *Angular Momentum*, 2nd. Oxford University Press, 1968.
{p. 14}

[46] *Mathematica (version 13.3)*, Champaign, IL, 2023.
{pp. 15, 236, 246}

[47] A. Meurer *et al.*, "SymPy: Symbolic computing in Python," *PeerJ Computer Science*, vol. 3, e103, 2017. DOI: 10.7717/peerj-cs.103.
{pp. 15, 236}

[48] N. Šibalić, J. Pritchard, C. Adams, and K. Weatherill, "ARC: An open-source library for calculating properties of alkali Rydberg atoms," *Computer Physics Communications*, vol. 220, pp. 319–331, 2017. DOI: 10.1016/j.cpc.2017.06.015. arXiv: 1612.05529.
{pp. 15, 35, 36}

[49] M. Auzinsh, D. Budker, and S. M. Rochester, *Optically Polarized Atoms*. Oxford University Press, 2010.
{pp. 16, 27, 30, 43, 45, 235–238}

[50] D. A. Steck, *Rubidium 87 D Line Data*, 2003.
{pp. 17, 19, 21, 34–36, 38, 46, 48, 110, 125, 128, 129, 148, 151, 177}

[51] D. Suter, *The Physics of Laser-Atom Interactions*. Cambridge, UK: Cambridge University Press, 1997.
{pp. 22, 24, 29, 42, 49, 55, 57}

[52] A. Zee, *Group Theory in a Nutshell for Physicists*. Princeton, NJ: Princeton University Press, 2016.
{pp. 26, 235}

[53] Y. Wu and X. Yang, "Strong-coupling theory of periodically driven two-level systems," *Physical Review Letters*, vol. 98, no. 1, p. 013601, 2007. DOI: 10.1103/PhysRevLett.98.013601.
{p. 27}

[54] M. Fox, *Quantum Optics: An Introduction*. Oxford University Press, 2006.
{pp. 29, 42}

[55] R. Loudon, *The Quantum Theory of Light*. Oxford University Press, 1983.
{pp. 29, 42, 55, 196}

[56] H. J. Metcalf and P. van der Straten, *Laser Cooling and Trapping*. New York, NY: Springer, 1999.
{pp. 30, 31}

[57] J. R. Johansson, P. D. Nation, and F. Nori, "QuTiP: An open-source Python framework for the dynamics of open quantum systems," *Computer Physics Communications*, vol. 183, no. 8, pp. 1760–1772, 2012. DOI: 10.1016/j.cpc.2012.02.021. arXiv: 1110.0573.
{pp. 30, 31}

[58] D. Manzano, "A short introduction to the Lindblad master equation," *AIP Advances*, vol. 10, no. 2, p. 025106, 2020. DOI: 10.1063/1.5115323. arXiv: 1906.04478.
{pp. 30, 31}

[59] A. Tretiakov, "Manipulating optical properties of rubidium through microwave interactions," Ph.D. dissertation, University of Alberta, 2021.
{pp. 31, 120, 122}

[60] L. Downes, "Simple Python tools for modelling few-level atom-light interactions," *Journal of Physics B: Atomic, Molecular and Optical Physics*, vol. 56, no. 22, p. 223001, 2023. DOI: 10.1088/1361-6455/acee3a. arXiv: 2307.16839.
{pp. 31, 33}

[61] J. R. Johansson, P. D. Nation, and F. Nori, "QuTiP 2: A Python framework for the dynamics of open quantum systems," *Computer Physics Communications*, vol. 184, no. 4, pp. 1234–1240, 2013. DOI: 10.1016/j.cpc.2012.11.019. arXiv: 1211.6518.
{p. 31}

[62] S. Chang and V. Minogin, "Density-matrix approach to dynamics of multilevel atoms in laser fields," *Physics Reports*, vol. 365, no. 2, pp. 65–143, 2002. DOI: 10.1016/S0370-1573(02)00016-9.
{p. 33}

[63] M. Gegg and M. Richter, "Efficient and exact numerical approach for many multi-level systems in open system CQED," *New Journal of Physics*, vol. 18, no. 4, p. 043 037, 2016. DOI: 10.1088/1367-2630/18/4/043037.
{p. 33}

[64] M. Frasca, "A modern review of the two-level approximation," *Annals of Physics*, vol. 306, no. 2, pp. 193–208, 2003. DOI: 10.1016/S0003-4916(03)00078-2. arXiv: 0209056 [quant-ph].
{p. 33}

[65] R. Finkelstein, S. Bali, O. Firstenberg, and I. Novikova, "A practical guide to electromagnetically induced transparency in atomic vapor," *New Journal of Physics*, vol. 25, no. 3, p. 035 001, 2023. DOI: 10.1088/1367-2630/acbc40. arXiv: 2205.10959.
{pp. 33, 65, 166}

[66] M. S. Lazarow, "Simulating open quantum systems: Computational condensed matter via graphics processing units," Bachelor's Thesis, Northwestern University, 2017.
{p. 33}

[67] C. T. Fancher, D. R. Scherer, M. C. S. John, and B. L. S. Marlow, "Rydberg atom electric field sensors for communications and sensing," *IEEE Transactions on Quantum Engineering*, vol. 2, pp. 1–13, 2021. DOI: 10.1109/tqe.2021.3065227.
{p. 34}

[68] Y. Y. Jau and T. Carter, "Vapor-cell-based atomic electrometry for detection frequencies below 1 kHz," *Physical Review Applied*, vol. 13, no. 5, p. 054 034, 2020. DOI: 10.1103/PhysRevApplied.13.054034. arXiv: 2002.04145.
{p. 34}

[69] D. Budker, D. F. Kimball, D. P. Demille, and S. K. Lamoreaux, *Atomic Physics: An Exploration Through Problems and Solutions*, 2nd. Oxford University Press, 2008. DOI: 10.1063/1.1897567.
{pp. 39, 49, 52, 155, 156}

[70] P. Barakhshan, A. Bhosale, A. Kiruga, R. Eigenmann, M. S. Safronova, and B. Arora, *A Portal for High-Precision Atomic Data and Computation: Design and Best Practices*, Newark, DE, 2022. arXiv: 2212.10665.
{p. 41}

[71] R. H. Dicke, "Coherence in spontaneous radiation processes," *Physical Review*, vol. 93, no. 1, pp. 99–110, 1954. DOI: 10.1103/PhysRev.93.99.
{p. 42}

[72] H. Gould and J. Tobochnik, *Statistical and Thermal Physics: With Computer Applications.* Princeton, NJ: Princeton University Press, 2010.
{p. 43}

[73] P. Virtanen *et al.*, "SciPy 1.0: Fundamental algorithms for scientific computing in Python," *Nature Methods*, vol. 17, no. 3, pp. 261–272, 2020. DOI: 10.1038/s41592-019-0686-2.
{p. 45}

[74] E. Whiting, "An empirical approximation to the Voigt profile," *Journal of Quantitative Spectroscopy and Radiative Transfer*, vol. 8, no. 6, pp. 1379–1384, 1968. DOI: 10.1016/0022-4073(68)90081-2.
{p. 45}

[75] P. Siddons, C. S. Adams, C. Ge, and I. G. Hughes, "Absolute absorption on rubidium D lines: Comparison between theory and experiment," *Journal of Physics B: Atomic, Molecular and Optical Physics*, vol. 41, no. 15, p. 155 004, 2008. DOI: 10.1088/0953-4075/41/15/155004. arXiv: 0805.1139.
{pp. 46, 128, 129, 153}

[76] W. Happer, "Optical Pumping," *Reviews of Modern Physics*, vol. 44, no. 2, pp. 169–249, 1972.
{pp. 49–52}

[77] W. Happer, Y.-Y. Jau, and T. Walker, *Optically Pumped Atoms.* Wiley-VCH, 2010.
{pp. 50, 155}

[78] H. Chi, W. Quan, J. Zhang, L. Zhao, and J. Fang, "Advances in anti-relaxation coatings of alkali-metal vapor cells," *Applied Surface Science*, vol. 501, p. 143 897, 2020. DOI: 10.1016/j.apsusc.2019.143897.
{pp. 51, 166}

[79] M. A. Bouchiat and J. Brossel, "Relaxation of optically pumped Rb Atoms on paraffin-coated walls," *Physical Review*, vol. 147, no. 1, pp. 41–54, 1966. DOI: 10.1103/PhysRev.147.41.
{p. 51}

[80] S. J. Seltzer *et al.*, "Investigation of antirelaxation coatings for alkali-metal vapor cells using surface science techniques," *Journal of Chemical Physics*, vol. 133, no. 14, p. 144 703, 2010. DOI: 10.1063/1.3489922. arXiv: 1002.4417.
{p. 51}

207

[81] M. V. Balabas, T Karaulanov, M. P. Ledbetter, and D Budker, "Polarized alkali-metal vapor with minute-long transverse spin-relaxation time," *Physical Review Letters*, vol. 105, no. 7, p. 070 801, 2010. DOI: 10.1103/PhysRevLett. 105.070801.
{pp. 51, 166}

[82] D. Main *et al.*, "Preparing narrow velocity distributions for quantum memories in room-temperature alkali-metal vapors," *Physical Review A*, vol. 103, no. 4, p. 043 105, 2021. DOI: 10.1103/PhysRevA.103.043105. arXiv: 2011.03766.
{pp. 51, 196}

[83] D Budker, L Hollberg, D. F. Kimball, J Kitching, S Pustelny, and V. V. Yashchuk, "Microwave transitions and nonlinear magneto-optical rotation in anti-relaxation-coated cells," *Physical Review A*, vol. 71, p. 012 903, 2005. DOI: 10.1103/PhysRevA.71.012903.
{p. 51}

[84] M. Rosner *et al.*, "A highly drift-stable atomic magnetometer for fundamental physics experiments," *Applied Physics Letters*, vol. 120, no. 16, p. 161 102, 2022. DOI: 10.1063/5.0083854. arXiv: 2201.06936.
{p. 51}

[85] W. Happer and A. C. Tam, "Effect of rapid spin exchange on the magnetic-resonance spectrum of alkali vapors," *Physical Review A*, vol. 16, no. 5, pp. 1877– 1891, 1977. DOI: 10.1103/PhysRevA.16.1877.
{p. 51}

[86] J. C. Allred, R. N. Lyman, T. W. Kornack, and M. V. Romalis, "High-sensitivity atomic magnetometer unaffected by spin-exchange relaxation," *Physical Review Letters*, vol. 89, no. 13, pp. 1 308 011–1 308 014, 2002. DOI: 10.1103/ physrevlett.89.130801.
{p. 51}

[87] M. Dikopoltsev, U. Levy, and O. Katz, "Magnetic field independent SERF magnetometer," 2022. arXiv: 2209.13086.
{p. 52}

[88] R. W. Boyd, *Nonlinear Optics*. San Diego, CA: Academic Press, 1992.
{pp. 53–58, 67, 68, 70, 101}

[89] J. Peatross and M. Ware, *Physics of Light and Optics*. Brigham Young University, 2013.
{pp. 53, 54, 67, 232}

[90] D. J. Griffiths, *Introduction to Electrodynamics*, 4th. Pearson, 2013.
{pp. 53, 120}

[91] S. E. Harris, M. K. Oshman, and R. L. Byer, "Observation of tunable optical parametric fluorescence," *Physical Review Letters*, vol. 18, no. 18, pp. 732–734, 1967. DOI: 10.1103/PhysRevLett.18.732.
{p. 56}

[92] D. C. Burnham and D. L. Weinberg, "Observation of simultaneity in parametric production of optical photon pairs," *Physical Review Letters*, vol. 25, no. 2, pp. 84–87, 1970. DOI: 10.1103/PhysRevLett.25.84.
{p. 57}

[93] P. G. Kwiat, K. Mattle, H. Weinfurter, A. Zeilinger, A. V. Sergienko, and Y. Shih, "New high-intensity source of polarization-entangled photon pairs," *Physical Review Letters*, vol. 75, no. 24, pp. 4337–4341, 1995. DOI: 10.1103/PhysRevLett.75.4337.
{p. 57}

[94] G. Lerner, M. E. Tzur, O. Neufeld, A. Fleischer, and O. Cohen, "New photonic conservation laws in parametric nonlinear optics," 2023. arXiv: 2311.10371.
{p. 57}

[95] S. Merkouche, V. Thiel, and B. J. Smith, "Positive operator-valued measure for two-photon detection via sum-frequency generation," *Physical Review A*, vol. 103, no. 4, p. 043 711, 2021. DOI: 10.1103/PhysRevA.103.043711. arXiv: 2101.06360.
{p. 58}

[96] C. Couteau, "Spontaneous parametric down-conversion," *Contemporary Physics*, vol. 59, no. 3, pp. 291–304, 2018. DOI: 10.1080/00107514.2018.1488463. arXiv: 1809.00127.
{pp. 58, 70}

[97] P. A. Franken, A. E. Hill, C. W. Peters, and G. Weinreich, "Generation of optical harmonics," *Physical Review Letters*, vol. 7, no. 4, pp. 118–119, 1961. DOI: 10.1103/PhysRevLett.7.118.
{p. 59}

[98] K. V. Adwaith *et al.*, "Microwave controlled ground state coherence in an atom-based optical amplifier," *OSA Continuum*, vol. 4, no. 2, p. 702, 2021. DOI: 10.1364/OSAC.413297.
{pp. 62, 65, 67, 68}

[99] W. W. Erickson, "Electromagnetically induced transparency," Bachelor's Thesis, Reed College, 2012.
{p. 65}

[100] H. Li, V. A. Sautenkov, Y. V. Rostovtsev, G. R. Welch, P. R. Hemmer, and M. O. Scully, "Electromagnetically induced transparency controlled by a microwave field," *Physical Review A*, vol. 80, no. 2, p. 023 820, 2009. DOI: 10.1103/PhysRevA.80.023820. arXiv: arXiv:0903.1457v1.
{pp. 68, 197}

[101] T. P. Ogden, "Resonant pulse propagation in dense atomic vapours," Ph.D. dissertation, Durham University, 2016.
{pp. 68, 70, 196}

[102] L. L. Lewis, "An introduction to frequency standards," *Proceedings of the IEEE*, vol. 79, no. 7, p. 927, 1991. DOI: 10.1049/sqj.1942.0035.
{p. 69}

[103] P. Liu *et al.*, "Scheme for a compact cold-atom clock based on diffuse laser cooling in a cylindrical cavity," *Physical Review A*, vol. 92, no. 6, p. 062 101, 2015. DOI: 10.1103/PhysRevA.92.062101. arXiv: arXiv:1509.07650v1.
{p. 69}

[104] M. Gharavipour *et al.*, "High performance vapour-cell frequency standards," *Journal of Physics: Conference Series*, vol. 723, no. 1, p. 012 006, 2016. DOI: 10.1088/1742-6596/723/1/012006.
{p. 69}

[105] L. Lundberg *et al.*, "Phase-coherent lightwave communications with frequency combs," *Nature Communications*, vol. 11, no. 1, pp. 1–7, 2020. DOI: 10.1038/s41467-019-14010-7. arXiv: 1905.04963.
{pp. 73, 199}

[106] A. E. Willner, K. Pang, H. Song, K. Zou, and H. Zhou, "Orbital angular momentum of light for communications," *Applied Physics Reviews*, vol. 8, no. 4, p. 041 312, 2021. DOI: 10.1063/5.0054885.
{p. 73}

[107] G. D. VanWiggeren and R. Roy, "Communication with dynamically fluctuating states of light polarization," *Physical Review Letters*, vol. 88, no. 9, p. 097 903, 2002. DOI: 10.1103/PhysRevLett.88.097903.
{p. 73}

[108] A. Shikder and N. K. Nishchal, "Image encryption using binary polarization states of light beam," *Scientific Reports*, vol. 13, no. 1, p. 14 028, 2023. DOI: 10.1038/s41598-023-41251-w.
{p. 73}

[109] H. Li, "Encoding information as orbital angular momentum states of light for wireless optical communications," *Optical Engineering*, vol. 46, no. 1, p. 019 701, 2007. DOI: 10.1117/1.2431800.
{p. 73}

[110] J. Wang, J. Liu, S. Li, Y. Zhao, J. Du, and L. Zhu, "Orbital angular momentum and beyond in free-space optical communications," *Nanophotonics*, vol. 11, no. 4, pp. 645–680, 2022. DOI: 10.1515/nanoph-2021-0527.
{p. 73}

[111] F. Bouchard, D. England, P. J. Bustard, K. Heshami, and B. Sussman, "Quantum communication with ultrafast time-bin qubits," *PRX Quantum*, vol. 3, no. 1, p. 010 332, 2022. DOI: 10.1103/PRXQuantum.3.010332.
{p. 73}

[112] T. Hrushevskyi, "Quantum gas apparatus for Bose-Einstein condensation of 87Rb," Master's Thesis, University of Alberta, 2017.
{pp. 87, 90, 92, 105, 230}

[113] A. Sit, L. Giner, E. Karimi, and J. S. Lundeen, "General lossless spatial polarization transformations," *Journal of Optics*, vol. 19, no. 9, p. 094 003, 2017. DOI: 10.1088/2040-8986/aa7f65. arXiv: 1702.06108.
{p. 98}

[114] N. Peters, J. Altepeter, E. Jeffrey, D. Branning, and P. Kwiat, "Precise creation, characterization, and manipulation of single optical qubits," *Quantum Information and Computation*, vol. 3, pp. 503–517, 2003. DOI: 10.26421/QIC3.s-4. arXiv: 0502177 [quant-ph].
{p. 98}

[115] S. Zhang, X. Zhang, S. Liu, and Y. Liu, "Measurement of modulation index and half-wave voltage of an electro-optical phase modulator with a dispersion-based phase filter," *Optics Communications*, vol. 285, no. 24, pp. 5089–5093, 2012. DOI: 10.1016/j.optcom.2012.07.039.
{p. 102}

[116] K. Toki *et al.*, "Frequency response measurement of half-wave voltage and chirp parameter of LiNbO3 intensity modulators in low frequency range," in *2011 International Topical Meeting on Microwave Photonics jointly held with the 2011 Asia-Pacific Microwave Photonics Conference*, IEEE, 2011, pp. 354–356. DOI: 10.1109/MWP.2011.6088744.
{p. 102}

[117] M. Aillerie, P. Bourson, M. Mostefa, F. Abdi, and M. D. Fontana, "Photorefractive damage in congruent LiNbO3. Part I. Zinc doped lithium niobate crystals," *Journal of Physics: Conference Series*, vol. 416, no. 1, p. 012 001, 2013. DOI: 10.1088/1742-6596/416/1/012001.
{p. 104}

[118] J. Villarroel *et al.*, "Analysis of photorefractive optical damage in lithium niobate: Application to planar waveguides," *Optics Express*, vol. 18, no. 20, p. 20 852, 2010. DOI: 10.1364/OE.18.020852.
{p. 104}

[119] L. G. Kazovsky, "Optical heterodyning versus optical homodyning: A comparison," *Journal of Optical Communications*, vol. 6, no. 1, pp. 18–24, 1985. DOI: 10.1515/JOC.1985.6.1.18.
{p. 105}

[120] D. S. Batista, F. Granziera, M. C. Tosin, and L. F. De Melo, "Three-axial Helmholtz coil design and validation for aerospace applications," *IEEE Transactions on Aerospace and Electronic Systems*, vol. 54, no. 1, pp. 392–403, 2018. DOI: 10.1109/TAES.2017.2760560.
{pp. 108, 109}

[121] United States. National Bureau of Standards, *Copper wire tables*. Washington Government Printing Office, 1914.
{p. 108}

[122] M. E. V. Valkenburg and W. M. Middleton, *Reference Data for Engineers: Radio, Electronics, Computer, and Communications*, 9th. Newnes, 2002.
{p. 108}

[123] H.-H. Lu, E. M. Simmerman, P. Lougovski, A. M. Weiner, and J. M. Lukens, "Fully arbitrary control of frequency-bin qubits," *Physical Review Letters*, vol. 125, no. 12, p. 120 503, 2020. DOI: 10.1103/PhysRevLett.125.120503.
{pp. 109, 164, 199}

[124] D. M. Pozar, *Microwave Engineering*, 3rd. John Wiley & Sons, Inc., 2005.
{pp. 112, 117, 118, 122, 123, 125}

[125] D. Rieger, S. Günzler, M. Spiecker, A. Nambisan, W. Wernsdorfer, and I. Pop, "Fano interference in microwave resonator measurements," *Physical Review Applied*, vol. 20, no. 1, p. 014 059, 2023. DOI: 10.1103/PhysRevApplied.20.014059. arXiv: 2209.03036.
{p. 117}

[126] S. Probst, F. B. Song, P. A. Bushev, A. V. Ustinov, and M. Weides, "Efficient and robust analysis of complex scattering data under noise in microwave resonators," *Review of Scientific Instruments*, vol. 86, no. 2, p. 024 706, 2015. DOI: 10.1063/1.4907935. arXiv: 1410.3365.
{p. 118}

[127] M. S. Khalil, M. J. A. Stoutimore, F. C. Wellstood, and K. D. Osborn, "An analysis method for asymmetric resonator transmission applied to superconducting devices," *Journal of Applied Physics*, vol. 111, no. 5, p. 054 510, 2012. DOI: 10.1063/1.3692073. arXiv: 1108.3117.
{p. 118}

[128] R. T. Learn, E. Varga, V. Vadakkumbatt, and J. P. Davis, "Precision measurements of the zero-temperature dielectric constant and density of liquid 4He," *Physical Review B*, vol. 106, no. 21, p. 214 509, 2022. DOI: 10.1103/PhysRevB.106.214509. arXiv: 2207.08852.
{pp. 120, 121}

[129] H. Thal, "Cylindrical TE/sub 011/ /TM/sub 111/ Mode Control by Cavity Shaping," *IEEE Transactions on Microwave Theory and Techniques*, vol. 27, no. 12, pp. 982–986, 1979. DOI: 10.1109/TMTT.1979.1129777.
{p. 120}

[130] N Ashby, S. Romisch, and S. Jefferts, "Endcaps for TE/sub 01/ cavities in fountain frequency standards," in *IEEE International Frequency Control Sympposium and PDA Exhibition Jointly with the 17th European Frequency and Time Forum, 2003. Proceedings of the 2003*, vol. 0, IEEE, 2003, pp. 1076–1083. DOI: 10.1109/FREQ.2003.1275240.
{p. 120}

[131] T. M. Huang, W. M. Pan, G. W. Wang, T. Furuya, and S. Mitsunobu, "Calculation of the external quality factor of the high power input coupler for the BEPCII superconducting cavity," *Chinese Physics C*, vol. 32, no. 1, pp. 72–74, 2008. DOI: 10.1088/1674-1137/32/1/016.
{p. 124}

[132] G. Reinaudi, T. Lahaye, Z. Wang, and D. Guéry-Odelin, "Strong saturation absorption imaging of dense clouds of ultracold atoms," *Optics Letters*, vol. 32, no. 21, p. 3143, 2007. DOI: 10.1364/ol.32.003143. arXiv: 0707.2930.
{p. 127}

[133] T Karaulanov *et al.*, "Controlling atomic vapor density in paraffin-coated cells using light-induced atomic desorption," *Physical Review A*, vol. 79, no. 1, p. 012 902, 2009. DOI: 10.1103/PhysRevA.79.012902.
{p. 129}

[134] J. Lu *et al.*, "In-Situ Measurement of Electrical-Heating-Induced Magnetic Field for an Atomic Magnetometer," *Sensors*, vol. 20, no. 7, p. 1826, 2020. DOI: 10.3390/s20071826.
{p. 130}

[135] D. S. Durfee, *Physics phor Phanatics.* 2006.
{p. 131}

[136] C. Rauscher, *Fundamentals of Spectrum Analysis.* Munchen, Germany: Rohde & Schwarz, 2001.
{pp. 131, 133–136}

[137] Keysight Technologies, "Spectrum Analysis Basics: Application Note 150," Tech. Rep., 2014.
{pp. 133, 135, 136}

[138] F. Arute *et al.*, "Quantum supremacy using a programmable superconducting processor," *Nature*, vol. 574, no. 7779, pp. 505–510, 2019. DOI: 10.1038/s41586-019-1666-5.
{p. 140}

[139] N. T. Son *et al.*, "Developing silicon carbide for quantum spintronics," *Applied Physics Letters*, vol. 116, no. 19, p. 190 501, 2020. DOI: 10.1063/5.0004454.
{p. 140}

[140] S. Storz *et al.*, "Loophole-free Bell inequality violation with superconducting circuits," *Nature*, vol. 617, no. 7960, pp. 265–270, 2023. DOI: 10.1038/s41586-023-05885-0.
{p. 141}

[141] N. Lauk *et al.*, "Perspectives on quantum transduction," *Quantum Science and Technology*, vol. 5, no. 2, p. 020 501, 2020. DOI: 10.1088/2058-9565/ab788a. arXiv: 1910.04821.
{p. 141}

[142] L. Fan *et al.*, "Superconducting cavity electro-optics: A platform for coherent photon conversion between superconducting and photonic circuits," *Science Advances*, vol. 4, no. 8, eaar4994, 2018. DOI: 10.1126/sciadv.aar4994. arXiv: 1805.04509.
{p. 141}

[143] R. Hisatomi *et al.*, "Bidirectional conversion between microwave and light via ferromagnetic magnons," *Physical Review B*, vol. 93, no. 17, p. 174 427, 2016. DOI: 10.1103/PhysRevB.93.174427.
{pp. 141, 193}

[144] A. P. Higginbotham *et al.*, "Harnessing electro-optic correlations in an efficient mechanical converter," *Nature Physics*, vol. 14, no. 10, pp. 1038–1042, 2018. DOI: 10.1038/s41567-018-0210-0. arXiv: 1712.06535.
{p. 141}

[145] J. Han, T. Vogt, C. Gross, D. Jaksch, M. Kiffner, and W. Li, "Coherent microwave-to-optical conversion via six-wave mixing in Rydberg atoms," *Physical Review Letters*, vol. 120, no. 9, p. 093 201, 2018. DOI: 10.1103/PhysRevLett.120.093201.
{pp. 141, 156, 158, 165}

[146] K. V. Adwaith, A. Karigowda, C. Manwatkar, F. Bretenaker, and A. Narayanan, "Coherent microwave-to-optical conversion by three-wave mixing in a room temperature atomic system," *Optics Letters*, vol. 44, no. 1, p. 33, 2019. DOI: 10.1364/OL.44.000033.
{pp. 141, 150, 151, 156, 157, 166, 194}

[147] H.-T. Tu *et al.*, "High-efficiency coherent microwave-to-optics conversion via off-resonant scattering," *Nature Photonics*, vol. 16, no. 4, pp. 291–296, 2022. DOI: 10.1038/s41566-022-00959-3. arXiv: 2203.04178.
{pp. 141, 158, 165}

[148] S. Borówka, U. Pylypenko, M. Mazelanik, and M. Parniak, "Continuous wide-band microwave-to-optical converter based on room-temperature Rydberg atoms," *Nature Photonics*, vol. 18, no. 1, pp. 32–38, 2024. DOI: 10.1038/s41566-023-01295-w. arXiv: 2302.08380.
{pp. 141, 193}

[149] T. Vogt *et al.*, "Efficient microwave-to-optical conversion using Rydberg atoms," *Physical Review A*, vol. 99, no. 2, p. 023 832, 2019. DOI: 10.1103/PhysRevA.99.023832. arXiv: 1810.09722.
{p. 141}

[150] N. Zhu *et al.*, "Waveguide cavity optomagnonics for microwave-to-optics conversion," *Optica*, vol. 7, no. 10, p. 1291, 2020. DOI: 10.1364/optica.397967.
{pp. 141, 165, 166, 193}

[151] Y. Tsuchimoto *et al.*, "Large-bandwidth transduction between an optical single quantum dot molecule and a superconducting resonator," *PRX Quantum*, vol. 3, no. 3, p. 030 336, 2022. DOI: 10.1103/PRXQuantum.3.030336. arXiv: 2110.03230.
{p. 141}

[152] Z. Shen *et al.*, "Coherent coupling between phonons, magnons, and photons," *Physical Review Letters*, vol. 129, no. 24, p. 243 601, 2022. DOI: 10.1103/PhysRevLett.129.243601.
{pp. 141, 165, 166}

[153] H. H. Lu *et al.*, "Electro-optic frequency beam splitters and tritters for high-fidelity photonic quantum information processing," *Physical Review Letters*, vol. 120, no. 3, p. 30 502, 2018. DOI: 10.1103/PhysRevLett.120.030502.
{pp. 142, 164, 165, 199}

[154] J. M. Lukens, "Quantum information processing with frequency-bin qubits: Progress, status, and challenges," in *Conference on Lasers and Electro-Optics*, Washington, D.C.: OSA, 2019, JTu4A.3. DOI: 10.1364/CLEO_AT.2019.JTu4A.3.
{pp. 143, 166, 199}

[155] M. Ruether, C. A. Potts, J. P. Davis, and L. J. LeBlanc, "Polymer-loaded three dimensional microwave cavities for hybrid quantum systems," *Journal of Physics Communications*, vol. 5, no. 12, p. 121 001, 2021. DOI: 10.1088/2399-6528/ac3cff. arXiv: 2104.10237.
{p. 143}

[156] K. Campbell, Y.-J. Wang, I. Savukov, P. D. D. Schwindt, Y.-Y. Jau, and V. Shah, "Gradient field detection using interference of stimulated microwave optical sidebands," *Physical Review Letters*, vol. 128, no. 16, p. 163 602, 2022. DOI: 10.1103/PhysRevLett.128.163602.
{p. 144}

[157] N. Caselli *et al.*, "Generalized Fano lineshapes reveal exceptional points in photonic molecules," *Nature Communications*, vol. 9, no. 1, p. 396, 2018. DOI: 10.1038/s41467-018-02855-3.
{pp. 147, 148}

[158] D Pizzey, J. D. Briscoe, F. D. Logue, F. S. Ponciano-Ojeda, S. A. Wrathmall, and I. G. Hughes, "Laser spectroscopy of hot atomic vapours: From 'scope to theoretical fit," *New Journal of Physics*, vol. 24, no. 12, p. 125 001, 2022. DOI: 10.1088/1367-2630/ac9cfe.
{p. 153}

[159] T. G. Walker, "Estimates of spin-exchange parameters for alkali-metal–noble-gas pairs," *Physical Review A*, vol. 40, no. 9, pp. 4959–4964, 1989. DOI: 10.1103/PhysRevA.40.4959.
{p. 156}

[160] A. Kumar *et al.*, "Quantum-limited millimeter wave to optical transduction," 2022. arXiv: 2207.10121.
{p. 158}

[161] H. Tanji-Suzuki *et al.*, "Interaction between Atomic Ensembles and Optical Resonators," in *Advances in Atomic, Molecular and Optical Physics*, vol. 60, 2011, pp. 201–237. DOI: 10.1016/B978-0-12-385508-4.00004-8. arXiv: 1104.3594.
{pp. 158, 159}

[162] H. J. Kimble, "Strong interactions of single atoms and photons in cavity QED," *Physica Scripta*, vol. 1998, no. T76, p. 127, 1998. DOI: 10.1238/Physica.Topical.076a00127.
{p. 158}

[163] N. T. Otterstrom *et al.*, "Nonreciprocal frequency domain beam splitter," *Physical Review Letters*, vol. 127, no. 25, p. 253 603, 2021. DOI: 10.1103/PhysRevLett.127.253603.
{p. 164}

[164] C.-Z. Chai *et al.*, "Single-sideband microwave-to-optical conversion in high-Q ferrimagnetic microspheres," *Photonics Research*, vol. 10, no. 3, p. 820, 2022. DOI: 10.1364/prj.446226. arXiv: 2111.07325.
{pp. 164, 193}

[165] J. Peng, Z. Liu, K. Yin, S. Zou, and H. Yuan, "Determination of the partial and total pressures of the mixed gases in atomic vapor cells by optical absorption," *Journal of Physics D: Applied Physics*, vol. 55, no. 36, p. 365 005, 2022. DOI: 10.1088/1361-6463/ac73c0.
{p. 165}

[166] N. D. Zameroski, G. D. Hager, W. Rudolph, C. J. Erickson, and D. A. Hostutler, "Pressure broadening and collisional shift of the Rb D2 absorption line by CH4, C2H6, C3H8, n-C4H10, and He," *Journal of Quantitative Spectroscopy and Radiative Transfer*, vol. 112, no. 1, pp. 59–67, 2011. DOI: 10.1016/j.jqsrt.2010.08.016.
{p. 165}

[167] L.-C. Ha, X. Zhang, N. Dao, and K. R. Overstreet, "D1 line broadening and hyperfine frequency shift coefficients for 87Rb and 133Cs in Ne, Ar, and N2," *Physical Review A*, vol. 103, no. 2, p. 022 826, 2021. DOI: 10.1103/PhysRevA.103.022826.
{p. 165}

[168] A. Godone, F. Levi, and J. Vanier, "Coherent microwave emission in cesium under coherent population trapping," *Physical Review A*, vol. 59, no. 1, R12(R), 1999. DOI: 10.1103/PhysRevA.59.R12.
{p. 165}

[169] J. M. Lukens and P. Lougovski, "Frequency-encoded photonic qubits for scalable quantum information processing," *Optica*, vol. 4, no. 1, p. 8, 2017. DOI: 10.1364/OPTICA.4.000008.
{pp. 166, 199}

[170] L. Olislager *et al.*, "Frequency-bin entangled photons," *Physical Review A*, vol. 82, no. 1, p. 013 804, 2010. DOI: 10.1103/PhysRevA.82.013804. arXiv: 0910.1325.
{p. 166}

[171] W. Franzen, "Spin relaxation of optically aligned rubidium vapor," *Physical Review*, vol. 115, no. 4, pp. 850–856, 1959. DOI: 10.1103/PhysRev.115.850.
{p. 166}

[172] W. Li *et al.*, "Characterization of high-temperature performance of cesium vapor cells with anti-relaxation coating," *Journal of Applied Physics*, vol. 121, no. 6, p. 063 104, 2017. DOI: 10.1063/1.4976017. arXiv: 1609.04867.
{p. 166}

[173] S. Jiang *et al.*, "Observation of prolonged coherence time of the collective spin wave of an atomic ensemble in a paraffin-coated 87Rb vapor cell," *Physical Review A*, vol. 80, no. 6, p. 062 303, 2009. DOI: 10.1103/PhysRevA.80.062303.
{p. 166}

[174] J Radić, T. A. Sedrakyan, I. B. Spielman, and V Galitski, "Vortices in spin-orbit-coupled Bose-Einstein condensates," *Physical Review A*, vol. 84, no. 6, p. 063 604, 2011. DOI: 10.1103/PhysRevA.84.063604.
{pp. 168, 175–177, 179, 260, 261}

[175] F. Dalfovo, S. Giorgini, L. P. Pitaevskii, and S. Stringari, "Theory of Bose-Einstein condensation in trapped gases," *Reviews of Modern Physics*, vol. 71, no. 3, pp. 463–512, 1999. DOI: 10.1103/RevModPhys.71.463.
{pp. 168, 175, 265}

[176] W. Bao, "The nonlinear Schrödinger equation and applications in Bose-Einstein condensation and plasma physics," in *Dynamics in Models of Coarsening, Coagulation, Condensation and Quantization*, vol. 9, World Scientific Publishing Co., 2007, pp. 141–239. DOI: 10.1142/9789812770226_0003.
{p. 168}

[177] R. Caplan, "NLSEmagic: Nonlinear Schrödinger equation multi-dimensional Matlab-based GPU-accelerated integrators using compact high-order schemes," *Computer Physics Communications*, vol. 184, no. 4, pp. 1250–1271, 2013. DOI: 10.1016/j.cpc.2012.12.010.
{pp. 168, 189}

[178] G Kuracz, L. R. Kiperman, F Reyna, and P. I. Fierens, "Simulation of pulse propagation in nonlinear optical fibers using GPUs," in *2016 IEEE Congreso Argentino de Ciencias de la Informática y Desarrollos de Investigación (CACIDI)*, 2016, pp. 1–5. DOI: 10.1109/CACIDI.2016.7785989.
{pp. 168, 189}

[179] M. Brehler, M. Schirwon, D. Goddeke, and P. M. Krummrich, "A GPU-accelerated fourth-order Runge–Kutta in the interaction picture method for the simulation of nonlinear signal propagation in multimode fibers," *Journal of Lightwave Technology*, vol. 35, no. 17, pp. 3622–3628, 2017. DOI: 10.1109/JLT.2017.2715358.
{p. 168}

[180] G. Siyu and Z. Jianyong, "GPU-accelerated performance on numerically solving multimode Schrödinger equation," in *Sixth Symposium on Novel Optoelectronic Detection Technology and Applications*, H. Jiang and J. Chu, Eds., vol. 11455, 2020, p. 133. DOI: 10.1117/12.2563988.
{pp. 168, 189}

[181] D. H. Peregrine, "Water waves, nonlinear Schrödinger equations and their solutions," *The Journal of the Australian Mathematical Society. Series B. Applied Mathematics*, vol. 25, no. 1, pp. 16–43, 1983. DOI: 10.1017/S0334270000003891.
{p. 168}

[182] C. Chabalko, A. Moitra, and B. Balachandran, "Rogue waves: New forms enabled by GPU computing," *Physics Letters A*, vol. 378, no. 32-33, pp. 2377–2381, 2014. DOI: 10.1016/j.physleta.2014.06.013.
{pp. 168, 170, 181, 189}

[183] N. Karjanto, "The nonlinear Schrödinger equation: A mathematical model with its wide-ranging applications," in *Understanding the Schrödinger Equation: Some [Non]Linear Perspectives*, V. A. Simpao and H. C. Little, Eds., Nova Science Pub Inc, 2019, ch. 5. arXiv: 1912.10683.
{p. 169}

[184] M. Wróblewski, "Nonlinear Schrödinger approach to European option pricing," *Open Physics*, vol. 15, no. 1, pp. 280–291, 2017. DOI: 10.1515/phys-2017-0031.
{p. 169}

[185] N. M. A. Silva, "GASE: A high performance solver for the generalized nonlinear Schrödinger equation based on heterogeneous computing," Master's Thesis, Universidade do Porto, 2013.
{pp. 169, 173, 180}

[186] W. Bao, D. Jaksch, and P. A. Markowich, "Numerical solution of the Gross-Pitaevskii equation for Bose-Einstein condensation," *Journal of Computational Physics*, vol. 187, no. 1, pp. 318–342, 2003. DOI: 10.1016/S0021-9991(03)00102-5.
{pp. 169, 175}

[187] H. Wang, "A time-splitting spectral method for computing dynamics of spinor F=1 Bose–Einstein condensates," *International Journal of Computer Mathematics*, vol. 84, no. 6, pp. 925–944, 2007. DOI: 10.1080/00207160701458369.
{pp. 169, 175}

[188] W. Bao and Y. Cai, "Mathematical theory and numerical methods for Bose-Einstein condensation," *Kinetic and Related Models*, vol. 6, no. 1, pp. 1–135, 2013. DOI: 10.3934/krm.2013.6.1. arXiv: 1212.5341.
{pp. 169, 180}

[189] L. M. Symes and P. B. Blakie, "Solving the spin-2 Gross-Pitaevskii equation using exact nonlinear dynamics and symplectic composition," *Physical Review E*, vol. 95, no. 1, p. 013 311, 2017. DOI: 10.1103/PhysRevE.95.013311.
{pp. 169, 175}

[190] V. Lončar, "Hybrid parallel algorithms for solving nonlinear Schrödinger equation," Ph.D. dissertation, Novi Sad, 2017.
{p. 169}

[191] X. Antoine and R. Duboscq, "GPELab, a Matlab toolbox to solve Gross–Pitaevskii equations I: Computation of stationary solutions," *Computer Physics Communications*, vol. 185, no. 11, pp. 2969–2991, 2014. DOI: 10.1016/j.cpc.2014.06.026.
{pp. 169, 190}

[192] X. Antoine and R. Duboscq, "GPELab, a Matlab toolbox to solve Gross–Pitaevskii equations II: Dynamics and stochastic simulations," *Computer Physics Communications*, vol. 193, pp. 95–117, 2015. DOI: 10.1016/j.cpc.2015.03.012.
{pp. 169, 190}

[193] J. Gaidamour, Q. Tang, and X. Antoine, "BEC2HPC: A HPC spectral solver for nonlinear Schrödinger and rotating Gross-Pitaevskii equations. Stationary states computation," *Computer Physics Communications*, vol. 265, p. 108 007, 2021. DOI: 10.1016/j.cpc.2021.108007.
{pp. 169, 190}

[194] J. Schloss and L. O'Riordan, "GPUE: Graphics processing unit Gross-Pitaevskii equation solver," *Journal of Open Source Software*, vol. 3, no. 32, p. 1037, 2018. DOI: 10.21105/joss.01037.
{pp. 169, 190}

[195] R. M. Caplan and R. Carretero, "Simulating the nonlinear Schrödinger equation using the computational capability of NVIDIA graphics cards," in *ACSESS Proceedings*, 2010, AP10–04.
{pp. 169, 189}

[196] R Zamora-Zamora, G. A. Domínguez-Castro, C Trallero-Giner, R Paredes, and V Romero-Rochín, "Validity of Gross–Pitaevskii solutions of harmonically confined BEC gases in reduced dimensions," *Journal of Physics Communications*, vol. 3, no. 8, p. 085 003, 2019. DOI: 10.1088/2399-6528/ab360f.
{p. 169}

[197] J. Schloss, "Massively parallel split-step Fourier techniques for simulating quantum systems on graphics processing units," Ph.D. dissertation, Okinawa Institute of Science and Technology Graduate University, 2019.
{p. 170}

[198] V. Lončar, A. Balaž, A. Bogojević, S. Škrbić, P. Muruganandam, and S. K. Adhikari, "CUDA programs for solving the time-dependent dipolar Gross–Pitaevskii equation in an anisotropic trap," *Computer Physics Communications*, vol. 200, pp. 406–410, 2016. DOI: 10.1016/j.cpc.2015.11.014.
{pp. 170, 189, 191}

[199] O. L. Berman, R. Y. Kezerashvili, G. V. Kolmakov, and L. M. Pomirchi, "Spontaneous formation and nonequilibrium dynamics of a soliton-shaped Bose-Einstein condensate in a trap," *Physical Review E*, vol. 91, no. 6, p. 062 901, 2015. DOI: 10.1103/PhysRevE.91.062901.
{pp. 170, 189}

[200] A. Gothandaraman, S. Sadatian, M. Faryniarz, O. L. Berman, and G. V. Kolmakov, "Application of graphics processing units (GPUs) to the study of non-linear dynamics of the exciton Bose-Einstein condensate in a semiconductor quantum well," in *2011 Symposium on Application Accelerators in High-Performance Computing*, IEEE, IEEE, 2011, pp. 68–71. DOI: 10.1109/SAAHPC.2011.32.
{pp. 170, 173, 189}

[201] P. Wittek and F. M. Cucchietti, "A second-order distributed Trotter–Suzuki solver with a hybrid CPU–GPU kernel," *Computer Physics Communications*, vol. 184, no. 4, pp. 1165–1171, 2013. DOI: 10.1016/j.cpc.2012.12.008.
{p. 170}

[202] J. D. Owens *et al.*, "A survey of general-purpose computation on graphics hardware," *Computer Graphics Forum*, vol. 26, no. 1, pp. 80–113, 2007. DOI: 10.1111/j.1467-8659.2007.01012.x.
{p. 171}

[203] J. Owens, M Houston, D Luebke, S Green, J. Stone, and J. Phillips, "GPU computing," *Proceedings of the IEEE*, vol. 96, no. 5, pp. 879–899, 2008. DOI: 10.1109/JPROC.2008.917757.
{pp. 171, 172}

[204] J. L. Hennessy and D. A. Patterson, *Computer Architecture: A Quantitative Approach*, 5th ed. Morgan Kaufmann/Elsevier, 2012.
{p. 172}

[205] *CUDA C++ Programming Guide*, 2021.
{p. 172}

[206] *CUDA Toolkit Documentation, cuFFT*, v11.5.1, NVIDIA Corporation, 2021.
{p. 173}

[207] C. R. Harris *et al.*, *Array programming with NumPy*, 2020. DOI: 10.1038/s41586-020-2649-2. arXiv: 2006.10256.
{p. 173}

[208] P. A. Ruprecht, M. J. Holland, K. Burnett, and M. Edwards, "Time-dependent solution of the nonlinear Schrödinger equation for Bose-condensed trapped neutral atoms," *Physical Review A*, vol. 51, no. 6, pp. 4704–4711, 1995. DOI: 10.1103/PhysRevA.51.4704.
{p. 175}

[209] S. K. Adhikari, "Numerical solution of the two-dimensional Gross–Pitaevskii equation for trapped interacting atoms," *Physics Letters A*, vol. 265, no. 1-2, pp. 91–96, 2000. DOI: 10.1016/S0375-9601(99)00878-6. arXiv: 0001361 [cond-mat].
{p. 175}

[210] R. Dum, J. I. Cirac, M. Lewenstein, and P. Zoller, "Creation of dark solitons and vortices in Bose-Einstein condensates," *Physical Review Letters*, vol. 80, no. 14, pp. 2972–2975, 1998. DOI: 10.1103/PhysRevLett.80.2972.
{p. 175}

[211] B. Jackson, J. F. McCann, and C. S. Adams, "Vortex formation in dilute inhomogeneous Bose-Einstein condensates," *Physical Review Letters*, vol. 80, no. 18, pp. 3903–3906, 1998. DOI: 10.1103/PhysRevLett.80.3903.
{p. 175}

[212] D. L. Feder, C. W. Clark, and B. I. Schneider, "Vortex stability of interacting Bose-Einstein condensates confined in anisotropic harmonic traps," *Physical Review Letters*, vol. 82, no. 25, pp. 4956–4959, 1999. DOI: 10.1103/PhysRevLett.82.4956.
{p. 175}

[213] A. L. Fetter, "Rotating trapped Bose-Einstein condensates," *Reviews of Modern Physics*, vol. 81, no. 2, pp. 647–691, 2009. DOI: 10.1103/RevModPhys.81.647.
{p. 175}

[214] X.-F. Zhang, Z.-J. Du, R.-B. Tan, R.-F. Dong, H. Chang, and S.-G. Zhang, "Vortices in a rotating two-component Bose–Einstein condensate with tunable interactions and harmonic potential," *Annals of Physics*, vol. 346, pp. 154–163, 2014. DOI: 10.1016/j.aop.2014.04.015.
{p. 175}

[215] S. Eckel *et al.*, "Hysteresis in a quantized superfluid 'atomtronic' circuit," *Nature*, vol. 506, no. 7487, pp. 200–203, 2014. DOI: 10.1038/nature12958.
{p. 175}

[216] S. W. Seo, W. J. Kwon, S. Kang, and Y. Shin, "Collisional dynamics of half-quantum vortices in a spinor Bose-Einstein condensate," *Physical Review Letters*, vol. 116, no. 18, p. 185 301, 2016. DOI: 10.1103/PhysRevLett.116.185301.
{p. 175}

[217] Y.-K. Liu, H.-X. Yue, L.-L. Xu, and S.-J. Yang, "Vortex-pair states in spin-orbit-coupled Bose–Einstein condensates with coherent coupling," *Frontiers of Physics*, vol. 13, no. 5, p. 130 316, 2018. DOI: 10.1007/s11467-018-0821-z.
{p. 175}

[218] Z. Dutton and C. W. Clark, "Effective one-component description of two-component Bose-Einstein condensate dynamics," *Physical Review A*, vol. 71, no. 6, p. 063 618, 2005. DOI: 10.1103/PhysRevA.71.063618.
{p. 175}

[219] H. Saito and M. Ueda, "Spontaneous magnetization and structure formation in a spin-1 ferromagnetic Bose-Einstein condensate," *Physical Review A*, vol. 72, no. 2, p. 023 610, 2005. DOI: 10.1103/PhysRevA.72.023610.
{p. 175}

[220] W. Zhang, D. L. Zhou, M.-S. Chang, M. S. Chapman, and L. You, "Dynamical instability and domain formation in a spin-1 Bose-Einstein condensate," *Physical Review Letters*, vol. 95, no. 18, p. 180 403, 2005. DOI: 10.1103/PhysRevLett.95.180403.
{p. 175}

[221] S. De, D. L. Campbell, R. M. Price, A. Putra, B. M. Anderson, and I. B. Spielman, "Quenched binary Bose-Einstein condensates: Spin-domain formation and coarsening," *Physical Review A*, vol. 89, no. 3, p. 033 631, 2014. DOI: 10.1103/PhysRevA.89.033631.
{pp. 175, 177}

223

[222] E. Yukawa and M. Ueda, "Morphological superfluid in a nonmagnetic spin-2 Bose-Einstein condensate," *Physical Review Letters*, vol. 124, no. 10, p. 105 301, 2020. DOI: 10.1103/PhysRevLett.124.105301.
{p. 175}

[223] I. B. Spielman, "Raman processes and effective gauge potentials," *Physical Review A*, vol. 79, no. 6, p. 063 613, 2009. DOI: 10.1103/PhysRevA.79.063613.
{pp. 176, 177}

[224] J. Dalibard, F. Gerbier, G. Juzeliūnas, and P. Öhberg, "Colloquium: Artificial gauge potentials for neutral atoms," *Reviews of Modern Physics*, vol. 83, no. 4, pp. 1523–1543, 2011. DOI: 10.1103/RevModPhys.83.1523.
{p. 176}

[225] Z. Wu *et al.*, "Realization of two-dimensional spin-orbit coupling for Bose-Einstein condensates," *Science*, vol. 354, no. 6308, pp. 83–88, 2016. DOI: 10.1126/science.aaf6689.
{p. 176}

[226] B. M. Anderson, G. Juzeliūnas, V. M. Galitski, and I. B. Spielman, "Synthetic 3D spin-orbit coupling," *Physical Review Letters*, vol. 108, no. 23, p. 235 301, 2012. DOI: 10.1103/PhysRevLett.108.235301.
{p. 176}

[227] Y.-J. Lin, K. Jiménez-García, and I. B. Spielman, "Spin–orbit-coupled Bose–Einstein condensates," *Nature*, vol. 471, no. 7336, pp. 83–86, 2011. DOI: 10.1038/nature09887.
{pp. 176, 184–186}

[228] N. L. Smith, W. H. Heathcote, G Hechenblaikner, E Nugent, and C. J. Foot, "Quasi-2D confinement of a BEC in a combined optical and magnetic potential," *Journal of Physics B: Atomic, Molecular and Optical Physics*, vol. 38, no. 3, pp. 223–235, 2005. DOI: 10.1088/0953-4075/38/3/007. arXiv: 0410101 [cond-mat].
{p. 179}

[229] W. Bao, S. Jin, and P. A. Markowich, "On time-splitting spectral approximations for the Schrödinger equation in the semiclassical regime," *Journal of Computational Physics*, vol. 175, no. 2, pp. 487–524, 2002. DOI: 10.1006/jcph.2001.6956.
{p. 179}

[230] W. Bao, "Ground states and dynamics of multicomponent Bose-Einstein condensates," *Multiscale Modeling and Simulation*, vol. 2, no. 2, pp. 210–236, 2004. DOI: 10.1137/030600209.
{p. 180}

224

[231] W. Bao and J. Shen, "A fourth-order time-splitting Laguerre–Hermite pseudospectral method for Bose–Einstein condensates," *SIAM Journal on Scientific Computing*, vol. 26, no. 6, pp. 2010–2028, 2005. DOI: 10.1137/030601211.
{p. 180}

[232] T. Chen *et al.*, "Statistical performance comparisons of computers," *IEEE Transactions on Computers*, vol. 64, no. 5, pp. 1442–1455, 2015. DOI: 10.1109/TC.2014.2315614.
{p. 182}

[233] T. Hoefler and R. Belli, "Scientific benchmarking of parallel computing systems," in *Proceedings of the International Conference for High Performance Computing, Networking, Storage and Analysis*, 2015, pp. 1–12. DOI: 10.1145/2807591.2807644.
{p. 182}

[234] S. L. Zhu, H. Fu, C. J. Wu, S. C. Zhang, and L. M. Duan, "Spin Hall effects for cold atoms in a light-induced gauge potential," *Physical Review Letters*, vol. 97, no. 24, p. 240 401, 2006. DOI: 10.1103/PhysRevLett.97.240401. arXiv: 0607127 [cond-mat].
{p. 184}

[235] X.-J. Liu, X. Liu, L. C. Kwek, and C. H. Oh, "Optically induced spin-Hall effect in atoms," *Physical Review Letters*, vol. 98, no. 2, p. 026 602, 2007. DOI: 10.1103/PhysRevLett.98.026602.
{p. 184}

[236] M. C. Beeler, R. A. Williams, K Jiménez-García, L. J. Leblanc, A. R. Perry, and I. B. Spielman, "The spin Hall effect in a quantum gas," *Nature*, vol. 498, no. 7453, pp. 201–204, 2013. DOI: 10.1038/nature12185. arXiv: 1306.3579.
{pp. 184, 188}

[237] S. Furukawa and M. Ueda, "Quantum Hall phase diagram of two-component Bose gases: Intercomponent entanglement and pseudopotentials," *Physical Review A*, vol. 96, no. 5, p. 053 626, 2017. DOI: 10.1103/PhysRevA.96.053626.
{p. 184}

[238] S. Furukawa and M. Ueda, "Global phase diagram of two-component Bose gases in antiparallel magnetic fields," *Physical Review A*, vol. 90, no. 3, p. 033 602, 2014. DOI: 10.1103/PhysRevA.90.033602.
{p. 184}

[239] H. Takeuchi, "Quantum elliptic vortex in a nematic-spin Bose-Einstein condensate," *Physical Review Letters*, vol. 126, no. 19, p. 195 302, 2021. DOI: 10.1103/PhysRevLett.126.195302. arXiv: 2009.03556.
{p. 186}

[240] A. L. Gaunt, T. F. Schmidutz, I. Gotlibovych, R. P. Smith, and Z. Hadzibabic, "Bose-Einstein condensation of atoms in a uniform potential," *Physical Review Letters*, vol. 110, no. 20, p. 200 406, 2013. DOI: 10.1103/PhysRevLett.110.200406. arXiv: 1212.4453.
{p. 188}

[241] G. Demeter, "Solving the Maxwell–Bloch equations for resonant nonlinear optics using GPUs," *Computer Physics Communications*, vol. 184, no. 4, pp. 1203–1210, 2013. DOI: 10.1016/j.cpc.2012.12.019.
{p. 189}

[242] V. Lončar, L. E. Young, S. Škrbić, P. Muruganandam, S. K. Adhikari, and A. Balaž, "OpenMP, OpenMP/MPI, and CUDA/MPI C programs for solving the time-dependent dipolar Gross–Pitaevskii equation," *Computer Physics Communications*, vol. 209, pp. 190–196, 2016. DOI: 10.1016/j.cpc.2016.07.029.
{p. 189}

[243] X. Antoine, A. Levitt, and Q. Tang, "Efficient spectral computation of the stationary states of rotating Bose–Einstein condensates by preconditioned nonlinear conjugate gradient methods," *Journal of Computational Physics*, vol. 343, pp. 92–109, 2017. DOI: 10.1016/j.jcp.2017.04.040.
{p. 190}

[244] W. Bao and Q. Du, "Computing the ground state solution of Bose-Einstein condensates by a normalized gradient flow," *SIAM Journal on Scientific Computing*, vol. 25, no. 5, pp. 1674–1697, 2004. DOI: 10.1137/S1064827503422956. arXiv: 0303241 [cond-mat].
{p. 190}

[245] O. Katz and O. Firstenberg, "Light storage for one second in room-temperature alkali vapor," *Nature Communications*, vol. 9, no. 1, pp. 1–6, 2018. DOI: 10.1038/s41467-018-04458-4.
{pp. 194, 196}

[246] J. K. Saaswath, K. N. Pradosh, K. V. Adwaith, B. C. Sanders, F. Bretenaker, and A. Narayanan, "Microwave-driven generation and group delay control of optical pulses from an ultra-dilute atomic ensemble," *Optics Express*, vol. 29, no. 11, p. 15 940, 2021. DOI: 10.1364/OE.424110.
{p. 195}

[247] G. S. Agarwal, T. N. Dey, and S. Menon, "Knob for changing light propagation from subluminal to superluminal," *Physical Review A*, vol. 64, no. 5, p. 053 809, 2001. DOI: 10.1103/PhysRevA.64.053809. arXiv: 0106107 [quant-ph].
{p. 195}

[248] D.-S. Ding, Y. K. Jiang, W. Zhang, Z.-Y. Zhou, B.-S. Shi, and G.-C. Guo, "Optical precursor with four-wave mixing and storage based on a cold-atom ensemble," *Physical Review Letters*, vol. 114, no. 9, p. 093 601, 2015. DOI: 10.1103/PhysRevLett.114.093601.
{p. 196}

[249] S. Du, C. Belthangady, P. Kolchin, G. Y. Yin, and S. E. Harris, "Observation of optical precursors at the biphoton level," *Optics Letters*, vol. 33, no. 18, p. 2149, 2008. DOI: 10.1364/ol.33.002149.
{p. 196}

[250] D. Wei, J. F. Chen, M. M. T. Loy, G. K. L. Wong, and S. Du, "Optical precursors with electromagnetically induced transparency in cold atoms," *Physical Review Letters*, vol. 103, no. 9, p. 093 602, 2009. DOI: 10.1103/PhysRevLett.103.093602.
{p. 196}

[251] P. K. Jakobsen and M. Mansuripur, "On the nature of the Sommerfeld–Brillouin forerunners (or precursors)," *Quantum Studies: Mathematics and Foundations*, vol. 7, no. 3, pp. 315–339, 2020. DOI: 10.1007/s40509-019-00210-9.
{p. 196}

[252] M. Dujić, D. Buhin, N. Šantić, D. Aumiler, and T. Ban, "Comparative study of light storage in antirelaxation-coated and buffer-gas-filled alkali vapor cells," 2023. arXiv: 2310.03726.
{p. 196}

[253] E. Saglamyurek, T. Hrushevskyi, A. Rastogi, L. W. Cooke, B. D. Smith, and L. J. LeBlanc, "Storing short single-photon-level optical pulses in Bose–Einstein condensates for high-performance quantum memory," *New Journal of Physics*, vol. 23, no. 4, p. 043 028, 2021. DOI: 10.1088/1367-2630/abf1d9.
{pp. 196, 230}

[254] A. Rastogi, E. Saglamyurek, T. Hrushevskyi, and L. J. Leblanc, "Superradiance-mediated photon storage for broadband quantum memory," *Physical Review Letters*, vol. 129, no. 12, p. 120 502, 2022. DOI: 10.1103/PhysRevLett.129.120502. arXiv: 2112.09261.
{p. 196}

[255] J. C. Bardin, D. H. Slichter, and D. J. Reilly, "Microwaves in Quantum Computing," *IEEE Journal of Microwaves*, vol. 1, no. 1, pp. 403–427, 2021. DOI: 10.1109/JMW.2020.3034071. arXiv: 2011.01480.
{p. 196}

[256] D. Uhland, H. Dillmann, Y. Wang, and I. Gerhardt, "How to build an optical filter with an atomic vapor cell," 2023. arXiv: 2305.00570.
{p. 197}

[257] D. T. Stack, P. J. Lee, and Q. Quraishi, "Simple and efficient absorption filter for single photons from a cold atom quantum memory," *Optics Express*, vol. 23, no. 5, p. 6822, 2015. DOI: 10.1364/OE.23.006822. arXiv: 1405.6117.
{p. 197}

[258] M. Bashkansky, F. K. Fatemi, and I. Vurgaftman, "Quantum memory in warm rubidium vapor with buffer gas," *Optics Letters*, vol. 37, no. 2, p. 142, 2012. DOI: 10.1364/ol.37.000142.
{p. 197}

[259] J. A. Boyd and T. Lahaye, "A basic introduction to ultrastable optical cavities for laser stabilization," *American Journal of Physics*, vol. 92, no. 1, pp. 50–58, 2024. DOI: 10.1119/5.0161369. arXiv: 2308.08015.
{p. 197}

[260] P. Palittapongarnpim, A. MacRae, and A. I. Lvovsky, "Note: A monolithic filter cavity for experiments in quantum optics," *Review of Scientific Instruments*, vol. 83, no. 6, p. 66 101, 2012. DOI: 10.1063/1.4726458. arXiv: 1203.4843.
{p. 197}

[261] S. S. Sahoo, S. R. Mishra, G. Rajalakshmi, and A. K. Mohapatra, "Nonlinear magnetoelectric effect in atomic vapor and its application to precision radio-frequency magnetometry," *Physical Review A*, vol. 105, no. 6, p. 063 509, 2022. DOI: 10.1103/PhysRevA.105.063509.
{p. 198}

[262] H.-H. Lu, J. M. Lukens, N. A. Peters, B. P. Williams, A. M. Weiner, and P. Lougovski, "Quantum interference and correlation control of frequency-bin qubits," *Optica*, vol. 5, no. 11, p. 1455, 2018. DOI: 10.1364/OPTICA.5.001455.
{p. 199}

[263] R. C. Jones, "I . Description and discussion of the calculus," *Journal of the Optical Society of America*, vol. 31, no. 7, pp. 488–493, 1941.
{pp. 232, 233}

[264] E. Hecht, *Optics*, 5th. Pearson, 2017.
{pp. 232, 233}

[265] R. A. Chipman, "Mechanics of polarization ray tracing," *Optical Engineering*, vol. 34, no. 6, p. 1636, 1995. DOI: 10.1117/12.202061.
{p. 234}

[266] G. Yun, K. Crabtree, and R. A. Chipman, "Three-dimensional polarization ray-tracing calculus I: Definition and diattenuation," *Applied Optics*, vol. 50, no. 18, pp. 2855–2865, 2011. DOI: 10.1364/AO.50.002855.
{p. 234}

[267] M. Weissbluth, *Atoms and Molecules*. New York, NY, USA: Academic Press, 1978.
{pp. 234, 237}

[268] J. J. Sakuri, *Modern Quantum Mechanics*, S. F. Tuan, Ed. Addison-Wesley Publishing Company, 1994.
{pp. 234, 235}

[269] M. A. Morrison and G. A. Parker, "A guide to rotations in quantum mechanics," *Australian Journal of Physics*, vol. 40, no. 4, p. 465, 1987. DOI: 10.1071/PH870465.
{p. 235}

[270] I. K. Kominis, T. W. Kornack, J. C. Allred, and M. V. Romalis, "A sub-femtotesla multichannel atomic magnetometer," *Nature*, vol. 422, no. 6932, pp. 596–599, 2003. DOI: 10.1038/nature01484.
{p. 240}

Appendix A

Optical polarization & rotation

Many experimental apparatuses in atomic physics include a multi-level atomic sample, at least one polarized laser beam, and a controllable external magnetic field for setting a quantization axis. It is well-known that changing the input beam's polarization drives different multi-level transitions. To drive a specific transition in a multi-level atom, experimentalists usually take one of two approaches: (1) select polarization states with a high level of symmetry, given their quantization and beam geometry; or (2) empirically alter the polarization or magnetic field until only the desired transition appears [112, 253]. Each approach has shortcomings. The drawback of the first approach is that symmetric configurations may not always be possible given optical access or other experimental constraints. In the second approach, the apparatus becomes characterized in terms of apparatus-specific parameters (e.g. waveplate

rotation angles) instead of universal quantities, such as polarization states. In this appendix, we break free from the limitations of both approaches. We answer the question, "For an arbitrary beam geometry and given local input polarization, which polarization does the atom "see"? We begin with an overview of optical polarization and matrix methods for transforming the polarization state. Then we briefly discuss rotations of spherical vectors and operators in three-dimensional space. These two sections are combined in the final section to answer the question just posed.

Note that in this appendix, we refer to the polarization of a propagating beam of light; however, this approach also applies to the polarization of non-propagating electromagnetic waves, such as the TE_{011} microwave cavity mode used in this thesis. We also emphasize that this method applies only to multi-level atoms [see Section 3.2]; this discussion is not sensible for two-level atoms because they lack the same rotational properties in 3D space.

A.1 Optical polarization

A freely propagating electromagnetic wave is a transverse, oscillating vector field with orthogonal electric and magnetic components. Transverse waves possess a property called polarization, which is the spatial pattern of propagating oscillations. The wave may, for example, oscillate along a vertical plane or in a circular pattern. By convention, the polarization of an electromagnetic wave is defined according to the electric field component; Poynting's theorem then constrains the orthogonal magnetic field component.

A.1.1   Polarization vectors

We begin by considering a classical plane wave electric field of the form

$$\mathbf{E}(z,t) = \left(|\mathcal{E}_x|e^{i\phi_x}\hat{e}_x + |\mathcal{E}_y|e^{i\phi_y}\hat{e}_y\right)e^{i(kz-\omega t)}, \tag{A.1}$$

oscillating at a frequency ω and propagating along the z-axis with a wavenumber $k = \omega/c$ [89]. The field has vector components along the $\hat{e}_{x,y}$ axes with their respective amplitudes $|E_{x,y}|$ and phases $\phi_{x,y}$. We factor out the global phase factor and normalize by the total field amplitude $\mathcal{E}_0 = \sqrt{|\mathcal{E}_x|^2 + |\mathcal{E}_y|^2}$ to get the expression

$$\mathbf{E}(z,t) = E_{\text{eff}}(z,t)\left[A\hat{e}_x + Be^{i\delta}\hat{e}_y\right], \tag{A.2}$$

where $E_{\text{eff}}(z,t) = \mathcal{E}_0 e^{i(kz-\omega t+\phi_x)}$, the amplitudes $A \equiv |E_x|/\mathcal{E}_0$ and $B \equiv |E_y|/\mathcal{E}_0$, and the relative phase $\delta = \phi_y - \phi_x$. The expression in the square brackets is a complex unit vector in the $\hat{e}_x$-$\hat{e}_y$ plane. This vector describes the general polarization state of the light $|\psi\rangle$[1] and can be also represented as a column Jones vector [263]

$$|\psi\rangle = \begin{bmatrix} A \\ Be^{i\delta} \end{bmatrix}. \tag{A.3}$$

If either A or B equals 1, then the electric field oscillates purely along the $\hat{e}_x$ or $\hat{e}_y$ axes, respectively. These are examples of so-called linear polarization states. Real (i.e. $\delta = 0$) linear combinations of both axes produce linearly polarized light oscillating along a diagonal plane. Circular and elliptical polarizations are constructed from complex linear combinations (i.e. $\delta \neq 0$).

A.1.2   Convention

When performing calculations of optical polarizations, it is extremely important to be aware of the conventions employed by various sources [264]. In this thesis, we employ

---

[1]Here, we are describing classical states of light; bra-ket notation can also be used for single-photon polarization states.

the convention used in Hecht [264], where the phase of an electromagnetic wave is $(kz - \omega t)$ [2]. Any additional phase $\delta > 0$ in one of the polarization components delays the phase by a time δ/ω. Likewise, the phase is advanced when $\delta < 0$.

We also employ the "handedness" convention used by Hecht: when $\delta = -\pi/2$, the $\hat{e}_y$-component of Equation A.2 is advanced by a quarter wave ahead of the $\hat{e}_x$-component. If a screen is placed between the light source and an observer, the total electric field vector would be seen on the screen by the observer (looking back toward the source) to rotate clockwise. In the convention, this is called right-circularly polarized light. Similarly, when $\delta = \pi/2$, the $\hat{e}_y$-component is delayed by a quarter wave. The observer would see the electric field vector rotating counter-clockwise and is called left-circularly polarized light[3].

A.1.3   Matrix transformations of polarization vectors

Certain types of optical elements change the polarization state of the light. For example, waveplates produce unitary transformations of $|\psi\rangle$ and polarizers project the state along a certain axis. Transformations of $|\psi\rangle$ are calculated using a matrix multiplication method called Jones calculus [263]. In this approach, the action of optical elements are represented by 2x2 matrices $\check{J}$ applied to the left of the $|\psi\rangle$ in the order that the light encounters them, or

$$|\psi'\rangle = \check{J}_N \ldots \check{J}_3 \check{J}_2 \check{J}_1 |\psi\rangle. \tag{A.4}$$

Jones calculus is defined in the *local coordinates* of the beam. It is suitable for calculations where the light travels paraxially through the optical elements along a

---

[2]In contrast, some sources define the wave phase as $(\omega t - kz)$.

[3]Note that in this convention, the "right-hand rule"—where the thumb points along the propagation axis—is reversed: clockwise rotating field seen by a receiver (left hand) is called right circular polarized light. This convention is often specified as "from the point of view of the receiver." The opposite convention is called "from the point of view of the source" and is also widely used. *Caveat lector*!

single axis. This was the approach used in Section 7.3.4 to calibrate the angles of the experimental waveplates.

In the discussion that follows, we want to consider how an atom experiences the polarization state of a beam of light coming from different directions in the global laboratory coordinates. To do this, we may define a cartesian *polarization vector* by extending the Jones vector along a third cartesian axis [265, 266]

$$|\Psi\rangle = \begin{bmatrix} c_x \\ c_y \\ c_z \end{bmatrix},$$ (A.5)

where the c_i are complex values such that $\sqrt{c_x^2 + c_y^2 + c_z^2} = 1$. For a beam propagating along the z-axis, $c_z = 0$ and we recover the Jones calculus form. Propagation along an arbitrary axis will have three non-zero components. In Section A.3, we transform this vector to the spherical basis and consider its rotations in 3D space.

For reference, Appendix B lists the cartesian vectors for several special polarization states of a beam propagating along the $\hat{e}_z$-axis. It also includes the 3x3 matrices for polarizers $\check{P}$ and waveplate $\check{W}$ optical elements.

A.2   Rotations of spherical vectors

The spherical harmonics and vector operators defined in Section 2.4 are represented in a specific three-dimensional coordinate system. In this section, we will consider how these functions and operators transform under physical rotations. While the rotation occurs in $\mathbb{R}^3$ space, the result is typically manifested in the internal Hilbert space. This discussion will be a brief overview of rotations of spherical vectors in quantum mechanics; in-depth treatments are found in many other sources [26, 41, 267, 268].

A general rotation operator can be decomposed into three rotation operations about

234

certain axes. There is no one unique way to define these rotations, but typically a combination of three axes is chosen. In the ZYZ convention—commonly employed in the rotation of angular momentum operators [49, 268]— we first rotate by an angle α about the $\hat{e}_z$-axis, then by an angle β about the $\hat{e}_y$-axis, and finally by an angle γ about the $\hat{e}_z$-axis. The angles α, β, and γ are called Euler angles; they describe the orientation of objects in a fixed local coordinate frame[4]. When considered relative to *fixed* laboratory reference frame axes, the order of these rotation operations *reverses*, giving the general rotation operator [269]

$$\hat{\mathcal{R}}(\alpha, \beta, \gamma) = \hat{\mathcal{R}}_z(\alpha)\hat{\mathcal{R}}_y(\beta)\hat{\mathcal{R}}_z(\gamma). \tag{A.6}$$

The individual rotation operators about the $\hat{e}_i$-axis are defined as [26, 52, 269]

$$\hat{\mathcal{R}}_i(\theta) = \exp(-i\phi\hat{\mathbf{J}} \cdot \hat{e}_i/\hbar), \tag{A.7}$$

where $\hat{\mathbf{J}} = \hat{J}_x\hat{e}_x + \hat{J}_y\hat{e}_y + \hat{J}_z\hat{e}_z$ is the angular momentum operator[5].

To see how the total rotation operator $\hat{\mathcal{R}}(\alpha, \beta, \gamma)$ influences the internal state of the spherical vector, we take its matrix element to obtain the complex-valued Wigner

---

[4]The ZYZ rotation matrix acting on a *cartesian* vector in $\mathbb{R}^3$ takes the form [269]

$$\check{R}(\alpha, \beta, \gamma) = \begin{pmatrix} \cos\alpha & -\sin\alpha & 0 \\ \sin\alpha & \cos\alpha & 0 \\ 0 & 0 & 1 \end{pmatrix} \begin{pmatrix} \cos\beta & 0 & \sin\beta \\ 0 & 1 & 0 \\ \sin\beta & 0 & \cos\beta \end{pmatrix} \begin{pmatrix} \cos\gamma & -\sin\gamma & 0 \\ \sin\gamma & \cos\gamma & 0 \\ 0 & 0 & 1 \end{pmatrix}.$$

[5]This operator is constructed by breaking down the operator for the full rotation angle θ into an infinite product of infinitesimal rotations; in essence: "Do what you have to do a little bit at a time" [52]. The infinitesimal rotation operator is [26]

$$\hat{\mathcal{R}}_i(d\theta) = \hat{\mathbb{1}} - id\theta\hat{\mathbf{J}} \cdot \hat{e}_i/\hbar,$$

where $d\theta = \theta/N$, for some large integer N. By applying this infinitesimal rotation $N \to \infty$ times, we construct the full rotation operator [49, 52],

$$\hat{\mathcal{R}}_i(\theta) = \lim_{N \to \infty}[\hat{\mathbb{1}} - i\frac{\theta}{N}\hat{\mathbf{J}} \cdot \hat{\mathbf{n}}/\hbar]^N = \exp(-i\theta\hat{\mathbf{J}} \cdot \hat{e}_i/\hbar).$$

D-matrix in the spherical basis [49]

$$D^{(j)}_{m'_j m_j} = \langle j m'_j | \hat{\mathcal{R}}_z(\alpha) \hat{\mathcal{R}}_y(\beta) \hat{\mathcal{R}}_z(\gamma) | j m_j \rangle. \tag{A.8}$$

This is evaluated to

$$D^{(j)}_{m'_j m_j} = e^{-i(\alpha m' + \gamma m)} d^{(j)}_{m'_j m_j}(\beta), \tag{A.9}$$

where $d^{(j)}_{m'_j m_j}(\beta)$ is a non-trivial matrix, but which is be readily calculated with software [46, 47]. For $j = 1$ and $m_j, m'_j \in \{-1, 0, 1\}$, this matrix takes the explicit form of [49]

$$d^{(1)}_{m'_j m_j}(\beta) = \begin{pmatrix} \cos^2 \frac{\beta}{2} & -\frac{\sin \beta}{\sqrt{2}} & \sin^2 \frac{\beta}{2} \\ \frac{\sin \beta}{\sqrt{2}} & \cos \beta & -\frac{\sin \beta}{\sqrt{2}} \\ \sin^2 \frac{\beta}{2} & \frac{\sin \beta}{\sqrt{2}} & \cos^2 \frac{\beta}{2} \end{pmatrix}. \tag{A.10}$$

$D^{(j)}_{m'm}(\alpha, \beta, \gamma)$ multiplies an arbitrary spherical vector to transform its components under the rotation. Notice that due to the non-commutativity of 3D rotations, two individual, sequential rotations $D^{(j)}_{m'm}(0, \beta, 0) D^{(j)}_{m'm}(\alpha, 0, 0)$ are not the same as a single $D^{(j)}_{m'm}(\alpha, \beta, 0)$ rotation.

Users of the D-matrix should be aware that $d^{(j)}_{m'_j m_j}(0) = \delta_{m'_j m_j}$. In this case, when operations on certain spherical vectors (e.g. $\begin{bmatrix} 0 & 1 & 0 \end{bmatrix}^T$) lose sensitivity to certain rotation directions (e.g. γ). This is the spherical basis form of gimbal lock, a universal pathology of conventional 3D Euler rotation matrices. When this occurs, it is helpful to provide an initial rotation of the state $D^{(j)}_{m'm}(0, \beta, 0)$, followed by a second rotation $D^{(j)}_{m'm}(\alpha, -\beta, \gamma)$.

A.3 What the atom "sees": Rotations of polarization states

As explained in Section 3.1.1, the electric field of light interacts with the multi-level atom's induced electric dipole moment to change the electron's quantum state. Recall

that the matrix element for the E1 interaction is $\langle m'|e\hat{\mathbf{r}} \cdot \mathbf{E}|m\rangle$. Because the atomic states are represented in spherical $|jm_j\rangle$ notation, it is helpful to represent the electric field vector as $\mathbf{E} = [c_- \quad c_0 \quad c_+]^T$ and the position vector operator as $\hat{\mathbf{r}} = [\hat{r}_- \quad \hat{r}_0 \quad \hat{r}_+]^T$ in the spherical basis. Following Equation 2.7, the matrix equation

$$\begin{bmatrix} c_- \\ c_0 \\ c_+ \end{bmatrix} = \frac{1}{\sqrt{2}} \begin{pmatrix} 1 & -i & 0 \\ 0 & 0 & \sqrt{2} \\ -1 & -i & 0 \end{pmatrix} \begin{bmatrix} c_x \\ c_y \\ c_z \end{bmatrix} \tag{A.11}$$

shows the change-of-basis transformation of the electric field polarization vector from the cartesian to the spherical basis, where the quantization axis is chosen to lie along the z-axis [49]. In this form, the E1 matrix element becomes

$$\begin{aligned} \langle m'|e\hat{\mathbf{r}} \cdot \mathbf{E}|m\rangle &= \langle m'|e\left(c_-\hat{r}_- + c_0\hat{r}_0 + c_+\hat{r}_+\right)|m\rangle \\ &= c_-\langle m-1|\hat{d}_-|m\rangle + c_0\langle m|\hat{d}_0|m\rangle + c_+\langle m+1|\hat{d}_+|m\rangle, \end{aligned} \tag{A.12}$$

where the dipole operator $\hat{d}_q = e\hat{r}_q$ can only connect states $|m\rangle$ to $|m+q\rangle$. The relative Rabi frequency of the qth transition is $\Omega_q = c_q\langle m+q|\hat{d}_q|m\rangle/\hbar$.

How are these complex-valued c_q coefficients determined for a given experimental configuration?

In general, the c_q coefficients depend on (1) the input light's polarization state defined in local coordinates, measured experimentally using a polarizer and rotating waveplates [see Section 7.3.4], and (2) the relative angles between a beam's propagation axis and the atom's quantization axis, typically furnished by an externally applied magnetic field. Since a transverse vector field, in the spherical basis, has the same rotational properties as a spherical vector operator operator [267], we can use the Wigner D-matrix to rotate the spherical polarization state vector in 3D. Figure A.1(a) shows a coordinate system and Euler rotation angles of a linearly polarized beam.

Once the beam's local polarization state is identified (usually vertical/horizontal linear or right-/left-circular), the procedure begins by first initializing the propagation direction along an axis that makes the polarization coefficients simple [49]. For example:

- An initial propagation direction *along the quantization axis* produces polarization vectors $|\sigma_+\rangle = [0 \;\; 0 \;\; 1]^T$ for right-circular polarization and $|\sigma_-\rangle = [1 \;\; 0 \;\; 0]^T$ for left-circular polarization.

- Linearly polarized light propagating *orthogonal to the quantization axis*, with the polarization plane parallel to the quantization axis, produces the polarization vector $|\pi\rangle = \begin{bmatrix} 0 & 1 & 0 \end{bmatrix}^T$. For consistency, and to avoid gimbal-lock issues, it is often helpful to rotate this state to also point along the quantization axis, producing

$$|\pi'\rangle = D^{(1)}_{m'_j m_j}(0, \pi/2, 0)|\pi\rangle = [1 \;\; 0 \;\; 1]^T/\sqrt{2}. \tag{A.13}$$

Next, the Wigner D-matrix—with Euler angles chosen to rotate the initial axis to the real propagation axis—multiplies the initial polarization vector. In general, the resulting vector has complex coefficients. In Figure A.1, we demonstrate this procedure for two special cases: (c) shows the result of $D^{(1)}_{m'_j m_j}(0, \pi/2, \gamma)|\pi'\rangle$ as γ is varied from 0 to 2π, and (d) shows the result of $D^{(1)}_{m'_j m_j}(0, \beta, 0)|\sigma_-\rangle$ as β is varied from 0 to 2π. The diagrams depict these rotations in the fixed coordinates. The associated plots show how the norm squared of the coefficients $|c_q|^2$ vary with rotation angle. These plots may be interpreted as the polarization component fraction "seen" by the atom[6]. Notice that the phase information is not represented.

---

[6]The plot in Figure A.1(c) shows that the fractions in each polarization component are equal, i.e. $|c_q|^2 = 1/3$ when $\gamma = 54.7°$ and $125.3°$. There are many combinations of input polarization and rotation angles that produce this interesting scenario.
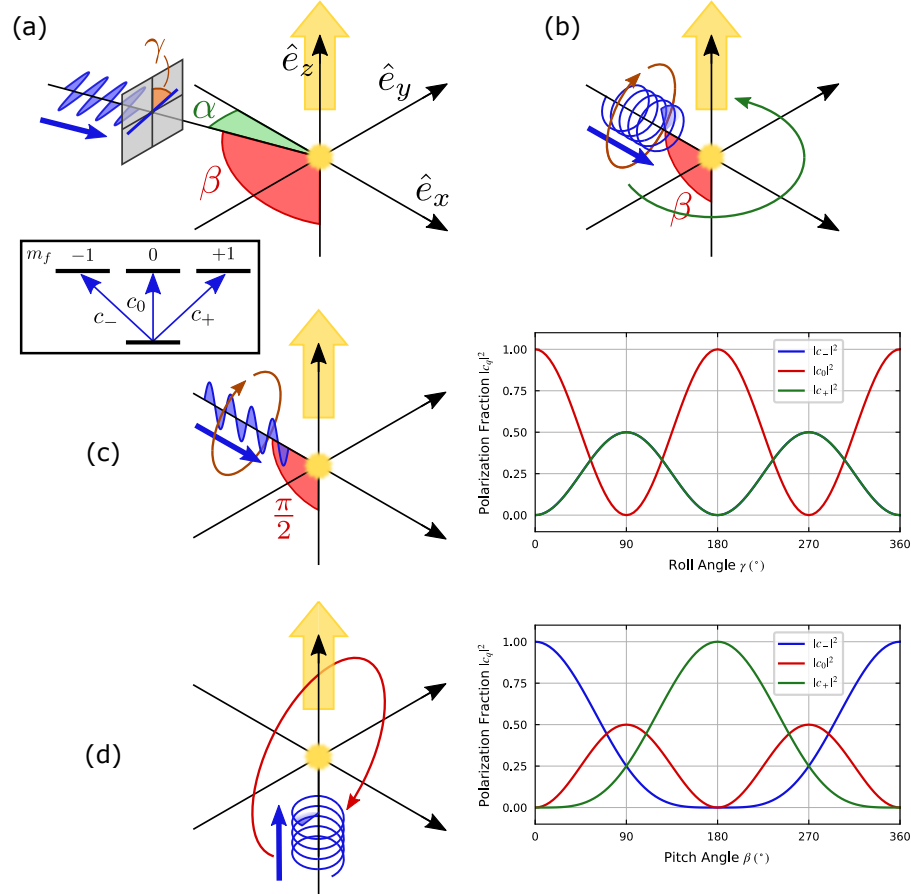
Figure A.1: Rotations of electromagnetic polarization states relative to a quantization axis. (a) The 3D coordinate system in which rotations are defined, with an atom (yellow) placed at the origin. The large yellow arrow is the atom's quantization axis, chosen to lie along the z-axis. The polarized light's electric field is shown as a blue sine wave, whose propagation direction toward the atom is shown by the blue arrow. The angles α, β, and γ indicate the heading, pitch, and roll angles of the electric field, all defined from an initial orientation along the quantization axis. Because the γ rotation is applied before the others, the gray plane is identical to the $\hat{e}_x$-$\hat{e}_y$ plane. The boxed inset shows transitions from a $f = 0$ state to three $f = 1$ Zeeman sublevels, with the transition matrix elements c_i indicated. (b) For every β, rotating circularly polarized light by angles α or γ does not affect the spherical dipole matrix element amplitudes; it does, however, alter their phase. This is also true for α rotations of linearly polarized light. (c) A γ rotation of linearly-polarized light propagating along the x-axis. The graph shows the squared matrix elements as a function of rotation angle in degrees. Note that the $|c_\pm|^2$ curves completely overlap. (d) The squared matrix elements for different angles throughout a β rotation of left-circularly polarized light.

Certain rotations of polarization vectors change the coefficients' complex phase but leave their amplitudes unaffected. Two examples of such rotations are depicted in Figure A.1(b). In many experimental configurations, a global phase change of the rotated polarization vector may be factorable and produce no change whatsoever in the measured atomic populations. However, in an interferometer scheme, or when multiple phase-coherent beams interact with the same atoms, these phase changes may be measurable and significant.

What determines the quantization axis when the magnetic field is zero?

There are specific experimental configurations where the magnetic field is nullified at the location of the atoms [270]. As before, the experimenter is free to choose any axis upon which to quantize the atom's angular momentum. In this case, however, a *convenient* axis is the propagation axis of the light. The situation becomes slightly more complicated when multiple beams interact with the atoms. One of the beam axes may be chosen as the quantization axis, and the polarization vectors of the other beams are related to that axis by the same rotation procedure described above.

Appendix B

Polarization vectors and matrices

This appendix lists special examples of three-component, cartesian polarization vectors $|\Psi\rangle$ used to describe the polarization state of light traveling along the $\hat{e}_z$-axis [see Table B.1]. It also lists several 3x3 matrices that operate on $|\Psi\rangle$: Table B.2 gives the projecting matrices for a polarizing beam splitter $\check{P}$, which can be used to analyze the polarization components; Table B.3 gives the unitary matrices for waveplates/phase retarders $\check{W}$ that can be used to transform between the states given in Table B.1.

The states and matrices in this appendix are equivalent to those used in the Jones calculus introduced in Section A.1 and follow the phase convention defined in Section A.1.2.

Waveplates are typically manufactured from a crystal, such as quartz, that hosts birefringence. This means that transmitting light experiences different indices of re-

fraction along orthogonal crystal axes. The axis with the lower (higher) index of refraction has a faster (slower) wave speed and is called the fast (slow) axis. The phase of light polarized along the slow axis will be delayed from that of the fast axis. For this reason, waveplates are also called phase retarders. A specific phase delay η can be engineered by carefully controlling the thickness of the crystal. A quarter waveplate has $\eta = \pi/2$, while a half waveplate has $\eta = \pi$.

Name	State	Form
Horizontal Linear	$\lvert H \rangle$	$\begin{bmatrix} 1 & 0 & 0 \end{bmatrix}^T$
Vertical Linear	$\lvert V \rangle$	$\begin{bmatrix} 0 & 1 & 0 \end{bmatrix}^T$
Angled Linear	$\lvert \theta \rangle$	$\begin{bmatrix} \cos\theta & \sin\theta & 0 \end{bmatrix}^T$
Right Circular	$\lvert R \rangle$	$\begin{bmatrix} 1 & -i & 0 \end{bmatrix}^T / \sqrt{2}$
Left Circular	$\lvert L \rangle$	$\begin{bmatrix} 1 & i & 0 \end{bmatrix}^T / \sqrt{2}$

Table B.1: Special polarization state vectors for a z-axis propagating beam. θ is the angle between the x-axis and the rotated linear polarization axis.

Name	State	Form
Polarizer, Transmitted	$\check{P}_T$	$\begin{bmatrix} 1 & 0 & 0 \\ 0 & 0 & 0 \\ 0 & 0 & 0 \end{bmatrix}$
Polarizer, Reflected	$\check{P}_R$	$\begin{bmatrix} 0 & 0 & 0 \\ 0 & 1 & 0 \\ 0 & 0 & 0 \end{bmatrix}$
Polarizer, Transmitted (Rotated)	$\check{P}(\theta)$	$\begin{bmatrix} \cos^2\theta & \sin\theta\cos\theta & 0 \\ \sin\theta\cos\theta & \sin^2\theta & 0 \\ 0 & 0 & 0 \end{bmatrix}$

Table B.2: Polarizer matrices for a z-axis propagating beam. These are specifically for a polarizing beam splitter (PBS), where the transmitted beam is $|H\rangle$ and the reflected beam is $|V\rangle$. θ is the angle between the x-axis and the polarizer axis.

Name	State	Form
General linear phase retarder	$\check{W}(\eta,\theta)$	$e^{-\frac{i\eta}{2}}\begin{bmatrix} \cos^2\theta + e^{i\eta}\sin^2\theta & (1-e^{i\eta})\cos\theta\sin\theta & 0 \\ (1-e^{i\eta})\cos\theta\sin\theta & \sin^2\theta + e^{i\eta}\cos^2\theta & 0 \\ 0 & 0 & 1 \end{bmatrix}$
Quarter WP	$\check{W}_Q(\theta)$	$e^{-\frac{i\pi}{4}}\begin{bmatrix} \cos^2\theta + i\sin^2\theta & \sin\theta\cos\theta - i\sin\theta\cos\theta & 0 \\ \sin\theta\cos\theta - i\sin\theta\cos\theta & \sin^2\theta + i\cos^2\theta & 0 \\ 0 & 0 & 1 \end{bmatrix}$
Half WP	$\check{W}_H(\theta)$	$e^{-\frac{i\pi}{2}}\begin{bmatrix} \cos 2\theta & \sin 2\theta & 0 \\ \sin 2\theta & -\cos 2\theta & 0 \\ 0 & 0 & 1 \end{bmatrix}$

Table B.3: Waveplate/phase retarder matrices for a z-propagating beam. θ is the angle between the x-axis and the crystal fast axis, while η is the relative phase delay between the fast and slow axes.

Appendix C

Evaluating reduced angular momentum matrix elements

In this appendix, we evaluate certain reduced matrix elements [41], starting with $\langle J||\hat{\mathbf{J}}||J'\rangle$. First, note that $\hat{\mathbf{J}} = \left(\hat{J}_x, \hat{J}_y, \hat{J}_z\right)$ is a vector of angular momentum operators with spherical components $\hat{J}_0^{(1)} = \hat{J}_z$ and $\hat{J}_\pm^{(1)} = \mp \left(\hat{J}_x \pm i\hat{J}_y\right)/\sqrt{2}$. We can thus evaluate

$$\langle Jm|\hat{J}_0^{(1)}|J'm'\rangle = m\hbar\langle Jm|J'm'\rangle = m\hbar\delta_{JJ'}\delta_{mm'}. \tag{C.1}$$

This same matrix element can also be evaluated using the Wigner-Eckart theorem [Equation 2.18] to give

Appendix C. Evaluating reduced matrix elements

$$\langle Jm|\hat{J}_0^{(1)}|J'm'\rangle = \langle J'm';10|Jm\rangle\langle J||\hat{\mathbf{J}}||J'\rangle$$

$$= (-1)^{-J'+1-m}\sqrt{2J+1}\begin{pmatrix} J' & 1 & J \\ m' & 0 & -m \end{pmatrix}\langle J||\hat{\mathbf{J}}||J\rangle. \tag{C.2}$$

Since Equation C.1 is equal to Equation C.2, we can make the early simplification $J = J'$ and $m = m'$. The 3j-symbol is then evaluated explicitly using Mathematica [46] to obtain

$$\begin{pmatrix} J & 1 & J \\ m & 0 & -m \end{pmatrix} = (-1)^{-J+1-m}\frac{m}{\sqrt{J(2J+1)(J+1)}}. \tag{C.3}$$

Substituting this result into Equation C.2 gives us

$$\langle Jm|\hat{J}_0^{(1)}|Jm'\rangle = (-1)^{-J+1-m} \times (-1)^{-J+1-m}\frac{m\sqrt{2J+1}}{\sqrt{J(2J+1)(J+1)}}\delta_{mm'}\langle J||\hat{\mathbf{J}}||J\rangle. \tag{C.4}$$

Since $J + m$ is an integer, $(-1)^{-2(J+m-1)} = 1$, producing

$$\langle Jm|\hat{J}_0^{(1)}|Jm'\rangle = \frac{m}{\sqrt{J(J+1)}}\delta_{mm'}\langle J||\hat{\mathbf{J}}||J\rangle. \tag{C.5}$$

This also equals Equation (1), hence

$$m\hbar\delta_{mm'} = \frac{m}{\sqrt{J(J+1)}}\delta_{mm'}\langle J||\hat{\mathbf{J}}||J\rangle. \tag{C.6}$$

Finally, we obtain

$$\langle J||\hat{\mathbf{J}}||J\rangle = \hbar\sqrt{J(J+1)}. \tag{C.7}$$

We can interpret this result as the average expectation value of $\overline{\langle\hat{\mathbf{J}}\rangle} \equiv \sqrt{\langle\hat{\mathbf{J}}^2\rangle}$.

Next, to evaluate $\langle\ell'||\mathbf{r}||\ell\rangle$, we notice that $\mathbf{r}$ is a spherical vector operator, whose reduced matrix element can be determined using a similar process as above. The Wigner-Eckart theorem allows us to relate $\langle\ell'||\mathbf{r}||\ell\rangle$ to the matrix element $\langle\ell'm_{\ell'}|r_q^1|\ell m_\ell\rangle$, which itself can be evaluated via an integration of a product of spherical harmonics.

By equating the two, we obtain the result

$$\langle \ell'||\mathbf{r}||\ell\rangle = (-1)^{\ell'}\sqrt{\frac{3}{4\pi}(2\ell'+1)(2\ell+1)}\begin{pmatrix} \ell' & 1 & \ell \\ 0 & 0 & 0 \end{pmatrix}. \tag{C.8}$$

The 3j-symbol is only nonzero for $\ell = \ell' \pm 1$, according to the triangle inequality Equation 2.13.

Appendix D

Spectrum analyzer programming and examples

D.1 Introduction

The Rohde & Schwartz FSV3013 spectrum analyzer is a self-contained instrument. Its functionalities and operation are described in Section 7.8. All of its functionalities are accessible through the front-panel touchscreen and soft key interfaces. However, the user frequently changes many parameters and controls during a given measurement; especially when many repeated measurements are needed, entering commands one by one can quickly grow tedious. To automate the measurement and data storage process, we developed several Python code listings for sending command sequences to the spectrum analyzer. The underlying class structure listing and several exam-

ple script listings are included in this appendix. The code listings are thoroughly commented for clarity.

The code communicates with the spectrum analyzer via a LAN ethernet connection using PyVISA, a Python package wrapper of the National Instruments's VISA library. VISA is a free library and must be downloaded and installed onto the computer for PyVISA to operate. PyVISA creates a resource object (`rs`) that connects with the spectrum analyzer at its preset IP address. This address can be read from a front panel menu.

The Python program sends SCPI commands to the instrument to configure its various functionalities. A SCPI command has a specific syntax. A list of all the SCPI commands available to the spectrum analyzer can be found in its user manual. It's helpful to think of each command as accessing a specific memory register on the instrument; it can either query the data on that register or write a new value for it. For example, the command to query the RBW value ends with a question mark (``[SENSe:]BANDwidth[:RESolution]?''), while the write command ends with a space, a value, and unit (``[SENSe:]BANDwidth[:RESolution] 1 MHz''). (The quotes indicate this is an ASCII text string.) In these examples, the square brackets are not part of the command string: the characters inside the brackets are optional—they can be included for clarity, or omitted for brevity. The full form of the command indicates a hierarchical structure of memory registers in the instrument. Additionally, the lowercase characters in the command can also be safely omitted. Thus the following SCPI commands are all equivalent:

- ``SENSe:BANDwidth:RESolution 1 MHz''

- ``SENS:BAND:RES 1 MHz''

- ``BANDwidth 1 MHz''

- ''BAND:RES 1 MHz''

- ''BAND 1 MHz''

Always consult the user manual for the proper commands and syntax when programming.

D.2   Class structure

The main class structure is shown in Listing D.1. The parent `SpectrumChannel`
class is used for spectrum traces. From the initialization parameters, it configures the
channel settings (i.e. number and name), directory settings (i.e. save directory and file
formats), and spectrum settings (e.g. center freq., span, RBW). It also has methods
to mark spectral peaks and save data files. The daughter `TimeChannel` class inherits
from the parent class and programs other instrument parameters that are specific to
a time trace in zero-span mode. Both classes use public methods to run continuous
measurements of a single channel or to run a sequence of measurements from multiple
channels. There are also methods to save PNG files of front-panel screenshots; saving
images along with their CSV files allows for easy visual identification of file contents.

```
1  import pyvisa
2  from datetime import datetime as dt
3
4
5  class SpectrumChannel:
6      """Define the attributes and methods of a spectral channel."""
7
8      def __init__(self, res, name, idx, sdir, cfreq, span, rlev,
9                   vran=100, npts=1001, navg=0, rbw=10, vbw=None,
10                  atten=30, preamp=None, det='RMS', mode='AVER',
11                  ftag='', subdir=''):
12         self.res = res         # VISA resource reference
13         self.name = name       # Channel name
14         self.idx = idx         # Channel index
15         self.sdir = sdir       # Top directory save path
16         self.cfreq = cfreq     # Center frequency, in Hz
17         self.span = span       # Span, in Hz
18         self.rlev = rlev       # Reference level, in dBm
19         self.vran = vran       # Vertical range, in dB
20         self.npts = npts       # Number of points
21         self.navg = navg       # Number of trace averages
```

```python
22          self.atten = atten      # Internal attenuation
23          self.preamp = preamp    # Preamplifier value, in dB; off if None
24          self.det = det          # Detector setting
25          self.mode = mode        # Measurement mode
26          self.ftag = ftag        # File tag
27          self.subdir = subdir    # Subdirectory
28          self.rbw = rbw          # Resolution bandwidth, in Hz
29          if vbw is None:         # Video bandwidth
30              self.vbw = self.rbw
31              self.res.write('SENS:BWID:VID:AUTO ON')  # RBW-VBW coupling on
32              self.res.write('SENS:BWID:VID:RAT 1')  # RBW-VBW ratio equal.
33          else:
34              self.vbw = vbw
35
36          self.channel_settings()
37          self.dir_settings()
38          self.spectrum_settings()
39
40      def dir_settings(self):
41          """Set directory settings."""
42          self.day = dt.today().strftime('%y%m%d')  # Today's date, 'YYMMDD'
43          self.res.write(f'MMEM:CDIR "{self.sdir}"')  # Sets cwd to sdir
44          contents = self.res.query('MMEM:CAT?')  # Reads the contents of sdir
45          if self.day not in contents:
46              print('Day not found. Creating...')
47              self.res.write(f'MMEM:MDIR "{self.day}"')  # Creates today's dir
48          folder = self.sdir + self.day + "\\"
49
50          if self.subdir != "":  # FIXME?: Treat subdirectory paths better
51              self.subdir = self.subdir + "\\"
52          self.res.write(f'MMEM:CDIR "{folder}"')
53          self.res.write('FORM:DEXP:CSEP COMM')  # Comma-delimiting
54          self.res.write('FORM:DEXP:DSEP POIN')  # Point as a decimal separator
55          self.res.write('FORM:DEXP:FORM CSV')  # Set CSV format for trace files
56          self.res.write('FORM:DEXP:XDIS STAR')  # Set x-value def.: start-end
57          self.res.write('FORM:DEXP:TRAC SING')  # Export a single trace
58
59      def channel_settings(self):
60          """Set channel name and other settings."""
61          if self.idx == 1:  # FIXME: I don't like that it depends on user entry
62              # Renames the first default spectrum channel
63              ch_names = self.res.query('INST:LIST?')  # Query channel name
64              ch_names = ch_names.strip('\n').split(',')[1::2]  # Split to list
65              self.res.write(f'INST:REN {ch_names[self.idx-1]}, "{self.name}"')
66          else:
67              # Creates and renames a new channel
68              self.res.write(f'INST:CRE:NEW SANALYZER, "{self.name}"')
69
70      def spectrum_settings(self):
71          """Set spectrum analyzer measurement settings."""
72          self.res.write(f'INST:SEL "{self.name}"; *WAI')
73
74          self.res.write('INIT:CONT OFF')
75          self.res.write(f'SENS:WIND1:DET:FUNC {self.det}')  # Channel detector
76          self.res.write(f'DISP:WIND1:SUBW:TRAC1:MODE {self.mode}')  # Sets mode
77          self.res.write(f'SENS:SWE:COUN {self.navg}')  # Sets trace average num.
78          self.res.write(f'SENS:SWE:WIND{self.idx}:POIN {self.npts}')  # Pts num.
79
80          self.res.write(f'FREQ:CENT {self.cfreq}Hz')  # Sets center frequency
81          self.res.write(f'FREQ:SPAN {self.span}Hz')  # Sets span
82
83          self.res.write(f'DISP:WIND1:TRAC:Y:SCAL:RLEV {self.rlev}')  # Ref. lev.
```

251

```python
 84            self.res.write(f'DISP:WIND1:TRAC:Y:SCAL {self.vran}')  # Dynamic range
 85            self.res.write(f'INP:ATT {self.atten}dB')  # Input attenuator value
 86            if self.preamp in [15, 30]:
 87                self.res.write('INP:GAIN:STAT ON')  # Turns on preamp
 88                self.res.write(f'INP:GAIN:VAL {self.preamp}')  # Sets preamp value
 89
 90            self.res.write('SENS:BWID:RES:AUTO OFF')  # RBW-Span coupling off
 91            self.res.write(f'SENS:BWID:RES {self.rbw}Hz')  # Sets the RBW
 92
 93        def mark_peak(self, cent=False):
 94            """Switches to channel, turns on marker, returns auto peak search."""
 95            self.res.write(f'INST:SEL "{self.name}";*WAI')
 96            self.res.write('CALC1:MARK1:STAT ON;*WAI')  # Marker on; peak search
 97            if cent:  # Marker to central frequency
 98                self.res.write(f'CALC1:MARK1:X {self.cfreq}Hz')
 99
100            pos = float(self.res.query('CALC1:MARK1:X?; *WAI'))  # Marker X-pos.
101            amp = float(self.res.query('CALC1:MARK1:Y?; *WAI'))  # Marker Y-pos.
102            return pos, amp
103
104        def save_trace(self, fn, ss=False):
105            """Save trace data to USB file."""
106            self.res.write(f'INST:SEL "{self.name}";*WAI')  # Select channel
107            file_path = self.subdir + fn + self.ftag  # File path
108            file_path_csv = file_path + ".CSV"
109            self.res.write(f'MMEM:STOR1:TRAC 1, "{file_path_csv}"')  # Saves file
110
111            if ss:  # save screenshot of individual trace
112                self.res.write('DISP:FORM SING')  # Display single channel
113                screenshot(self.res, file_path)
114
115
116 class TimeChannel(SpectrumChannel):
117     """Define the attributes and methods of a time-domain channel."""
118
119     def __init__(self, res, name, idx, sdir, cfreq, span, rlev,
120                  vran=100, npts=1001, navg=0, rbw=10, vbw=None,
121                  atten=30, preamp=None, det='RMS', mode='AVER',
122                  ftag='', subdir='', swtime=None):
123         SpectrumChannel.__init__(self, res, name, idx, sdir, cfreq, span,
124                                  rlev, vran=vran, npts=npts, navg=navg,
125                                  rbw=rbw, vbw=vbw, atten=atten, preamp=preamp,
126                                  det=det, mode=mode, ftag=ftag, subdir=subdir)
127
128         self.swtime = swtime  # Sweep time, in seconds
129         self.res.write('FREQ:SPAN 0Hz')  # Sets zero span mode
130         self.res.write('SENS:SWE:TIME:AUTO OFF')  # Turns off auto sweep time
131         self.res.write(f'SENS:SWE:TIME {self.swtime}s')
132
133         self.res.write('TRIG:SEQ:SOUR EXT2')
134         self.res.write('TRIG:LEV:EXT2 1.4V')
135         self.res.write('TRIG:HOLD: 0s')
136
137
138 def screenshot(res, fn):
139     """Save a single screenshot."""
140     cwd = res.query('MMEM:CDIR?').strip('\n').strip('\'')  # Read cwd
141     file_path_png = cwd + fn + ".PNG"  # file path
142     res.write(f'MMEM:NAME "{file_path_png}"')  # Configure the PNG file
143     res.write('HCOP:CMAP:DEF4')  # Same colors as the screen
144     res.write('HCOP:IMM')  # Save the screenshot
145
```

```
146
147  def multi_screenshot(res, fn):
148      """Save screenshot in MultiView."""
149      res.write('DISP:FORM SPL')  # Display split MultiView
150      screenshot(res, fn)
151
152
153  def run_sequence(res):
154      """Run a sequence measurement."""
155      res.write('DISP:FORM SPL')
156      res.write('SYST:SEQ ON')  # Enables sequencer
157      res.write('INIT:SEQ:MODE SING')  # Single sequence
158      res.write('INIT:SEQ:IMM;*OPC?')  # Runs sequence
159
160
161  def run_continuous(res, name=''):
162      """Run a continuous measurement."""
163      res.write('DISP:FORM SING')
164      res.write(f'INST:SEL "{name}";*WAI')  # Select channel
165      res.write('INIT:CONT ON')  # Single sequence
166
167  def stop_continuous(res):
168      res.write('INIT:CONT OFF')  # Single sequence
```

Listing D.1: The class description of the code used for programming the R&S spectrum analyzer.

D.3   Example scripts

Listing D.2 demonstrates how to program the basic spectral trace functionality of the instrument. The SETUP block forms a new connection with the instrument and resets it to a default state. The CHANNEL PARAMETERS block creates variables of the various spectral channel parameters. The RUN MEASUREMENT block initializes a SpectrumChannel object named gen_ch using the parameter variables and begins a measurement sequence. The final block saves the data trace and screenshot.

Listing D.3 demonstrates how to program the measurement of a zero-span time trace at a given frequency. Specifically, this code was used to measure signal amplitude drifts over about 1.4 hours. The code samples 1000 traces separated by 5 seconds, marking and saving the time and amplitude of a target peak. Because the SETUP and PARAMETERS blocks are largely identical to those in Listing D.2, these are omitted.

Finally, Listing D.4 demonstrates how to initialize multiple channels and measure

each in a sequence. Specifically, we create a spectrum (`gen_s_ch1`) and zero-span (`gen_z_ch2`) channel objects, and then save their trace data. In this listing, the `SETUP` and `PARAMETERS` blocks are included for clarity.

```python
1  import pyvisa
2  import numpy as np
3  from sanalyzer import (SpectrumChannel, run_sequence, save_trace)
4
5
6  # SETUP
7  rm = pyvisa.ResourceManager()
8  rs = rm.open_resource('TCPIP0::169.254.32.226::inst0::INSTR')
9  rs.timeout = 25000  # Set the timeout to 25 seconds
10 idn = rs.query('*IDN?')
11 print(idn)
12 rs.write('*RST')  # Resets to default state
13 rs.write('*CLS')  # Clears status
14 psc = int(rs.query('*PSC?'))  # Checks power-on-status-clear
15 if psc != 1:
16     raise SystemError("Power-on-status-clear is False.")
17 rs.write('SYST:DISP:UPD ON')  # Enables display during remote control
18
19 rs.write('SENS:ROSC:EXT:FALL ON')  # FIXME: Ref. fallback
20 rs.write('SENS:ROSC:EXT:SOUR EXT')  # Sets clock reference to external
21
22
23 # CHANNEL PARAMETERS
24 CH_NAME = 'Gen Spectrum'
25 IDX = 1
26 SAVE_DIR = "D:\\spectrum analyzer\\"
27 SUB_DIR = "test"
28 FILE_NAME = "all_screens_"
29 num = '0'
30 tag = ''
31
32 CLOCK_FREQ = 6834682612.904  # Atomic transition frequency, in Hz
33 LO_FREQ = 76.6e6  # AOM shift frequency for the LO beam, in Hz
34 gen_freq = CLOCK_FREQ + LO_FREQ  # Central generated frequency
35 SPAN = 50e3  # Span, in Hz
36 RLEV = -80  # Reference level, in dBm
37 VRAN = 50  # The vertical dynamic range, in dB
38 ATTEN = 0  # Attenuation, in dB
39 RBW = 20  # Resolution bandwidth, in Hz
40 NPTS = 1001  # Number of sweep points
41 NAVG = 8  # Number of averages
42 LO_RLEV = -80  # Ref. level for LO signals
43 GEN_RLEV = -110  # Ref. level for generated signals
44
45
46 # RUN MEASUREMENT
47 gen_ch = SpectrumChannel(rs, CH_NAME, IDX, SAVE_DIR,
48                          gen_freq, SPAN, GEN_RLEV, vran=VRAN,
49                          rbw=RBW, npts=NPTS, navg=NAVG, atten=0,
50                          preamp=15, det='RMS', mode='AVER',
51                          subdir=SUB_DIR, ftag=tag)
52 run_sequence(rs)
53
54
55 # SAVE TRACE DATA & SCREENSHOT
56 gen_ch.save_trace('gentrace_' + num, ss=True)
57 print('Operation Complete!')
```

Listing D.2: Code used to collect and save a spectrum trace with a span of 50 kHz around the generated frequency 6.911 GHz, an RBW of 20 Hz, averaged 8 times.

```python
53  NSAMPLES = 1000
54
55  # This initializes a channel in zero-span mode.
56  gen_zs_ch = TimeChannel(rs, NAME, 1, SAVE_DIR,
57                          sum_freq, SPAN, GEN_RLEV, vran=GEN_VRAN,
58                          rbw=RBW, npts=NPTS, navg=NAVG, atten=ATTEN,
59                          preamp=None, det='RMS', mode='AVER',
60                          subdir=SUB_DIR, swtime=SWTIME)
61
62  poss, amps, times = [], [], []
63  # Start a continuous measurement. This is generally not recommended in remote
64  # mode because you don't know a priori when a sweep will termninate.
65  # We can get around it by averaging for a long time; shot-to-shot variations
66  # are more negligible.
67  run_continuous(rs, NAME)
68  sleep(10)  # Average for enough time, in s.
69  for i in tqdm(range(NSAMPLES)):
70      time = dt.now()
71      pos, amp = gen_zs_ch.mark_peak()  # Measure the height of the peak
72      poss.append(pos)
73      amps.append(amp)
74      times.append(time)
75      sleep(5)  # Wait a certain amount of time, in s.
76
77  stop_continuous(rs)
78  poss = np.array(poss)
79  amps = np.array(amps)
80  times = np.array(times)
```

Listing D.3: Excerpt from code used to collect and save the peak power of an averaged pulse in zero-span mode at the generated frequency 6.911 GHz with an RBW of 2 MHz, a sweep time of 20 μs. This is repeated 1000 times over 1.4 hours. This helps identify and characterize long-term drifts in the signal amplitude.

```python
import pyvisa
from sanalyzer import (SpectrumChannel, run_sequence, multi_screenshot,
                       TimeChannel)

rm = pyvisa.ResourceManager()
# rm.list_resources()
rs = rm.open_resource('TCPIP0::169.254.32.226::inst0::INSTR')
rs.timeout = None  # Set the timeout to infinty seconds
idn = rs.query('*IDN?')
print(idn)

rs.write('*RST')  # Resets to default state
rs.write('*CLS')  # Clears status
psc = int(rs.query('*PSC?'))  # Checks power-on-status-clear
if psc != 1:
    raise SystemError("Power-on-status-clear is False.")
rs.write('SYST:DISP:UPD ON')  # Enables display during remote control

rs.write('SENS:ROSC:EXT:FALL ON')  # FIXME: Ref. fallback
rs.write('SENS:ROSC:EXT:SOUR EXT')  # Sets clock reference to external

CH_NAME = 'Gen Spectrum'
# IDX = 1
SAVE_DIR = "D:\\spectrum analyzer\\"
SUB_DIR = "sweep"
FILE_NAME = "all_screens_"
num = '01'  # FIXME: Make file update automatic
num = num.zfill(2)  # Make sure file num. is zero-padded

EOM_FREQ = 0.0e3  # EOM drive frequency, in Hz
CLOCK_FREQ = 6834682612.904  # Atomic transition frequency, in Hz
LO_FREQ = 76.6e6  # AOM shift frequency for the LO beam, in Hz

sum_freq = CLOCK_FREQ + LO_FREQ
# diff_freq = CLOCK_FREQ - LO_FREQ

SPAN_s = 1e6  # Span for spectrum channel, in Hz
SPAN_z = 0e3  # Span for zero-span channel, in Hz
ATTEN = 0  # Attenuation, in dB
RBW_s = 20  # Resolution bandwidth for spectrum channel, in Hz
RBW_z = 2e6  # Resolution bandwidth for zero-span channel, in Hz

NPTS = 1001  # Number of sweep points
NAVG_s = 10  # Number of averages for spectrum channel
NAVG_z = 1000  # Number of averages for zero-span channel
SWTIME = 20e-6  # Sweep time, in s


RLEV_s = -74  # Ref. level for spectrum channel, in dBm
RLEV_z = -74  # Ref. level for zero-span channel, in dBm
VRAN_s = 20  # The vertical dynamic range for spectrum channel, in dB
VRAN_z = 6  # The vertical dynamic range for zero-span channel, in dB
NAME_s = 'Gen (spectrum)'
NAME_z = 'Gen (zero-span)'
NSAMPLES = 1

# This initializes a channel in zero-span mode.
gen_s_ch1 = SpectrumChannel(rs, NAME_s, 1, SAVE_DIR,
                            sum_freq, SPAN_s, RLEV_s, vran=VRAN_s,
                            preamp=None, det='RMS', mode='AVER', navg=NAVG_s,
                            subdir=SUB_DIR)
```

```
63  gen_z_ch2 = TimeChannel(rs, NAME_z, 2, SAVE_DIR,
64                          sum_freq, SPAN_z, RLEV_z, vran=VRAN_z,
65                          preamp=None, det='RMS', mode='AVER', navg=NAVG_z,
66                          subdir=SUB_DIR, swtime=SWTIME)
67
68
69  run_sequence(rs)
70
71  gen_s_ch1.save_trace('spectrum_' + num, ss=True)
72  gen_z_ch2.save_trace('zspan_' + num, ss=True)
73  multi_screenshot(rs, SUB_DIR + '\\' + FILE_NAME + num)
74  print('Operation Complete!')
```

Listing D.4: Code to capture spectral and time traces of the generated signal in two chanels in a sequence.

Appendix E

Non-dimensionalization of the Gross-Pitaevskii equation

Nonlinear systems are notoriously difficult or impossible to solve using the same analytical techniques developed for linear ones, and generally numerical methods are employed. This is true for a Gross-Pitaevskii equation that describes a trapped Bose-Einstein condensate with Raman coupling. In this appendix, we outline the steps taken to express the GPE in a way that can be readily solved with numerics, as demonstrated in Chapter 9. This involves reducing the number of dimensions, discretizing real and momentum space, and recasting physical quantities into dimensionless units. Although this construction is eventually applied to a two-component spinor condensate in Chapter 9, we consider here only a scalar BEC wavefunction.

E.1 Reduction to 2D

The GPE is most naturally an equation of a complex-valued BEC wavefunction $\Phi_r(x, y, z)$ in real three-dimensional space. The BEC is composed of atoms with mass m and generally resides in a 3D trapping potential of the form

$$V(x, y, z) = \frac{1}{2} m \left(\omega_x^2 x^2 + \omega_y^2 y^2 + \omega_z^2 z^2 \right), \tag{E.1}$$

where the trap frequencies along the three axes are $(\omega_x, \omega_y, \omega_z) \equiv \omega \times (1, \gamma, \eta)$. Accurately representing Φ on a 3D grid is very resource-intensive. We can simplify the problem by reducing the dimensionality to 2D. If we assume that $\eta \gg 1$, the BEC will be confined tightly in a "pancake-shaped" trap in the x-y plane, equivalent to the trapping potential produced by a 1D optical lattice [174]. We assume that no dynamics occur along the z-direction and the wavefunction can be separated as

$$\Phi_r(x, y, z) = \phi_r(x, y) \otimes \psi_r(z), \tag{E.2}$$

where the ansatz for the z-component is

$$\psi_r(z) = \left(\frac{m \omega_z}{\pi \hbar} \right)^{1/4} e^{-z^2/2a_z^2}. \tag{E.3}$$

This Gaussian profile is the ground state wavefunction of a 1D quantum harmonic oscillator with frequency $\omega_z = \eta \omega$, where the harmonic oscillator length along the $\hat{e}_i$ axis is $a_i = \sqrt{\hbar/m\omega_i}$. When the kinetic energy of the BEC is negligibly small, the analytic solution $\phi(x, y)$ of the scalar GPE is the usual Thomas-Fermi wavefunction,

$$\phi_r^{(\text{TF})}(x, y) = \sqrt{\frac{\mu - V(x, y, 0)}{g^{2D}}}, \tag{E.4}$$

where

$$g^{2D} = \frac{g^{3D}}{a_z \sqrt{2\pi}} \tag{E.5a}$$

$$= \frac{1}{a_z \sqrt{2\pi}} \left(\frac{4\pi \hbar^2 a_{\text{sc}}}{m} \right) \tag{E.5b}$$

is the two-dimensional scattering coupling strength, and a_{sc} is the s-wave scattering length [174]. The chemical potential μ is the energy that normalizes $\Phi_r(x, y, z)$ to the atom number N for a given $V(x, y, z)$.

E.2 Dimensionless scales

We identify characteristic energy, time, and length scales for non-dimensionalizing the energies and wavefunctions. The potential energy definition of Equation E.1 lends a natural energy scale of $\hbar\omega$. Its inverse gives the time scale $\tau = 2\pi/\omega$; for a typical trap frequency of $\omega = 2\pi \times 100$ Hz, $\tau = 10$ ms. The natural length scale is the corresponding harmonic oscillator length

$$a = \sqrt{\frac{\hbar}{m\omega}} \approx 1 \ \mu\text{m}. \tag{E.6}$$

In subsequent sections, dimensionless quantities are identified by a tilde $\sim$ accent. For example, the Raman recoil momentum k_L is rescaled as $\tilde{k}_L \equiv k_L a$, and the recoil energy $E_L = \hbar^2 k_L^2/2m$ becomes $\tilde{E}_L \equiv \tilde{k}_L^2/2$. Other unitless Raman frequency parameters, such as the Rabi frequency $\tilde{\Omega}$, detuning $\tilde{\delta}$, and quadratic Zeeman shift $\tilde{\epsilon}$, are expressed in units of the natural trap frequency ω. Additionally, if the detuning energy exhibits a spatial gradient as

$$\hbar\delta(x) \equiv \hbar\delta' x, \tag{E.7}$$

its dimensionless form is

$$\tilde{\delta}(\tilde{x}) \equiv \frac{\hbar\delta' x}{\hbar\omega} \frac{a}{a} = \tilde{\delta}' \tilde{x}, \tag{E.8}$$

where $\tilde{\delta}'$ has units of ω/a.

E.3   Position and momentum coordinates

The spinor wavefunction ϕ_r is numerically approximated on 2D grids of $[N_x, N_y] = [2^n, 2^m] : n, m \in \mathbb{Z}$ points in real position space and momentum space. Throughout the computation algorithm described in Section 9.4, we repeatedly Fourier transform ϕ_r between the two to avoid gradients in the time-evolution operators. This requires we maintain two sets of grid arrays for the wavefunction in each domain. All real-space coordinates $\mathbf{r} = (x, y, z)$ are rescaled such that $\tilde{\mathbf{r}} \equiv \mathbf{r}/a$. Additionally, we rescale the momentum-space coordinates $\mathbf{k} = (k_x, k_y, k_z)$ as $\tilde{\mathbf{k}} \equiv \mathbf{k}a$. Since the position and momentum space coordinates are scaled oppositely, the Fourier transforms are unaffected.

E.4   Normalization of the wavefunctions

We observe that $\psi_r(z)$ in Equation E.3 has units of $\text{m}^{-1/2}$. To make it unitless, we multiply ψ_r by $a^{1/2}$, using the fact that

$$a_z = a\eta^{-1/2} \tag{E.9}$$

and $\tilde{z} \equiv z/a$, to obtain

$$\tilde{\psi}_r(\tilde{z}) = \left(\frac{\eta}{\pi}\right)^{1/4} e^{-\eta\tilde{z}^2/2}. \tag{E.10}$$

As expected, the probability density of $\tilde{\psi}_r$ is properly normalized,

$$\int_{-\infty}^{\infty} |\tilde{\psi}_r(\tilde{z})|^2 d\tilde{z} = 1. \tag{E.11}$$

The Fourier transform of ψ_r,

$$\mathcal{F}\{\tilde{\psi}_r(\tilde{z})\} \equiv \tilde{\psi}_k(\tilde{k}_z) = \int_{-\infty}^{\infty} \left(\frac{\eta}{\pi}\right)^{1/4} e^{-\eta\tilde{z}^2/2} e^{-2\pi i\tilde{z}\tilde{k}_z} d\tilde{z}, \tag{E.12a}$$

$$= \left(\frac{\eta}{\pi}\right)^{1/4} \sqrt{\frac{2\pi}{\eta}} e^{-2\pi^2/\eta \, \tilde{k}_z^2}, \tag{E.12b}$$

has a probability density that is also properly normalized,

$$\int_{-\infty}^{\infty} |\tilde{\psi}_k(\tilde{k}_z)|^2 d\tilde{k}_z = 1. \tag{E.13}$$

During the numerical propagation steps, the non-commutivity of evolution operators introduce non-unitary errors on $\tilde{\phi}_r$ and $\tilde{\phi}_k$. Normalization to the total atom number is enforced at each step by summing over the square of the position wavefunction grids and multiplying by the grid spacings

$$\sum_{\tilde{x}_i} \sum_{\tilde{y}_j} |\tilde{\phi}_r(\tilde{x}_i, \tilde{y}_j)|^2 \Delta\tilde{x}\Delta\tilde{y} \overset{!}{=} N. \tag{E.14}$$

In reciprocal space, the sum is multiplied by $\Delta\tilde{k}_x\Delta\tilde{k}_y$ and also by $(N_x N_y)^2$, due to the way the way the 2D discrete-FFTs are computed, to get the condition

$$\sum_{\tilde{k}_{xi}} \sum_{\tilde{k}_{yj}} |\tilde{\phi}_k(\tilde{k}_{xi}, \tilde{k}_{yj})|^2 (N_x N_y)^2 \Delta\tilde{k}_x\Delta\tilde{k}_y \overset{!}{=} N. \tag{E.15}$$

E.5 Dimensionless energies

Potential

We first consider the potential energy components of Equation E.1 in the x-y plane. The dimensionless potential energy is obtained by dividing this by $\hbar\omega$ and substituting $\mathbf{x} = \tilde{\mathbf{x}}a$. Factors of a^2 cancel to produce

$$\tilde{V}(\tilde{x}, \tilde{y}) = \frac{1}{2}\left(\tilde{x}^2 + \gamma^2\tilde{y}^2\right). \tag{E.16}$$

Kinetic

In the momentum basis, the kinetic energy term of the GPE Hamiltonian takes the form

$$K(\mathbf{k}) = \frac{\hbar^2\mathbf{k}^2}{2m}. \tag{E.17}$$

Similarly, by substituting $\mathbf{k} = \tilde{\mathbf{k}}/a$, and dividing by $\hbar\omega$, we find that factors of a^2 also cancel, leaving the dimensionless kinetic energy

$$\tilde{K}(\tilde{\mathbf{k}}) = \frac{1}{2}\tilde{\mathbf{k}}^2. \tag{E.18}$$

If we instead began with the Raman kinetic energy term

$$K_R(k_x) = \frac{\hbar^2}{2m}(k_x \pm k_L)^2, \tag{E.19}$$

its dimensionless form is

$$\tilde{K}(\tilde{k}_x) = \frac{1}{2}\tilde{k}_x^2 \pm \tilde{k}_L\tilde{k}_x, \tag{E.20}$$

where the constant energy offset $\tilde{k}_L^2$ has been removed.

Interaction

The GPE Hamiltonian also has a nonlinear scattering interaction term with energy

$$g^{2D}|\phi(x,y)|^2, \tag{E.21}$$

where we notice that the scattering coupling strength has units of $[\mathrm{J}\cdot\mathrm{m}^2]$. Its dimensionless form is obtained by substituting Equation E.9 into E.5b, dividing by $\hbar\omega \cdot a^2$, and simplifying to get

$$\tilde{g}^{2D} = \tilde{a}_{sc}\sqrt{8\eta\pi}, \tag{E.22}$$

where $\tilde{a}_{sc} \equiv a_{sc}/a$. ^{87}Rb has a scattering length of $a_{sc} = 100.4\ a_0$, where a_0 is the Bohr radius, giving $\tilde{a}_{\mathrm{sc}} \simeq 4.9 \times 10^{-3}$.

Chemical potential

Finally, we are in a position to determine the dimensionless chemical potential $\tilde{\mu}$ for the particular trapping geometry and atom number N in the Thomas-Fermi approximation. This is done by evaluating the integral of the Thomas-Fermi probabilty

density $\left|\tilde{\Phi}^{(\mathrm{TF})}\right|^2$ over all space and equating it to the atom number.

$$N = \int \left|\tilde{\Phi}_r(\tilde{x}, \tilde{y}, \tilde{z})\right|^2 d\tilde{V} = \int \left|\frac{\tilde{\mu} - \tilde{V}(\tilde{x}, \tilde{y})}{\tilde{g}^{2D}}\right| \left|\tilde{\psi}_r(\tilde{z})\right|^2 d\tilde{x}\, d\tilde{y}\, d\tilde{z} \qquad \text{(E.23)}$$

The integral over $\tilde{z}$ evaluates to 1, and we substitute Equations E.16 and E.22 to obtain

$$N = \frac{1}{2\tilde{a}_{sc}\sqrt{8\eta\pi}} \int \left[2\tilde{\mu} - (\tilde{x}^2 + \gamma^2\tilde{y}^2)\right] d\tilde{x}\, d\tilde{y}. \qquad \text{(E.24)}$$

With the substitutions $2\tilde{\mu} \to A^2$, $\tilde{x} \to u$, $\gamma\tilde{y} \to v$, the integral becomes

$$N = \frac{1}{2\tilde{a}_{sc}\gamma\sqrt{8\eta\pi}} \int \left[A^2 - (u^2 + v^2)\right] du\, dv, \qquad \text{(E.25)}$$

where the integrand is the equation of a circle with radius A. Making an additional substitution $u^2 + v^2 \to r^2$, we integrate along r from 0 to A (the wavefunction is zero outside of the Thomas-Fermi profile) as

$$N = \frac{\pi}{\tilde{a}_{sc}\gamma\sqrt{8\eta\pi}} \int_0^A \mathrm{d}r\, r\left(A^2 - r^2\right) = \sqrt{\frac{\pi}{8\eta}} \left(\frac{1}{\tilde{a}_{sc}\gamma}\right) \left(\frac{1}{4}A^4\right). \qquad \text{(E.26)}$$

Replacing the substituted value for A^2, we obtain the expression

$$N = \frac{1}{2}\sqrt{\frac{\pi}{2\eta}} \left(\frac{\tilde{\mu}^2}{\tilde{a}_{sc}\gamma}\right), \qquad \text{(E.27)}$$

or rearranging to get

$$\tilde{\mu} = \frac{1}{2}\left(16N\tilde{a}_{sc}\sqrt{\frac{\eta\gamma^2}{2\pi}}\right)^{1/2}. \qquad \text{(E.28)}$$

The factor of $\sqrt{2\pi}$ comes from our transforming the 3D scattering coupling strength to a two-dimensional form; the $\eta\gamma^2$ term comes from the asymmetry of the trapping potential; the power of $1/2$ reflects the two-dimensional character of our problem, in contrast to the $2/5$ power found in [175] arising from a 3D trap. We also define the Thomas-Fermi radius $\tilde{x}_{\mathrm{rad}}$ as the distance along the $\tilde{x}$-axis where the Thomas-Fermi

profile terminates at zero, or

$$\tilde{x}_{rad} \equiv A = \sqrt{2\tilde{\mu}} = \left(16N\tilde{a}_{sc}\sqrt{\frac{\eta\gamma^2}{2\pi}}\right)^{1/4}. \qquad (E.29)$$

In general, the calculated BEC wavefunctions will not have the same form as the Thomas-Fermi one. However, this chemical potential and radius give rough estimates of the energy and size of the BEC for a given trapping geometry and atom number.

Appendix F

Open-source `spinor-gpe` Python package

`spinor-gpe` is high-level, object-oriented Python package for numerically solving the quasi-2D, psuedospinor (two component) Gross-Piteavskii equation (GPE), for both ground state solutions and real-time dynamics. This project grew out of a desire to make high-performance simulations of the GPE more accessible to the entering researcher.

While this package is primarily built on NumPy, the main computational heavy-lifting is performed using PyTorch, a deep neural network library commonly used in machine learning applications. PyTorch has a NumPy-like interface, but a back-end that can run either on a conventional processor or a CUDA-enabled NVIDIA(R)

graphics card. Accessing a CUDA device will provide a significant hardware acceleration of the simulations.

This package has been tested on Windows, Mac, and Linux systems.

F.1   Installation

F.1.1   Dependencies

The dependencies for `spinor-gpe` can be installed directly into a new `conda` virtual environment `spinor` using the `environment.yml` file included with the package:

```
1   conda env create --file environment.yml
```

This installation may take a while.

Note: The version of CUDA used in this package does not support macOS. Users on these computers may still install PyTorch and run the examples on their CPU. To install correctly on macOS, remove the ``- cudatoolkit=11.1'' line from the `environment.yml` file. After installation, you will need to modify the example code to run on the cpu device instead of the cuda device.

The above dependencies can also be installed manually using conda into a virtual environment:

```
1   conda activate <new_virt_env_name>
2   conda install pytorch torchvision torchaudio cudatoolkit=11.1 -c
     pytorch -c conda-forge
3   conda install numpy matplotlib tqdm scikit-image ffmpeg spyder
```

For more information on installing PyTorch, see its installation instructions page. To verify that Pytorch was installed correctly, you should be able to import it:

```
1   import torch
2   >>> x = torch.rand(5, 3)
3   >>> print(x)
4   tensor([[0.2757, 0.3957, 0.9074],
5   [0.6304, 0.1279, 0.7565],
6   [0.0946, 0.7667, 0.2934],
7   [0.9395, 0.4782, 0.9530],
```

Name	Version	Purpose
Primary Packages		
Numpy		
PyTorch	$\geq 1.8.0$	
cudatoolkit	≥ 11.1	
Additional Packages		
matplotlib		Visualizing results
tqdm		Progress messages
scikit-image		Matrix signal processing
ffmpeg	$= 4.3.1$	Animation generation

Table F.1: Python package dependencies for installing the `spinor-gpe` package.

```
8    [0.2400, 0.0020, 0.9569]])
```

Listing F.1: Verify PyTorch installation

Also, if you have an NVIDIA GPU, you can test that it is available for GPU computing:

```
1    >>> torch.cuda.is_available()
2    True
```

Listing F.2: Verify PyTorch installation

F.2 Basic Operation

This package has a simple, object-oriented interface for imaginary- and real-time propagations of the pseudospinor-GPE. While there are other operations and features to this package, all simulations will have the following basic structure:

1. Setup: Data path and PSpinor object

```
1    >>> import pspinor as spin
```

```
2   >>> DATA_PATH = '<project_name >/Trial_XXX '
3   >>> ps = spin.PSpinor ( DATA_PATH )
```
<div align="center">Listing F.3: Setup example</div>

The program will create a new directory **DATA_PATH**, in which the data and results from this simulation trial will be saved. If **DATA_PATH** is a relative path, as shown above, then the trial data will be located in the **/data/** folder. When working with multiple simulation projects, it can be helpful to specify a **<project_name>** directory; furthermore, the form **Trial_XXX** is convenient, but not strictly required.

2. Run: Begin Propagation

The example below demonstrates imaginary-time propagation. The method **PSpinor.imaginary** performs the propagation loop and returns a **PropResult** object. This object contains the results, including the final wavefunctions and populations, and analysis and plotting methods (described below).

```
1   >>> DT = 1/50
2   >>> N_STEPS = 1000
3   >>> DEVICE = 'cuda '
4   >>> res = ps.imaginary(DT, N_STEPS , DEVICE , is_sampling=True ,
     n_samples =50)
```
<div align="center">Listing F.4: Run example</div>

For real-time propagation, use the method **PSpinor.real**.

3. Analyze: Plot the results

PropResult provides several methods for viewing and understanding the final results. The code block below demonstrates several of them:

```
1   >>> res.plot_spins ()   # Plots the spin-dependent densities and
     phases .
2   >>> res.plot_total ()   # Plots the total densities and phases .
3   >>> res.plot_pops ()    # Plots the spin populations throughout the
     propagation .
```

```
4    >>> res.make_movie()   # Generates a movie from the sampled
     wavefunctions.
```

Listing F.5: Analysis example

Note that `PSpinor` also exposes methods to plot the spin and total densities. These can be used independent of `PropResult`:

```
1    >>> ps.plot_spins()
```

4. Repeat

Likely you will want to repeat or chain together different segments of this structure.

F.3   Examples

Examples of this package demonstrating evolution in imaginary (ground-state solutions) and real time (dynamics) can be found at the package documentation at https://spinor-gpe.readthedocs.io/en/latest/source/auto_examples/index.html.